

University of St Andrews



Full metadata for this thesis is available in
St Andrews Research Repository
at:

<http://research-repository.st-andrews.ac.uk/>

This thesis is protected by original copyright

*Continuous-wave, singly-resonant
optical parametric oscillation
internal to the Ti:sapphire laser*



Thomas J Edwards MSci.

A thesis submitted to the University of St Andrews
in application for the degree of Doctor of Philosophy

30th September 2000



Tr D 846

Declarations

I, Thomas John Edwards, hereby certify that this thesis, which is approximately 45,000 words in length, has been written by me, that it is the record of the work carried out by me and that it has not been submitted in any previous application for a higher degree.

Thomas J Edwards

30th September 2000

I was admitted as a research student in October 1996 and as a candidate for the degree of Doctor in Philosophy in October 1996; the higher study for which this is a record was carried out in the University of St Andrews between 1996 and 2000

Thomas J Edwards

30th September 2000

We hereby certify that the candidate has fulfilled the conditions of the Resolution and Regulations appropriate for the degree of Doctor of Philosophy in the University of St Andrews and that the candidate is qualified to submit this thesis in application for that degree.

Malcolm H. Dunn

30th September 2000

Majid Ebrahimzadeh

30th September 2000

Copyright Declaration

In submitting this thesis to the University of St Andrews I understand that I am giving permission for it to be made available for use in accordance with the regulations of the University Library for the time being in force, subject to any copyright vested in the work not being affected thereby. I also understand that the title and abstract will be published, and that a copy of the work may be made and supplied to any *bona fide* library or research worker.

Thomas J Edwards

30th September 2000

Acknowledgements

Thanks go to friends, colleagues, my supervisors and family for all your support. Finally, a small debt of thanks to P.S. Mirade and J.D. Daudin for reminding of the need to get out more often [1].

- 1 P. S. Mirade and J. D. Daudin, "A numerical study of the airflow patterns in a sausage dryer," *Drying Technology* **18**, 81-97 (2000).

Abstract

This thesis details the experimental implementation of a novel continuous-wave (cw) optical parametric oscillator configuration: the singly-resonant intracavity optical parametric oscillator (ICSRO). This device utilises the high circulating field found within a laser cavity to drive the high-threshold parametric process of the singly-resonant configuration. The optical parametric oscillator (OPO) efficiently converts the resonant laser field into two broadly tunable coherent fields of lower photon energy. In this way, a coherent source generating Watt-level output at near to mid-infrared wavelengths is realised.

Background principles and design considerations are presented with reference to the frequency conversion of the Ti:sapphire laser. Four separate ICSRO devices are characterised. The first is based on the conventional birefringent nonlinear material KTiOAsO_4 . This device operates with efficiencies approaching 90% and generates Watt-level output powers within the 1 to 3 μm spectral range limited by mirror coating bandwidths.

The second ICSRO configuration is based on the nonlinear material periodically poled LiNbO_3 (PPLN). The wide degree of temperature tunability accessible from this material, coupled with the broad tunability of the Ti:sapphire laser provides a means of generating integer ratio frequency outputs. Thermal lensing in the PPLN crystal is found to limit ICSRO power scaling.

Chapter 6 describes an ICSRO based on periodically poled RbTiOAsO_4 . This represents the first observation of cw OPO operation using this nonlinear material. The flexibility of the ICSRO pumping approach is well illustrated by the operation of this device using a nonlinear crystal with just 4.5mm of interaction length.

The ICSRO configuration is extended to the nonlinear material periodically poled KTiOPO_4 (PPKTP). This material is shown to exhibit a useful degree of temperature tuning. Uncertainties in the published Sellmeier data for KTiOPO_4 highlight an important aspect of the Ti:sapphire-pumped scheme in that the laser may be tuned to accommodate discrepancies between theoretical quasi-phase-matched grating performance and actual phase-matched measurements. The PPKTP ICSRO is further configured in a ring-cavity design, enabling the generation of single-frequency idler output at powers exceeding 100mW. The ring design is far from optimised and substantial increments in power performance are envisioned.

The work presented in this thesis is well placed to form a complementary component of current cw OPO research. It imparts a broad perspective of the potential offered by the ICSRO approach and clearly demonstrates this potential through the use of a diverse range of nonlinear materials. Clear possibilities for further refinements and research are detailed.

Table of contents

1. Introduction

1.1	Background.....	1
1.2	The cw optical parametric oscillator.....	2
1.3	Thesis summary.....	5
	Chapter 1 references.....	6

2. Nonlinear Optics & Phase-Matching

2.1	Introduction.....	9
2.2	Theoretical aspects.....	9
2.2-1	Linear - Nonlinear optical polarisation.....	10
2.2-2	Second-order nonlinear interaction.....	11
2.2-3	Frequency mixing via the $\chi^{(2)}$ interaction.....	12
2.2-4	Magnitude of the $\chi^{(2)}$ interaction.....	13
2.3	Coupled wave equations.....	17
2.3-1	The Maxwell wave equation & nonlinear coupling.....	17
2.4	Focussed Gaussian interactions.....	21
2.5	Phase matching.....	26
2.5-1	Phase-matching in birefringent crystals.....	28
2.5-2	Walk-off.....	32
2.5-3	Quasi-phase-matching.....	34
2.5-4	Quasi-phase-matching theory.....	39
2.6	Phase-matching acceptance parameters.....	42
2.6-1	Acceptance parameters for QPM materials.....	45
2.7	Chapter 2 summary.....	47
	Chapter 2 references.....	48

3. *ICSRO Implementation*

3.1	Introduction	51
3.2	Pump laser source	51
3.2-1	Ti:Sapphire material characteristics	52
3.2-2	Cavity geometry, design and stability.....	54
3.2-3	ABCD matrix analysis of laser and OPO cavities.....	59
3.2-4	Tuning the Ti:Sapphire laser.....	68
3.3	ICSRO Power analysis	72
3.3-1	Theoretical background.....	72
3.3-2	Power analysis.....	73
3.3-3	The ICSRO steady-state power characteristics	78
3.3-4	Power optimisation	81
3.4	Chapter 3 summary	86
	Chapter 3 references	87

4. *ICSRO based on $KTiOAsO_4$*

4.1	Introduction	90
4.2	Experimental design	91
4.2-1	Nonlinear material	95
4.2-2	SRO cavity alignment.....	96
4.3	KTA ICSRO power characteristics	98
4.3-1	Intracavity power	98
4.3-2	Output power and efficiency	100
4.3-3	Signal output coupling.....	104
4.4	ICSRO spectral properties	109
4.4-1	Resonant field linewidths	110
4.5	Chapter 4 Summary	112
	Chapter 4 references	113

5. *ICSRO based on QPM- LiNbO₃*

5.1	Introduction	114
5.2	Experimental design	115
5.2-1	Nonlinear material	117
5.2-2	SRO cavity alignment.....	120
5.3	PPLN ICSRO power characteristics	121
5.3-1	PPLN thermal lens effects	123
5.4	Spectral properties	126
5.5	Chapter 5 summary	129
	Chapter 5 references	131

6. *ICSRO based on QPM- RbTiOAsO₄*

6.1	Introduction	133
6.2	Experimental design	134
6.2-1	Nonlinear material	137
6.2-2	SRO cavity alignment.....	142
6.3	PPRTA ICSRO power characteristics	142
6.3-1	Intracavity power	143
6.3-2	Output power and efficiency	144
6.4	PPRTA ICSRO spectral properties	148
6.5	Chapter 6 summary	152
	Chapter 6 references	154

7. *ICSRO based on QPM-KTiOPO₄*

7.1	Introduction	155
7.2	Experimental design	156
7.2-1	Power and pump tuning analysis - cavity design.....	156
7.2-2	Temperature tuning analysis - cavity design.....	159

7.2-3	Nonlinear material	161
7.2-3	SRO cavity alignment.....	166
7.3	PPKTP ICSRO power characteristics	167
7.3-1	Intracavity power	167
7.3-2	Output power and efficiency	168
7.4	PPKTP ICSRO spectral characteristics	171
7.4-1	Pump tuning	171
7.4-2	Temperature tuning.....	174
7.4-3	Fine frequency studies.....	175
7.5	Ring cavity PPKTP ICSRO	176
7.5-1	Cavity layout and design	177
7.5-2	Cavity stability and mode waist analysis.....	179
7.5-3	Cavity alignment.....	185
7.5-4	PPKTP RICSRO operation.....	190
7.6	Chapter 7 summary.....	193
	Chapter 7 references.....	195

8. *Conclusion*

8.1	Concluding summary of results.....	197
8.2	Further research and development.....	200
	Chapter 8 references.....	207

Appendix A

A 1.0	KTP sellmeier equations along n_z	208
--------------	---	------------

Appendix B

B 1.0	Journal Publications	210
B 1.1	Conference Publications	211

1. Introduction

2.1 Background

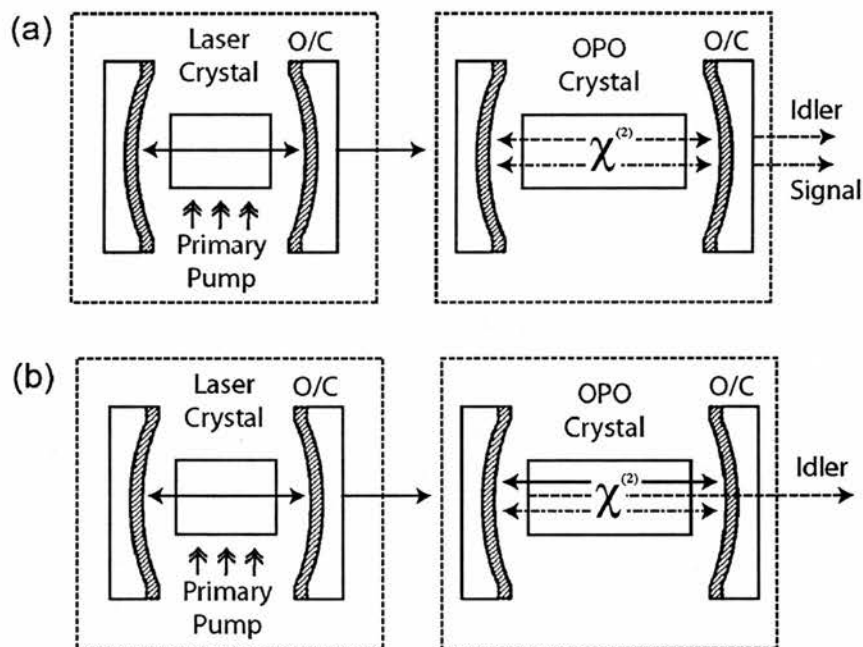
The visible and near-to-mid-infrared optical spectrum has a limited and discontinuous number of continuous-wave (cw) laser sources. While there are a number of these sources that provide a broad tuning range such as dye lasers (visible) and Ti:Sapphire lasers (near-infrared), the mid-infrared spectral region (2-5 μm) has few practical sources that can provide similar output characteristics. The ideal source should provide coherent output of high amplitude and frequency stability, narrow linewidth and broad tunability with high efficiency for the required application. In a spectral range that boasts a wealth of important atmospheric absorption features, and a broad range of fundamental organic and inorganic compound "frequency signatures" the demand for a practical and frequency-agile source is high. The provision of such a source is of great interest to a wide range of scientific disciplines and has many innovative industrial applications.

This thesis aims to describe the development and implementation of one member of the growing family of coherent optical sources that derive their functionality and principal mode of operation from the physical principals of nonlinear optics. The device outlined herein is a *continuous-wave, singly-resonant, intracavity optical parametric oscillator* [1]. This device shows great promise as a flexible, efficient and broadly tunable source of mid-infrared coherent radiation. Common to many fields of science, classification often leads to names that, although descriptive, can be rather long and tedious (albeit suitably scientific). For the remainder of this thesis the *continuous-wave, singly-resonant, intracavity optical parametric oscillator* will be termed the ICSRO.

1.2 The cw optical parametric oscillator

The optical parametric oscillator (OPO) is a nonlinear frequency converter. Central to the operation of such a device is the utilisation of a nonlinear material possessing a χ_2 nonlinear susceptibility. Franken et al achieved the first observation of frequency conversion using such a material in 1961 [2] and since this time a broad range of efficient and practical devices have been demonstrated that harness the available frequency mixing schemes of the second order nonlinear process described in Chapter 2. As one of the most attractive schemes of frequency conversion, the OPO has received considerable research interest over the intervening years since Franken's experiment.

The operational principles of the OPO are well documented [3-9]. Among the broad conclusions that may be drawn from the literature, those that concern the cw operation of OPOs are focused primarily upon device threshold. The four main configurations of cw OPOs are illustrated in figure 1.



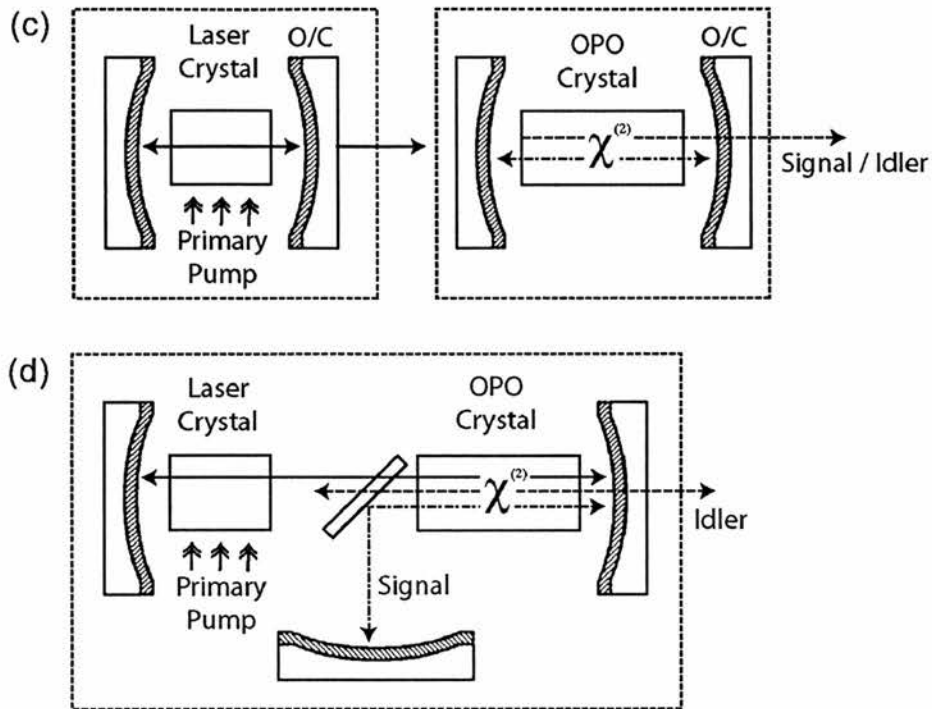


Figure 1. Common configurations of the cw OPO pumped by a cw coherent laser source. (a) Doubly resonant OPO with both signal and idler waves resonated. (b) Pump enhanced OPO with resonant signal field and resonant pump enhancement. (c) Externally-pumped singly resonant OPO with resonant signal field. (d) Internally-pumped singly resonant OPO with resonant signal field (ICSRO).

The most practically robust and simple OPO configuration is that of the externally pumped singly resonant OPO shown in figure 1(c). Unfortunately, typical device thresholds for this configuration are of the order of a few Watts of laser pump power even using state-of-the-art poled nonlinear materials [10]. For conventional birefringent nonlinear materials and the new emergent poled arsenates and phosphates, such as PPKTP, PPRTA and PPKTA, singly resonant cw OPO thresholds are often of the order of a few tens of Watts. This places stringent power requirements on the pump laser source which often negates the low-scale engineering aims of pursuing such a simple OPO configuration.

A significant reduction in threshold (down to typically a few tens of milliwatts) may be observed by employing either a doubly resonant (DRO) or pump-enhanced

configuration shown in figure 1(a)&(b). Indeed, the very first cw OPO was a doubly resonant device developed by Smith *et al.* [11]. The DRO was pumped by a frequency-doubled Nd:YAG laser - just 7 years after Franken's pioneering experiment - illustrating how rapidly research in the field had progressed at this time. The spectral and amplitude stability of this device was so poor that after the initial observation of cw parametric oscillation and further experimental work, the DRO was largely abandoned as a spectroscopic source in the early 1970s with the coming of the dye laser [12]. The observed instabilities of the DRO were a consequence of the resonance requirements of this configuration. To keep both signal and idler fields on-resonance the DRO cavity mirrors must be servo-controlled to within $\sim 1\text{nm}$ [8, 13] adding to the engineering complexity of the device. Frequency tuning of the DRO whilst maintaining simultaneous signal and idler resonance is a non-trivial task. Recent advances in single-frequency pump sources and electronic locking schemes have begun to address these problems [14-17] and the DRO is on course to realise the promise envisioned in the early development of cw OPOs.

Whilst still necessitating the use of active frequency locking schemes, the singly-resonant pump enhanced OPO has recently emerged as a practical source for tunable narrow-linewidth coherent radiation [18-22]. The key to the success of this device is that the resonated pump field remains on in the absence of SRO operation. The implications of this are that the SRO cavity may be servo controlled in a constant manner and, with a suitably stable single-frequency pump source, need only react *rapidly* to frequency transients of the parametric resonant field. In contrast, with the DRO there is a finite parametric build-up "lock time" over which the device must be brought on resonance and held [23].

Removing the constraints placed by the double-resonance condition of the DRO and pump enhanced SRO requires the implementation of the passively-stable SRO configuration. In the cw time domain, SRO operation has been limited in the past by the prohibitively high thresholds of these devices. The advent of quasi-phase-matched (QPM) materials has driven renewed interest in these devices as the operational thresholds are brought within the range of modest cw lasers [10, 24].

Within the context of the growing research interest in CW SROs, a further SRO configuration, the intracavity singly-resonant OPO (ICSRO) has been demonstrated [1, 25]. The ICSRO aims to access the high circulating fields within a laser resonator in order to overcome the high SRO oscillation thresholds, this thesis aims to present the operational characteristics of this SRO pumping geometry and details an experimental investigation of several ICSRO devices pumped within the resonant cavity of a Ti:sapphire laser.

1.3 Thesis summary

The work presented in this thesis complements the research efforts instigated by reference [1]. A broad review of this work and its complementary theoretical studies is given in references [26, 27]. This thesis describes four ICSRO devices, built and studied over a period of three years with the aim of demonstrating the practical advantages of the ICSRO pumping approach. The research presented addresses the need to provoke interest and activity in this young research area.

There are many characteristics of the ICSRO that are unique. In particular, the ability to accommodate an unparalleled variety of nonlinear materials whilst operating with high efficiency is clearly demonstrated by this work.

Chapters 2 & 3 provide an overview of the physical principles of nonlinear optics and describe the design of the devices detailed in later chapters. Chapters 4 to 7 are devoted to each ICSRO device in chronological order of research. The work is concluded in chapter 8.

Chapter 1 References

- 1 F. G. Colville, M. H. Dunn and M. Ebrahimzadeh, "Continuous-wave, singly resonant, intracavity parametric oscillator," *Optics Letters* **22**, 75-77 (1997).
- 2 P. A. Franken, A. E. Hill, C. W. Peters and G. Weinreich, "Generation of optical harmonics," *Physical Review Letters* **7**, 118 (1961).
- 3 A. Yariv and W. H. Louisell, "Theory of the Optical Parametric Oscillator," *IEEE Journal of Quantum Electronics* **QE-2**, 418-424 (1966).
- 4 S. E. Harris, "Tunable Optical Parametric Oscillators," *Proceedings of the IEEE* **57**, 2096-2113 (1969).
- 5 R. L. Byer, *Optical Parametric Oscillators*. in *Quantum Electronics: A Treatise* H. Rabin and C. L. Tang, Eds. (Academic Press, New York, 1975).
- 6 R. G. Smith, *Optical parametric oscillators*. in *Lasers: a series of advances* A.K. Levine and A.J. DeMaria, Eds. (Marcel Dekker, New York, 1976) pp. 189.
- 7 R. Fischer and L. A. Kulevskii, "Optical parametric oscillators (review)," *Soviet Journal of Quantum Electronics* **7**, 135 (1977).
- 8 R. C. Eckardt, C. D. Nabors, W. J. Kozlovsky and R. L. Byer, "Optical Parametric Oscillator Frequency Tuning and Control," *Journal of the Optical Society of America B-Optical Physics* **8**, 647-667 (1991).
- 9 M. H. Dunn and M. Ebrahimzadeh, "Parametric Generation of Tunable Light from Continuous-Wave to Femtosecond Pulses," *Science* **286**, 1513-1517 (1999).
- 10 W. R. Bosenberg, A. Drobshoff, J. I. Alexander, L. E. Myers and R. L. Byer, "Continuous-wave singly resonant optical parametric oscillator based on periodically poled LiNbO₃," *Optics Letters* **21**, 713 (1996).
- 11 R. G. Smith, J. E. Geusic, H. J. Levinstein, J. J. Rubin, S. Singh and V. Uitert, "Continuous optical parametric oscillation in Ba₂NaNb₅O₁₅," *Applied Physics Letters* **12**, 308-310 (1968).
- 12 F. G. Colville, *An analysis of the performance characteristics of continuous-wave optical parametric oscillators*, PhD thesis, University of St Andrews (1994). (Includes a comprehensive review of cw OPO's up to 1994).
- 13 A. J. Henderson, M. J. Padgett, F. G. Colville, J. Zhang and M. H. Dunn, "Doubly-resonant optical parametric oscillators: Tuning behaviour and stability requirements," *Optics Communications* **119**, 256 (1995).

- 14 A. J. Henderson, P. M. Roper, L. A. Borschowa and R. D. Mead, "Stable, continuously tunable operation of a diode-pumped doubly resonant optical parametric oscillator," *Optics Letters* **25**, 1264-1266 (2000).
- 15 R. Al-Tahtamouni, K. Bencheikh, R. Storz, K. Schneider, M. Lang, J. Mlynek and S. Schiller, "Long-term stable operation and absolute frequency stabilization of a doubly resonant parametric oscillator," *Applied Physics B-Lasers and Optics* **66**, 733-739 (1998).
- 16 M. Bode, P. K. Lam, I. Freitag, A. Tunnermann, H. A. Bachor and H. Welling, "Continuously-tunable doubly resonant optical parametric oscillator," *Optics Communications* **148**, 117-121 (1998).
- 17 T. Ikegami, S. Slyusarev, S. I. Ohshima and E. Sakuma, "Long term operation of a CW doubly resonant optical parametric oscillator," *Japanese Journal of Applied Physics Part 1-Regular Papers Short Notes & Review Papers* **35**, 2690-2691 (1996).
- 18 G. Robertson, M. J. Padgett and M. H. Dunn, "Continuous-Wave Singly Resonant Pump-Enhanced Type-II LiNbO₃ Optical Parametric Oscillator," *Optics Letters* **19**, 1735-1737 (1994).
- 19 M. Scheidt, B. Beier, K. J. Boller and R. Wallenstein, "Frequency-stable operation of a diode-pumped continuous-wave RbTiOAsO₄ optical parametric oscillator," *Optics Letters* **22**, 1287-1289 (1997).
- 20 M. E. Klein, D. H. Lee, J. P. Meyn, B. Beier, K. J. Boller and R. Wallenstein, "Diode-pumped continuous-wave widely tunable optical parametric oscillator based on periodically poled lithium tantalate," *Optics Letters* **23**, 831-833 (1998).
- 21 D. Chen, D. Hinkley, J. Pyo, J. Swenson and R. Fields, "Single-frequency low-threshold continuous-wave 3- μ m periodically poled lithium niobate optical parametric oscillator," *Journal of the Optical Society of America B-Optical Physics* **15**, 1693 (1998).
- 22 G. A. Turnbull, D. McGloin, I. D. Lindsay, M. Ebrahimzadeh and M. H. Dunn, "Extended mode-hop-free tuning by use of a dual-cavity, pump-enhanced optical parametric oscillator," *Optics Letters* **25**, 341-343 (2000).
- 23 G. M. Gibson, G. R. Morrison, P. L. Hansen, M. H. Dunn and M. J. Padgett, "Dynamic behaviour of a doubly resonant optical parametric oscillator," *Optics Communications* **136**, 423-428 (1997).
- 24 W. R. Bosenberg, A. Drobshoff, J. I. Alexander, L. E. Myers and R. L. Byer, "93% pump depletion, 3.5-W continuous-wave, singly resonant optical parametric oscillator," *Optics Letters* **21**, 1336 (1996).
- 25 L. R. Marshall, Conference on Lasers and Electro-Optics Technical Digest (1995), vol. 15, 401.

- 26 G. A. Turnbull, *Continuous-wave intracavity optical parametric oscillators*, PhD thesis, St Andrews University (1999).
- 27 M. Ebrahimzadeh, G. A. Turnbull, T. J. Edwards, D. J. M. Stothard, I. D. Lindsay and M. H. Dunn, "Intracavity continuous-wave singly resonant optical parametric oscillators," *Journal of the Optical Society of America B-Optical Physics* **16**, 1499-1511 (1999).

2. *Nonlinear Optics & Phase-Matching*

2.1 *Introduction*

Nonlinear Optics came of age in the early sixties soon after the development of the first Laser [1]. Prior to this, the intense optical fields necessary for the experimental observation of the broad range of nonlinear optical phenomena, predicted through the notable theoretical efforts of Armstrong *et al.* [2], were unavailable in the laboratory. In the forty years since the introduction of the laser as a laboratory tool, the field of nonlinear optics has realised much of the promise envisioned in early theoretical work [3-6]. It provides the basis of a wide range of frequency conversion techniques applicable to an equally broad variety of coherent sources of radiation. This chapter outlines the physical basis of Nonlinear Optics and describes the processes that give rise to nonlinear frequency conversion.

2.2 *Theoretical aspects*

All materials are nonlinear. Given a suitably intense driving field, the electrons responsible for the optical properties of a medium will not adhere to ideal harmonic oscillation. The Coulomb field acting upon a valence electron does not generally provide a linear restoring force when large deviations from equilibrium are considered. The following discussion will look at the transition from linear to nonlinear optical polarisation and aims to outline the important consequences for the re-radiated field arising from this transition.

2.2-1 Linear - Nonlinear optical polarisation

A classical optical field propagating within a dielectric medium will establish a macroscopic polarisation that, under normal circumstances with weak interacting fields, has a linear relationship to this field. This linear relationship between polarisation and incident field may be expressed, in scalar notation, as

$$P = \varepsilon_0 \chi^{(1)} E \quad (2.1)$$

where ε_0 is the permittivity of free space and $\chi^{(1)}$ is the linear optical susceptibility of the dielectric material concerned. This linear susceptibility is a function of the field frequency and governs the properties of refraction, reflection and absorption that are familiar within the field of linear optics. Equation (2.1) is a sufficient approximation to the full constitutive relation between the incident field E and the resultant macroscopic polarisation P when the amplitude of this field is small compared to that of the inter-atomic fields acting on the electrons within the material. For fields of sufficiently large amplitude, equation (2.1) may be expressed as an expansion in powers of the applied field

$$P = \varepsilon_0 (\chi^{(1)} + \chi^{(2)} E + \chi^{(3)} E^2 + \dots) E \quad (2.2)$$

where $\chi^{(2)}$ and $\chi^{(3)}$ represent the second and third order nonlinear optical susceptibility respectively. The second-order susceptibility, $\chi^{(2)}$, is responsible for nonlinear interactions such as second harmonic generation (SHG), the linear electro-optic effect and, central to operation of OPOs, frequency mixing (sum-frequency generation (SFG) and difference-frequency generation (DFG)). There are many other interesting phenomena that arise from interactions coupled through the $\chi^{(3)}$ susceptibility, such as the Kerr effect [7], two-photon absorption [8] and Brillouin and Raman scattering [9-11]. For the purposes of this chapter discussion will be limited to the processes coupled through the $\chi^{(2)}$ nonlinear susceptibility only. It is this interaction that is the basis on which the principle of operation of the ICOPO will be developed.

2.2-2 Second-order nonlinear interaction

We shall consider the second-order polarisation term of equation (2.2), namely

$$P = \epsilon_0 \chi^{(2)} E^2 \quad (2.3)$$

where it is assumed that the \bar{P} and \bar{E} vectors lie in the same direction. The direction along which \bar{P} and \bar{E} interact is an arbitrary choice and a general treatment of the $\chi^{(2)}$ process must include the symmetry relationship between $\chi^{(2)}$ and the dielectric medium. Since $\chi^{(2)}$ and the linear susceptibility uniquely reflect the symmetry properties of the medium, this medium must possess a noncentrosymmetric crystal structure if $\chi^{(2)}$ is to have non-vanishing components. For a free atom the second order susceptibility vanishes due complete inversion symmetry, once bound within a crystal lattice, the dynamics of the valence electrons of the atom are influenced by interactions with neighbouring atoms. The symmetry of the crystal will then dictate the symmetry of $\chi^{(2)}$ for each member of the crystal lattice. An example of a crystal structure within which the valence electrons of the bound atoms have non-vanishing $\chi^{(2)}$ components is shown in figure 1.

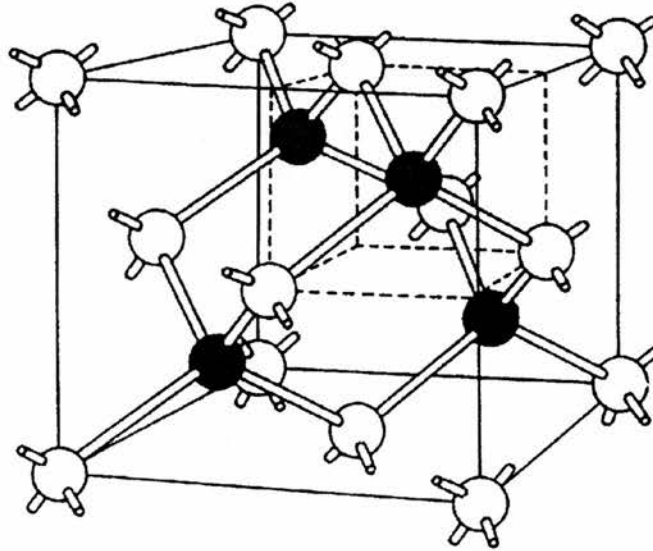


Figure 1. Noncentrosymmetric crystal structure (zinc blende)

At the heart of every nonlinear optical device there is a material that, through some asymmetric atomic arrangement or engineered structure, lacks an inversion symmetry and, in turn, impresses this asymmetry upon the dynamics of its own polarisation.

We shall first examine the significance of the expansion expressed in equation (2.2) and in particular the second-order term of equation (2.3). The following analysis considers the implication of equation (2.2) with respect to the re-radiated field of the second-order $\chi^{(2)}$ polarisation. The way in which the asymmetry of the nonlinear material allows $\chi^{(2)}$ to maintain non-vanishing components will be discussed once a clear picture of the frequency-mixing processes involved has emerged.

2.2-3 Frequency mixing via the $\chi^{(2)}$ interaction

To gain an insight into the physical processes that arise from the nonlinear polarisation described by equation (2.3) we will consider a superposition of two optical fields at different frequencies propagating in the z direction through a nonlinear material. The resultant field is

$$\mathbf{E} = [\mathbf{E}_1 \cos(k_1 z - \omega_1 t) + \mathbf{E}_2 \cos(k_2 z - \omega_2 t)] \quad (2.4)$$

where k_1, ω_1 and k_2, ω_2 are the wave vectors and angular frequencies of \mathbf{E}_1 and \mathbf{E}_2 respectively. Substitution of equation (2.4) into equation (2.3) yields

$$\begin{aligned} \mathbf{P} = \frac{1}{2} \epsilon_0 \chi^{(2)} & [\mathbf{E}_1^2 (\cos(2k_1 z - 2\omega_1 t)) + \mathbf{E}_2^2 (\cos(2k_2 z - 2\omega_2 t)) \\ & + 2\mathbf{E}_1 \mathbf{E}_2 (\cos\{(k_1 + k_2)z - (\omega_1 + \omega_2)t\}) \\ & + 2\mathbf{E}_1 \mathbf{E}_2 (\cos\{(k_1 - k_2)z - (\omega_1 - \omega_2)t\}) \\ & + \mathbf{E}_1^2 + \mathbf{E}_2^2] \end{aligned} \quad (2.5)$$

Equation (2.5) contains all the terms relating to the fundamental processes of $\chi^{(2)}$ coupled interactions. Examination of these terms shows that the second-order

nonlinear polarisation simultaneously gives rise to frequency components at twice the frequency of the interacting fields (SHG), the difference-frequency (DFG) and the sum-frequency (SFG). The two remaining frequency independent terms describe optical dc rectification across the dielectric medium. The frequency components of equation (2.5) that fall within the transparency bandwidth of the material concerned, represent the fundamental processes of $\chi^{(2)}$ nonlinear optics. It is the preferential selection of one of these processes, at the expense of the others, that is one of the primary design criteria of any efficient nonlinear optical device. Discussion of this selection process - phase-matching - will be examined in the second half of this chapter.

2.2-4 Magnitude of the $\chi^{(2)}$ interaction

Before progressing to the coupled wave equations that govern the dynamics of the frequency conversion processes described by equation (2.5) we must relate the magnitude of $\chi^{(2)}$ to the properties of the nonlinear material. As previously mentioned, $\chi^{(2)}$ reflects the symmetry properties of the crystal medium, thus, any interaction governed by $\chi^{(2)}$ will depend on the direction and orientation of the interacting fields. It is therefore necessary to fully express the tensor property of $\chi^{(2)}$ by writing the nonlinear polarisation in the form

$$P_i(t) = \epsilon_0 \sum_{ijk} \chi_{ijk}^{(2)} E_j(t) E_k(t) \quad (2.6)$$

where $\chi_{ijk}^{(2)}$ is a third-rank nonlinear susceptibility tensor and the indices ijk correspond to the Cartesian components of the interacting fields which, by convention, are specified in the crystalline piezoelectric axis system (XYZ). The piezoelectric coefficients of the crystal possess identical symmetry to that of the $\chi_{ijk}^{(2)}$ tensor. As we are confining our discussion to three-wave frequency mixing processes consideration must be given to the conservation laws of nonlinear interactions involving the interacting fields. The first, and generally the most intuitive, is the conservation of energy of the interacting waves

$$\omega_3 = \omega_1 + \omega_2 \quad (2.7)$$

which describes conservation of energy for the sum-frequency mixing process. Although essentially intuitive, it should be noted that equation (2.7) implies that no energy is transferred to the nonlinear medium via higher-order scattering processes. One consequence of the energy conservation (2.7) and the original arbitrary choice of the two interacting waves of equation (2.4) is the multitude of possible frequency components for the $\chi^{(2)}$ polarisation described by equation (2.6) (within the material transparency). We may define the field component at some frequency ω by the Fourier relation

$$U(t) = \frac{1}{2} [U(\omega)e^{i(k \cdot r - \omega t)} + cc] \quad (2.8)$$

Substitution into equation (2.6) gives

$$P_i(-\omega_3) = \varepsilon_0 \sum_{ijk} \frac{\chi_{ijk}^{(2)}}{2} (-\omega_3, \omega_2, \omega_1) E_j(\omega_2) E_k(\omega_1) e^{i[(k_2 + k_1 - k_3) \cdot r]} \quad (2.9)$$

where, in addition to the energy conservation of (2.7), two symmetry conditions have been observed. The first states that for a lossless medium, $\chi_{ijk}^{(2)}$ is invariant under all permutations of the frequency components hence [2]

$$\chi_{ijk}^{(2)}(-\omega_3, \omega_2, \omega_1) = \chi_{ikj}^{(2)}(-\omega_3, \omega_1, \omega_2) = \chi_{jki}^{(2)}(\omega_2, \omega_1, -\omega_3) = \chi_{kij}^{(2)}(\omega_1, -\omega_3, \omega_2) \quad (2.10)$$

which ensures that the magnitude of the nonlinear coefficient is independent of mixing process involved. The second symmetry relation is that of Kleinman [12] which states that $\chi_{ijk}^{(2)}$ is invariant under any permutation of the indices ijk and, in a lossless medium, is independent of the permutation of the frequencies involved. Thus, knowledge of the magnitude of $\chi^{(2)}$ allows us to formulate a consistent model of the second-order nonlinear interaction for all the processes described by equation (2.5) and for all the frequency components (2.8) that satisfy energy conservation for the process concerned. Before proceeding with an overview of the

coupled wave equations that govern the dynamics of the nonlinear interaction in dielectric media there is one further simplification to make. Rather than express the full 81 constants of the $\chi^{(2)}$ tensor, a reduced notation is used. It is customary to express $\chi^{(2)}$ in terms of the nonlinear tensor d using the simple relation

$$\chi_{ijk}^{(2)}(-\omega_3, \omega_2, \omega_1) = 2d_{ijk}(-\omega_3, \omega_2, \omega_1) \quad (2.11)$$

The nonlinear tensor d_{ijk} is the conventional representation of the nonlinear coefficient used within nonlinear optics. To simplify notation and taking account of the previous symmetry permutation conditions outlined above, d_{ijk} can be written in the reduced notation as d_{im} where m takes values from 1 to 6 according to table 1.

(jk)	11	22	33	23	13	12
m	1	2	3	4	5	6

Table 1. Reduced notation indices

This reduces d_{im} to a 3×6 matrix with the following form

$$\begin{pmatrix} d_{11} & d_{12} & d_{13} & d_{14} & d_{15} & d_{16} \\ d_{21} & d_{22} & d_{23} & d_{24} & d_{25} & d_{26} \\ d_{31} & d_{32} & d_{33} & d_{34} & d_{35} & d_{36} \end{pmatrix} \quad (2.12)$$

which operates on the column vector $E_m E_m$ which, for the case of second harmonic generation, is given by

$$E_m E_m = \begin{pmatrix} E_x^2 \\ E_y^2 \\ E_z^2 \\ 2E_y E_z \\ 2E_x E_z \\ 2E_x E_y \end{pmatrix} \quad (2.13)$$

We may now fully express the second-order nonlinear polarisation and relate it to the material properties of the medium concerned via the d tensor (2.12). For example, in the case of frequency mixing processes in crystals with point group symmetry of $\bar{4}2m$ (the chalcopyrite crystal family illustrated in figure 1) the second-order nonlinear polarisation has the components

$$P_x = 2\varepsilon_0 d_{14} E_y E_z \quad (2.14)(a)$$

$$P_y = 2\varepsilon_0 d_{14} E_x E_z \quad (2.14)(b)$$

$$P_z = 2\varepsilon_0 d_{36} E_x E_y \quad (2.14)(c)$$

where, in the case of $\bar{4}2m$ symmetry, $d_{25} = d_{14}$. While the tensor d fully describes the second-order nonlinear susceptibility of a given medium, in practice, the effective magnitude of d is calculated from the projection of the interacting field polarisation on the crystal axes. In this way, the individual components of d are scaled and combined to give an effective nonlinear coefficient d_{eff} . We may now express the three fundamental frequency-mixing processes of equation (2.5), in the form

$$P(r, \omega_3 = \omega_1 + \omega_2) = 2\varepsilon_0 d_{eff} E(r, \omega_1) E(r, \omega_2) \quad (\text{SFG}) \quad (2.15)(a)$$

$$P(r, \omega_2 = \omega_3 - \omega_1) = 2\varepsilon_0 d_{eff} E(r, \omega_3) E^*(r, \omega_1) \quad (\text{DFG}) \quad (2.15)(b)$$

$$P(r, 2\omega_1) = \varepsilon_0 d_{eff} E^2(r, \omega_1) \quad (\text{SHG}) \quad (2.15)(c)$$

2.3 Coupled wave equations

The second-order nonlinear polarisation outlined in the preceding sections allows for the transfer of energy between interacting field components at different frequencies. We have shown how the $\chi^{(2)}$ -coupled processes can give rise to frequency components at the sum, difference and second harmonic frequency of interacting field components within a nonlinear medium. The following sections discuss the mechanism for the transfer of energy between the $\chi^{(2)}$ -coupled waves. It is this energy transfer that is the central aim for the implementation of a nonlinear optical device such as the OPO, and insight gained from the analysis of this mechanism will shed light on the methods that must be employed in order to efficiently exploit the mixing process.

2.3-1 The Maxwell wave equation & nonlinear coupling

The first step is to insert the nonlinear polarisation term (2.6) into the Maxwell wave equation

$$\nabla^2 \mathbf{E} = \mu_0 \sigma \frac{\partial \mathbf{E}}{\partial t} + \mu_0 \varepsilon \frac{\partial^2 \mathbf{E}}{\partial t^2} + \mu_0 \frac{\partial^2 \mathbf{P}^{NL}}{\partial t^2} \quad (2.16)$$

where $\varepsilon = \varepsilon_0(1 + \chi^{(1)})$ and \mathbf{P}^{NL} is the nonlinear polarisation term. The terms ε and μ are the electric permittivity and magnetic permeabilities of the medium and σ is the coefficient of absorption. For the purpose of this analysis, the higher order terms of equation (2.2) beyond $\chi^{(2)}$ are neglected. Equation (2.16) represents the most general formulation of wave propagation within a material with a quadratic nonlinearity. The analytical solution of equation (2.16) is confined to the plane wave approximation only, an exact solution for Gaussian beam propagation is not possible. For the parametric generation process, we shall consider the solution of (2.16) for interacting fields propagating in the z direction with frequencies ω_1 , ω_2 and ω_3 as follows [13]

$$E_{\omega_1}(z, t) = \frac{1}{2} \left[E_1(z) e^{i(\omega_1 t - k_1 z)} + c.c. \right] \quad (2.17)(a)$$

$$E_{\omega_2}(z, t) = \frac{1}{2} \left[E_2(z) e^{i(\omega_2 t - k_2 z)} + c.c. \right] \quad (2.17)(b)$$

$$E_{\omega_3}(z, t) = \frac{1}{2} \left[E_3(z) e^{i(\omega_3 t - k_3 z)} + c.c. \right] \quad (2.17)(c)$$

the sum of these three fields will then give the total instantaneous field $E_T(z, t)$

$$E_T(z, t) = \sum_{i=1}^3 E_{\omega_i}(z, t) \quad (2.18)$$

where $\omega_3 = \omega_1 + \omega_2$. Since we are considering the plane wave approximation, the derivatives of the fields in the x and y directions are zero and substitution of equation (2.18) into the Maxwell wave equation (2.16) gives

$$\frac{\partial E_{\omega_1}}{\partial z} = -\alpha_1 E_{\omega_1} + i\kappa_1 E_3 E_2^* e^{i\Delta k z} \quad (2.19)(a)$$

$$\frac{\partial E_{\omega_2}}{\partial z} = -\alpha_2 E_{\omega_2} + i\kappa_2 E_3 E_1^* e^{i\Delta k z} \quad (2.19)(b)$$

$$\frac{\partial E_{\omega_3}}{\partial z} = -\alpha_3 E_{\omega_3} + i\kappa_3 E_1 E_2 e^{-i\Delta k z} \quad (2.19)(c)$$

where

$$\alpha_i = \sigma_i \frac{\mu_0 c}{2} \quad (2.20)(a)$$

$$\kappa_i = \frac{\omega_i}{c n_i} d_{eff} \quad (2.20)(b)$$

and

$$\Delta k = k_3 - k_2 - k_1 \quad (2.21)$$

here we have made use of the slowly varying envelope approximation [2] ($k \partial E / \partial z \gg \partial^2 E / \partial z^2$) and sorted the terms into their respective frequency components.

Examination of the amplitude terms in equations (2.19) show that the three interacting fields are coupled through the nonlinear coefficient d_{eff} which enables energy flow from one frequency component to another. This is the fundamental mechanism of second-order nonlinear optics and by utilising equations (2.19) we are now able to formulate expressions for the growth in intensity of the interacting fields ω_1, ω_2 and ω_3 .

Before proceeding with an analysis of the *intensity* gain for the parametric process associated with the optical parametric oscillator it is common to introduce the following field variable

$$A_i(z) = \sqrt{\frac{n_i}{\omega_i}} E_i(z) \quad (2.22)$$

which is proportional to the photon flux at frequency ω_i . The coupled wave equations (2.19) may now be written in terms of this new variable. For the case of a parametric amplifier with input at the signal (ω_s) and idler (ω_i) and pumped by a field at (ω_p) we have

$$\frac{dA_s(z)}{dz} = i\kappa A_p(z) A_i^*(z) e^{i\Delta kz} \quad (2.23)(a)$$

$$\frac{dA_i(z)}{dz} = i\kappa A_p(z) A_s^*(z) e^{i\Delta kz} \quad (2.23)(b)$$

$$\frac{dA_p(z)}{dz} = i\kappa A_i(z) A_s(z) e^{-i\Delta kz} \quad (2.23)(c)$$

where absorption has been neglected ($\alpha_i = 0$ in (2.19)) and where κ is given by

$$\kappa = \frac{d_{eff}}{c} \sqrt{\frac{\omega_p \omega_s \omega_i}{n_p n_s n_i}} \quad (2.24)$$

The intensity of a field component with wave amplitude $E_i(z)$ may be expressed as

$$I_i = \frac{1}{2} \varepsilon_0 n_i c |E_i(z)|^2 \quad (2.25)$$

and in terms of the field variable $A_i(z)$

$$I_i = \frac{1}{2} \varepsilon_0 \omega_i c |A_i(z)|^2 \quad (2.26)$$

thus, multiplying each of (2.23) by its respective field variable conjugate $A_p^*(z)$, $A_s^*(z)$ and $A_i^*(z)$, we can make the observation that, from equation (2.26) $|A_i(z)|^2 \propto I_i/\omega_i$ and that the following equations may be formulated

$$-\frac{d|A_p(z)|^2}{dz} = \frac{d|A_s(z)|^2}{dz} = \frac{d|A_i(z)|^2}{dz} \quad (2.27)$$

$$-\frac{d}{dz} \left(\frac{I_p}{\omega_p} \right) = \frac{d}{dz} \left(\frac{I_s}{\omega_s} \right) = \frac{d}{dz} \left(\frac{I_i}{\omega_i} \right) \quad (2.28)$$

Equations (2.27) and (2.28) describe the *intensity* change for the three interacting waves of the parametric process. They imply that the total intensity is conserved and that the growth in one field component will be at the expense of another of the fields coupled through the $\chi^{(2)}$ interaction. The direction of power flow is dictated by the relative phasing of the fields. The derivation of the gain expressions for the interacting signal and idler fields of an OPO may now be obtained by solving the coupled wave equations (2.23)(a)&(b). We must first take a more pragmatic view of the experimental implementation of the OPO. In particular the transverse geometry of the interacting fields will, in most practical situations, fail to subscribe to the simple plane-wave theory detailed above. The Gaussian nature of the interacting fields will set constraints on the transverse spatial overlap of each field component. Clearly, only where there is a spatial coincidence of the interacting fields within a nonlinear material will there also be parametric gain. The next section seeks to outline the modification of the theory so far presented in order to take account of the focusing parameters involved in the nonlinear process.

2.4 Focussed Gaussian interactions

In practice, the implementation of a nonlinear optical device will involve the use of focussed Gaussian beams which may be appropriate modes of a resonant optical cavity. Clearly, the move from theoretical principles involving infinite plane waves and interaction mediums of arbitrary dimensions, will have to be assessed. The development of the plane wave theory above, to include practical focussing situations and their associated parameters, was undertaken by a number of authors early on in the development of nonlinear optics [4, 14-17]. Boyd and Kleinman [18] consolidated this body of work. Their paper details the focussing parameters required for the optimisation of second harmonic generation and parametric generation. We shall consider the implications of the finite spatial overlap of the coupled interacting fields in a particular nonlinear process and outline the modifications that must be made to the plane wave analysis obtained from the Maxwell wave equation.

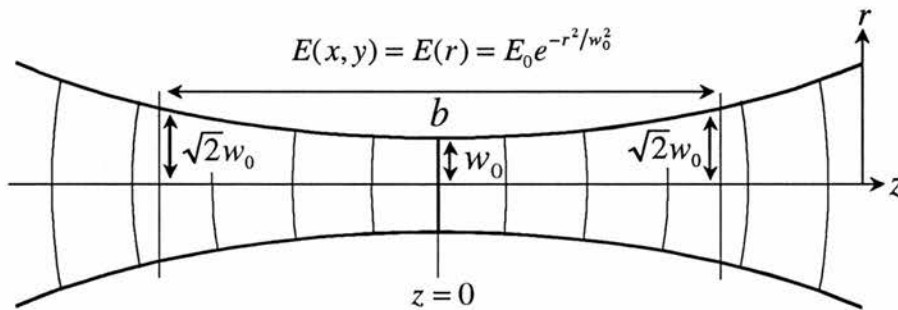


Figure 2. Geometry of a Gaussian beam focus with beam radius w_0 at the beam waist $z = 0$. $b = 2\pi w_0^2/\lambda$ is termed the confocal parameter of the beam. Vertical lines indicate the increasing curvature of the wave-fronts along the direction of the beam.

A clearer picture of the parameters used to characterise a focussed Gaussian beam is given by figure 2. The region of the beam that extends over the confocal parameter b is approximately collimated and for the analysis of reference [18] it is

assumed that wave-front radii are constant over this range. In this near-field limit, the field expression in the x, y plane is independent of z and reduces to

$$E(x, y) = E_0 e^{-r^2/w_0^2} \quad (2.29)$$

where r is perpendicular to the direction of propagation z . The coupled amplitude equations (2.19) may, then be expressed as

$$\frac{\partial E_{\omega_i}}{\partial z} e^{-r^2/w_i^2} = i\kappa_i E_p e^{-r^2/w_p^2} E_s^* e^{-r^2/w_s^2} e^{i\Delta kz} \quad (2.30)(a)$$

$$\frac{\partial E_{\omega_s}}{\partial z} e^{-r^2/w_s^2} = i\kappa_s E_p e^{-r^2/w_p^2} E_i^* e^{-r^2/w_i^2} e^{i\Delta kz} \quad (2.30)(b)$$

$$\frac{\partial E_{\omega_p}}{\partial z} e^{-r^2/w_p^2} = -i\kappa_p E_i e^{-r^2/w_i^2} E_s e^{-r^2/w_s^2} e^{-i\Delta kz} \quad (2.30)(c)$$

where we have assumed that $\sigma_1 = \sigma_2 = \sigma_3 = 0$ for the nonlinear medium (within the transparency bandwidth of the material). The beam waist \bar{w}_i of the polarisation distribution created through the mixing of two Gaussian beams at frequencies ω_j and ω_k with beam waists w_j and w_k is given by [16]

$$\frac{1}{\bar{w}_i^2} = \frac{1}{w_j^2} + \frac{1}{w_k^2} \quad (2.31)(a)$$

$$\frac{1}{\bar{w}_j^2} = \frac{1}{w_i^2} + \frac{1}{w_k^2} \quad (2.31)(b)$$

$$\frac{1}{\bar{w}_k^2} = \frac{1}{w_j^2} + \frac{1}{w_i^2} \quad (2.31)(c)$$

Using equations (2.31) to define the appropriate beam waists and integrating (2.30) (a)-(c) over the radial co-ordinate r to calculate the degree of overlap (and hence coupling) between the interacting fields we have

$$\frac{\partial E_{\omega_i}}{\partial z} = i\kappa_i g_i E_p E_s^* e^{i\Delta kz} \quad (2.32)(a)$$

$$\frac{\partial E_{\omega_s}}{\partial z} = i\kappa_s g_s E_p E_i e^{i\Delta kz} \quad (2.32)(b)$$

$$\frac{\partial E_{\omega_p}}{\partial z} = i\kappa_p g_p E_i E_s e^{-i\Delta kz} \quad (2.32)(c)$$

which are identical to equations (2.19) with the exception of the coupling factors g_n , that have the form

$$g_i = \frac{2}{\left[1 + \left(w_i^2 / \bar{w}_i^2\right)\right]} \quad (2.33)(a)$$

$$g_s = \frac{2}{\left[1 + \left(w_s^2 / \bar{w}_s^2\right)\right]} \quad (2.33)(b)$$

$$g_p = \frac{2}{\left[1 + \left(w_p^2 / \bar{w}_p^2\right)\right]} \quad (2.33)(c)$$

and now account for the spatial Gaussian overlap of the interacting beams and the driving polarisations of a given nonlinear process. Common with the introduction of the field variable $A_i(z)$ in the formulation of equations (2.23)(a)-(c) we now follow the analysis of Debuisschert et al [19] and formulate equations (2.32) as

$$\frac{d\alpha_p}{dz} = -2\kappa' \alpha_i(z) \alpha_s(z) e^{-i\Delta kz} \quad (2.34)(a)$$

$$\frac{d\alpha_s}{dz} = 2\kappa' \alpha_p(z) \alpha_i^*(z) e^{i\Delta kz} \quad (2.34)(b)$$

$$\frac{d\alpha_i}{dz} = 2\kappa' \alpha_p(z) \alpha_s^*(z) e^{i\Delta kz} \quad (2.34)(c)$$

where $\alpha_j(z)$ is defined by

$$\alpha_p(z) = i \left(\frac{n_p c \epsilon_0 \pi \omega_p^2}{4 \hbar \omega_p} \right)^{1/2} E_{\omega_p}(z) \quad (2.35)(a)$$

$$\alpha_s(z) = \left(\frac{n_s c \epsilon_0 \pi \omega_s^2}{4 \hbar \omega_s} \right)^{1/2} E_{\omega_s}(z) \quad (2.35)(b)$$

$$\alpha_i(z) = \left(\frac{n_i c \epsilon_0 \pi \omega_i^2}{4 \hbar \omega_i} \right)^{1/2} E_{\omega_i}(z) \quad (2.35)(c)$$

and κ' is given by

$$\kappa' = d_{\text{eff}} \frac{w_p w_s w_i}{(w_i^2 w_s^2 + w_s^2 w_p^2 + w_p^2 w_i^2)} \left[\frac{\hbar \omega_p \omega_s \omega_i}{\pi \epsilon_0 c^3 n_p n_s n_i} \right]^{1/2} \quad (2.36)$$

The integration of equations (2.34)(a)-(c) has been performed [19] by expressing the fields in powers of z and considering only zeroth-order terms of the fields concerned to yield

$$\alpha_p(l) = \alpha_p(0) - 2\zeta^* \alpha_s(0) \alpha_i(0) \quad (2.37)(a)$$

$$\alpha_s(l) = \alpha_s(0) + 2\zeta \alpha_p(0) \alpha_i^*(0) \quad (2.37)(b)$$

$$\alpha_i(l) = \alpha_i(0) + 2\zeta \alpha_p(0) \alpha_s^*(0) \quad (2.37)(c)$$

where l is the interaction length of the nonlinear medium and χ is given by

$$\zeta = \kappa' l \frac{\sin(\Delta k l / 2)}{(\Delta k l / 2)} e^{(i \Delta k l / 2)} \quad (2.38)$$

and the momentum mismatch Δk is

$$\Delta k = k_p - k_s - k_i \quad (2.39)$$

Equations (2.37) describe the *amplitude* gain of the field components at ω_p , ω_s and ω_i . Multiplying these equations by their respective complex conjugates will result in expressions $|\alpha_j|^2$ that are in terms of photon flows and obey the following proportional relations

$$|\alpha_j|^2 \propto \left[\frac{\sin(\Delta kl/2)}{(\Delta kl/2)} \right]^2 \quad (2.40)$$

Thus the parametric gain of a particular nonlinear process will scale with $\text{sinc}^2(\Delta kl/2)$ outlining the importance of satisfying the phase-matched condition

$$k_p - k_s - k_i = 0 \quad (2.41)$$

which will form the basis of the next section of this chapter.

We have now introduced the salient principles with which the threshold conditions and gain characteristics of an OPO may be derived. While the formulation of suitable expressions for the operational parameters of the ICOPO will be briefly outlined in the next chapter, the main insight to be taken from the preceding discussion is the $\text{sinc}^2(\Delta kl/2)$ relationship of the parametric gain and also that

$$|\alpha_j|^2 \propto \frac{d_{eff}^2}{n_p n_s n_i} \omega_p \omega_s \omega_i \quad (2.42)$$

Relation (2.42) reminds us that we are always limited by the material properties of the nonlinear medium chosen and the wavelength range over which the device is intended to operate. No matter how elegant or sophisticated our device engineering may be, (2.42) is the bottom-line factor of nonlinear optics and illustrates why advances in this field often go hand-in-hand with the development of new nonlinear materials.

2.5 Phase matching

We have seen from the nonlinear processes described above that, in order to maintain the energy flow of a particular $\chi^{(2)}$ -coupled process, a correctly phased relationship between the interacting fields must be maintained. For example, examining equations (2.37) and (2.38) it is clear that the parametric *Intensity* gain process scales with

$$\text{sinc}^2\left(\frac{\Delta k L}{2}\right) \quad (2.43)$$

as shown in figure 3.

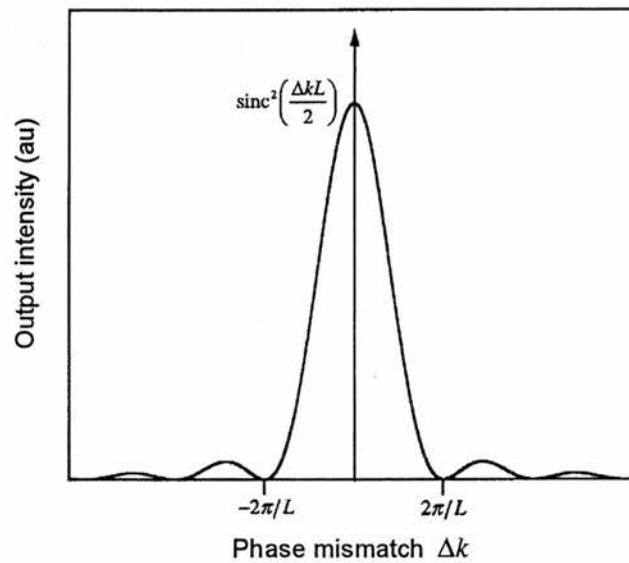


Figure 3. Plot of the function $\text{sinc}^2(\Delta k L/2)$ describing the output intensity generated by a parametric process governed by equations (2.37) and (2.38). The output is a maximum when $\Delta k = 0$.

Thus, parametric gain is a maximum for $\Delta k L = 0$ which is termed the phase-matched condition. In order to maintain the maximum efficiency for any quadratic nonlinear process care must be taken to ensure that this condition is satisfied

throughout the interaction length of the nonlinear medium concerned. For the case of parametric amplification the phase-matched condition is

$$k_p = k_s + k_i \quad (2.44)$$

More usefully, (2.44) may be expressed as follows

$$n_p \omega_p = n_s \omega_s + n_i \omega_i \quad (2.45)$$

where n_p , n_s and n_i are the refractive indices of the pump, signal and idler fields respectively. Equation (2.45) is key to one of the most attractive technical aspects of the nonlinear optical parametric process - its tunability. It shows us that the frequencies of the generated fields at the signal and idler for which the process is most efficient, depend on the magnitude of the refractive index of the nonlinear material *at the frequencies concerned*. Thus, of all the frequency components that satisfy the conservation of energy condition (2.7) within the transparency bandwidth of the material concerned, only those that satisfy (or very nearly satisfy) equation (2.44) build up from the background parametric fluorescence. The phase-matching process, from the perspective of the physicist trying to implement an optical parametric device, is essentially concerned with manipulating the refractive indices of equation (2.45) in order to facilitate the generation of either a specific frequency component, at ω_s or ω_i , or a continuously tunable range of frequency components, for some specific application (preferably one that has a significant financial advantage as nonlinear optics can be an expensive business).

The question arises: "how are we to impress our will upon the parametric process and take full advantage of the opportunities that equation (2.45) offers us?" We have already discussed how the nonlinear coefficients of a material are dependent on the spatial orientation of the interacting fields within that medium. We have also drawn upon the observations of Kleinman [12] and have assumed that the values of these coefficients are independent of frequency as long as the frequencies concerned are in a lossless region of the material (which also allows us to make a number of useful assumptions when deriving the coupled wave equations (2.19)).

An analysis of the material properties of the nonlinear medium will, in general, allow us to make two useful observations:

- 1 *The refractive indices of the material will depend on the spatial orientation of the interacting fields (for uniaxial and biaxial crystals)*
- 2 *The refractive indices of the material will be frequency dependent (due to material dispersion) and may well possess a significant temperature dependency.*

By adjusting the spatial orientation of the interacting fields with respect to the nonlinear material or through temperature tuning, we can tune the parametric process by dictating a specific set of refractive indices n_p, n_s and n_i for which $\Delta kL = 0$ and thus choose a specific ratio for ω_s and ω_i . It is worthy of note that the effective nonlinear coefficient of the interaction is also a function of the spatial orientation of the fields and care must be taken to allow for the variation of d_{eff} as different phase-matched crystal geometries are explored.

2.5-1 Phase-matching in birefringent crystals

The utilisation of the natural birefringence of a nonlinear material to satisfy the $\Delta k = 0$ phase-matched condition was first demonstrated by Giordmaine [20] and Maker *et al* [17]. These experiments observed a greatly enhanced second harmonic intensity generated for certain propagation directions of a ruby laser pump beam within a potassium dihydrogen phosphate (KDP) crystal. The direction in which the enhanced second harmonic intensity was observed, corresponded with an angular coincidence of the ordinary ruby pump, and extraordinary second harmonic wave index of refraction surfaces as shown in figure 4 (after Maker *et al* [17]). What Giordmaine and Maker *et al* observed, was a spatial representation of the locus of directions for which $\Delta kL \approx 0$ as determined by the material dispersion of KDP. This work illustrated the practical advantages of utilising the natural birefringence of nonlinear materials to set $\Delta kL \approx 0$ for a particular propagation direction. This

angular phase-matching is only possible if at least one interacting wave has an extraordinary polarisation and one has an ordinary polarisation. This is illustrated for the example of Lithium Niobate in figure 5.

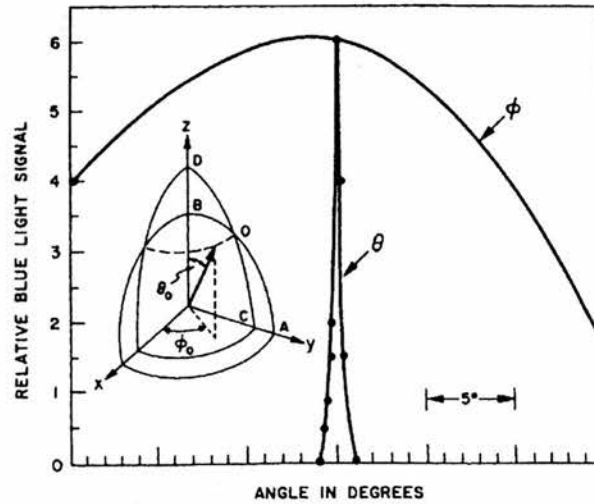


Figure 4. Blue light intensity as a function of crystal orientation for KDP. Maximum output occurs at $\theta_0 = 52^\circ \pm 2^\circ$, $\phi_0 = 45^\circ$. AOB is an arc on the index of refraction surface for red ordinary rays, COD for blue extraordinary rays [17].

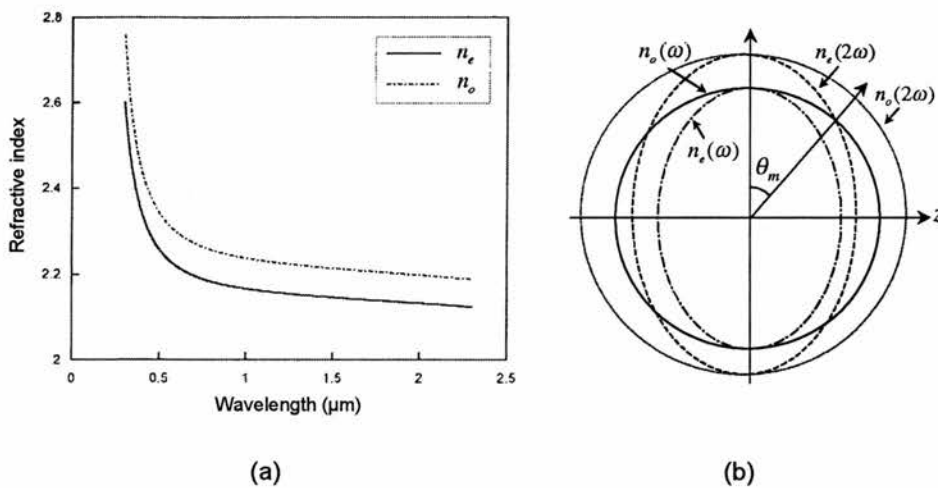


Figure 5. (a): Refractive index dispersion for ordinary and extraordinary refractive indices of LiNbO_3 . (b): LiNbO_3 second harmonic phase matching scheme with ordinary-polarised pump producing extraordinary-polarised second harmonic with a phase-matched angle of θ_m .

Figure 5(b) can be visualised by constructing a three-dimensional surface commonly termed the "index ellipsoid" which, in its most general form, has principal axes given by

$$\frac{x^2}{n_x^2} + \frac{y^2}{n_y^2} + \frac{z^2}{n_z^2} = 1 \quad (2.46)$$

Here we shall consider the uniaxial crystal Lithium Niobate (LiNbO_3) of figure 5. LiNbO_3 is typical of many birefringent nonlinear materials and thus serves as a good example for this discussion. As a uniaxial crystal, LiNbO_3 has an index ellipsoid of the form

$$\frac{x^2}{n_o^2} + \frac{y^2}{n_o^2} + \frac{z^2}{n_e^2} = 1 \quad (2.47)$$

where we have made the substitution $n_x = n_y = n_o \neq n_z$. The three-dimensional surface of equation (2.47) is represented in figure 6.

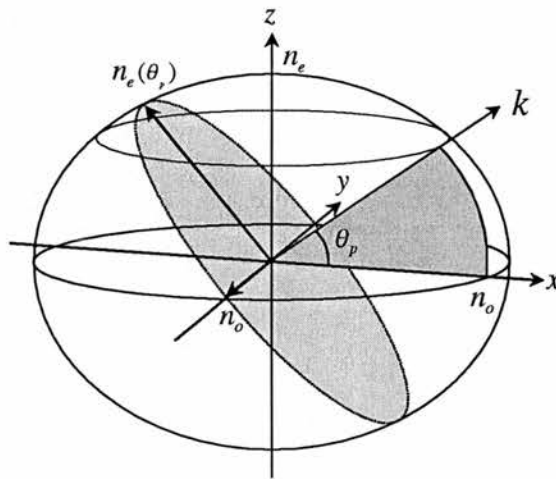


Figure 6. Index ellipsoid for LiNbO_3 . The direction of propagation is indicated by k , with the refractive index of the extraordinary wave indicated by $n_e(\theta_p)$.

Figure 6 illustrates a wave propagating through LiNbO₃ with a wave-vector k at an angle θ_p to the x,y plane of the crystal. The ordinary polarisation of this wave lies in the x,y plane and experiences a linear refractive index of n_o (as $n_x = n_y = n_o$) regardless of the rotation of the k vector around the z axis. The extraordinary polarisation of this wave will experience a refractive index $n_e(\theta_p)$ that is a function of the angle θ_p . Thus, by varying the angle θ_p we can vary the absolute refractive index of the extraordinary polarisation. Returning to figure 4(b), we see that at an angle θ_m an extraordinary polarisation at frequency 2ω will experience the same refractive index as an ordinary polarisation at frequency ω . This point represents the phase-matched condition where $\Delta k = 0$. It can be seen from figures 5 and 6 that

$$\frac{1}{n_e^2(\theta_p)} = \frac{\cos^2(\theta_p)}{n_o^2} + \frac{\sin^2(\theta_p)}{n_e^2} \quad (2.48)$$

and that the phase-matched angle θ_m will be

$$\sin^2(\theta_m) = \frac{(n_o(\omega))^{-2} - (n_o(2\omega))^{-2}}{(n_e(2\omega))^{-2} - (n_o(2\omega))^{-2}} \quad (2.49)$$

There is an overwhelming variety of birefringent phase-matching schemes. Where a particular scheme has direct relevance to the work presented in this thesis, the phase-matched geometry used will be detailed in the relevant experimental chapter together with an appropriate calculation of the effective nonlinear coefficient. For a detailed discussion on general birefringent phase-matching geometries see Dmitriev [21]. For now, we shall conclude this section with a discussion of one of the major practical impediments encountered through the implementation of certain birefringent phase-matching schemes: walk-off.

2.5-2 Walk-off

The walk-off effect was encountered early on in the experimental foundations of nonlinear optics. Originally termed the aperture effect, walk-off was observed in phase-matched experiments involving nonlinear materials with second harmonic interaction lengths of up to 10 cm. It was observed that the fundamental and second harmonic beams became displaced by a few millimetres after propagating through these long samples. In a paper outlining these observations Boyd *et al* [15] put forward a theory which accounted for the deviation of the second harmonic beam through this aperture effect within a uniaxial sample of Ammonium Dihydrogen Phosphate (ADP). The process of walk-off for critically phase-matched interactions in uniaxial crystals is illustrated in figure 7.

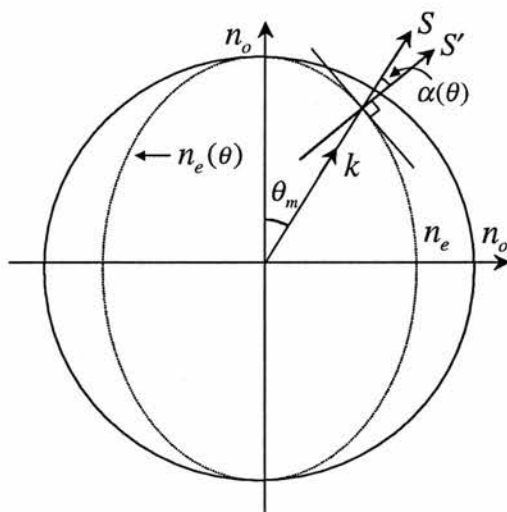


Figure 7. The walk-off effect for critically phase-matched birefringent interactions. At a phase-matched angle of θ_m the propagation vector \mathbf{k} is normal to the ordinary index of refraction wave surface, as is the associated Poynting vector \mathbf{S} for this polarisation. For the extraordinary polarisation, the normal to the wave surface is at an angle $\alpha(\theta)$ to the propagation vector \mathbf{k} . The Poynting vector for this polarisation \mathbf{S}' lies in the direction of this normal.

In an anisotropic medium, the Poynting vector \mathbf{S} associated with a plane wave propagating along some direction defined by a propagation vector \mathbf{k} , is defined by

$$\mathbf{S} = \mathbf{E} \times \mathbf{H} \quad (2.50)$$

where \mathbf{E} and \mathbf{H} are the electric and magnetic field vectors associated with the wave. The Poynting vector describes the magnitude and direction of the propagating wave and (2.50) clearly shows that it is normal to the plane containing \mathbf{E} and \mathbf{H} . Since \mathbf{S} and \mathbf{E} are perpendicular, when \mathbf{E} and the propagation vector \mathbf{k} are perpendicular (as in an isotropic medium), \mathbf{S} and \mathbf{k} will lie in the same direction and power flow will be *along* the direction of propagation \mathbf{k} . In an anisotropic medium, the wave propagation vector \mathbf{k} and \mathbf{E} may not, in general, be perpendicular as \mathbf{k} is the normal to the electric displacement vector \mathbf{D} where $\mathbf{D} = \epsilon_r \mathbf{E}$ and ϵ_r has a spatial dependence (and is thus non-scalar). Hence, the non-scalar nature of ϵ_r (birefringence) allows \mathbf{D} and \mathbf{E} to lie in different directions for the extraordinary wave. The implication of this is that \mathbf{k} (normal to \mathbf{D}) no longer retains its perpendicular relationship to \mathbf{E} which, through equation (2.50) is always normal to the direction of \mathbf{S} , the direction of the power flow. The result being: \mathbf{S} and \mathbf{k} lie along different directions and, for a particular phase-matching direction (θ_m in figure 7), the power flow of the extraordinary polarised wave (in this case the second harmonic) will be away from the direction of propagation along a normal to the extraordinary wave surface shown by \mathbf{S}' in figure 7. The consequence of walk-off in nonlinear frequency conversion is that the deviation of the interacting waves can be a limiting factor to efficiency. A good spatial overlap of the interacting fields is essential, for sufficiently long interaction lengths walk-off can cause the two fields to diverge outwith the beam diameter of the fundamental field and they will cease to interact.

From this brief discussion of birefringent phase-matching and its salient features, it can be seen that there are important design considerations to examine before implementing a particular phase-matching scheme. Importantly, we must rely on the inflexible material dispersion properties of the medium concerned in order to implement a suitable angular phase-matching scheme. This may result in the interaction efficiency being penalised by prohibitive walk-off effects or a significant reduction in the effective nonlinear coefficient for the direction involved. Whilst there are birefringent geometries that minimise walk-off and offer acceptable nonlinear

coefficients, a more flexible control of phase-matching parameters brings clear advantages in terms of efficiency and improved bandwidth over which a mixing scheme may be implemented. One such method that offers a far greater degree of flexibility than birefringent phase-matching whilst avoiding the penalties associated with this type of scheme is that of quasi-phase-matching.

2.5-3 Quasi-phase-matching

Determined readers of the pioneering paper of Armstrong *et al* [2], which did much to set a solid theoretical foundation for the field of nonlinear optics, will find (twenty pages into the work and after some remarkably long equations) a discussion on the possible methods of phase-matching. One such method discussed, which has instigated a minor revolution in nonlinear optics over the last decade, is that of quasi-phase-matching.

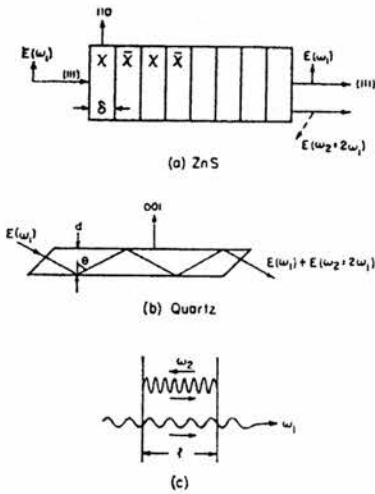


FIG. 10. Three experimental arrangements to provide phase correction, if the phase velocities of the fundamental and second harmonic are not perfectly matched. (a) After a distance $\delta = \pi(k_2 - 2k_1)^{-1}$ the crystal is replaced by its inversion image. The nonlinear susceptibility χ_{xyz} changes sign. The linear optical properties remain the same. This scheme can, of course, also be used in noncubic piezoelectric crystals. (b) Both fundamental and second harmonic undergo multiple total reflections in a crystal of thickness $d = (k_2 - 2k_1)^{-1} \pi \cos \theta$. On each reflection E_1 and E_2 undergo a 180° phase shift, the product $E_2 E_1^2$ changes sign. (c) The traveling wave at ω_1 pumps the interferometer cavity, which contains a nonlinear dielectric and is resonant at ω_2 , $l = n\lambda_2/2 < (k_2 - 2k_1)^{-1} \pi$. The backward harmonic wave does not interact with the pump. On each forward pass it has the correct phase for amplification.

Figure 8. Suggestion for three separate means of quasi-phase-matching taken from Figure 10 of Armstrong *et al* [2]. (a) represents the method of quasi-phase-matching commonly applied to modern nonlinear materials where the sign of the nonlinear coefficient is modulated every coherence length for the appropriate phase-matched interaction.

Thirty years after the birth of nonlinear optics as a practical field of experimental research, quasi-phase-matching is driving new interest in, and enabling the design of, a new range of highly flexible phase-matching geometries. Quasi-phase-matched (QPM) materials offer four distinct advantages over birefringent materials

- 1 *QPM materials are able to utilise the highest d coefficient of a nonlinear material (subject to a $2/\pi$ scaling factor).*
- 2 *The phase-matched scheme is a flexible engineered variable and is not dictated by the dispersion properties of the material. It allows interactions that fall outwith the birefringently phase-matched possibilities of a material to be investigated.*
- 3 *The interacting waves are (in general) polarised along a principal optical axis of the material and thus walk-off is no longer a prohibitive factor in the implementation of a particular phase-matched interaction. Orthogonal QPM polarisations are also subject to zero walk-off.*
- 4 *The common polarisation of the interacting waves allows for temperature-tuning schemes that are inaccessible to birefringently phase-matched materials (whereas the birefringence of a material may change little with temperature, the individual indices of refraction may show significant temperature dispersion)*

The advent of QPM (or periodically poled (PP)) materials has had a significant impact on the current state of OPO research. In particular, the once prohibitively high thresholds of continuous-wave singly resonant OPOs (CWSROs) now approach the accessible output powers available from conventional continuous-wave lasers [22, 23]. The utilisation of QPM materials in the work presented in this thesis mirrors the implementation of such materials in a wide range of χ^2 -based nonlinear devices in general. We shall see later that the intracavity approach to the

pumping of SROs utilising these new materials has the significant advantage of a pump-power flexibility that does not limit the ICSRO to QPM materials with long (30-50mm) interaction lengths and high ($>10\text{pmV}^{-1}$) effective nonlinear coefficients. We shall now examine the physical basics of quasi-phase-matched interactions and the important factors governing the design of phase-matched regimes for different nonlinear interactions in periodically poled materials.

The best starting point for an insightful discussion on the process of quasi-phase-matching is to return to the case of perfect phase-matching when $\Delta k = 0$, that is

$$n_p(\omega_p) - n_s(\omega_s) - n_i(\omega_i) = 0 \quad (2.51)$$

or for second harmonic generation

$$n(\omega) - n(2\omega) = 0 \quad (2.52)$$

where we have implemented a birefringent phase-matched scheme involving some permutation of orthogonal polarisations. Now, considering the case of second harmonic generation, let us propagate the interacting waves with all polarisation directions along a common crystal axis. We can see from the typical material dispersion curves of figure 4 and section 2.5-1 that the material dispersion of the nonlinear medium will mean that equation (2.52) above no longer holds. Thus, the second harmonic field propagating through the medium will no longer maintain a correct phase relationship with the pump field. As the two interacting waves propagate their phase relationship will deviate until their phase difference is π . The distance over which the waves propagate before they become π "out of phase" is termed the *coherence* length, l_c , where

$$l_c = \frac{\lambda(\omega)}{4(n(2\omega) - n(\omega))} \quad (2.53)$$

In terms of second harmonic intensity, the power flow, coupled through the nonlinear polarisation from the fundamental field at ω to the second harmonic field

at 2ω is positive until the propagation distance reaches l_c . After this point the power flow is then from the second harmonic field to the fundamental until, after a further coherence length, the second-harmonic intensity is reduced to its initial value. This process continues throughout the interaction length of the nonlinear medium. Thus, despite the fact that the propagating waves are not phase-matched, there is still a periodic positive flow of power from the fundamental to the second harmonic wave. In order to maintain this positive power transfer to the second harmonic wave we must prevent the phase relationship from increasing beyond π after the waves have travelled over one coherence length. If, after propagating a distance l_c in the nonlinear medium, the phase relationship between the two waves is "reset" by some means, then this positive flow of power from the fundamental to the second harmonic wave would be maintained. This is exactly the suggestion outlined in figure 8. The way to periodically reset the phase relationship between the fundamental and the second harmonic wave is to invert the sign of the nonlinear coefficient every coherence length. The resultant growth in second harmonic power is illustrated in figure 9(c). In the case of perfect birefringent phase-matching, the exponential growth in the intensity of the second harmonic is shown by the trace of figure 9(e). Figure 9(b) shows the cycle of forward and backward conversion for the non-phase-matched condition. The periodic growth and decay of the second harmonic intensity is clearly indicated.

By introducing a periodic inversion of the nonlinear coefficient shown by figure 6(a), the conversion to back-conversion cycle of trace (b) is now transformed to an average gain in second harmonic intensity (c). As can be seen, the overall build-up in second harmonic intensity of this first-order QPM process is less than that of the perfectly phase-matched case of trace (e). We shall see later that this reduction is, in fact, exactly a factor of $2/\pi$ from the perfectly phase-matched case. Since the QPM process is less efficient than the perfectly phase-matched case we may ask the question: "what advantage does a QPM interaction have over a similar interaction that is birefringently phase-matched?" The answer lies in the ability of a QPM process to allow the interacting fields to assume polarisation directions along the crystallographic axis that utilises the highest nonlinear coefficient of the nonlinear material. Figure 6 takes no account of the fact that the $\chi^{(2)}$ -coupling of

the interacting fields may well be significantly higher for the QPM interaction than for the birefringently phase-matched one, for which the effective nonlinear coefficient is a pre-determined function of the utilised phase-matching geometry. We now have a clear picture of the basic principles that lie at the heart of a QPM process.

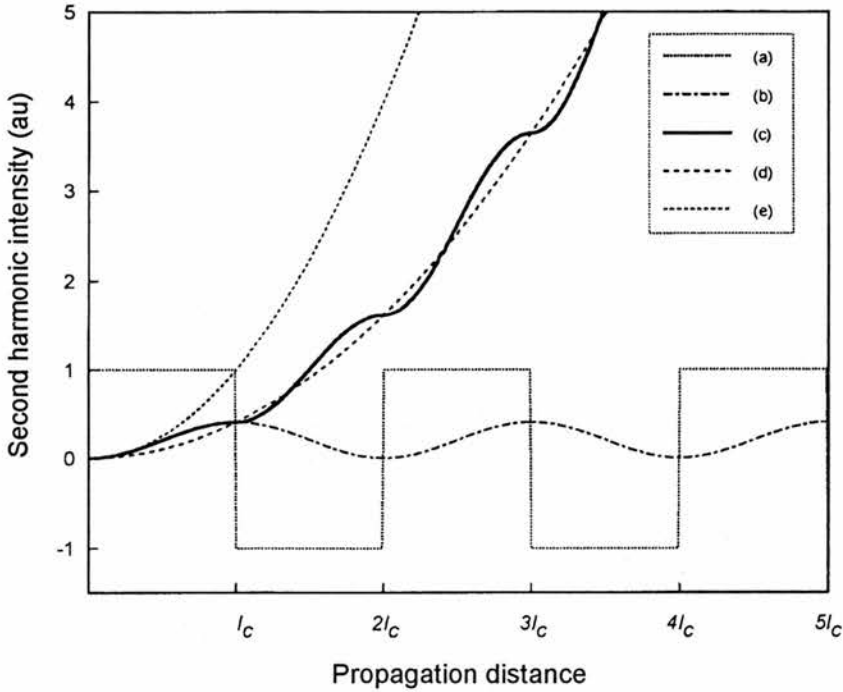


Figure 9. Growth of second harmonic intensity under different phase-matched conditions. (a): periodic modulation of the nonlinear coefficient. (b): non-phase-matched second harmonic intensity. (c): QPM growth of second harmonic intensity under periodic domain inversion described by (a). (d): approximation to QPM growth assuming a $2/\pi$ reduction of perfect phase-matched condition (e). (e) Growth of second harmonic under perfect phase-matched conditions. (l_c =coherence length)

It now remains to quantify these principles and to formulate appropriate expressions from which we may derive suitable phase-matching regimes, and design appropriate periodic poling schemes for various nonlinear materials.

2.5-4 Quasi-phase-matching theory

The theory of quasi-phase-matching has been detailed by a number of authors [24-27] and an overview of the relevant expressions obtained is as follows.

Consider the case of second harmonic generation for which we have

$$\Delta k = k_{2\omega} - 2k_{\omega} \quad (2.54)$$

For the case of $\Delta k \neq 0$, we can introduce a grating vector K_m such that the phase-matching condition is satisfied as follows

$$\Delta k_m = k_{2\omega} - 2k_{\omega} - K_m = 0 \quad (2.55)$$

where the grating vector results from the periodic inversion of the nonlinear coefficient as illustrated in figure 6. The expression for K_m has been derived [27] from a Fourier analysis of the periodic grating function. The basis of this method starts from the premise that the amplitude of the generated frequency components of a nonlinear process over a distance L may be obtained by integrating the appropriate equation (2.19)

$$E_L = \Gamma \int_0^L d(z) e^{-i\Delta k z} dz \quad (2.56)$$

where $\Gamma = i\omega_i E^2 / n_i c$ and $d(z)$ represents the periodically inverted nonlinear coefficient. The function $d(z)$ may be represented by a Fourier series as

$$d(z) = d_{eff} \sum_{m=-\infty}^{\infty} G_m e^{iK_m z} \quad (2.57)$$

where, assuming that $d(z)$ is a function periodic in z and with a period Λ , where the m th harmonic grating vector of (2.55) is given by

$$K_m = \frac{2\pi m}{\Lambda} \quad (2.58)$$

From (2.57) and (2.58) we can see that m defines the order of the phase-matched interaction of (2.55). Further analysis shows that for a process where $\Delta k \approx K_m$ the m th order interaction dominates [27]. In this case, $d_Q \approx d_{eff} G_m$ and the Fourier coefficient of (2.57) becomes

$$G_m = \frac{2}{\pi m} \sin(\pi m D) \quad (2.59)$$

where D is the duty cycle of the periodic inversion of the nonlinear coefficient with period Λ and positive domain length l , and is defined as

$$D = \frac{l}{\Lambda} \quad (2.60)$$

For an optimum domain inversion scheme as illustrated in figure 6, the duty cycle D will be such that the domains invert every coherence length and hence $\Lambda = 2l = 2l_c$. This allows us to relate the effective quasi-phase-matched nonlinear coefficient d_Q to the actual material value of the nonlinear medium concerned d_{eff} . Thus, for the m th order process

$$d_Q = \frac{2}{\pi m} d_{eff} \quad (2.61)$$

In practice, it is the first order quasi-phase-matched process that is utilised in practical QPM schemes as this offers the highest effective nonlinear coefficient. Thus the QPM method can, at best, offer just under two thirds of the effective nonlinearity of a perfectly phase-matched process. The key to the success of this method is that every interacting polarisation of the QPM process can access the highest nonlinear coefficient of a specific medium (for example $d_{eff} = d_{33}$). In most practical situations, the $2/\pi$ penalty is offset by this advantage and d_Q is often

significantly higher than d_{eff} for a birefringently phase-matched scheme. A consequence of equation (2.59) is that for the optimum duty cycle ($D = 1/2$) only odd ordered QPM processes can occur. It should be noted that higher order processes may well result in a small net gain in intensity for any of the possible $\chi^{(2)}$ frequency processes possible for the interacting fields of a nonlinear device. Thus, for an intracavity OPO pumped at 800nm and with a designed QPM interaction giving signal and idler wavelengths of 1200nm and 2400nm it will often be possible to observe a number of other mixing processes with the naked eye. In particular, sum frequency mixing of the pump and signal wave will give visible output at 480nm in the blue and second harmonic generation of the signal will produce orange light at 600nm. This provides an excellent visual indication of when the lengthy process of cavity alignment for the OPO has been successful and it is worth noting that, as well as elevating the efficiency and practicality of nonlinear optics for infrared applications, quasi-phase-matching has also brought a little welcome colour to the field.

We have outlined the basic principles of phase-matching as applied to a particular nonlinear process. The advantages of quasi-phase-matched interactions, with high effective nonlinearities and flexible design parameters have been noted. For many applications, the long interaction lengths, and high d_e of QPM materials (in particular periodically poled LiNbO₃) have placed the traditionally prohibitive threshold pump powers of a number of nonlinear devices within the reach of conventional continuous-wave (CW) laser output powers. Of particular note, and central to the work presented in this thesis, the operation of CW singly-resonant OPOs (CWSROs) has been brought down from the multi-watt-level pump threshold domain to the sub-5 watt level. We shall see later that the intracavity pumping approach is uniquely placed to take full advantage of a wide range of new QPM materials whilst still remaining a practical option for the pumping of birefringently phase-matched devices. Before concluding this chapter, one more aspect of the phase-matching process must be examined, phase-matching acceptance parameters.

2.6 Phase-matching acceptance parameters

One consequence of the necessity to phase-match a nonlinear interaction to provide efficient frequency conversion is that the phase-matching process itself will determine the frequency bandwidth over which the interacting fields constructively participate. Clearly, we must decide what is to be considered a "constructive" participation to a particular nonlinear process. The conventional definition of the acceptance bandwidth in this case is that for which the phase mismatch Δk varies over the range $-\pi/L \leq \Delta k \leq \pi/L$. Thus, for a particular phase-matching scheme we can formulate expressions for the acceptance parameters of temperature, angle and input wavelength for a specified nonlinear process. The problem of acceptance parameters in nonlinear optical process has been investigated by Barnes & Corcoran [28] and the following brief overview reflects their analysis.

We shall consider the wavelength acceptance bandwidth for a collinear birefringently phase-matched interaction. With very few exceptions, the acceptance bandwidth for a particular phase-matched process is evaluated around the perfectly phase-matched condition. The function of Δk may be expanded as a Taylor series about the point Δk_0

$$\Delta k = \Delta k_0 + \left. \frac{\partial \Delta k}{\partial \lambda_i} \right|_{\lambda_{i-pm}} \delta \lambda_i + \frac{1}{2} \left. \frac{\partial^2 \Delta k}{\partial \lambda_i^2} \right|_{\lambda_{i-pm}} \delta \lambda_i^2 + \dots \quad (2.62)$$

where for the case of perfect phase-matching, $\Delta k_0 = 0$ and λ_{i-pm} is the value of λ_i at $\Delta k = \Delta k_0$. Taking the definition of acceptance bandwidth $-\pi/L \leq \Delta k \leq \pi/L$ and setting $\Delta k_0 = 0$ for a bandwidth around the phase-matched condition, we have

$$\left. \frac{\partial \Delta k}{\partial \lambda_i} \right|_{\lambda_{i-pm}} \delta \lambda_i + \frac{1}{2} \left. \frac{\partial^2 \Delta k}{\partial \lambda_i^2} \right|_{\lambda_{i-pm}} \delta \lambda_i^2 + \dots = \pm \frac{\pi}{L} \quad (2.63)$$

the full expression for the phase mismatch Δk in terms of the interacting wavelengths is

$$\Delta k = 2\pi \left[\frac{n_p(\lambda_p)}{\lambda_p} - \frac{n_s(\lambda_s)}{\lambda_s} - \frac{n_i(\lambda_i)}{\lambda_i} \right] \quad (2.64)$$

where the subscripts p , s and i refer to the pump, signal and idler fields respectively. The functional dependence of the indices of refraction of these waves has been indicated, as it is the derivative of these indices which will determine the resultant bandwidth. Recalling the energy conservation relation

$$\frac{1}{\lambda_p} = \frac{1}{\lambda_s} + \frac{1}{\lambda_i} \quad (2.65)$$

and noting that the full bandwidth, from (2.63) is given by

$$\Delta\lambda_i = 2\delta\lambda_i \quad (2.66)$$

the first derivative with respect to the pump wavelength will be

$$\frac{\partial\Delta k}{\partial\lambda_p} = 2\pi \left[\frac{\partial n_p(\lambda_p)}{\partial\lambda_p} \Big|_{\lambda_p} \frac{1}{\lambda_p} - \frac{n_p(\lambda_p)}{\lambda_p^2} - \frac{\partial n_s(\lambda_s)}{\partial\lambda_s} \Big|_{\lambda_s} \frac{\lambda_s}{\lambda_p^2} + \frac{n_s(\lambda_s)}{\lambda_p^2} \right] \quad (2.67)$$

with the first derivative of (2.62) dominating the acceptance bandwidth in the overwhelming number of cases. Equation (2.67) may be used to express the wavelength acceptance bandwidth using (2.63) and (2.66) resulting in the following expression

$$\Delta\lambda_p = \frac{1}{L} \left[\frac{\partial n_p(\lambda_p)}{\partial\lambda_p} \Big|_{\lambda_p} \frac{1}{\lambda_p} - \frac{n_p(\lambda_p)}{\lambda_p^2} - \frac{\partial n_s(\lambda_s)}{\partial\lambda_s} \Big|_{\lambda_s} \frac{\lambda_s}{\lambda_p^2} + \frac{n_s(\lambda_s)}{\lambda_p^2} \right]^{-1} \quad (2.68)$$

Let us take as an example, the pump acceptance bandwidth of the nonlinear material KTA pumped at 810nm as described in chapter 4. The sellmeier equations governing the refractive indices of KTA are given by Fenimore *et al* [29] as follows

$$n_x(\lambda) = \sqrt{1.90713 + \frac{1.23522}{1 - \left(\frac{0.19692}{\lambda}\right)^2} - 0.01025\lambda^2} \quad (2.69)(a)$$

$$n_y(\lambda) = \sqrt{2.15912 + \frac{1.00099}{1 - \left(\frac{0.21844}{\lambda}\right)^2} - 0.01096\lambda^2} \quad (2.69)(b)$$

$$n_z(\lambda) = \sqrt{2.14786 + \frac{1.29559}{1 - \left(\frac{0.22719}{\lambda}\right)^2} - 0.01436\lambda^2} \quad (2.69)(c)$$

where λ is in μm . To calculate the appropriate wavelength parameters at $\Delta k = 0$ we may solve equation (2.64) for pump, signal and idler polarisations along y , y , and z axes respectively (for collinear pumping along the x -axis) by using (2.65) and the sellmeier equations (2.69)(b)&(c) (setting $\Delta k = 0$, $\lambda_p = 0.810\mu\text{m}$). The phase-matched signal and idler wavelengths calculated by this method are $1.156\mu\text{m}$ and $2.707\mu\text{m}$ respectively. Substitution of the pump and calculated signal wavelengths into (2.68) for a crystal interaction length of 11mm gives a pump acceptance bandwidth $\Delta\lambda_p = 1.7\text{nm}$. This is the maximum bandwidth of an input pump field that will contribute constructively to the nonlinear process for a phase mismatch range of $-\pi/L \leq \Delta k \leq \pi/L$. Clearly, further narrowing of the pump bandwidth will have an advantageous effect on efficiency as the wavelength extremes of the phase mismatch range provide a less efficient contribution than the central wavelength for which $\Delta k = 0$. Similar acceptance parameters may be calculated for the temperature acceptance bandwidth of a process. The appropriate expression is given by

$$\Delta T = \frac{1}{L} \left[\frac{1}{\lambda_p} \frac{\partial n_p}{\partial T} \Big|_T - \frac{1}{\lambda_s} \frac{\partial n_s}{\partial T} \Big|_T - \frac{1}{\lambda_i} \frac{\partial n_i}{\partial T} \Big|_T \right]^{-1} \quad (2.70)$$

Temperature derivatives have been measured for many nonlinear materials and are comprehensively documented by Dmitriev [21]. Angular acceptance bandwidths may also be calculated in the same manner [28].

2.6-1 Acceptance parameters for QPM materials

We have already seen that the QPM process provides additional flexibility to the phase-matching process by adding a further user-engineered parameter to the phase-mismatch expression as follows

$$\Delta k_m = k_p - k_s - k_i - \frac{2m\pi}{\Lambda} \quad (2.71)$$

where Λ is the grating period for the QPM material. Clearly, Λ is independent of wavelength thus any derivative with respect to this parameter will be zero and the expression for the pump acceptance bandwidth will assume the same form as that for the birefringent material given by

$$\Delta\lambda_p = \frac{1}{L} \left[\frac{\partial n_p(\lambda_p)}{\partial \lambda_p} \Big|_{\lambda_p} \frac{1}{\lambda_p} - \frac{n_p(\lambda_p)}{\lambda_p^2} - \frac{\partial n_s(\lambda_s)}{\partial \lambda_s} \Big|_{\lambda_s} \frac{\lambda_s}{\lambda_p^2} + \frac{n_s(\lambda_s)}{\lambda_p^2} \right]^{-1} \quad (2.72)$$

There is one important difference between the absolute value of the pump acceptance bandwidth of the QPM material and that of the birefringently phase-matched case. In the vast majority of cases, the interacting fields will be polarised along one crystal axis only for the QPM process, this will lead to the values of $n_p(\lambda)$ and $n_s(\lambda)$ in (2.72) being derived from only one sellmeier equation (for poled KTA (PPKTA) this will be $n_z(\lambda)$). Thus, from (2.69)(c) and (2.72), the QPM pump acceptance bandwidth of KTA has a value of $\Delta\lambda_p = 1.3nm$ compared to $\Delta\lambda_p = 1.7nm$ for the birefringently phase-matched case. As before, it is also possible to obtain expressions for the temperature, and angular acceptance bandwidths of QPM materials. In the case of temperature acceptance bandwidth, the grating period may well be a function of temperature as the material thermally expands. Thus an additional term must be added to equation (2.70) to give

$$\Delta T_{QPM} = \frac{1}{L} \left[\frac{1}{\lambda_p} \frac{\partial n_p}{\partial T} \Big|_T - \frac{1}{\lambda_s} \frac{\partial n_s}{\partial T} \Big|_T - \frac{1}{\lambda_i} \frac{\partial n_i}{\partial T} \Big|_T - m \frac{\partial}{\partial T} \left(\frac{1}{\Lambda} \right) \right]^{-1} \quad (2.73)$$

Where the term

$$\frac{\partial}{\partial T} \left(\frac{1}{\Lambda} \right) \quad (2.74)$$

must be calculated from knowledge of the thermal expansion coefficient of the material concerned. The angular acceptance bandwidth of a QPM material is obtained from analysis that is significantly more involved than that for the birefringent case [27]. The angular shift of apparent grating period must be accounted for as well as the angular dependence of the indices of refraction. For most cases, the high effective nonlinearity of QPM materials will mean that, in practice, tight focussing conditions are rarely used and the interaction propagation constants k_j may be assumed to lie along a common direction.

2.7 Chapter 2 summary

Chapter 2 has served as an introduction to the field of nonlinear optics and has provided an overview of the process of phase-matching which is a fundamental design parameter in any nonlinear frequency conversion process. The concepts that have been outlined are applicable to a very broad range of nonlinear optical devices and it has not been the purpose of this chapter to provide an in-depth insight into any one particular device. This thesis presents the experimental analysis of one particular device: the continuous-wave intracavity singly-resonant optical parametric oscillator (ICSRO). The second-order $\chi^{(2)}$ nonlinearity discussed above has little regard as to which process it will favour. It is the physicist that must, through judicious choice of materials and cavity geometries, engineer a scheme of operation that will encourage one of the many $\chi^{(2)}$ processes to dominate. In this way, the parameters that will allow efficient transformation of coherent laser light from one frequency domain to another may be explored. The next chapter serves to detail the design parameters of the ICSRO. Cavity geometry, laser source and mode of operation will all be outlined. Reference will be made to many of the concepts introduced in chapter 2 and these will be utilised to provide a clear framework for the analysis of the experimental observations of later chapters.

Chapter 2 references

- 1 T. H. Maiman, "Stimulated Optical Radiation in Ruby," *Nature* **187**, 493-494 (1960).
- 2 J. A. Armstrong, N. Bloembergen, J. Ducuing and P. S. Pershan, "Interactions between Light Waves in a Nonlinear Dielectric," *Physical Review* **127**, 1918 (1962).
- 3 A. A. Akhmanov, A. I. Kovrigin, R. V. Khokhlov and O. N. Chunaev, "Coherent Interaction Length of Light Waves in a Nonlinear Medium," *Soviet Physics JETP* **18**, 919 (1964).
- 4 D. A. Kleinman, "Theory of Second Harmonic Generation of Light," *Physical Review* **128**, 1761-1775 (1962).
- 5 N. M. Kroll, "Parametric amplification in spatially extended media and application to the design of tuneable oscillators at optical frequencies," *Physical Review* **127**, 1207 (1962).
- 6 P. A. Franken and J. F. Ward, "Optical harmonics and nonlinear phenomena," *Review of Modern Physics* **35**, 23 (1963).
- 7 R. W. Minck, R. W. Terhune and C. C. Wang, "Nonlinear Optics," *Applied Optics* **5**, 1595-1612 (1966).
- 8 W. Kaiser and G. C. B. Garrett, "Two-Photon Excitation in CaF₂:Eu²⁺," *Physical Review Letters* **7**, 229-231 (1961).
- 9 R. Y. Chiao and B. P. Stoicheff, "Brillouin scattering in liquids excited by a He-Ne laser," *Journal of the Optical Society of America* **54**, 1286-1287 (1964).
- 10 G. Eckhardt, R. W. Hellwarth, F. J. McClung, S. E. Schwarz, D. Weiner and E. J. Woodbury, "Stimulated Raman scattering from organic liquids," *Physical Review Letters* **9**, 455-457 (1962).
- 11 Y. R. Shen and N. Bloembergen, "Theory of stimulated Brillouin and Raman scattering," *Physical Review* **137**, A1787-A1805 (1965).
- 12 D. A. Kleinman, "Nonlinear Dielectric Polarization in Optical Media," *Physical Review* **126**, 1977 (1962).
- 13 A. Yariv, *Quantum Electronics*. (3rd ed.) (Wiley, New York, 1989).
- 14 J. E. Bjorkholm, "Optical Second-Harmonic Generation Using a Focused Gaussian Laser Beam," *Physical Review* **142**, 126 (1966).

- 15 G. D. Boyd, A. Ashkin, J. M. Dziedzic and D. A. Kleinman, "Second-harmonic generation of light with double refraction," *Physical Review A* **137**, 1305 (1965).
- 16 G. D. Boyd and A. Ashkin, "Theory of Parametric Oscillator Threshold with Single-Mode Optical Masers and Observation of Amplification in LiNbO₃," *Physical Review* **146**, 187-198 (1966).
- 17 P. D. Maker, R. W. Terhune, N. Nisenoff and C. Savage, "Effects of dispersion and focusing on the production of optical harmonics," *Physical Review Letters* **8**, 21-22 (1962).
- 18 G. D. Boyd and D. A. Kleinman, "Parametric Interaction of Focused Gaussian Light Beams," *Journal of Applied Physics* **39**, 3597 (1968).
- 19 T. Debuisschert, A. Sizmann, E. Giacobino and C. Fabre, "Type-II continuous-wave optical parametric oscillators: Oscillation and frequency-tuning characteristics," *Journal of the Optical Society of America B-Optical Physics* **10**, 1668-1680 (1993).
- 20 J. A. Giordmaine, "Mixing of light beams in crystals," *Physical Review Letters* **8**, 19-20 (1962).
- 21 V. G. Dmitriev, G. G. Gurzadyan and D. N. Nikogosyan, *Handbook of nonlinear optical crystals*. (2nd ed.) (Springer-Verlag, Berlin, Heidelberg, New York, 1997).
- 22 W. R. Bosenberg, A. Drobshoff, J. I. Alexander, L. E. Myers and R. L. Byer, "Continuous-wave singly resonant optical parametric oscillator based on periodically poled LiNbO₃," *Optics Letters* **21**, 713 (1996).
- 23 W. R. Bosenberg, A. Drobshoff, J. I. Alexander, L. E. Myers and R. L. Byer, "93% pump depletion, 3.5-W continuous-wave, singly resonant optical parametric oscillator," *Optics Letters* **21**, 1336 (1996).
- 24 S. Somekh and A. Yariv, "Phase matching by periodic modulation of the nonlinear optical properties," *Optics Communications* **6**, 301-304 (1972).
- 25 A. Szilagy, A. Hordvik and H. Schlossberg, "A quasi-phase-matching technique for efficient optical mixing and frequency doubling," *Journal of Applied Physics* **47**, 2025-2032 (1976).
- 26 K. C. Rustagi, S. C. Mehendale and S. Meenakshi, "Optical Frequency Conversion in Quasi-Phase-Matched Stacks of Nonlinear Crystals," *IEEE Journal of Quantum Electronics* **QE-18**, 1029-1041 (1982).
- 27 M. M. Fejer, G. A. Magel, D. H. Jundt and R. L. Byer, "Quasi-Phase-Matched Second Harmonic Generation: Tuning and Tolerances," *IEEE Journal of Quantum Electronics* **QE-28**, 2631 (1992).

-
- 28 N. P. Barnes and V. J. Corcoran, "Parametric generation processes: spectral bandwidth and acceptance angles," *Applied Optics* **15**, 696-699 (1976).
- 29 D. L. Fenimore, K. L. Schepler, U. B. Ramabadran and S. R. McPherson, "Infrared corrected Sellmeier coefficients for potassium titanyl arsenate," *Journal of the Optical Society of America B-Optical Physics* **12**, 794 (1995).

3. *ICSRO Implementation*

3.1 *Introduction*

This chapter introduces the design concepts of the continuous wave intracavity singly resonant optical parametric oscillator. The pump laser source, cavity design and utilised nonlinear materials will be discussed, with emphasis placed on the practical implementation of the devices described in the latter part of this thesis. To conclude, the operational characteristics of the ICSRO as predicted by a simple theory will be analysed and the significant conclusions of this analysis will be presented.

3.2 *Pump laser source*

The choice of a Ti:Sapphire laser for the pump source of the first ICSRO [1] was based primarily on the tunability of this laser material. The original device was based on a non-critically phase-matched KTiOPO_4 (KTP) nonlinear crystal, a material which may be angle-tuned for certain other birefringent geometries. The first, and most intuitive, design factor for an intracavity-pumped nonlinear material is that, as an integral part of the laser cavity, misalignment of the nonlinear medium will cause a subsequent misalignment of the laser cavity. The consequence of any attempt to angle-tune such a nonlinear device will be that the laser will, in most practical cases, cease to operate. The resolution of this problem involves the implementation of complicated servo controlled mirrors or expensive spherically-polished nonlinear materials with the added drawback that critically phase-matched geometry will introduce Poynting-vector walk-off which results in a reduction in nonlinear gain and hence substantial increase in oscillation threshold. In the absence of practical

temperature-tunability of KTP another method of tuning a device based on this material, and other non-critically phase-matched materials, is to tune the pump source. If the material dispersion of KTP assigns a particular signal and idler ratio for the parametric mixing process ω_s/ω_i where from the conservation of energy we have

$$\omega_p = \omega_s + \omega_i \quad (3.1)$$

then the tuning of the pump frequency ω_p will cause a subsequent tuning of the signal and idler frequencies. To obtain a widely tunable device it is necessary to tune the pump laser over as broad a range as possible. The Ti:Sapphire laser is one such tunable pump laser source.

3.2-1 Ti:Sapphire material characteristics

Titanium-doped Sapphire ($\text{Ti:Al}_2\text{O}_3$) is a well-known tunable laser material. Since the first observation of laser action in $\text{Ti:Al}_2\text{O}_3$ by Moulton in 1982 [2], the material has been extensively characterised [3-8]. Among the many desirable characteristics of $\text{Ti:Al}_2\text{O}_3$, its good thermal conductivity, large gain cross-section and high damage threshold make it an ideal laser medium for high-power CW laser applications.

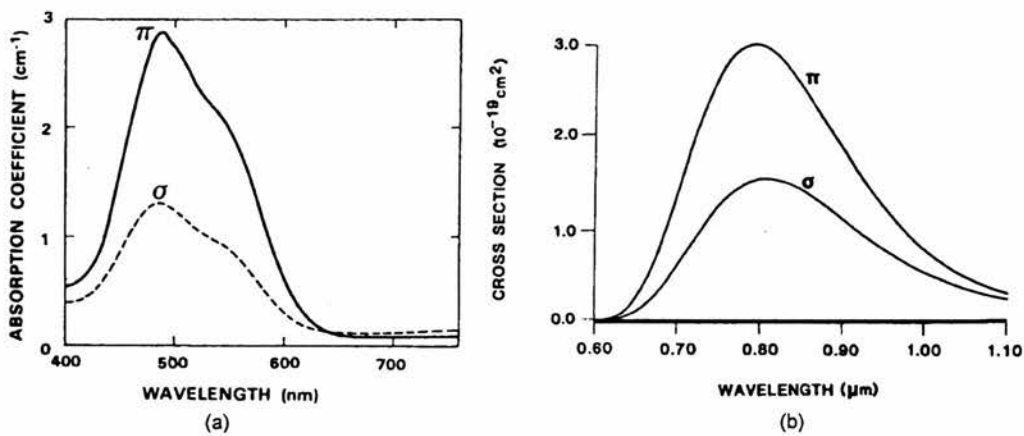


Figure 1. (a) Absorption coefficient of $\text{Ti:Al}_2\text{O}_3$ with light parallel (π) or perpendicular (σ) to the crystal c axis (after Sanchez et al [8]). (b) Emission cross section of $\text{Ti:Al}_2\text{O}_3$ (after Eggleston et al [9]).

Strong coupling between the Ti^{3+} ions in the sapphire lattice causes characteristically broad vibronic absorption and emission bands for the material, which makes $\text{Ti:Al}_2\text{O}_3$ one of the most widely tunable laser materials available. Figure 1 shows the absorption coefficient and emission cross-section spectra of $\text{Ti:Al}_2\text{O}_3$. The spectral range of the absorption coefficient (figure 1(a) after Sanchez *et al* [8]) covers a useful pump range exceeding 100nm. The peak of the π -polarised absorption is centred at 500nm which makes this material ideal for pumping with argon-ion, or frequency doubled Nd-based lasers. The emission cross-section spectra (figure 1(b) after Eggleston *et al* [9]) illustrates the broad tunability of $\text{Ti:Al}_2\text{O}_3$. The two curves of figure 1(b) are fitted distributions obtained from experimental observations of the fluorescence spectra of the material. Laser operation is readily obtained at room temperature if care is taken to remove excess thermal load on the material with a suitable cooling scheme. The importance of cooling is illustrated in figure 2, this graph shows the temperature dependence of the upper-state lifetime, τ_p , for $\text{Ti:Al}_2\text{O}_3$.

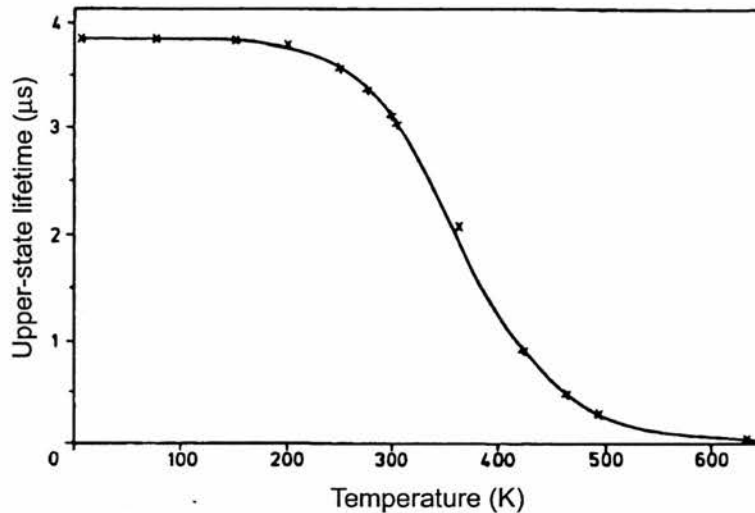


Figure 2. Temperature dependence of upper-state lifetime for $\text{Ti:Al}_2\text{O}_3$ (after Albers *et al* [4]).

It can be seen from figure 2 that the lifetime is essentially independent of temperature from the low-temperature limit up to approximately 200K with $\tau_p \approx 3.85\mu\text{s}$. At room temperature, τ_p falls rapidly and at 400K it is roughly 30% of

its initial low-temperature value. Thus, a fundamental design parameter of any Ti:Sapphire laser based system will be adequate cooling of the laser crystal, as the threshold pump power of the laser is inversely proportional to the upper-state lifetime. Whilst the pump and fluorescence bands of $\text{Ti:Al}_2\text{O}_3$ are well spaced, the material can suffer from residual absorption at the lasing wavelength, which has been attributed to the presence of quadruply ionised Ti^{4+} ions [7]. This has led to a common convention for assigning a figure of merit (FOM) for $\text{Ti:Al}_2\text{O}_3$ defined as the ratio of the absorption coefficient at the peak of the absorption band (at about 490nm) to the absorption coefficient at the peak of the laser gain (at about 800nm). Early samples of the material had FOM values as low as 5, whilst advances in crystal growth and annealing methods have pushed this to values of 250 or more for modern commercial samples.

3.2-2 Cavity geometry, design and stability

In order to implement the intracavity OPO, a suitable cavity geometry must be designed such that two separate foci are established for the resonant laser mode within the laser gain medium and the nonlinear gain medium. The resonant cavity must also present as little loss as possible to the laser field in order to optimise efficiency. A general rule is that the more optical surfaces a cavity contains, the greater is the loss incurred for each round trip and the more technically challenging the optical alignment becomes. There must be a compromise between cavity simplicity and practicality once the critical spot-size specifications for efficient laser and OPO operation have been satisfied. The geometry utilised must also allow the further implementation of a stable high-finesse singly-resonant OPO cavity with good spatial overlap of resonant pump and signal (or idler) modes. A further design consideration is the choice of standing-wave or travelling-wave (ring) cavity. The choice of which of these two configurations should be implemented will depend on the frequency characteristics required of the output fields. While technically challenging to align, the ring geometry allows problems associated with spatial hole burning to be avoided and is commonly utilised to obtain single-frequency laser operation [10]. The utilisation of a ring cavity design and the consequent single longitudinal mode (SLM) operation of the laser, allows for the SLM operation of both the signal and idler modes of the OPO as the singly-resonant field commonly

operates on one mode only [1]. The standing-wave laser cavity configuration is much simpler to align and does not require the utilisation of lossy intracavity unidirectional devices. Whilst the ultimate aim of any ideal laser source is SLM operation at all wavelengths, for the majority of the work presented in this thesis, the simple standing-wave cavity is utilised. This approach is undertaken from the viewpoint that the insight gained from devices based on this technically simpler cavity, will allow a more informed progress towards the design of ICSROs utilising ring cavity geometries. Thus, for the following analysis, cavity design will be limited to the standing-wave resonator.

The Ti:Sapphire laser used for the vast majority of the experimental research is a modified Schwartz Electro-Optics (SEO) Titan laser [11], the basic standing-wave configuration of which is shown in figure 3.

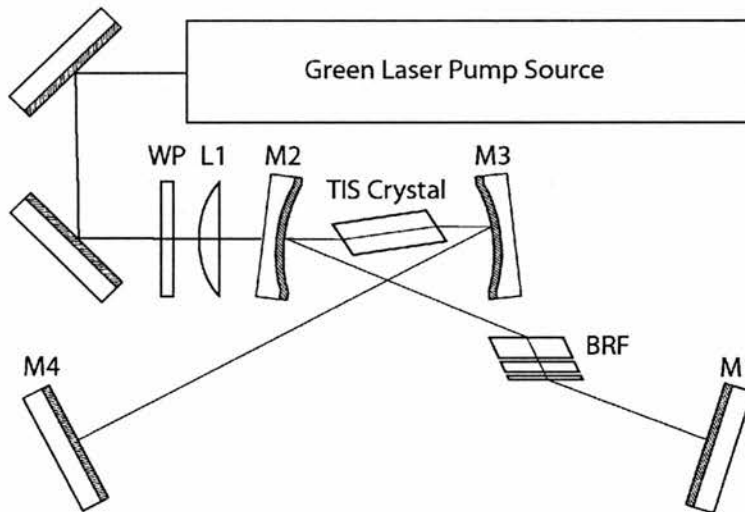


Figure 3. Standing wave configuration of SEO Titan laser. BRF is a 3-plate birefringent filter. WP indicates a half-wave plate. L1 is a focusing lens for the input pump beam. M1-4 are the cavity mirrors.

The cavity of figure 3 is a common four-mirror standing-wave "bow-tie" configuration. The Ti:Sapphire crystal is a Brewster-cut rhomb which is placed at the centre of the intracavity focus of the resonator between two 100mm radius of curvature (ROC) mirrors, M2 & M3. Astigmatism introduced by the Brewster-cut crystal is compensated by the fold half-angle θ of these mirrors according to [12]

$$R \sin \theta \tan \theta = \frac{(n^2 - 1)L}{n^3} \quad (3.2)$$

where R is the ROC of the fold mirror, n is the refractive index of Ti:Sapphire and L is the length of the crystal. The cavity stability and focussing parameters of the resonator may be analysed through the ABCD matrix method [13, 14]. The cavity configuration of figure 3 has been analysed previously by Kane [15] with reference to the optimisation of the focussing geometry. This analysis may be extended to investigate the spot sizes and stability characteristics of a modified two-foci resonator based on the commercial SEO laser, a similar analysis has also been performed for a ring-resonator containing two coupled foci [16]. There are a number of options for the modification of the SEO laser cavity. Three practical possibilities are illustrated in figures 4, 5 and 6.

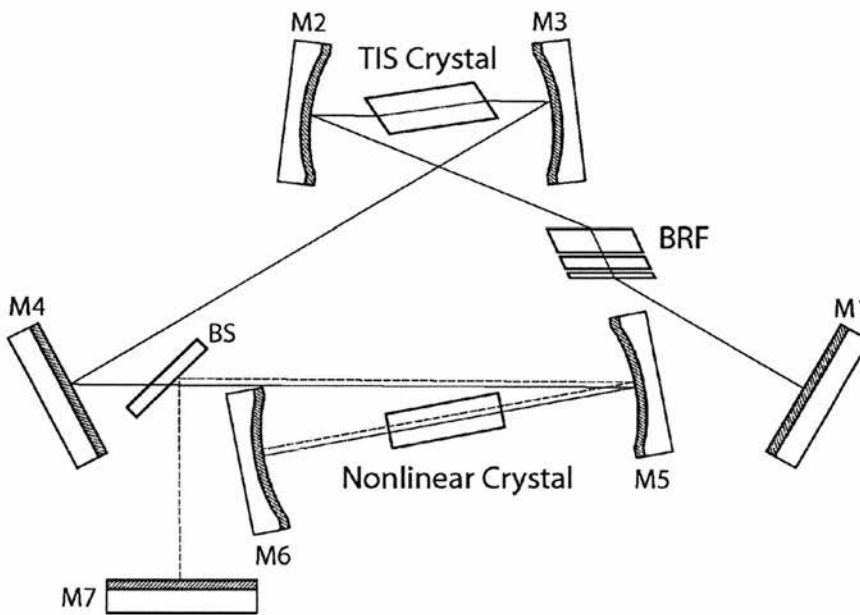


Figure 4. Modified cavity design incorporating a second intracavity focus located at the centre of the nonlinear crystal and utilising a further curved mirror arrangement. Dotted line represents the resonant signal field. BS indicates a beam-splitter specified highly reflecting (HR) at the signal and highly transmitting (HT) at the pump wavelength. Resonant signal field is shown by dotted line.

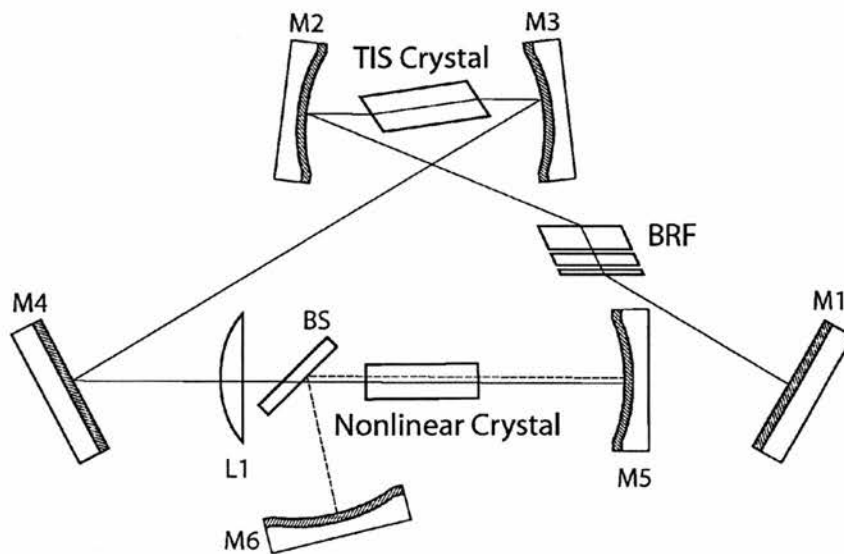


Figure 5. Cavity design incorporating an intracavity lens L1, and utilising one less surface for the signal cavity configuration compared to figure 4. Resonant signal field is shown by dotted line.

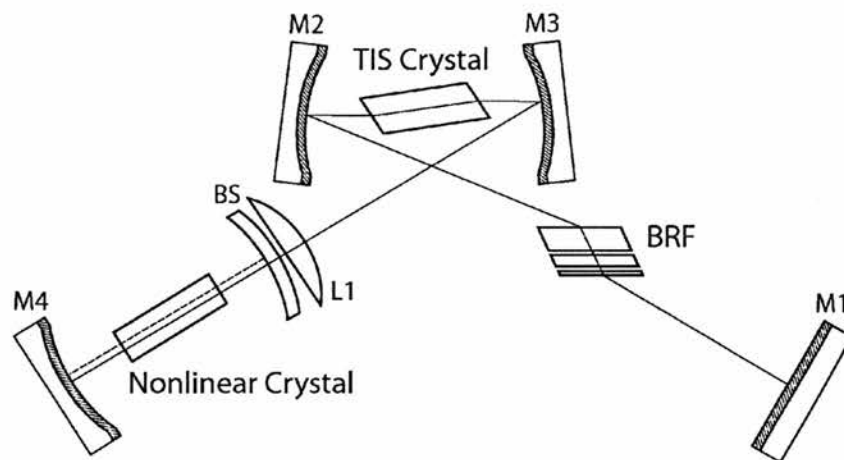


Figure 6. Cavity design with the implementation of the simplest signal cavity configuration (with the exception of monolithic cavity designs). Resonant signal field is shown by dotted line. Here the beam-splitter optic (BS) is a curved zero-power meniscus lens. L1 is an intracavity pump-focusing lens.

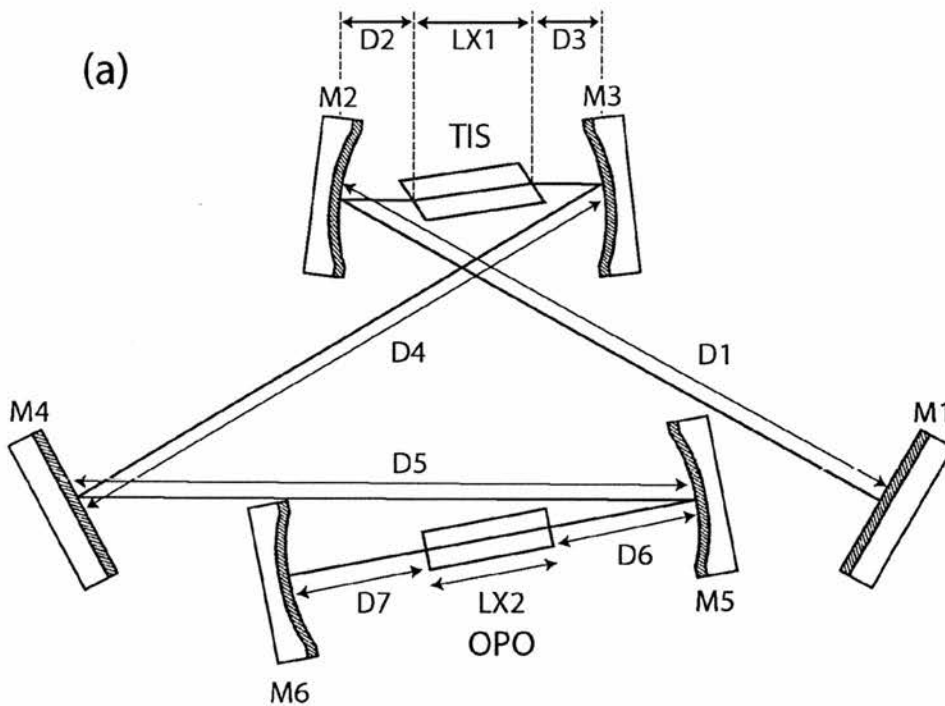
There are merits and also drawbacks with each of the cavity designs of figures 4-6. Each design is able to satisfy the stability and focussing requirements of the ICOPO, whilst, to a greater or lesser degree, accommodating further design requirements such as the ability to include a temperature-controlled oven around the nonlinear crystal or to minimise signal cavity losses. The design most commonly used for the experimental work presented in this thesis is that of figure 4. It should be noted that this design involves the greatest round-trip loss for the signal field as it requires the most number of surfaces to be used of the three arrangements. In practice, this design has proved to be the simplest to align and was readily constructed from optics purchased at the start of the experimental study. Despite the greater loss in the cavity, and hence reduced efficiency, the advantages of having an extended collimated signal branch (BS to mirror M7) outweigh this penalty for robust practical investigation of the device. The access it provides for inserting components into the signal cavity without effecting the pump field, ease of alignment and easily substituted end mirror M7 (the majority of the output-coupling optics used have been plane mirrors) makes this cavity the most flexible of the three for characterisation purposes. The exception arises when an oven is inserted around the nonlinear crystal. In this case, increasing the fold-angle of mirrors M5 and M6 to accommodate an oven introduces a prohibitively large amount of astigmatism to be a practical option. In this case the geometry illustrated in figure 5 is most practical, indeed, the temperature tuning data of the devices presented in the later chapters of this thesis have often been obtained with this cavity design. The design illustrated in figure 6 has yet to be implemented as a device. The benefits of this design are not only the reduced round-trip loss of the signal field, the simplicity is also attractive. The section of cavity extending from lens L1 to mirror M4 in figure 6 is optically equivalent to a plane output coupler from the perspective of the laser. It is evident that such a design encompasses the possibility of a modular "add-on" ICOPO for existing Ti:Sapphire lasers. Further discussions of this geometry are found in the concluding chapter of this thesis.

We have introduced the standing-wave cavity utilised for the experimental implementation of the ICOPO devices presented in this thesis. Illustrations of three separate cavity designs have been briefly discussed with the intention of highlighting the driving factors of simplicity, ease of alignment and experimental versatility upon

which the choice of cavity design has been made. Deviations from this basic design and progress towards alternative technical implementations of the ICOPO will be discussed in the appropriate experimental chapters. For the present section, we shall proceed to analyse the cavities (pump and signal) of figure 4 through the ABCD matrix approach. This methodology may then be extended and modified for alternative cavity geometries.

3.2-3 ABCD matrix analysis of laser and OPO cavities

The ABCD matrix analysis of resonant laser cavities is an integral part of laser and OPO device design [13-15]. Through this analysis, spot sizes, stability ranges and sensitivity to thermal-lensing characteristics may be explored and appropriate design parameters can be identified. The flexibility of this analysis lies in the fact that each element of a laser cavity may be represented by a four-element matrix. The propagation of a resonant Gaussian mode through the cavity elements may be explored through consecutive matrix-multiplication to obtain suitable stability and mode parameters for one round-trip of the laser cavity. In this approach, each focussing element of the round-trip cavity (mirrors M2, M3, M5 & M6 in figure 4) is represented by a lens as shown in figure 7.



(b)

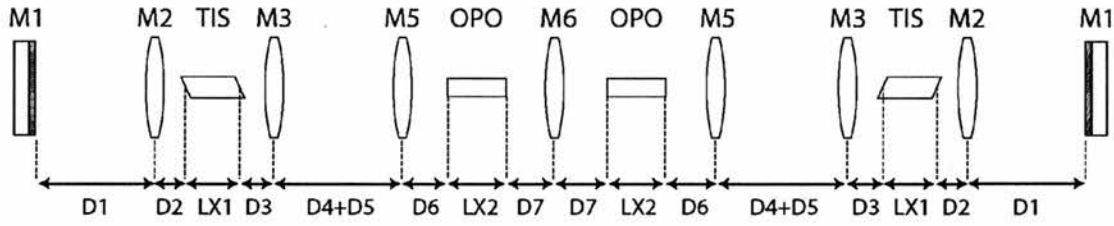


Figure 7. Dual-focus laser cavity parameters for ABCD analysis (a) and expanded cavity model for one round-trip with each focussing element (b). Mirror M4 does not feature in the analysis as the total distance $D4+D5$ is considered between M3 & M5.

Each of the components and free-space elements of figure 7(b) may be represented by a separate ABCD matrix [14]. Due to the astigmatic nature of the cavity, a separate analysis must be made for the sagittal and tangential planes of the cavity where stability criteria must be satisfied for both planes of the cavity to support a stable resonant mode. The appropriate ABCD matrix representations are given in table 1.

ABCD Element	Sagittal Plane	Tangential Plane
 Free Space	$\begin{pmatrix} 1 & d \\ 0 & 1 \end{pmatrix}$	$\begin{pmatrix} 1 & d \\ 0 & 1 \end{pmatrix}$
 Lens	$\begin{pmatrix} 1 & 0 \\ -\frac{\cos\theta}{f} & 1 \end{pmatrix}$	$\begin{pmatrix} 1 & 0 \\ \frac{-1}{f \cos\theta} & 1 \end{pmatrix}$

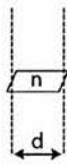
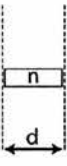
	$\begin{pmatrix} 1 & d/n \\ 0 & 1 \end{pmatrix}$	$\begin{pmatrix} 1 & d/n^3 \\ 0 & 1 \end{pmatrix}$
<i>Brewster Rod</i>		
	$\begin{pmatrix} 1 & d/n \\ 0 & 1 \end{pmatrix}$	$\begin{pmatrix} 1 & d/n \\ 0 & 1 \end{pmatrix}$
<i>Plane Crystal</i>		

Table 1. ABCD ray transfer matrices for the optical elements illustrated in figure 7(b). For the lens matrix, R indicates the radius of curvature of the mirror represented by the element and θ is the fold half-angle of the mirror given by equation (3.2).

The sagittal and tangential ray transfer matrices for the round trip cavity of figure 7 may be calculated by successive multiplication of matrix elements encountered for each plane. The combined product of each ABCD matrix element over one round trip will yield an overall ABCD matrix for the cavity of the form

$$M_s = \begin{pmatrix} A & B \\ C & D \end{pmatrix}_s \quad (3.3)(a)$$

$$M_t = \begin{pmatrix} A & B \\ C & D \end{pmatrix}_t \quad (3.3)(b)$$

where the subscripts s and t refer to the sagittal and tangential matrices respectively. The analysis involves the complex Gaussian beam parameter q which is given by

$$\frac{1}{q} = \frac{1}{R_w} - i \frac{\lambda}{\pi w^2} \quad (3.4)$$

where R_w is the wavefront curvature of the resonant cavity mode and w and λ are the mode radius and wavelength respectively. This complex parameter is related to the round-trip ABCD matrices (3.3)(a)&(b) through the expression

$$q(z_1) = \frac{Aq(z_1) + B}{Cq(z_1) + D} \quad (3.5)$$

which satisfies the condition that the cavity mode must be self-consistent and repeat itself after one round-trip of the cavity from position z_1 . Thus, by analysing a particular cavity geometry, identifying the appropriate matrix elements and evaluating the resulting round-trip matrix, the parameters of the beam may be calculated at the starting position z_1 using (3.4) and (3.5). For a particular cavity to support a stable mode with real solutions the following expression must be satisfied

$$\frac{|A+D|}{2} < 1 \quad (3.6)$$

For any cavity geometry satisfying (3.6) the mode radius at the input plane is given by

$$w = \left[\frac{|B|\lambda}{\pi} \sqrt{\frac{1}{1 - (A+D)^2/4}} \right]^{\frac{1}{2}} \quad (3.7)$$

The laser cavity of figure 7 may be analysed using this matrix method. The stability ranges and spot sizes at the foci are readily calculated for various separations and radii of curvature of mirrors M5 and M6. The separation of mirrors M2 and M3 remains fixed as this has been optimised for the Ti:Sapphire rod length and primary (green) laser pump focusing geometry of the commercial laser used. The analysis of the cavity mode and stability parameters of the OPO cavity is identical to that of the laser cavity with the appropriate parameters of shared components (mirrors M5 & M6 of figures 7 & 8) included as appropriate. Spot sizes for the resonant signal field may be calculated for the cavity illustrated in figure 8, where mirrors M5 & M6 are the common laser - OPO mirrors (see figure 4). The nature of this cavity

arrangement, with shared focussing optics, requires that the chosen mirror ROC and separation must satisfy the stability and focusing requirements of both cavities. The only independent design parameters are the length of the section $D1+D2$ and the ROC of mirror M7 for the signal cavity of figure 8. In practice, it is seldom that there are suitable ranges of ROC for the high-specification optics required for implementing the high-finesse cavities used for these devices. This means that in general, the only true degree of freedom (that can be employed quickly and practically) for independent adjustment of the signal cavity parameters is that of adjusting distance $D1+D2$.

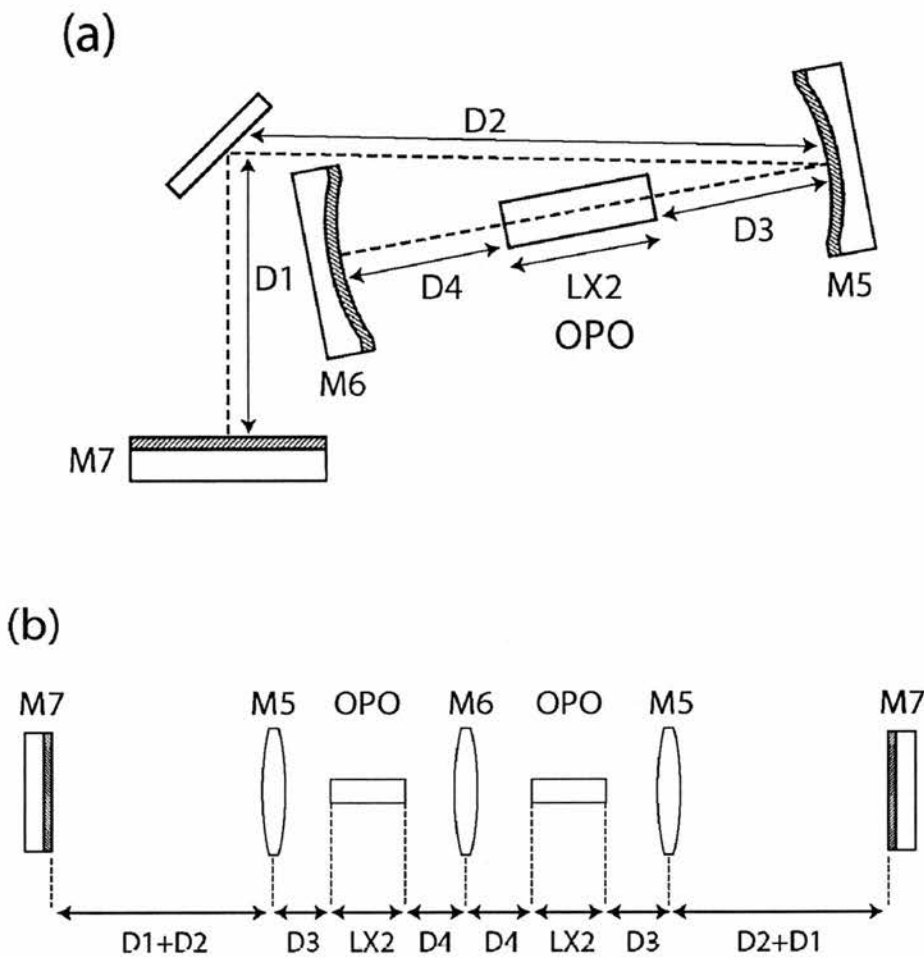


Figure 8. Cavity geometry for the signal field showing shared optics M5 & M6 common to the cavity of figure 7 (a). Expanded round-trip cavity for ABCD analysis of the mode and stability parameters (b).

Diagrams illustrating the form of the stable cavity eigenmodes within the cavities of figures 7 and 8 are shown below for optimum cavity parameters. These optimum parameters are given in table 2.

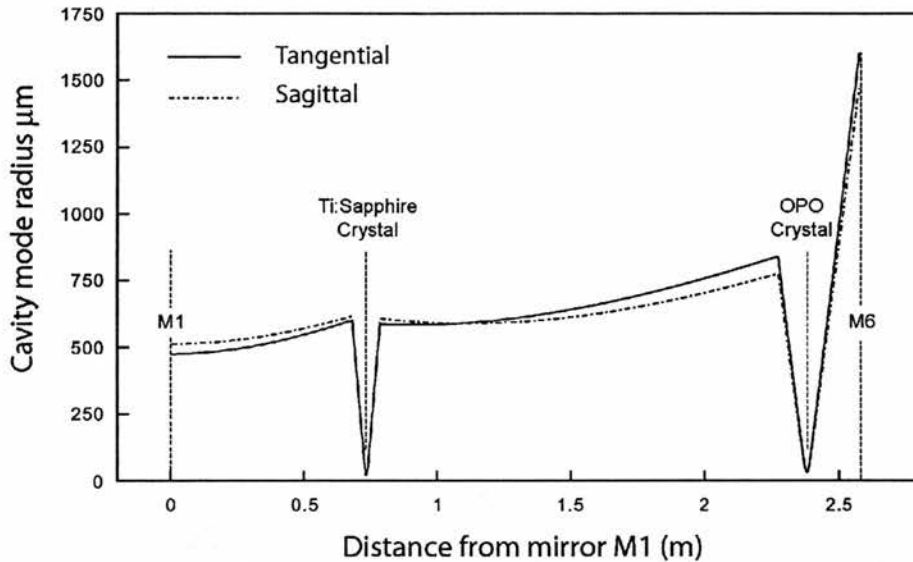


Figure 9. Eigenmode structure for the Ti:Sapphire laser cavity illustrated in figure 7(a). Appropriate optimum cavity parameters are given in table 2. Pump mode wavelength is 810 nm.

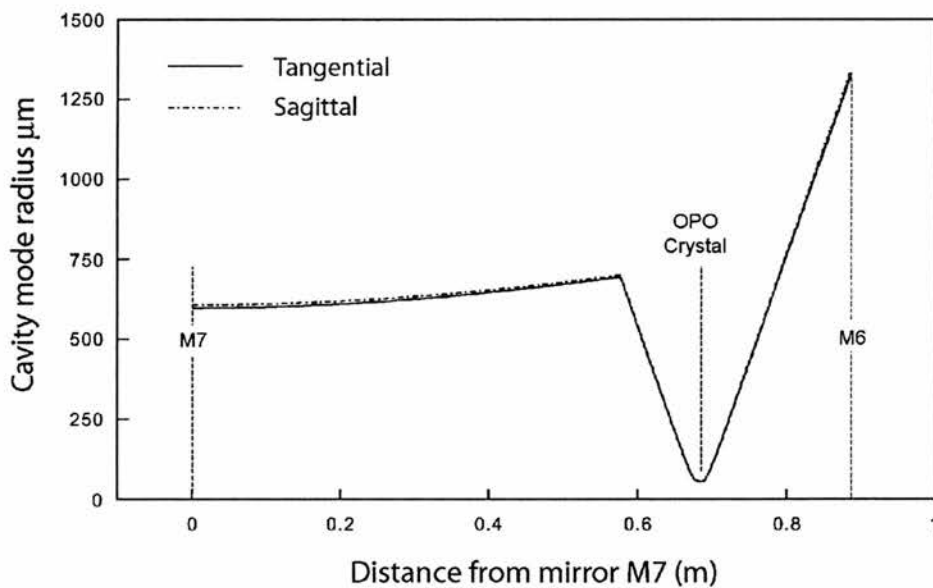


Figure 10. Eigenmode structure for the OPO cavity illustrated in figure 8(a). Cavity parameters are given in table 3. Signal mode wavelength is 1200 nm.

Figures 9 and 10 illustrate the mode structure of the laser and OPO cavities under optimum component spacing. The optimisation of the cavity design is dependent on several critical design goals. The first, and most obvious, of these is that both cavities must support stable eigenmodes. Preference is given to cavity component spacing that supports eigenmodes suitably removed from the edge of the stability criterion of equation (3.6). Clearly, when $|A + D|/2 \approx 1$ but still stable, any small perturbation of the cavity through thermal effects may cause one or both of the cavities to become unstable. The designer of an ICOPO based on Nd^{3+} - laser materials [17] must pay particular attention to this point as the common crystal hosts of this ion are particularly susceptible to thermal lensing effects which must be accounted for using suitable ABCD matrix elements in the design stage. In the context of Ti:Sapphire laser cavity design, a similar approach is required for modelling high peak-power mode locked cavities where thermal lensing must be accounted for as well as further $\chi^{(3)}$ Kerr-lens effects [18]. Another substantial problem of working close to the stability range of the resonant cavity is that mode sizes within the cavity begin to rapidly change with small changes in cavity length. For applications within nonlinear optics, where the efficiency of the processes involved rapidly scale with pump intensity, rapid changes in focused mode size are to be avoided.

Ti:Sapphire Laser Cavity Parameters				
Mirror	ROC (mm)	Angle (Deg)	Separation	Distance (mm)
M1	∞	N/A	D1	645.0
M2	100	9.8	D2	48.7
			LX1	7.6
M3	100	9.8	D3	48.7
M4	∞	N/A	D4	700.0
			D5	786.0
M5	200	2	D6	98.8
			LX2	11.5
M6	200	2	D7	198.4

Table 2. Ti:Sapphire laser cavity parameters from figure 7(a).

OPO Cavity Parameters				
Mirror	ROC (mm)	Angle (Deg)	Separation	Distance (mm)
M7	∞	N/A	D1	200.0
			D2	376.0
M5	200	2	D3	98.8
			LX2	11.5
M6	200	2	D4	198.4

Table 3. OPO Cavity parameters from figure 8(a).

As previously mentioned, the laser used in the majority of the experimental work of this thesis is a modified commercial Ti:Sapphire *Titan* laser [11]. Thus, the optimisation of the Ti:Sapphire crystal length and fold mirror separation has already been undertaken and the optics involved are rigidly embedded on a purpose-built mount with very little scope for manipulation. This may be regarded as something of a blessing as the resultant laser cavity is well engineered and shows excellent stability characteristics. This, in general, makes the modification of the cavity to support a further intracavity focus (between M5 & M6 of figure 7(a)) simpler in that the modification itself should closely maintain the original cavity parameters at the centre of the Ti:Sapphire crystal. It is then a matter of trying to match a suitable spot size at the secondary intracavity focus to the intended length of the nonlinear material to be utilised. There are two adjustable variables that may be utilised to achieve this: the radius of curvature of the focussing mirrors and the separation of these, and other components within the cavity. The most pragmatic and useful view is that only one of these variables is *continuous*, the component spacing. It is prohibitively expensive to specify high-finesse multi-band optical coatings on every radius of curvature that may be useful in obtaining the exact spot size required. Standard optical substrates often increase in radius of curvature in steps of 10 to 50 mm and due to this factor the majority of *experimental* OPO and laser devices are found to contain optics that have radii in multiples of 25 or 50 mm. The optics used in the design and implementation of every device presented in this work are either plane, 50, 100, 150 or 200 mm ROC. This places the optimisation of spot size in its correct context. The methodology involves choosing the nearest ROC for the required pump spot and then optimising the focusing mirror separation of the secondary intracavity focus until the correct spot is obtained at the centre of the

Ti:Sapphire crystal. The mirror separation obtained is then used to model the separate OPO cavity to ensure that it can support a resonant signal mode and is reasonably within the stability range criterion (3.6).

ABCD analysis of the two resonant cavities shows that the stability ranges of the Laser and OPO cavities overlap over a displacement range of approximately 4mm for the mirror separation of M5 and M6. Over this range the pump and signal waist radii vary by as much as 50% from their optimum values shown in table 4 for the cavity component spacing of tables 2 and 3.

Waist Radii (μm) @ M5-M6		
<i>Waist</i>	<i>Sagittal</i>	<i>Tangential</i>
Laser	35	32
OPO	54	55

Table 4. Resonant Laser and OPO waist radii between mirrors M5 and M6 for the cavity spacing of tables 2 & 3.

The waist radii at the pump wavelength correspond to a confocal parameter $b \approx 9\text{mm}$ (where $b = 2\pi w_0^2/\lambda$) for a nonlinear crystal of length 11.5 mm (as utilised in the device of chapter 4). Optimum focussing conditions occur for pump focussing parameters $l/b > 1$ [19] and thus, the cavity arrangement described above is a sound basis for initial characterisation of the ICOPO. It should be re-affirmed that that particular cavity chosen here is one that provides the most flexibility in terms of simple alignment and ease of characterisation. The cavities of figures 5 and 6 decouple the pump and signal focussing as the pump focus is maintained with a single lens. This factor provides a far broader scope for signal and pump waist optimisation for these geometries which makes both cavities attractive options for devices with tight design requirements in terms of efficiency and power-scaling. The details of specific cavity designs will be given in the appropriate experimental chapters. The discussion of Ti:Sapphire laser design will now address the issue of line-narrowing and tuning.

3.2-4 Tuning the Ti:Sapphire laser

The large gain bandwidth of $\text{Ti:Al}_2\text{O}_3$ results in a broad spectral output under free-running conditions. In practice, this broad output (usually a function of both the gain bandwidth and appropriate mirror reflectivities) falls outwith the acceptance bandwidth of most parametric processes by over an order of magnitude. As a homogeneously-broadened laser medium, $\text{Ti:Al}_2\text{O}_3$ will naturally lase at the centre of the transition gain-bandwidth within a given mirror bandwidth. In order to narrow the laser output and provide frequency selectivity within the gain bandwidth a tuning mechanism is required that will suppress laser oscillation on all but one mode. This mechanism must present as little loss as possible to the selected mode and ideally provide continuous tuning of this mode over the entire gain bandwidth (some 150 nm). The device most commonly used to satisfy these two conditions is the intracavity birefringent-plate tuner as described by Bloom [20]. The principle of this mechanism is that the natural spectral dispersion of a birefringent material (commonly crystal quartz) may be utilised to resolve the polarised laser mode along two orthogonal directions within a birefringent plate. The plate is inserted internally to the laser cavity at Brewster's angle for the polarised laser mode (see figure 3) and rotated about the axis of the beam to access different phase-retardations for the orthogonal modes resolved in the axis of the plate. In general, the resultant mode will be elliptical and suffer loss at further Brewster surfaces within the cavity. As the phase-retardation, and hence the ellipticity, of the mode will be a function of wavelength (due to dispersion) the Brewster plate may be designed as a wavelength-tunable filter. A common three-plate birefringent filter (BRF) is illustrated in figure 11. The band-pass characteristic of the filter shown may be analysed using Jones-matrix analysis as undertaken by Preuss and Gole [21] although care should be taken to use the appendix of the paper for the correct analytic expressions [22]. To a good approximation, the transmitted *field* amplitude E_t of one of the birefringent plates illustrated in figure 11 may be given by [21]

$$E_t(\theta, \phi) = (n_o^2 - \cos^2(\phi)\cos^2(\theta))^{-1} \times \dots \\ \dots [\exp(i\delta_e(\theta, \phi))n_o^2 \sin^2(\phi) + \exp(i\delta_o(\theta, \phi))(n_o^2 - \cos^2(\theta))\cos^2(\phi)] \quad (3.8)$$

where

$$\delta_e(\theta, \phi) = \frac{2\pi n_e t}{\lambda} \frac{\left[1 + \frac{\cos^2(\theta)\cos^2(\phi)}{n_e^2} - \frac{\cos^2(\theta)\cos^2(\phi)}{n_o^2} \right]}{\left[1 - \frac{\cos^2(\theta)\sin^2(\phi)}{n_e^2} - \frac{\cos^2(\theta)\cos^2(\phi)}{n_o^2} \right]^{\frac{1}{2}}} \quad (3.9)$$

$$\delta_o(\theta, \phi) = \frac{2\pi n_o t}{\lambda} \frac{1}{\left[1 - \frac{\cos^2(\theta)}{n_o^2} \right]^{\frac{1}{2}}} \quad (3.10)$$

n_e and n_o are the extraordinary and ordinary refractive indices of the birefringent plate, t is the thickness, λ is the wavelength, ϕ is the angle of rotation around the crystal axis and θ is the angle between the incident ray and the plate surface ($\theta = \pi/2 - \theta_B$).

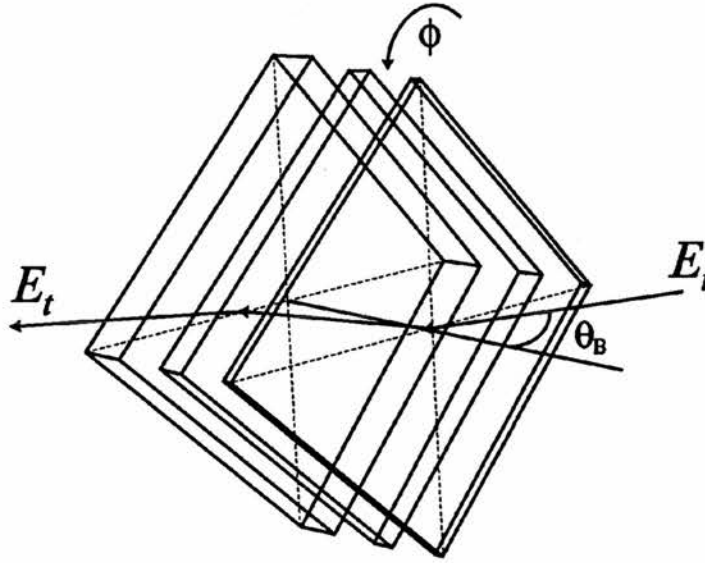


Figure 11. Three-stage intracavity birefringent filter (BRF) inserted at Brewster's angle θ_B . E_i and E_t are the incident and transmitted field amplitudes respectively. ϕ is the rotation angle of the plate about the plate axis.

A plot of the spectral transmission characteristic of the 3-plate filter of figure 11 may be calculated from equations (3.8), (3.9) and (3.10) using Sellmeier data for quartz [23]. The transmitted intensity of each plate is given by

$$I_t(\theta, \phi) = E_t(\theta, \phi) \cdot E_t^*(\theta, \phi) \quad (3.11)$$

A qualitative picture of the combined transmission may be found by multiplying the transmission functions of each plate in turn to give an overall curve as shown in figure 12. The spectral location of the peaks is correct but the actual loss incurred has been exaggerated as the loss per Brewster surface is only about 17% for the TE polarisation.

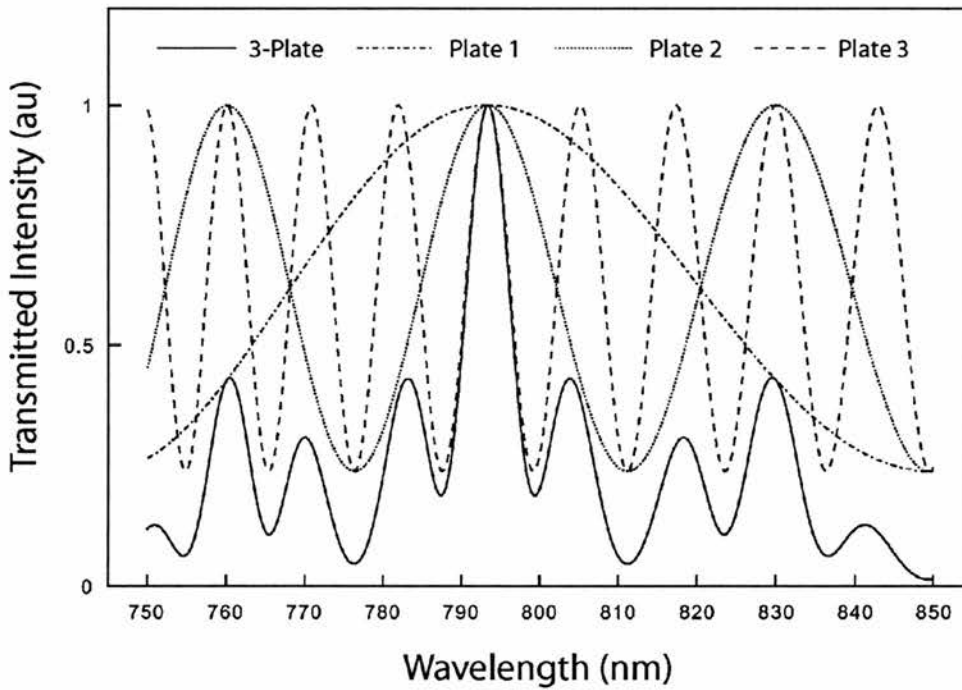


Figure 12. Transmission function of a 3-plate Quartz filter illustrated in figure 11. The solid line shows the overall transmission and the dotted lines show the individual contributions from each plate. Plate 1 $t = 1\text{mm}$, Plate 2 $t = 3\text{mm}$, Plate 3 $t = 9\text{mm}$. Ratio is 1:3:9. Values of θ and ϕ are 33 and 55 degrees respectively.

Rotating the filter assembly around the axis of the filter (rotation angle ϕ) tunes the central transmission peak. This rotation changes the absolute refractive index "seen" by the resolved polarisation components. In order to emerge from the birefringent plate with an unchanged polarisation mode, the wavelength of the resonant mode must adjust to access different values of the material dispersion that will counteract the index change due to rotation. The manufacture of such a birefringent filter requires tight tolerances. An important factor in its design is that the plates must be in an exact integer ratio. Examination of figure 12 and equations (3.9) and (3.10) show that the spectral location of the peak transmission of each plate is a function of the plate thickness if each plate is aligned to a common angle ϕ . In order for these transmission peaks to align in frequency space, the thickness of the plates must be in an exact integer ratio to \sim one part in 10^4 [21]. Corrections for tolerance errors in the plate thickness may be made by a small rotation $\Delta\phi$ of each plate relative to the others in order to maximise transmission although this will affect the absolute tuning range of the filter assembly. The theory presented by Preuss and Gole in reference [21] provides a useful insight into the design and implementation of the BRF and makes a number of approximations. It does not undertake a quantitative analysis of the loss experienced by the rejected TE mode of the induced elliptical polarisation states, nor does it fully account for the spatial splitting of the two polarisation modes. Zhu [24] has addressed the spatial displacement of these modes and finds that the optical path length difference is a significant factor in the operation of the BRF. Both authors avoid including the effects of optical activity in the Quartz plates. For the present purpose of outlining the tuning *mechanism* of the Ti:Sapphire laser containing a 1:3:9 ratio BRF, the approximations made do not detract from the useful insight gained from the cited analysis. More rigorous analysis of birefringent filters may be found in the literature [25, 26].

3.3 ICSRO Power analysis

The final implementation of the ICSRO requires background knowledge of the power characteristics of these devices in terms of the laser and OPO thresholds. This will allow appropriate bounds to be placed on the primary pump laser requirements, and ultimate efficiencies of the devices outlined in the later chapters. More importantly, the scope and versatility of the intracavity pumping approach and its application to a broad range of nonlinear materials and power domains will become clearer once its full mode of operation has been explored.

3.3-1 Theoretical background

The theoretical analysis of the *continuous-wave* intracavity OPO began with a paper investigating the efficiency and dynamics of the doubly-resonant (DRO) configuration by Oshman and Harris [27] in 1968. Their work identified three operation regimes for the ICDRO. The first is a stable efficient mode with a fixed phase relationship between the pump, signal and idler fields of $\Delta\phi = \pi/2$. The second is a stable inefficient mode where $\Delta\phi \neq \pi/2$ and the parametric process begins to drive the phase of the interacting fields rather than the amplitude. The third mode, which occurs at pump powers ≈ 3 times above OPO threshold, is a repetitively pulsing regime. The factors that will dictate which mode will operate are governed by the relative losses and gains of each interacting field of the parametric interaction as well as the relative gains of the laser and parametric processes. The implications for CW power scaling are greatly affected by the limits placed by these regimes. While there were a number of early reports of ICDRO operation [28-31], the operation of the ICSRO remained neglected until a theoretical treatment in the mid 1980s [32] and later analysis of the pulsed ICSRO [33]. The work of references [32, 33] has been extended to include multi-frequency pump schemes and power stability by Turnbull *et al* [34] and the salient conclusions of this analysis are outlined below. Further discussion and detailed derivation of the expressions used may be found in reference [35].

3.3-2 Power analysis

The analysis outlined in the following section is based on the work of Graham A. Turnbull, undertaken in the School of Physics and Astronomy at St Andrews University [35]. I wish to acknowledge that the following section draws exclusively from his work and is reproduced here for completeness.

A simplified generic ICSRO cavity geometry is shown in figure 13. The high-finesse laser and OPO cavities are discriminated by a beam splitter. The nonlinear medium of length l is placed at the end of the laser cavity and its end face coincides with the cavity origin $z = 0$. A laser gain medium is located in the pump field branch of the cavity and is pumped by an external pump laser source through the end mirror. The idler field exits from the cavity in a single pass and is non-resonant.

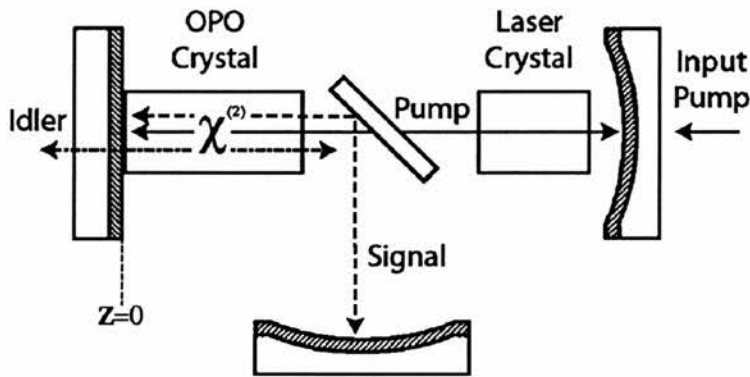


Figure 13. Schematic of the ICSRO cavity geometry.

The standing-wave pump cavity illustrated in figure 13 will, in practice, produce a multi-frequency laser field due to spatial hole burning in the homogeneously broadened gain medium. It is assumed that all the modes of this field fall well within the acceptance bandwidth of the nonlinear material. The resonant signal is assumed to be single frequency which is found to be in good agreement with experimental observations [1, 36]. Overall cavity lengths are L_s and L_p for the signal and pump cavities respectively. The Gaussian pump and signal fields are defined as [34]

$$E_p(z, r, t) = \sum_j 2E_{pj}(t) \exp(-r^2/w_p^2) \sin(k_{pj}z) \cos(\omega_{pj}t + \phi_{pj}) \quad (3.12)$$

$$E_s(z, r, t) = 2E_s(t) \exp(-r^2/w_s^2) \sin(k_s z) \cos(\omega_s t + \phi_s) \quad (3.13)$$

where $k_{pj} = n_{pj}\omega_{pj}/c$ and $k_s = n_s\omega_s/c$ with n_s and n_p averaged over the cavity. The laser and signal waist radii are given by w_p and w_s respectively. The analysis assumes that each of the j axial modes of the laser mix with the single frequency signal mode to produce j idler modes. For the standing-wave geometry of figure 13, the parametric interaction must be investigated for both $\pm z$ directions, hence equations (3.12) and (3.13) may be generally expressed in the form

$$E_p(z, r, t) = \frac{1}{2} \{E_p^+(z, r, t) - E_p^-(z, r, t)\} + c.c. \quad (3.14)$$

$$E_s(z, r, t) = \frac{1}{2} \{E_s^+(z, r, t) - E_s^-(z, r, t)\} + c.c. \quad (3.15)$$

$$E_p^\pm(z, r, t) = \sum_j E_{pj}^\pm(t) \exp(\pm ik_{pj}z) \exp(-i(\omega_{pj}t + \phi_{pj}^\pm)) \exp(-r^2/w_p^2) \quad (3.16)$$

$$E_s^\pm(z, r, t) = E_s(t) \exp(\pm ik_s z) \exp(-i(\omega_s t + \phi_s^\pm)) \exp(-r^2/w_s^2) \quad (3.17)$$

with the travelling-wave field-components having $\pm k_{pj,s}z$ being denoted with \pm . Equations (3.14)-(3.17) may be substituted into the Maxwell wave equation in a manner similar to that described in chapter 2 by inserting appropriate polarisation terms for the parametric process and taking care to preserve the directional (\pm) interaction notation. The polarisation term of the idler field is found to re-radiate idler field components (in both \pm directions) given by

$$E_i^\pm(z, r, t) = \sum_j E_{ij}^\pm(t) \exp(\pm ik_{ij}z) \exp(-i(\omega_{ij}t + \phi_{ij}^\pm)) + c.c. \quad (3.18)$$

The important consequence of the singly resonant condition is that the idler field (for which the cavity has a very low finesse) exits from the crystal after one pass only. Thus, for each pass of the nonlinear medium the initial idler phase is dictated by the dominant resonant pump and signal fields maintaining a phase relationship given by $\Delta\phi_j = \phi_{pj} - \phi_s - \phi_{ij} = \pi/2$. This liberates the parametric interaction from the inefficient, phase-driven regime of the ICDRO. The spatial transverse variation of the idler field is assumed to take the form of the driving polarisation. A further

assumption is that the temporal variation of the idler occurs on timescales dictated by the resonant fields (as these provide the source terms for the idler field). As the pump and signal fields are confined in high-finesse cavities, their cavity lifetimes are long and over the transit time for these fields within the nonlinear medium, they provide an almost constant polarisation source term for the idler. Thus, time derivatives arising from the Maxwell wave equation are small compared to the spatial derivative and may be neglected. The highly qualitative view is that in the single-pass idler scheme, the idler goes from "nothing" to "something" over the transit time along z of the nonlinear medium whereas the idler source term simply goes from "something" to "almost the same something". The resulting idler field may be expressed as

$$\begin{aligned}
 E_i^\pm(z, r, t) &= \frac{d_{eff}}{i\Delta k n_i c} \exp(-r^2(w_p^{-2} + w_s^{-2})) E_s(t) \\
 &\times \sum_j \left\{ \omega_i E_{pj}(t) \exp(-(\omega_{ij}t + \phi_{ij}^\pm) \pm k_{ij}z) \right. \\
 &\quad \left. \times \left(\exp\left(\Delta k \left(\begin{matrix} z \\ l-z \end{matrix} \right) \right) - 1 \right) \right\} + c.c.
 \end{aligned} \tag{3.19}$$

where the individual phase mis-match of each j^{th} mode is replaced by a common Δk as all the j modes are assumed to lie well within the parametric gain bandwidth. The coupled rate equations for the ICSRO may be derived following the example of reference [33]. The fields within the resonator are commonly described using Lamb's self-consistency equations [37]. These equations describe the axial field modes arising from polarisation source terms that re-radiate consistent fields identical to the driving fields. The resonant laser field will contain polarisation terms that are anchored in the laser and nonlinear mediums whereas the resonant signal field is self-consistent with nonlinear polarisation source terms only. Both fields are coupled through the $\chi^{(2)}$ nonlinear process, a factor that has significant implications for the transient dynamics of the ICSRO [38]. The relevant self-consistency equation for the pump and signal fields with cavity decay times τ'_p , and τ'_s respectively are given by

$$\frac{\partial E_s(t)}{\partial t} + \frac{E_s(t)}{\tau'_s} = -\frac{\omega_s}{2\varepsilon_0 n_s^2} \text{Im}[\mathbf{P}_s^+(t) + \mathbf{P}_s^-(t)] \quad (3.20)$$

$$\frac{\partial E_{pj}(t)}{\partial t} + \frac{E_{pj}(t)}{\tau'_p} = -\frac{\omega_{pj}}{2\varepsilon_0 n_p^2} \text{Im}[\mathbf{P}_{pj}^+(t) + \mathbf{P}_{pj}^-(t)] - \frac{\omega_{pj}}{2\varepsilon_0 n_p^2} \text{Im}[\mathbf{P}_{laserj}(t)] \quad (3.21)$$

Where the parametric process polarisation terms $\mathbf{P}_{pj}^\pm(t)$ and $\mathbf{P}_s^\pm(t)$, are related to the nonlinear polarisation terms through volume integrals over the crystal length and radial transverse co-ordinates to yield

$$\text{Im}(\mathbf{P}_s^\pm(t)) = -\frac{2}{1 + w_s^2/\bar{w}_s^2} \frac{\varepsilon_0 l d_{eff}^2}{c n_i} \frac{l}{2L_s} \text{sinc}^2\left(\frac{\Delta kl}{2}\right) E_s(t) \sum_j \omega_{ij} E_{pj}(t)^2 \quad (3.22)$$

$$\text{Im}(\mathbf{P}_{pj}^\pm(t)) = -\frac{2}{1 + w_p^2/\bar{w}_p^2} \frac{\varepsilon_0 l d_{eff}^2}{c n_i} \frac{l}{2L_p} \text{sinc}^2\left(\frac{\Delta kl}{2}\right) E_{pj}(t) \omega_{ij} E_s(t)^2 \quad (3.23)$$

where we have set the relative phase difference of the parametrically coupled fields as $\Delta\phi^+ = \pi/2$ and $\Delta\phi^- = \pi/2 - \Delta kl$ and the waist radius of the nonlinear polarisation $\bar{w}_{s,p}$ is given by [39]

$$1/\bar{w}_{s,p}^2 = 1/w_i^2 + 1/w_{p,s}^2 \quad (3.24)$$

The last substitution that must be made is to replace the laser polarisation term $\text{Im}(\mathbf{P}_{laserj}^\pm(t))$ in equation (3.21) with the expression [35]

$$\frac{G_j E_{pj}}{G_{j-th} \tau'_p} \quad (3.25)$$

to give

$$\tau'_p \frac{\partial E_{pj}}{\partial t} = \left(\frac{G_j}{G_{j-th}} - 1 \right) E_{pj} - \frac{\tau'_p \omega_p C_{pj}}{\varepsilon_0 n_p^2} \quad (3.26)$$

where G_j is the saturated laser gain of the j^{th} laser mode and G_{j-th} is the threshold gain required for the oscillation of the j^{th} mode. The analysis of the steady-state

power characteristics is further simplified through the introduction of the following photon flow expressions for the resonant modes

$$F_s = n_s c \epsilon_0 E_s^2 \pi w_s^2 / 4 \hbar \omega_s \quad (3.27)$$

$$F_{pj} = n_p c \epsilon_0 E_{pj}^2 \pi w_p^2 / 4 \hbar \omega_{pj} \quad (3.28)$$

The laser photon flow threshold value may be obtained from equations (3.22) and (3.20) and is given by

$$\left[\sum_j F_{pj} \right]_{th} = \frac{n_p n_s^2 n_i c^2 \epsilon_0 L_s}{\hbar \omega_p \omega_s \omega_i \tau_s' d_{eff}^2 l^2} \frac{\pi (w_s^2 + w_p^2)}{2} \frac{1}{\text{sinc}^2(\Delta k l / 2)}$$

This result is the multi-mode threshold expression for the ICSRO. Here the photon flow of each laser mode contributes to the threshold condition and we see the familiar $\text{sinc}^2(\Delta k l / 2)$ expression encountered in the phase-matching section of chapter 2. If the laser bandwidth is sufficiently small all the j modes of the laser may be considered as phase-matched and the multi-mode laser will provide the same threshold condition as a single frequency laser of the same total power, consistent with the analysis of Harris [40]. The normalised gain, signal power and laser power are given by

$$N_j = G_j / G_{j-th} \quad (3.29)$$

$$P_s = F_s / \left[\sum F_{pj} \right]_{th} \quad (3.30)$$

$$P_{pj} = F_{pj} / \left[\sum F_{pj} \right]_{th} \quad (3.31)$$

which give appropriate expressions for equations (3.20) and (3.21) as

$$\tau_s \frac{\partial P_s}{\partial t} = P_s (\sum P_{pj} - 1) \quad (3.32)$$

$$\tau_s \frac{\partial P_{pj}}{\partial t} = P_{pj} (N_j - 1 - F P_s) \quad (3.33)$$

where

$$F = \frac{\tau'_p n_s L_s}{\tau'_s n_p L_p} \quad (3.34)$$

is the ratio of the laser and signal cavity finesse and τ_p , τ_s are the laser and signal cavity photon lifetimes (where $\tau_{p,s} = \tau'_{p,s}/2$). The final equation that completes the full compliment of expressions that describe the steady-state and transients of the ICSRO is an evolution equation for the saturated laser gain

$$\tau_u \frac{\partial N_j}{\partial t} = \sigma_j - N_j \left(1 + x P_{pj} + x \mu \sum_{k \neq j} P_{pk} \right) \quad (3.35)$$

where τ_u is the upper-state lifetime of the laser medium, σ_j is a pumping-rate term equal to the number of times that the j^{th} mode is pumped above threshold and x is a saturation parameter given by

$$x = \frac{\left[\sum_j F_{pj} \right]}{F_{sat}} \quad (3.36)$$

with the saturation parameter, F_{sat} , representing the laser saturation photon flow. Cross saturation between pairs of laser modes is introduced by the coefficient $\mu < 1$, a concept introduced in the analysis of intracavity SHG [41] to account for partial inhomogeneous broadening caused by spatial hole burning.

3.3-3 The ICSRO steady-state power characteristics

Equations (3.32)-(3.35) may be solved for the steady-state by setting time derivatives to zero. For a single-frequency pump laser, the general solutions are

$$P_p^0 = 0 \quad (3.37)$$

$$N^0 = \sigma \quad (3.38)$$

$$P_s^0 = 0 \quad (3.39)$$

where (3.37)-(3.39) represent the rather uninspiring steady-state solutions of the laser below threshold where the only thing happening is a linear increase in laser gain with external pumping rate σ . Between the laser threshold pumping and the SRO threshold pumping rate ($\sigma_{th-L} \leq \sigma \leq \sigma_{th-SRO}$) the solutions take the form

$$P_p^0 = \frac{\sigma - 1}{x} \quad (3.40)$$

$$N^0 = 1 \quad (3.41)$$

$$P_s^0 = 0 \quad (3.42)$$

Equations (3.40)-(3.42) now describe the operation of a normal single-frequency laser with the laser gain clamped at threshold. The intracavity power is increasing linearly with the pumping rate. The SRO is still below threshold and is merely contributing to the internal losses of the laser via the parasitic loss of its optics. The steady-state solutions above OPO threshold ($\sigma_{th-SRO} \leq \sigma$) are

$$P_p^0 = 1 \quad (3.43)$$

$$N^0 = \frac{\sigma}{1+x} \quad (3.44)$$

$$P_s^0 = \frac{(N^0 - 1)}{F} \quad (3.45)$$

The final solutions (3.43)-(3.45) describe the power characteristics above SRO threshold. Equation (3.43) shows that the laser field photon flow is now clamped at its threshold value, a concept outlined in 1962 by Siegman [42] as a possible nonlinear optical power limiter. Any increase in the external pumping rate σ induces a linear increase in laser gain, which is now coupled through the nonlinear process to produce a linear increase in down-converted signal and idler fields. This is illustrated in figure 14 where, we have replaced the *photon flow* pumping thresholds σ_{th-L} and σ_{th-SRO} with their respective pumping *power* thresholds P_{th}^L and P_{th}^{SRO} . The extension of solutions (3.37)-(3.45), to involve the multi-frequency laser pump introduces further terms relating to the cross-saturation coefficient μ in (3.35) and appropriate summation over the laser modes. The overall nature of the equations

remains identical to the single frequency case when power optimisation and behaviour are considered. One consequence of the multi-frequency analysis is a small amount of narrowing of the pump laser field as the peripheral modes of the laser bandwidth "die out" through the onset of the nonlinear loss presented by the SRO operation above threshold [34].

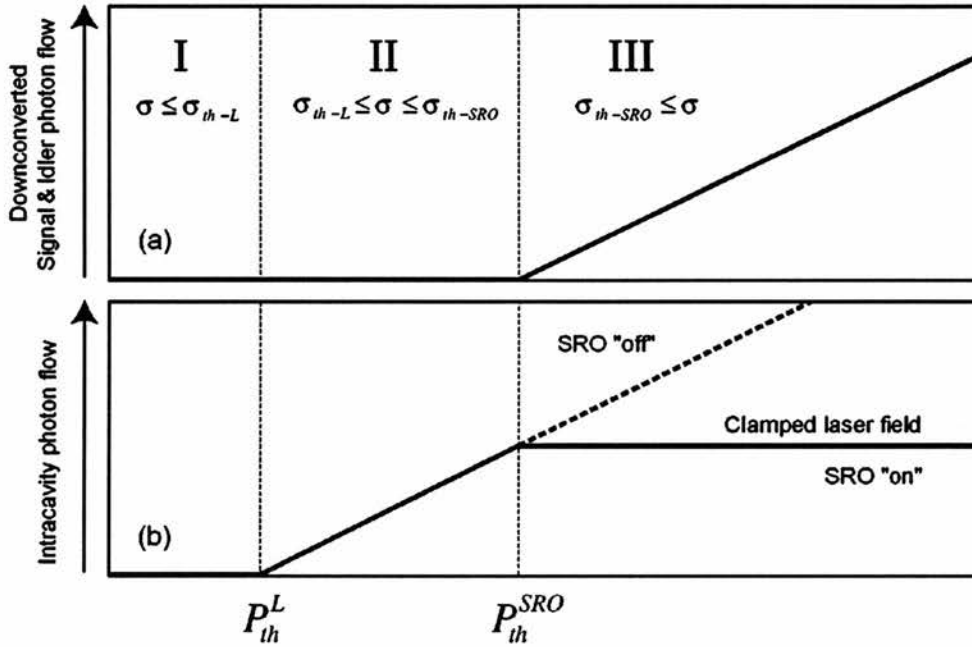


Figure 14. (a) Downconverted photon flow characteristic for the ICSRO. Regions I, II & III are described by equations (3.37)-(3.45). Here we have replaced the photon flow pumping thresholds σ_{th-L} and σ_{th-SRO} with their respective pumping power thresholds P_{th}^L and P_{th}^{SRO} on the x-axis. (b) Laser intracavity photon flow in each region of operation. The clamping effect is shown for pumping rates above SRO threshold.

It can be seen from equations (3.43)-(3.45) and figure 14 that the intracavity SRO is now acting as a nonlinear output-coupler. If this is indeed the case, then there will be some optimum ratio of this output-coupling to input pumping rate. This is discussed next.

3.3-4 Power optimisation

Optimisation procedures for the output powers of the ICSRO provide the necessary insight needed to make judicial choices regarding specific laser pumping schemes. Relating this optimisation to relative SRO and laser thresholds and to available external pump powers, a clear picture of the flexibility of the ICSRO concept becomes apparent. Perhaps the most attractive feature of the ICSRO is its ability, under optimum conditions, to downconvert 100% of the available optimum output power of its "host" pump laser source to signal and idler fields [32]. Examination of equations (3.30), (3.36) and (3.43)-(3.45) yields

$$F_s = F_{sat} \frac{\alpha_p}{\alpha_s} (\sigma - \sigma_{th-SRO}) \left(1 - \frac{\sigma_{th-L}}{\sigma_{th-SRO}} \right) \quad (3.46)$$

where the substitution $F = \alpha_s / \alpha_p$ has been made and α_s, α_p are the round-trip photon losses in the signal and pump resonant cavities. Equating the round-trip signal and idler photon losses in the steady-state gives an idler output of

$$(F_i)_{out} = F_{sat} \alpha_p (\sigma - \sigma_{th-SRO}) \left(1 - \frac{\sigma_{th-L}}{\sigma_{th-SRO}} \right) \quad (3.47)$$

Combining equations (3.46) and (3.47) we may express the total downconverted power P_{DC} of the laser photon flow to signal and idler photon flows in terms of input laser power and thresholds as

$$P_{DC} = \gamma_{max} (P_{in} - P_{th}^{SRO}) \left(1 - \frac{P_{th}^L}{P_{th}^{SRO}} \right) \quad (3.48)$$

where table 5 lists the new power terms that have been introduced. The term γ_{max} is equal to the output slope efficiency of the laser and accounts for the coupling efficiency between the primary pump input power and the circulating laser field. The expression for γ_{max} is

$$\gamma_{\max} = \eta_{in} \eta_{abs} \frac{\lambda_{p-in}}{\lambda_p} \quad (3.49)$$

where η_{in} is the optical coupling efficiency of the input primary pump laser at wavelength λ_{p-in} into the pump laser crystal, η_{abs} is the amount of this pump power that is absorbed and λ_{p-in} , λ_p are the wavelengths of the input primary pump laser and the pump laser respectively.

Equivalent terms		
Term	Field power	Photon flow
Input pump	P_{in}	σ
Laser threshold	P_{th}^L	σ_{th-L}
SRO threshold	P_{th}^{SRO}	σ_{th-SRO}

Table 5. Equivalent terms of input pump rates and device thresholds of equations (3.46), (3.47) and (3.48).

Optimisation of equation (3.48) for a specific input power P_{in} is realised through the solution of the equation

$$\frac{\partial P_{DC}}{\partial P_{th}^{SRO}} = 0 \quad (3.50)$$

which gives the SRO threshold condition that satisfies the maximum downconverted power obtainable for a specific input power and laser threshold as

$$P_{th}^{SRO} = \sqrt{P_{th}^L \cdot P_{in}} \quad (3.51)$$

The condition (3.51) can be used to derive the maximum obtainable downconversion for a specific laser threshold and input pump power under optimum SRO threshold conditions. This is given by

$$(P_{DC})_{\max} = \gamma_{\max} \left(\sqrt{P_{in}} - \sqrt{P_{th}^L} \right)^2 \quad (3.52)$$

This expression is identical to that describing the optimum output power $(P_{out}^L)_{\max}$ of the pump laser that contains the ICSRO, which is

$$(P_{out}^L)_{\max} = \gamma_{\max} \left(\sqrt{P_{in}} - \sqrt{P_{th}^L} \right)^2 \quad (3.53)$$

Thus, under optimum conditions we have, from (3.48) and (3.53)

$$\gamma_{\max} (P_{in} - P_{th}^{SRO}) \left(1 - \frac{P_{th}^L}{P_{th}^{SRO}} \right) = \gamma_{\max} \left(\sqrt{P_{in}} - \sqrt{P_{th}^L} \right)^2 \quad (3.54)$$

and

$$P_{in} = \frac{(P_{th}^{SRO})^2}{P_{th}^L} \quad (3.55)$$

These optimisation conditions may be illustrated graphically by plotting the appropriate functions that describe optimum downconverted power and optimum laser output for a range of input powers as shown in figure 15.

A clear insight into the operational characteristics of the ICSRO may be obtained from examining figure 15. We see that above threshold, the SRO rapidly approaches 100% efficiency under the optimum laser and SRO threshold condition (3.55). Thus to maximise the output power at the non-resonant idler field for a given laser threshold and input pump power, the SRO threshold should be set to satisfy equation (3.55). The three regions of operation I, II and III are the equivalent regions illustrated in figure 14. It should be noted that the optimum output power of the laser $(P_{out}^L)_{\max}$ has been plotted in figure 15 in order to give a clear picture of the optimum downconversion condition. Under ideal operating conditions, the pump laser cavity will only output-couple power in the form of downconverted signal and idler fields

and not at the pump wavelength as all mirrors of the laser cavity are specified to be highly reflecting for the pump.

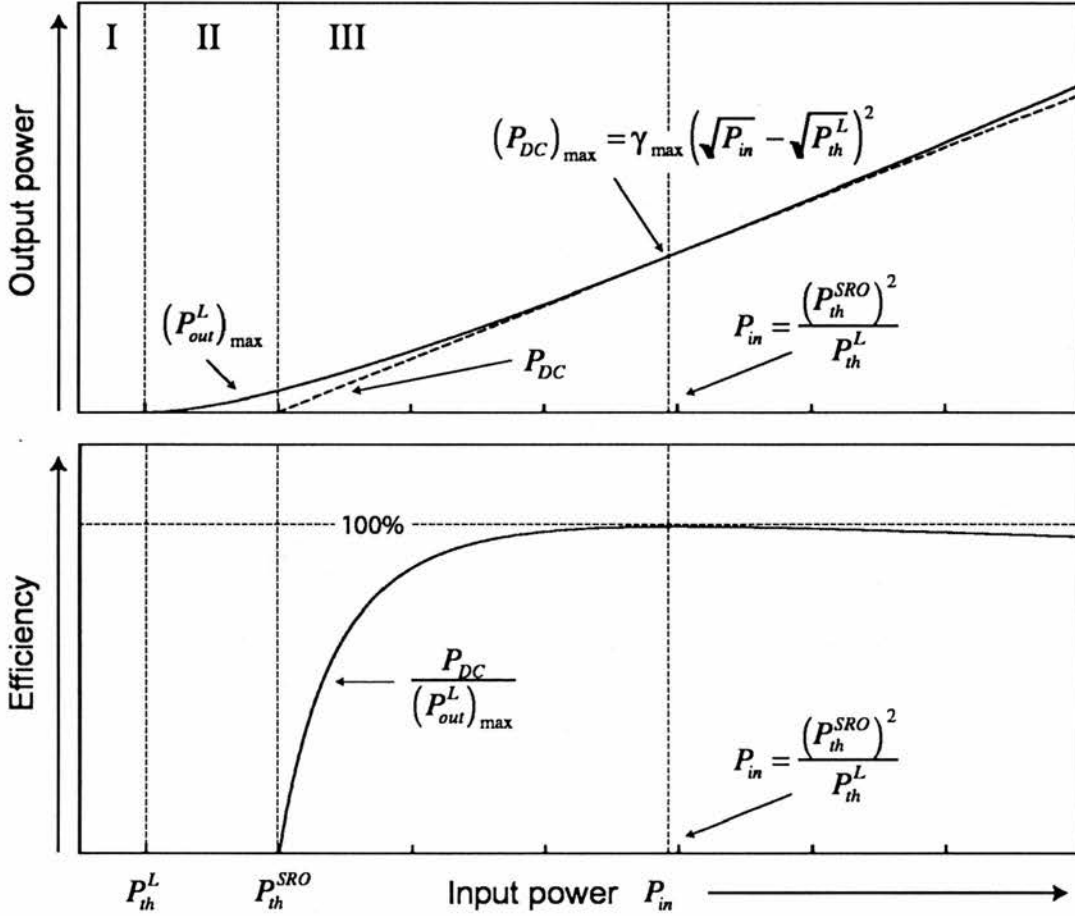


Figure 15. Graphical illustration of the ICSRO downconversion optimisation parameters. Regions I, II and III correspond the same regions of figure 14.

Optimisation of the signal output power requires the separation of the signal field round-trip losses into parasitic and useful output coupling losses [34]. Differentiating the appropriate expression for the signal output flux with respect to the output-coupling loss yields the solution

$$(P_{th}^{SRO})_{oc} = \sqrt{(P_{th}^{SRO})_{min} \cdot P_{in}} \tag{3.56}$$

where $(P_{th}^{SRO})_{\min}$ is the minimum SRO threshold in the absence of signal output coupling and $(P_{th}^{SRO})_{oc}$ is the threshold of the SRO in the presence of output-coupling. When equation (3.56) is satisfied, the optimum powers obtainable as useful signal and idler outputs are given by

$$(P_{out}^s)_{\max} = \eta_{\omega_s} \gamma_{\max} \left[\sqrt{P_{in}} - \sqrt{(P_{th}^{SRO})_{\min}} \right]^2 \quad (3.57)$$

$$(P_{out}^i)^{s-oc} = \left[\frac{1}{\eta_{\omega_s}} - 1 \right] (P_{out}^s)_{\max} \quad (3.58)$$

where $\eta_{\omega_s} = \omega_s / \omega_p$ is the ratio of the signal and idler photon energies. The consequent optimisation strategy for maximising signal output power is to minimise the SRO threshold $(P_{th}^{SRO})_{\min}$. This is achieved through maximising the nonlinear coupling and minimising the round-trip parasitic losses. Once $(P_{th}^{SRO})_{\min}$ has been reduced as much as is practically possible, SRO output-coupling should be increased until the new threshold satisfies equation (3.56). If the total output power (at the signal and idler fields) is to be maximised, this new threshold should be set to satisfy (3.51) instead.

3.4 Chapter 3 summary

Chapter 3 has introduced some important design factors for the implementation of a Ti:Sapphire ICSRO. Characteristics of the pump laser have been detailed, and appropriate cavity geometries for the introduction of a secondary intracavity focus have been described. The important factors governing the stability of the modified laser cavity and implications arising from different choices of signal cavities have been provided. The factors affecting the subsequent choice of cavity are primarily ones of convenience and flexibility in the experimental implementation of this device. The tuning mechanism of the Ti:Sapphire has been discussed, this factor will become an important issue for phase-matching geometries that cannot be temperature-tuned (angle-tuning being initially ruled-out due to cavity misalignment). Finally, the steady-state theory of the ICSRO as derived by Turnbull [34] has been outlined and the subsequent optimisation analysis re-expressed in terms of experimentally measured power levels. This analysis will be applied to each of the experimental devices outlined in the next four chapters.

Chapter 3 references

- 1 F. G. Colville, M. H. Dunn and M. Ebrahimzadeh, "Continuous-wave, singly resonant, intracavity parametric oscillator," *Optics Letters* **22**, 75 (1997).
- 2 P. F. Moulton, Solid State Research Report, DTIC AD-A124305/4, M.I.T. Lincoln Lab., pp. 15-21 (1982).
- 3 P. F. Moulton, "Spectroscopic and Laser Characteristics of Ti-Al₂O₃," *Journal of the Optical Society of America B-Optical Physics* **3**, 125-133 (1986).
- 4 P. Albers, E. Stark and G. Huber, "Continuous-Wave Laser Operation and Quantum Efficiency of Titanium- Doped Sapphire," *Journal of the Optical Society of America B-Optical Physics* **3**, 134-139 (1986).
- 5 R. L. Aggarwal, A. Sanchez, R. E. Fahey and A. J. Strauss, "Magnetic and Optical Measurements on Ti-Al₂O₃ Crystals for Laser Applications - Concentration and Absorption Cross-Section of Ti-3+ Ions," *Applied Physics Letters* **48**, 1345-1347 (1986).
- 6 A. Sanchez, R. E. Fahey, A. J. Strauss and R. L. Aggarwal, "Room-Temperature Continuous-Wave Operation of a Ti-Al₂O₃ Laser," *Optics Letters* **11**, 363-364 (1986).
- 7 R. L. Aggarwal, A. Sanchez, M. M. Stuppi, R. E. Fahey, A. J. Strauss, W. R. Rapoport and C. P. Khattak, "Residual Infrared-Absorption in as-Grown and Annealed Crystals of Ti- Al₂O₃," *IEEE Journal of Quantum Electronics* **24**, 1003-1008 (1988).
- 8 A. Sanchez, A. J. Strauss, R. L. Aggarwal and R. E. Fahey, "Crystal-Growth, Spectroscopy, and Laser Characteristics of Ti-Al₂O₃," *IEEE Journal of Quantum Electronics* **24**, 995-1002 (1988).
- 9 J. M. Eggleston, L. G. Deshazer and K. W. Kangas, "Characteristics and Kinetics of Laser-Pumped Ti-Sapphire Oscillators," *IEEE Journal of Quantum Electronics* **24**, 1009-1015 (1988).
- 10 P. A. Schulz, "Single-Frequency Ti-Al₂O₃ Ring Laser," *IEEE Journal of Quantum Electronics* **24**, 1039-1044 (1988).
- 11 Titan Ti:Sapphire Laser, Schwartz Electro Optics Inc. 3404, N. Orange Blossom Trail, Orlando, FL 32804 USA,
- 12 D. M. Kane, "Astigmatism compensation in off-axis laser resonators with two or more coupled foci," *Optics Communications* **25**, 379 (1989).
- 13 H. Kogelnik and T. Li, "Laser Beams and Resonators," *Proceedings of the IEEE* **54**, 1312-1329 (1966).

- 14 A. E. Siegman, *Lasers*. (University Science Books, Mill Valley, 1986).
- 15 D. M. Kane, "Ti-Sapphire Laser Cavity Mode and Pump-Laser Mode Calculations," *Applied Optics* **33**, 3849-3856 (1994).
- 16 K. K. Li, "Stability and astigmatic analysis of a six-mirror ring cavity for mode-locked dye lasers," *Applied Optics* **21**, 967-970 (1982).
- 17 D. J. M. Stothard, M. Ebrahimzadeh and M. H. Dunn, "Low pump threshold, continuous-wave, singly resonant, optical parametric oscillator," *Optics Letters* **23**, 1895 (1998).
- 18 A. Penzkofer, M. Wittmann, M. Lorenz, E. Siegert and S. MacNamara, "Kerr lens effects in a folded-cavity four-mirror linear resonator," *Optical and Quantum Electronics* **28**, 423-442 (1996).
- 19 G. D. Boyd and D. A. Kleinman, "Parametric Interaction of Focused Gaussian Light Beams," *Journal of Applied Physics* **39**, 3597 (1968).
- 20 A. L. Bloom, "Modes of a laser resonator containing tilted birefringent plates," *Journal of the Optical Society of America* **64**, 447 (1974).
- 21 D. R. Preuss and J. L. Gole, "Three-stage birefringent filter tuning smoothly over the visible region: theoretical treatment and experimental design," *Applied Optics* **19**, 702-710 (1980).
- 22 "There are typographic errors in the body-text of this paper. Equations (4), (5) and (3) should be replaced with (A13), (A11) and (A22) respectively from the appendix.",
- 23 G. Ghosh, "Dispersion-equation coefficients for the refractive index and birefringence of calcite and quartz crystals," *Optics Communications* **163**, 95-102 (1999).
- 24 X. Zhu, "Explicit Jones Transformation matrix for a tilted birefringent plate with its optic axis parallel to the plate surface," *Applied Optics* **33**, 3502-3506 (1994).
- 25 J. Mentel, E. Schmidt and T. Mavrudis, "Birefringent Filter with Arbitrary Orientation of the Optic Axis - an Analysis of Improved Accuracy," *Applied Optics* **31**, 5022-5029 (1992).
- 26 P. J. Valle and F. Moreno, "Theoretical-Study of Birefringent Filters as Intracavity Wavelength Selectors," *Applied Optics* **31**, 528-535 (1992).
- 27 M. K. Oshman and S. E. Harris, "Theory of Optical Parametric Oscillation Internal to the Laser Cavity," *IEEE Journal of Quantum Electronics* **QE-4**, 491-502 (1968).
- 28 A. Ashkin and J. E. Bjorkholm, "Patent," *US Patent Application 808,767*, (1969).

- 29 R. G. Smith and J. V. Parker, "Experimental observation of and comments on optical parametric oscillation internal to the laser cavity," *Journal of Applied Physics* **41**, 3401 (1970).
- 30 E. O. Ammann, J. M. Yarborough, M. K. Oshman and P. C. Montgomery, "Efficient internal optical parametric oscillation," *Applied Physics Letters* **16**, 309 (1970).
- 31 J. Falk, J. M. Yarborough and E. O. Ammann, "Internal optical parametric oscillation," *IEEE Journal of Quantum Electronics* **QE-7**, 359 (1971).
- 32 Tran-Ba-Chu and M. Broyer, "Intracavity single resonance optical parametric oscillator," *Journal de Physique* **45**, 1599 (1984).
- 33 T. Debuisschert, J. Raffy, J. P. Pocholle and M. Papuchon, "Intracavity optical parametric oscillator: Study of the dynamics in pulsed regime," *Journal of the Optical Society of America B-Optical Physics* **13**, 1569-1587 (1996).
- 34 G. A. Turnbull, M. H. Dunn and M. Ebrahimzadeh, "Continuous-wave, intracavity optical parametric oscillators: an analysis of power characteristics," *Applied Physics B-Lasers and Optics* **66**, 701 (1998).
- 35 G. A. Turnbull, *Continuous-wave intracavity optical parametric oscillators*, PhD thesis, St Andrews University (1999).
- 36 T. J. Edwards, G. A. Turnbull, M. H. Dunn, M. Ebrahimzadeh and F. G. Colville, "High-power, continuous-wave, singly resonant, intracavity optical parametric oscillator," *Applied Physics Letters* **72**, 1527-1529 (1998).
- 37 W. E. Lamb, Jr., "Theory of an optical maser," *Physical Review* **134**, A1429 (1964).
- 38 G. A. Turnbull, D. J. M. Stothard, M. Ebrahimzadeh and M. H. Dunn, "Transient dynamics of CW intracavity singly resonant optical parametric oscillators," *IEEE Journal of Quantum Electronics* **35**, 1666-1672 (1999).
- 39 G. D. Boyd and A. Ashkin, "Theory of Parametric Oscillator Threshold with Single-Mode Optical Masers and Observation of Amplification in LiNbO₃," *Physical Review* **146**, 187-198 (1966).
- 40 S. E. Harris, "Threshold of multi-mode parametric oscillators," *IEEE Journal of Quantum Electronics* **QE-2**, 701 (1966).
- 41 T. Baer, "Large amplitude fluctuations due to longitudinal mode-coupling in diode-pumped intracavity doubled Nd:YAG lasers.," *Journal of the Optical Society of America B-Optical Physics* **3**, 1175 (1986).
- 42 A. E. Siegman, "Nonlinear optical effects: an optical power limiter," *Applied Optics* **1**, 739-744 (1962).

4. ICSRO based on $KTiOAsO_4$

4.1 Introduction

Paper T. J. Edwards, G. A. Turnbull, M. H. Dunn, M. Ebrahimzadeh and F. G. Colville, "High-power, continuous-wave, singly resonant, intracavity optical parametric oscillator," *Applied Physics Letters*, **72**, 1527-1529 (1998).

Abstract *A high-power continuous-wave optical parametric oscillator based on the nonlinear material $KTiOAsO_4$ and pumped internal to a tunable Ti:Sapphire laser is described. The use of the intracavity pumping approach has enabled operation of a singly-resonant oscillator (SRO), resulting in the generation of as much as 1.46 W of infrared power in a 11.5-mm-long crystal. Amplitude-stable signal and idler outputs, each in excess of 500 mW, over the respective wavelength ranges of 1.11-1.20 and of 2.44-2.86 μm have been extracted from the SRO. We demonstrate up to 90% down-conversion of the optimum Ti:Sapphire output power to the SRO, confirming our recent theoretical predictions. The performance characteristics of the device demonstrate that practical, stable, and efficient operation of continuous-wave SROs at watt-level output power can be readily achieved in conventional birefringent materials by exploiting the intracavity pumping approach.*

The work presented in this chapter has been published as detailed above. The experimental study was jointly undertaken with Graham Turnbull and Finlay Colville in the School of Physics and Astronomy, University of St Andrews. Due credit and recognition is given to them both for their contributions to this experimental work.

This chapter describes the study of a continuous-wave Ti:Sapphire pumped intracavity SRO based on the nonlinear material KTiOAsO_4 (KTA). The experimental arrangement, and mode of operation is similar to that reported by Colville *et al* [1] using the same laser system and optics. The advances undertaken with the work presented here include the observation of significant operational efficiencies approaching 90% and Watt-level output powers over a broad tuning range.

4.2 Experimental design

The design and layout of this device is identical to that discussed in the previous chapter on the general implementation of the ICSRO. The cavity arrangement and primary pump layout is illustrated in figure 1.

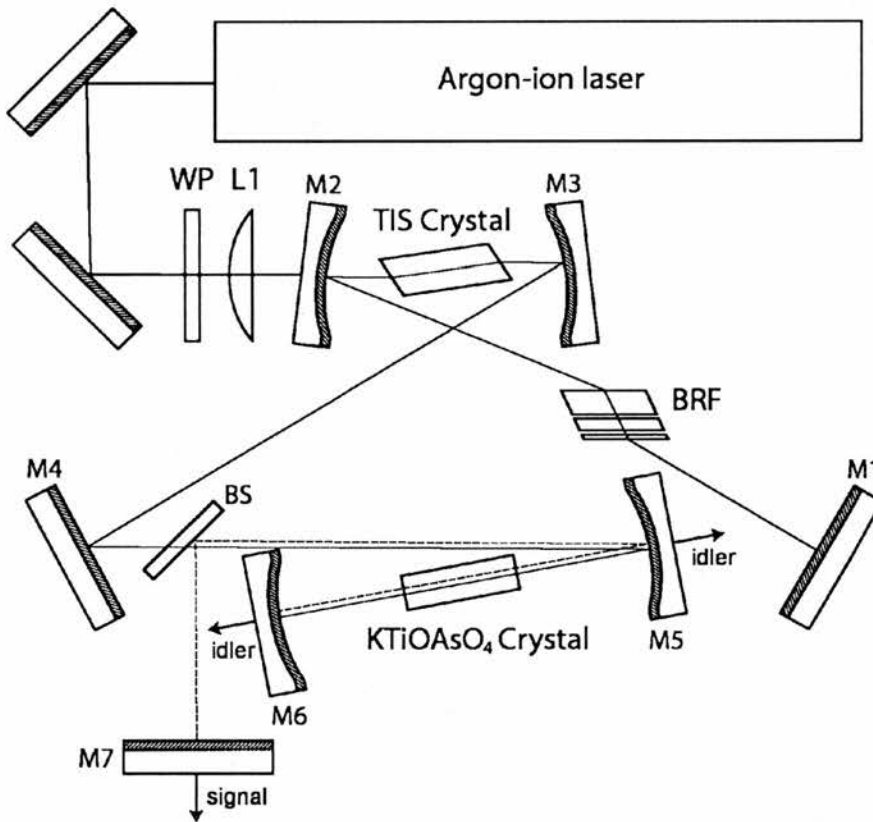


Figure 1. Layout of the KTA ICSRO experiment. BRF is the birefringent tuner. WP is a half-wave-plate and L1 is the argon-ion pump focusing lens.

The KTA crystal is located at a secondary intracavity focus of a standing-wave Ti:Sapphire laser. The Ti:Sapphire laser itself is a modified commercial laser [2] based on the common bow-tie geometry. The Ti:Sapphire crystal is located at an optimised intracavity focus between two 100mm ROC focussing mirrors M2 and M3. The crystal is Brewster-cut to minimise losses at the horizontally-polarised pump field and astigmatism introduced to the resonant laser by this component is minimised by rotating mirrors through an angle of 9.8 degrees to compensate for the angle of the Brewster surfaces [3] as discussed in chapter 3. This 7.6 mm long crystal is pumped at the centre of its absorption band by a large-frame argon-ion laser (Spectra-Physics-171) delivering a maximum output power of 14 W on multiple-lines all of which couple near to the centre of the Ti^{3+} absorption band illustrated in figure 1(a) of chapter 3. In order to pump at the π -polarised peak of this absorption the emerging polarisation from the argon-ion laser is rotated through 90° via a half-wave-plate (WP) to match the incident polarisation parallel to the c-axis of the Ti:Sapphire crystal. The argon-ion beam is focused into the laser crystal using a 90 mm focal length lens (L1) to form a $\sim 10 \mu\text{m}$ beam waist. Cooling is via a water-cooled block upon which the crystal is bonded with good thermal contact. Owing to the excellent thermal conductivity of $Ti:Al_2O_3$, crystal temperature may be assumed to be the same as that of the cooling water at approximately 20°C . This maintains an upper state lifetime of $\sim 3.2 \mu\text{s}$ for the laser medium (see figure 2 of chapter 3).

The Ti:Sapphire laser is chosen to operate close to the centre of its gain bandwidth at $\sim 800\text{nm}$. This requires the utilisation of the mid-band mirror set supplied with the commercial *Titan* laser. These mirrors have a reflectivity of $>99.7\%$ over a 100nm range centred upon 800nm. The implementation of the SRO branch of the cavity (mirrors M5, M6, M7 and the beamsplitter (BS)) requires custom-made multi-layer coated optics. Mirrors M5, M6 and M7 are all specified with broad-band coatings to as high a specification as possible. The priority is to minimise the signal cavity losses whilst maintaining a high reflectivity at the pump wavelength. The signal field specifications are a reflectivity $R > 99.9\%$ centred at 1200nm and $R > 99.7\%$ over 1100-1300nm. Pump wavelength specifications for M5, M6 and M7 are the same as those for the laser mirrors M1-M4 namely $R > 99.7\%$ over 750-850nm. It should be

noted that there is no need for mirror M7 to meet this pump specification, it is simply far cheaper to place this optic into the same coating-run as the other substrates. The dichroic-coated beamsplitter (BS) is specified to be highly reflecting $R > 99.7\%$ at 45° over the signal mirror bandwidth, and highly transmitting $T > 99.5\%$ for the pump field. All coatings are specified for horizontally polarised signal and pump fields. The non-resonant idler specifications for these optics are that they have high transmission $T > 85\%$ over a wavelength range of 2-3 μm . To realise this transmission, mirrors M5 and M6 are coated on calcium-fluoride substrates. Mirror M7 may be interchanged with an output-coupling optic for the signal field. This is discussed later in the appropriate section. Total losses for the signal cavity are calculated from finesse measurements and found to be $2.4 \pm 0.5\%$ [1]. Tuning of the Ti:Sapphire laser is by means of a birefringent tuner (BRF) as described in chapter 3. The tuner has a three-plate Quartz design with a plate ratio of 1:3:9 with plate thickness' 1, 3 and 9 mm respectively. This tuner continuously scans the laser wavelength over the entire pump mirror bandwidth.

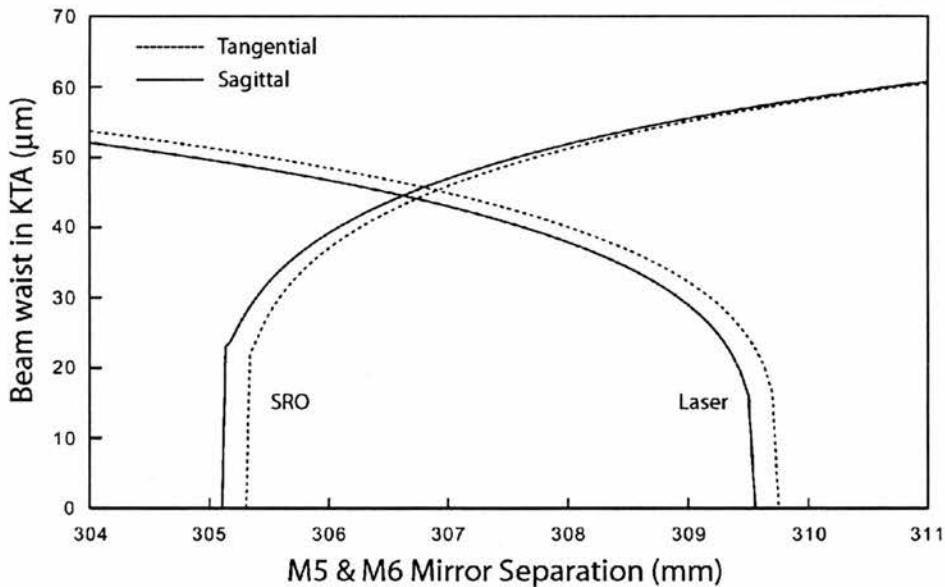


Figure 2. Beam waist in the centre of the KTA crystal as a function of mirror separation of M5 & M6. Laser and SRO cavities are stable over a ~4mm range.

Stability analysis of the laser and SRO cavities shows that cavity stability criteria are satisfied for both cavities over a mirror displacement range of ~ 4 mm as illustrated in figure 2. The cavity spacing and mirror radius of curvature (ROC) for the optics of both cavities are given in tables 1 & 2 (from chapter 3)

Ti:Sapphire Laser Cavity Parameters				
Mirror	ROC (mm)	Angle (Deg)	Separation	Distance (mm)
M1	∞	N/A	D1	645.0
M2	100	9.8	D2	48.7
			LX1	7.6
M3	100	9.8	D3	48.7
M4	∞	N/A	D4	700.0
			D5	786.0
M5	200	2	D6	98.8
			LX2	11.5
M6	200	0	D7	198.4

Table 1. Ti:Sapphire laser cavity parameters of the layout illustrated in figure 1. Separation notation refers to figure 7(a) of chapter 3.

OPO Cavity Parameters				
Mirror	ROC (mm)	Angle (Deg)	Separation	Distance (mm)
M7	∞	N/A	D1	200.0
			D2	376.0
M5	200	2	D3	98.8
			LX2	11.5
M6	200	0	D4	198.4

Table 1. SRO Cavity parameters of the layout illustrated in figure 1. Separation notation refers to figure 8(a) of chapter 3.

The optimum separation of mirrors M5 and M6 is found to be 308.7 mm after optimisation of the SRO output power. At this mirror separation, the laser mode waist size measures $22\mu\text{m}$ in the Ti:Sapphire crystal and $35 \times 32\mu\text{m}$ in the KTA crystal for a pump laser wavelength of 810nm. The signal waist size in the KTA crystal is $54 \times 55\mu\text{m}$ at a wavelength of 1200nm.

4.2-1 Nonlinear material

The nonlinear crystal used in this experiment is an 11.5mm long $KTiOAsO_4$ obtained from Crystal Associates Inc. [4]. The crystal was x-cut and polished for type II non-critical phase-matching ($\theta = 90^\circ$, $\phi = 0^\circ$). Figure 3 Shows the orientation of the crystal axes with respect to the pump polarisation. The non-critical geometry is free from walk-off effects and may be tuned through variation of the pump wavelength. The type II interaction involves the horizontally polarised pump field driving a phase-matched parametric process with signal and idler fields assuming horizontal and vertical polarisations respectively.

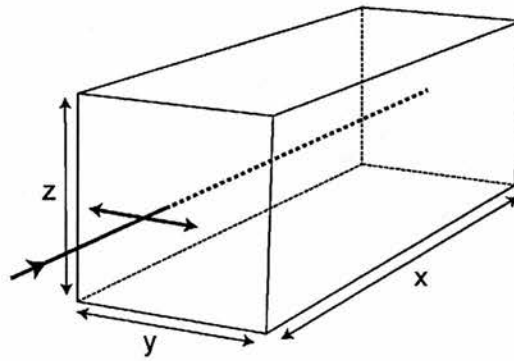


Figure 3. Dimensions and orientation of the KTA crystal. The incident pump field is shown polarised along the crystallographic y axis. Dimensions are $x \times y \times z = 11.5 \times 3 \times 3$ mm.

The wavelength transparency range of this material extends to $>4.5 \mu\text{m}$ which is well beyond the phase-matched idler range obtainable with the mirror bandwidths. The crystal was anti-reflection coated to have low loss at the pump, signal and idler fields. The measured transmission *per surface* was $T_{sf} < 0.3\%$ for the centre of the signal and pump field bandwidths and $T_{sf} < 10\%$ for the non-resonant idler field.

Tuning calculations for the non-critical geometry are performed through the solution of the following equation with respect to λ_s where conservation of photon energy and momentum have been observed.

$$\Delta k = \frac{n_y(\lambda_p)}{\lambda_p} - \frac{n_y(\lambda_s)}{\lambda_s} - \frac{n_z \left(\frac{\lambda_p \lambda_s}{\lambda_s - \lambda_p} \right)}{\left(\frac{\lambda_p \lambda_s}{\lambda_s - \lambda_p} \right)} = 0 \quad (4.1)$$

Values for $n_y(\lambda)$, $n_z(\lambda)$ may be calculated from sellmeier data published in the literature [5]

4.2-2 SRO cavity alignment

The alignment of the SRO cavity requires the experimenter to follow a few simple procedures. The first of these involves the optimisation of the pump laser cavity itself. This is a simple procedure for the standing-wave cavity due to the presence of fluorescence reflections from the cavity mirrors. Assuming that the laser cavity has been power-optimised at the central pump wavelength of the SRO phase-matched bandwidth, and now includes all the correct SRO components, the SRO cavity may be aligned to obtain oscillation.

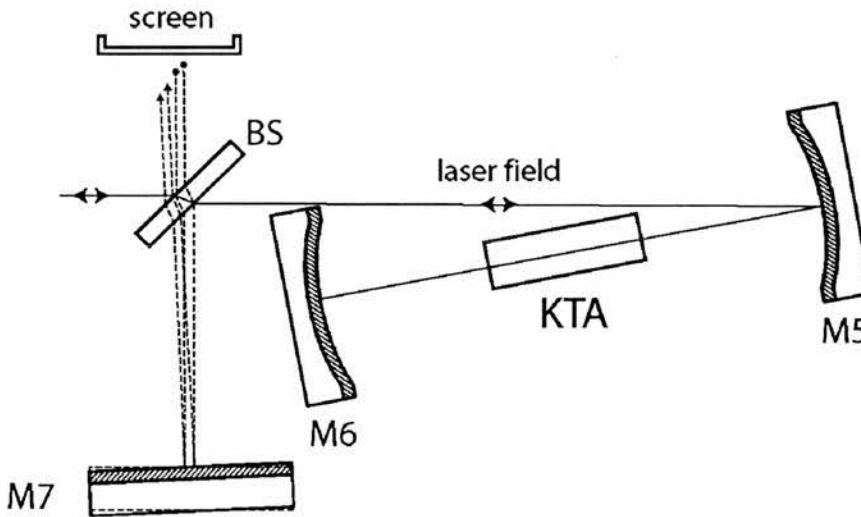


Figure 4. SRO branch of the laser cavity illustrating misalignment of mirror M7 and the associated divergence of the residual reflected pump field.

A useful guide to alignment is the residual argon-ion pump light that circulates around the laser cavity, a certain amount of this light will be reflected from the beamsplitter (BS) towards mirror M7. Returning this reflected light back towards the beamsplitter will roughly align M7. The SRO may now be aligned using the residual pump light reflected from the beamsplitter as shown in figure 4. Despite being specified as highly transmitting for the pump field, the beamsplitter can reflect a significant amount of pump light. Once the fact that, in the absence of SRO operation, circulating fields totalling over 100 W of power are regularly found inside the laser resonator has been appreciated, the discovery that over 100mW of this laser light reflects off the beamsplitter is not unsurprising. In practice four separate "alignment beams" can be attributed to pump reflections from the beamsplitter. Two beams per surface for both field directions illustrated by the dotted lines in figure 4. The reflections from the first two surfaces (travelling from left to right in the diagram) are terminated with filled circles. The return field reflections, after subsequent reflection from mirror M7, are terminated with arrows.

Alignment of mirror M7 involves overlapping the pairs of beams emerging from the beamsplitter in the far-field using a suitable screen and an infrared viewing scope. The cost-conscious ICSRO developer can dispense with expensive laboratory viewing scopes (often costing >£1000) by taking advantage of the fact that Ti:Sapphire wavelengths fall conveniently within the wavelength ranges of cheaply-obtained "night-scopes" often sold in high-street electronics stores. They have an excellent response at 800nm and, if the packaging is to be believed, may well assist in the monitoring of suspicious activities. Another advantage of this alignment procedure is that, once aligned, M7 will return the reflected pump light back into the laser cavity causing a small degree of enhancement. Monitoring of the intracavity pump field leaking through any of the cavity mirrors with a photodiode connected to an oscilloscope will allow this enhancement to be observed visually, confirming alignment. If all is well the SRO should burst into life and the monitored laser field should suddenly drop to its clamped level. Care should be taken that the SRO output fields are not potentially incident on the monitoring photodiode, otherwise the oscilloscope trace will disappear upwards. In both cases, a sudden change in the monitor photodiode signal (with the exception of the far smaller enhancement effect) often signals success. One last note regards the visual appearance of the

SRO once parametric oscillation has been achieved. When using birefringently phase-matched materials, a working ICSRO looks exactly the same as a one that has failed to work. Power meters, filters and photodiodes will have to act as eyes in this case. It is far better to have these items in place, preferably coupled to an oscilloscope trace within the experimental field of view, *before* attempting to align the cavity as they will aid the rapid confirmation of SRO action. In the case of QPM materials, confirmation of SRO operation is simple and conclusive. The high-order phase-matching processes in these materials give rise to parasitic nonlinear processes (SHG, SFM and DFG) the outputs of which, often fall within the visible spectrum as will be shown in chapter 5.

4.3 KTA ICSRO power characteristics

This section details the continuous-wave power characteristics of the KTA ICSRO outlined in the preceding sections. The tunable nature of the Ti:Sapphire pump laser means that a full power characterisation over the entire tuning bandwidth is not practical. For the purpose of this study, the device was initially characterised at its optimum power performance and subsequently tuned over the operational bandwidth to obtain an output power spectrum. The results obtained are discussed in context with the theoretical analysis of chapter 3. And the overall performance of the device, in terms of efficiency, output powers and tunability, is evaluated with reference to contemporary methods for obtaining coherent mid-infrared CW radiation.

4.3-1 Intracavity power

The Ti:Sapphire laser, configured with all mirrors highly reflecting at the pump wavelength and containing all relevant SRO optics, was studied and the circulating intracavity power measured. The measurement was made by monitoring the laser field leaking through the high-reflector M4 at a pump wavelength of 810nm. Calibration of this "leakage" field was performed by operating the Ti:Sapphire laser with a range of known output-couplings and obtaining a ratio of intracavity field to leakage field. The resultant intracavity power characteristic is shown in figure 5.

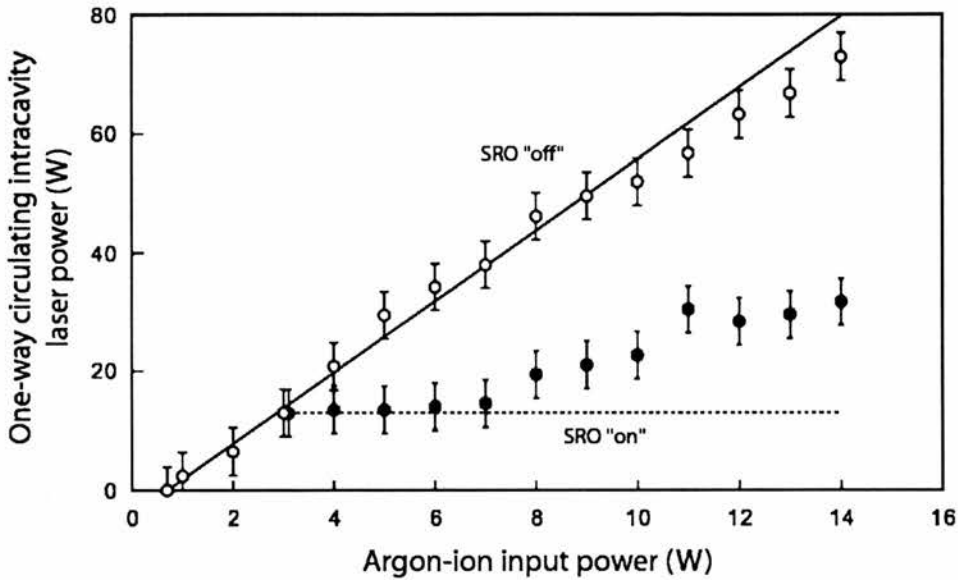


Figure 5. Intracavity (IC) laser power circulating within the resonator with and without SRO operation. Argon-ion input thresholds for the laser and SRO are 0.6W and 3.1W respectively. Open circles show IC power in the absence of SRO operation. Filled circles show IC power under SRO operating conditions.

The Ti:Sapphire laser operates with an incident argon-ion input threshold of 0.6W. Above threshold the intracavity field increases to a maximum circulating field of ~75W at 810nm for 14W of input power, as shown by the open circles in figure 5. This *circulating* field corresponds to a total field of 150W inside the laser cavity at maximum pump power. The input power threshold for the SRO is measured to be 3.1W. The circulating pump power inside the laser cavity at this threshold value is 13 ± 4 W which remains clamped for further increases in input power up to 7W shown by the filled circles of figure 5. Beyond 7W the increase in intracavity clamping is attributed to the degradation of the input argon-ion beam quality at high powers. When operating close to its maximum output power the argon-ion beam mode begins to deviate from TEM-00 operation. The consequence on laser operation is that the focusing conditions inside the laser crystal are altered, reducing mode-matching efficiency slightly. There may be a possible feedback effect on the resonant cavity mode size also, which in turn will alter the SRO waist radii. This remains a point of conjecture and confirmation of the true nature of this effect is hard to establish. This serves to illustrate the fact that the operation of the SRO is

always coupled to the characteristics of the pump laser and those of the primary input power source. The theory presented in chapter 3 assumes that the laser threshold remains unchanged throughout the power-scaling of the ICSRO. For very high incident powers this may not be the case and for devices based on laser media with strong thermal-lensing characteristics this assumption will not be appropriate at all.

4.3-2 Output power and efficiency

The non-resonant idler field is generated in both directions of the pump and signal fields within the KTA crystal. It exits through the crystal surfaces and cavity optics with a coupling efficiency $\eta_i = 0.87$ and forms two separate outputs as shown in figure 1. The total *measured* idler output power accounting for both outputs but not for the coupling efficiency of the optics is shown in figure 6.

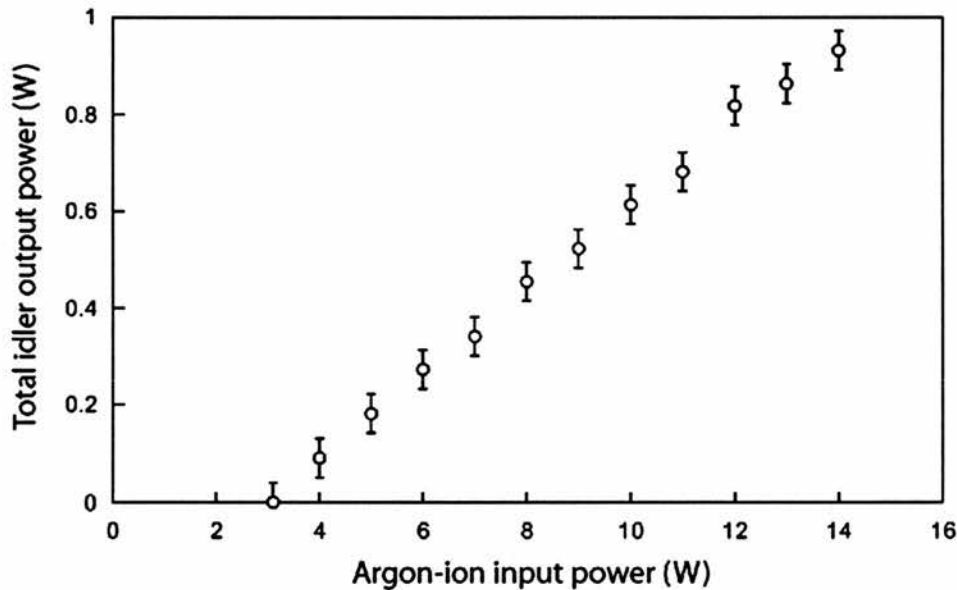


Figure 6. Total (two-way) idler output power as a function of incident argon-ion input power. The total power scales to 930mW for 14W of input power. Idler wavelength is 2.72 μm .

Above threshold, the measured idler output power at a wavelength of 2.72 μm reaches a maximum value of 930mW for 14W of input argon-ion pump power. This

output can be used to calculate the total laser power, P_{DC} , downconverted by the parametric process using the following expression

$$P_{DC} = \left(2 \frac{P_i}{\eta_i} \right) \left(1 + \frac{\lambda_i}{\lambda_s} \right) \quad (4.2)$$

where $\eta_i = 0.87$ is the idler cavity-coupling efficiency, P_i is the *one-way* generated idler power and λ_i , λ_s are the idler and signal wavelengths respectively. For idler and signal wavelengths of 2.72 and 1.15 μm respectively, the maximum downconverted laser power to signal and idler fields is 3.6 W at 14 W of argon-ion input power as illustrated in figure 7.

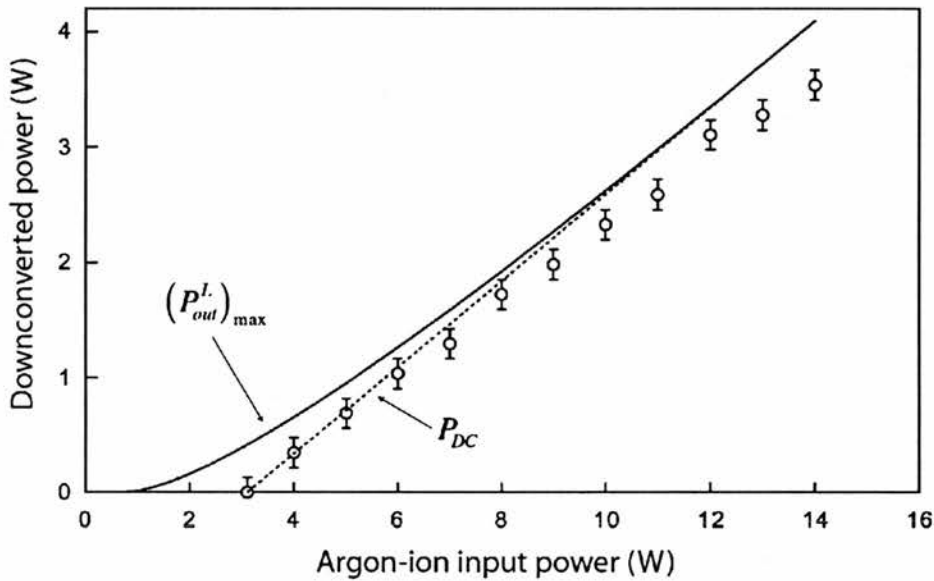


Figure 7. Downconverted power of the KTA ICSRO. The two lines show the theoretical predictions based on the measured threshold values and using equations (3.48), (3.49) and (3.53) of chapter 3. The data points represent measured downconverted power inferred from idler power measurements.

Figure 7 shows the downconverted power characteristics of the KTA ICSRO. Theoretical predictions of the total downconverted power and optimum output power

of the laser are calculated from equations (3.48), (3.49) and (3.53) of chapter 3 namely

$$P_{DC} = \gamma_{\max} (P_{in} - P_{th}^{SRO}) \left(1 - \frac{P_{th}^L}{P_{th}^{SRO}} \right) \quad (4.3)$$

where

$$\gamma_{\max} = \eta_{in} \eta_{abs} \frac{\lambda_{p-in}}{\lambda_p} \quad (4.4)$$

and the optimum laser output power expression

$$(P_{out}^L)_{\max} = \gamma_{\max} \left(\sqrt{P_{in}} - \sqrt{P_{th}^L} \right)^2 \quad (4.5)$$

Here, γ_{\max} has a measured value of 0.47 at 810nm for argon-ion pumping. Equations (4.3) and (4.5) describe the optimum downconverted power and Ti:Sapphire laser output as illustrated in figure 7. From the measured SRO and laser thresholds of 0.6 W and 3.1 W respectively the input pump power required to achieve 100% theoretical downconversion may be calculated from equation (3.55) of chapter 3 which is

$$P_{in} = \frac{(P_{th}^{SRO})^2}{P_{th}^L} \quad (4.6)$$

Solving (4.6) for the measured thresholds gives an optimum argon-ion input power of 16 W, slightly above the maximum power output power of 14 W available from the argon-ion laser used. To achieve 100% theoretical downconversion at 14 W of input power, the SRO threshold must be reduced to 2.9 W by increasing the magnitude of the nonlinear interaction or lowering the SRO cavity losses. Better insight into the efficiencies achieved in this experiment may be obtained by plotting the ratio of downconverted power to optimum laser output power as shown in figure 8.

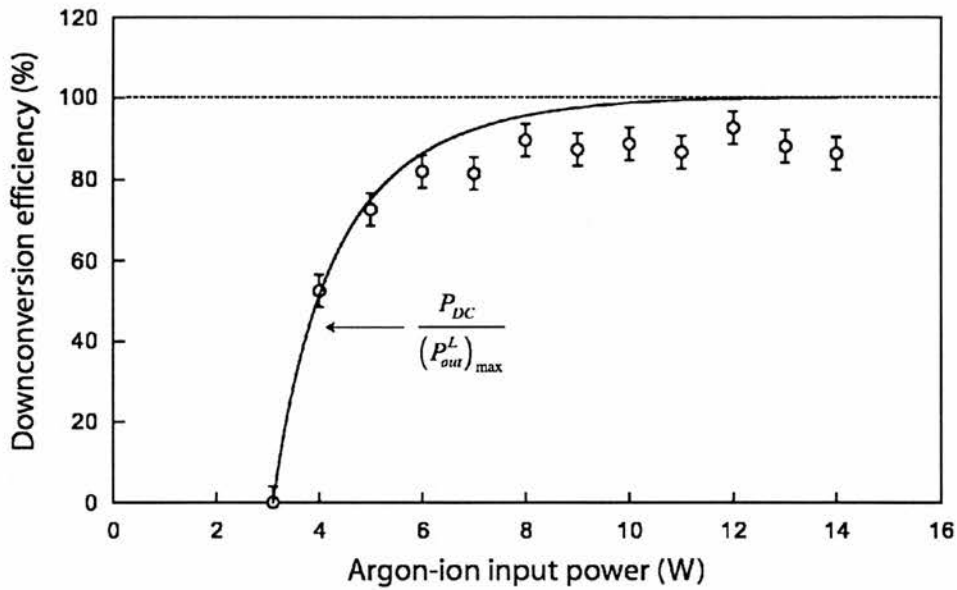


Figure 8. Showing the ICSRO Downconversion efficiency as a function of input argon-ion power.

The conversion efficiency of the KTA ICSRO rapidly rises above threshold to reach levels of ~85-90% at high pump powers. This efficiency is a measure of the *total* downconverted power to signal and idler fields as a percentage of the available optimum output power of the Ti:Sapphire laser. It should be noted that at this stage the only extracted power is that at the non-resonant idler wavelength. This output accounts for approximately 1/3 of the total downconverted power (due to the photon energy ratio of the signal and idler), a further ~13% of this power is lost through the coupling efficiency of the SRO optics at the idler wavelength of 2.72 μm .

The degradation of the argon-ion beam quality, evident in figure 5, can be observed in the form of reduced efficiency compared to the theoretical predictions of equations (4.3) and (4.5). As discussed previously, these expressions assume that the laser and SRO thresholds remain constant over the entire input power range. For the present experimental arrangement we speculate that this is not the case. To obtain the correct downconversion efficiency of this experimental arrangement it would be necessary to directly measure the optimum output power of the Ti:Sapphire laser over the entire range of argon-ion input powers in order to account

for the change in laser threshold over this range. At the time of this experimental work, the range of output couplers available did not allow for such a measurement.

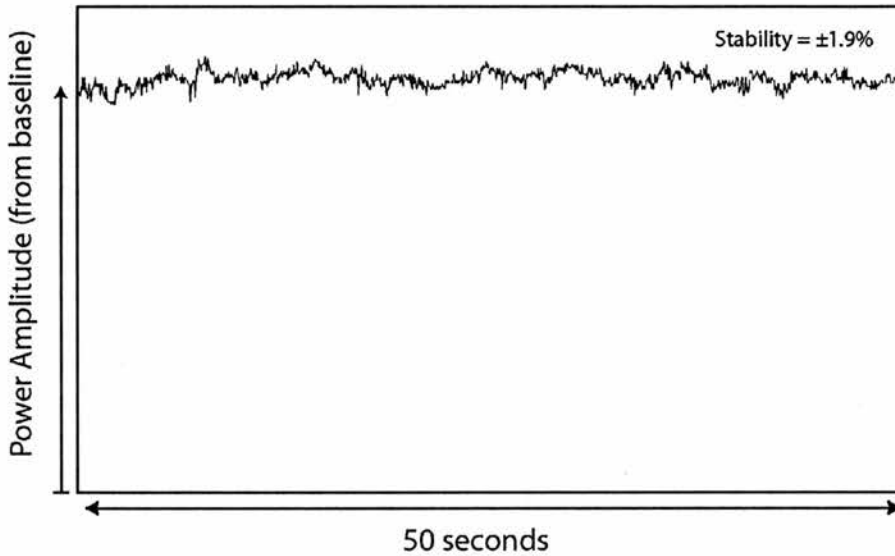


Figure 9. 50 second amplitude stability of the resonant signal field for the SRO >4 times above threshold. The y-axis covers the full amplitude of the signal.

Short-term power stability of the resonant signal field is shown in figure 9 for pump powers greater than four times above SRO threshold. The measurement is taken from leakage field coupled out of the signal high-reflector M7 using a 1mm^2 area germanium photodiode. Power stability shows no indication of the inefficient repetitively-pulsing regime, characteristic of the ICDRO pumped over three times above threshold [6].

4.3-3 Signal output coupling

The experimental results detailed in the previous section are based on a high-finesse signal cavity design for which the round-trip losses are minimised to reduce SRO threshold. This design favours infrared output at the idler field only. By replacing mirror M7 with an output-coupling optic for the signal field, significant output powers at the signal field may be achieved at the expense of SRO threshold.

Figure 10 shows the output powers obtained at the signal and idler fields by replacing mirror M7 with a signal output coupler.

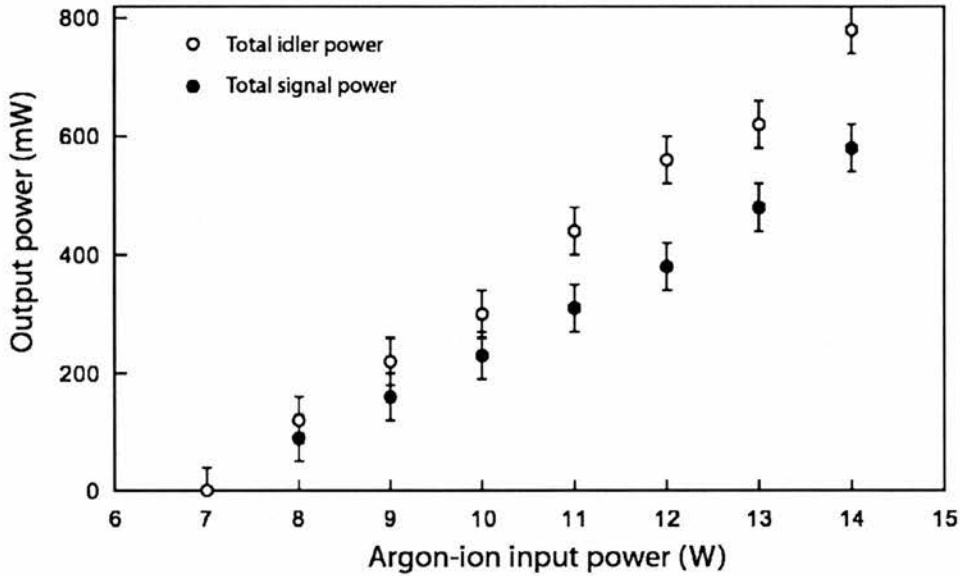


Figure 10. Signal and total (two-way) idler output powers in the presence of signal output coupling. Maximum measured values of 780 mW and 580 mW are observed at idler and signal outputs for 14 W of argon-ion input power.

The plane-parallel output coupler had a measured transmission of 1.14% and introduced a total loss of $1.7 \pm 0.3\%$ to the signal cavity. Thus, $\sim 33\%$ of the output signal field was absorbed in the substrate itself. This additional loss to the signal cavity raised the SRO threshold to 7 W of argon-ion input power corresponding to a circulating intracavity laser field of 38 ± 5 W. Total output powers of 780 mW at a wavelength of $2.72 \mu\text{m}$ for the idler and 580 mW at a wavelength of $1.15 \mu\text{m}$ for the signal are obtained at the maximum argon-ion input power of 14 W. Accounting for the idler cavity-coupling efficiency $\eta_i = 0.87$, total downconverted power at this maximum pump input is 3 W. This amounts to a total of 2.1 W of signal power at $1.15 \mu\text{m}$ and 0.9 W of idler power at $2.72 \mu\text{m}$. Thus, if 580 mW amounts to 1.14% loss at the signal field there must be a total loss of 4.1%, in excellent agreement with the previously measured loss ($2.4 \pm 0.5\%$) plus the additional insertion loss of $1.7 \pm 3\%$. The $\sim 70\%$ increase in signal cavity loss that the insertion of the output-coupling optic introduces should increase the SRO threshold by 70% from 3.1 to 5.3

W of incident argon-ion pump power. The higher increase in threshold that is observed (3.1 to 7 W) indicates that as well as introducing a linear loss of $1.7\pm 3\%$ to the signal cavity the output-coupling has caused a reduction in parametric gain for the nonlinear process. One possible mechanism for this is that the reduction in circulating signal field and subsequent expected rise in intracavity laser power has altered the cavity waist geometry through a small amount of residual thermal lensing in either the Ti:Sapphire or KTA crystals. If this lensing is indeed caused by an increase in the intracavity laser field then a linear parasitic loss will also have an associated parametric-gain loss as the higher field clamping it demands alters the focussing in the KTA crystal. As always, factors of this nature must remain complete conjecture until a thorough experimental investigation can be performed. At the time of investigation, issues associated with the quality of the KTA crystal and lack of faith in the failing argon-ion laser put an experiment of this nature beyond the scope of practicality.

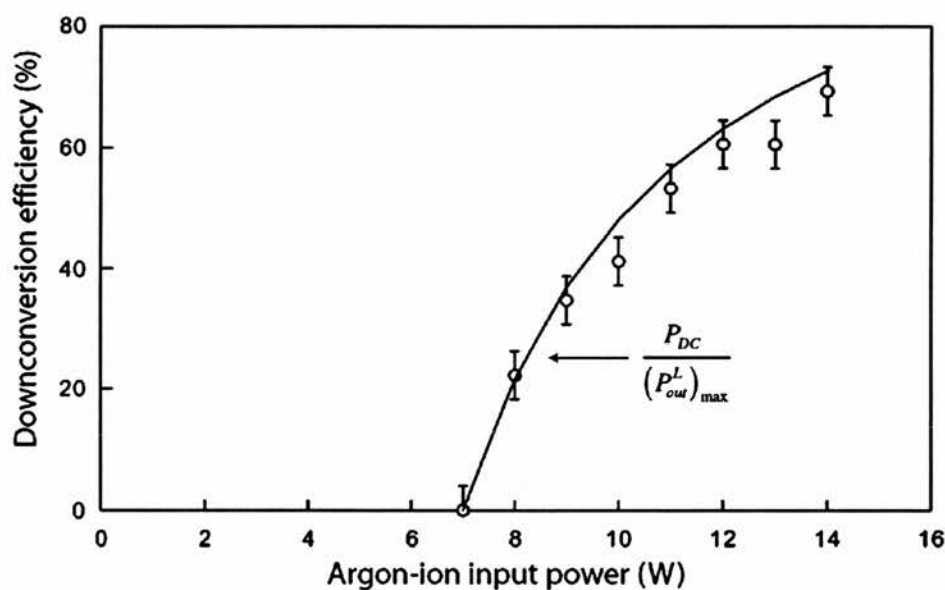


Figure 11. Downconversion efficiency for KTA ICSRO under signal output-coupling conditions.

It is useful to examine the consequences experienced in terms of efficiency by output-coupling the signal field. Returning to the simple expression for calculating the optimum input power for a given laser and SRO threshold (4.6) we find that a

laser threshold of 0.6 W and an SRO threshold of 7 W would require 82 W of input argon-ion power (and a remarkably safe pair of safety glasses) to achieve the 100% downconversion condition. This would reward the adventurous experimenter with over 30 W of downconverted infrared power. Over the modest input power range available from the argon-ion laser the efficiency varied according to figure 11. The total downconversion efficiency reaches 69% for 14 W of argon-ion input power. The measured downconverted power closely follows the theoretical prediction based on laser and SRO thresholds of 0.6 W and 7 W respectively. Here, the measured downconverted power has again been inferred from idler power measurements.

Optimisation of the output field may be achieved by following the method described at the end of chapter 3. For a minimum SRO threshold $(P_{th}^{SRO})_{\min}$ of 3.1 W, optimum signal output coupling is achieved by raising the SRO threshold according to

$$P_{th}^{SRO} = \sqrt{(P_{th}^{SRO})_{\min} \cdot P_{in}} \quad (4.7)$$

Thus, for an available 14 W of input pump power, the optimum output coupling will be such that the SRO threshold rises to 6.6 W. Under ideal conditions the insertion of a perfectly transmitting 2.7% output coupler would maximise signal output power. As has been noted previously, because this would more than double the clamped laser field, it may have possible implications for thermally-induced cavity waist changes that may alter the parametric gain of the SRO itself, further increasing threshold.

So far the power characteristics of the device have been reported for fixed-wavelength values of 0.81, 1.15 and 2.72 μm for the pump, signal and idler fields respectively. A primary feature of this ICSRO is its ability to tune rapidly with pump wavelength. In the signal output-coupling regime outlined above, the device was pump-tuned over the SRO mirror bandwidths using the birefringent tuner. The subsequent spectral variation in signal and idler output power is illustrated in figure 12.

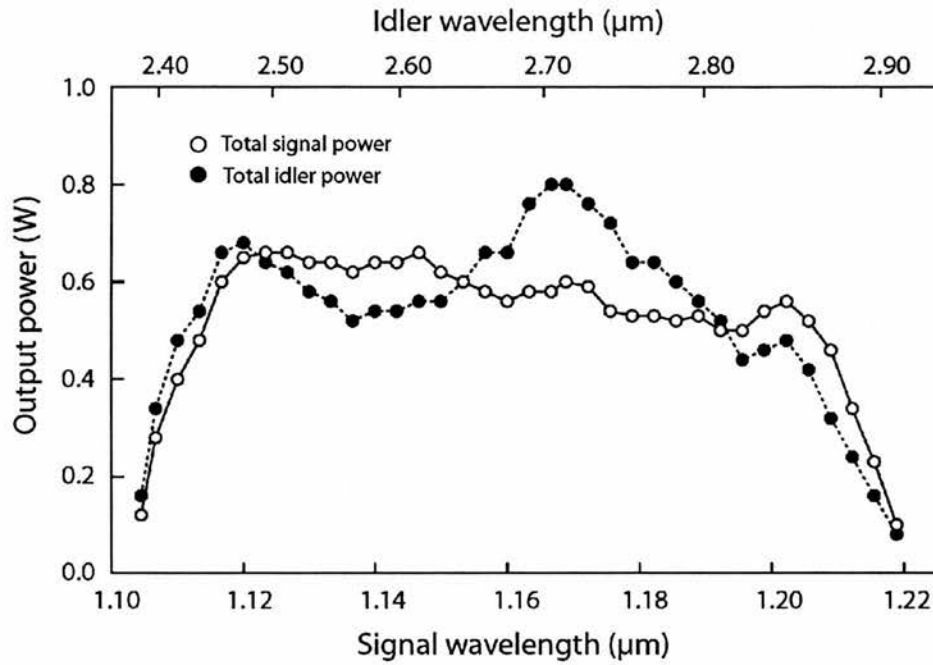


Figure 12. Power spectrum of the signal and idler fields under signal output coupling conditions.

Under signal output-coupling conditions the ICSRO shows a wide degree of tunability. Signal and idler output powers are in excess of 500 mW over a respective wavelength range of 1.12-1.20 μm and 2.43-2.82 μm . The limits of this tuning range are attributed to the finite bandwidths of the SRO optical coatings, alternative tuning ranges should be accessible with optical components specified with different mirror and antireflection coating bands. Figure 12 illustrates the practical high-power generation of continuous-wave near- to mid-infrared coherent radiation obtainable from the ICSRO approach. The power levels obtained here are not optimised for the incident argon-ion pump power and do not account for the $\sim 33\%$ loss in signal power through transmission of the output-coupler and the $\sim 13\%$ coupling efficiency of the idler field from the laser cavity. Addressing these transmission efficiencies with optimised optical components may result in significant improvements. The tuning range of the device may be extended by returning to the high-finesse signal cavity configuration thus reducing SRO threshold, allowing the device to tolerate a greater loss at the periphery of the mirror bandwidths. The resultant tuning range, and further spectral properties of the KTA ICSRO are discussed in the next section

4.4 ICSRO spectral properties

Extension of the SRO pump-tuning range in the absence of signal output coupling is shown in figure 13. The solid lines are calculated tuning ranges based on sellmeier data from Fenimore *et al* [5].

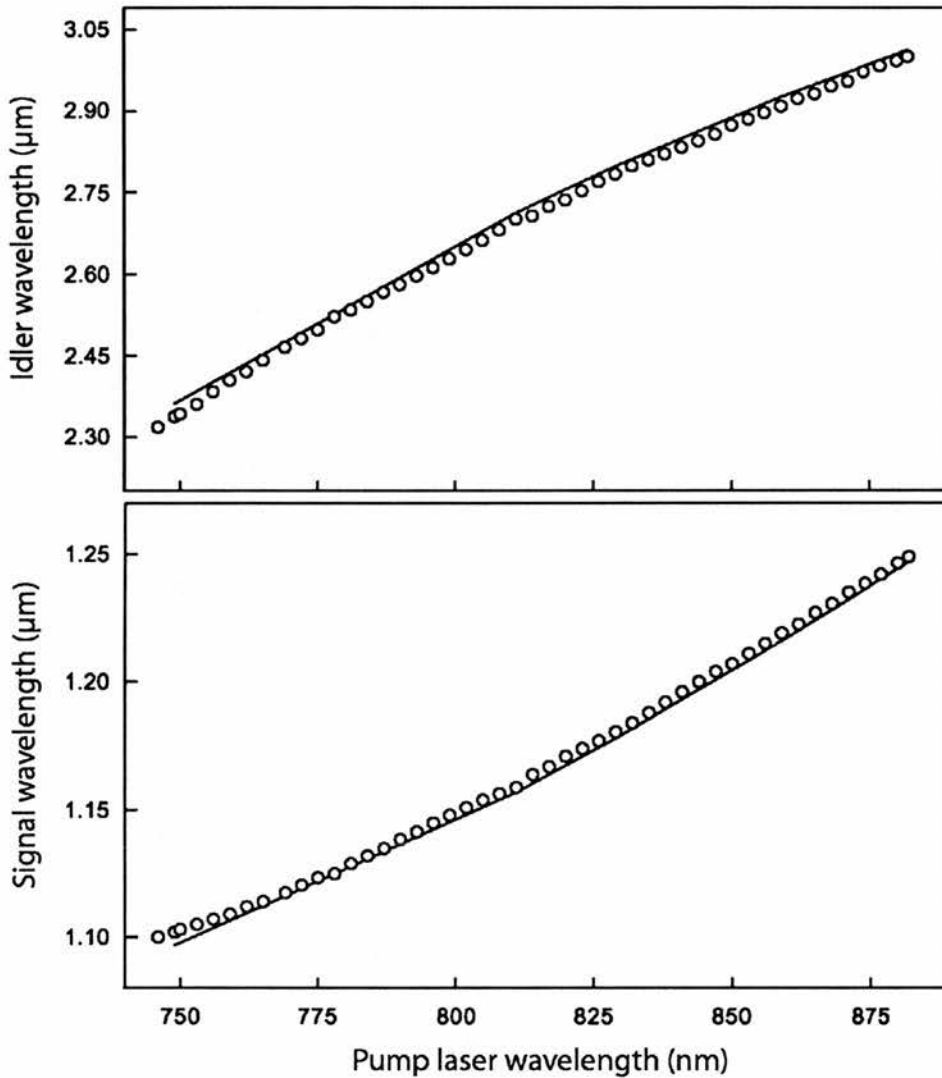


Figure 13. Signal and idler tuning ranges of the KTA ICSRO in the absence of signal output-coupling. The solid lines represent sellmeier-based calculations which are solutions of equation (4.1). Both traces share a common x-axis scale.

It can be seen from figure 13, that the signal and idler tuning data is in excellent agreement with the predicted curves. Tuning ranges of 1.10-1.25 μm at the signal (measured through leakage field from M7) and 2.32-3.00 μm at the idler are observed for a total pump tuning range of 748-880 nm. Again, the limits of these ranges are attributed to increased SRO loss at the limits of the mirror bandwidths and also, owing to the large pump tuning range, increased laser loss at the extremes of its own mirror bandwidths.

4.4-1 Resonant field linewidths

The standing-wave configured Ti:Sapphire laser operates on multiple longitudinal modes. The frequency spectrum of the resultant laser linewidth has been measured previously [7] for the Ti:Sapphire laser. This measurement was made using a scanning Fabry-Perot interferometer with a free spectral range of $70\pm 5\text{GHz}$. The laser was configured to accommodate a KTiOPO_4 nonlinear crystal as reported in reference [1] and was otherwise identical in its layout to the laser cavity described above.

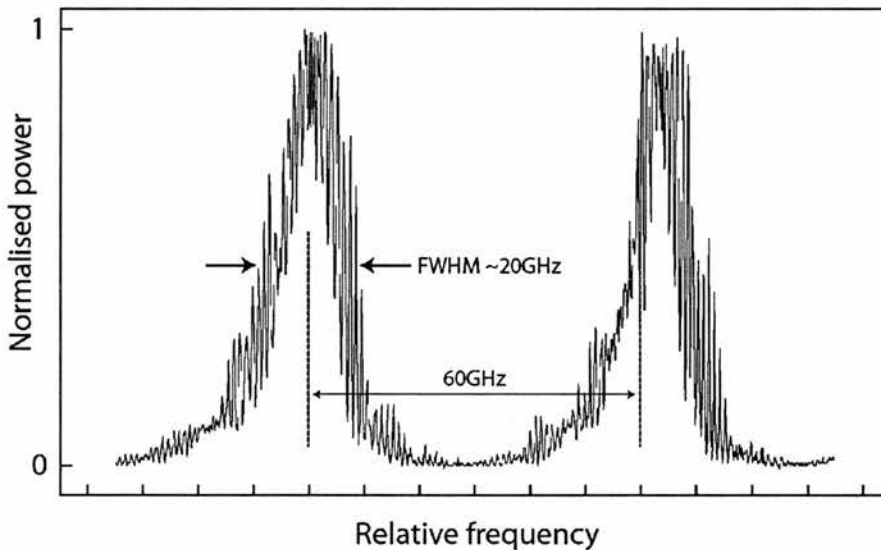


Figure 14. Resonant Ti:Sapphire laser field linewidth (after Colville et al [7]). The scale on the x-axis represents 10GHz divisions of frequency.

The full-width at half maximum (FWHM) of the laser linewidth, shown in figure 14, is measured to be $20\pm 5\text{GHz}$ and falls well within the 380GHz pump acceptance

bandwidth of the KTA crystal. Thus, the assumption that all the longitudinal modes of the laser resonator may be considered as phase-matched within the linewidth shown in figure 14, is a good approximation. The signal frequency spectral linewidth is shown in figure 15.

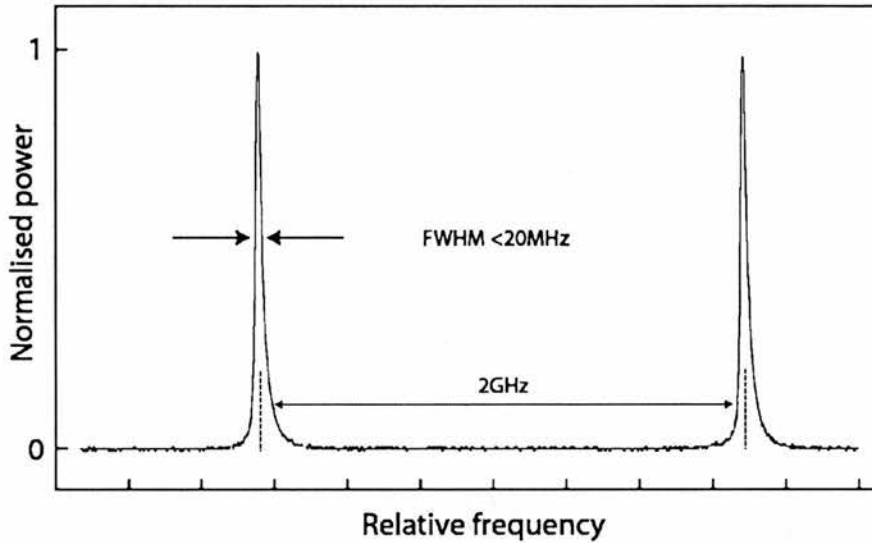


Figure 15. Resonant signal field linewidth. The scale on the x-axis represents 300MHz divisions of frequency.

The trace shown in figure 15 shows the linewidth of the ICSRO resonant signal field at pump powers ~ 4 times above threshold and in the absence of signal output coupling. The measurement was made using a 2GHz free spectral range scanning confocal interferometer. The signal field commonly operates on a single longitudinal mode of FWHM < 20 MHz with mode hops to adjacent cavity modes occurring under free-running conditions. In the absence of active frequency control, the insertion of a ~ 1 mm-thick glass étalon between M7 and the beamsplitter suppressed mode hops on a timescale of several minutes.

The frequency spectrum of the idler field could not be directly measured, as a suitable interferometer was not available at the time. The spectrum of the idler may be inferred from that of the pump as each longitudinal mode of the pump will couple through the single frequency signal field to produce an idler field that adopts the bandwidth of the pump laser. Thus, single frequency operation at the idler would require a single frequency laser configuration.

4.5 Chapter 4 Summary

The experimental work presented in this chapter confirms many of the operational characteristics of continuous-wave ICSROs predicted by theory. Power stability at pumping rates >4.5 times above threshold confirms that the singly-resonant condition liberates the ICSRO from the inefficient repetitively pulsed regime of the ICDRO. The device is found to operate with efficiencies approaching 90% and delivers over 1W of tunable infrared radiation under signal output coupling conditions.

There is evidence that the cavity parameters that define SRO threshold, especially the strength of the parametric interaction may alter over the pumping range of the argon-ion laser. Whilst it has not been possible to confirm a suitable mechanism for this conjecture, the reduction in expected efficiency at high pump powers serves to illustrate that power-scaling of these devices to Watt level output power will have to account for changes in cavity waist sizes caused by thermal effects at high pump powers. Problems associated with the output beam quality of the argon-ion laser at high pump powers compound the issue of reduced efficiency and further investigation of this effect is required.

Alternative geometries may allow a greater flexibility in the optimisation of the signal spot size relative to that of the pump within the nonlinear material. The current system denies flexible focussing differentiation through the use of mutual laser and pump focusing mirrors.

To conclude, this device has shown the practical implementation of a continuous-wave infrared source, delivering high output power through the use of an 11.5 mm long KTA crystal. The ICSRO approach is thus well placed to utilise any material offering similar or higher nonlinear properties.

Chapter 4 references

- 1 F. G. Colville, M. H. Dunn and M. Ebrahimzadeh, "Continuous-wave, singly resonant, intracavity parametric oscillator," *Optics Letters* **22**, 75-77 (1997).
- 2 Titan Ti:Sapphire Laser, Schwartz Electro Optics Inc. 3404, N. Orange Blossom Trail, Orlando, FL 32804 USA,
- 3 D. M. Kane, "Astigmatism compensation in off-axis laser resonators with two or more coupled foci," *Optics Communications* **25**, 379 (1989).
- 4 KTA Crystal, Crystal Associates Inc., 31 Fannella Drive, East Hanover, NJ 07936 USA,
- 5 D. L. Fenimore, K. L. Schepler, U. B. Ramabadran and S. R. McPherson, "Infrared corrected Sellmeier coefficients for potassium titanyl arsenate," *Journal of the Optical Society of America B-Optical Physics* **12**, 794 (1995).
- 6 M. K. Oshman and S. E. Harris, "Theory of Optical Parametric Oscillation Internal to the Laser Cavity," *IEEE Journal of Quantum Electronics* **QE-4**, 491-502 (1968).
- 7 F. G. Colville, M. H. Dunn and M. Ebrahimzadeh, "Continuous-wave, singly resonant, intracavity optical parametric oscillator," *CLEO Europe*, paper CPD1.5 (1996).

5. ICSRO based on QPM- LiNbO_3

5.1 Introduction

Paper G. A. Turnbull, T. J. Edwards, M. H. Dunn and M. Ebrahimzadeh, "Continuous-wave singly-resonant intracavity optical parametric oscillator based on periodically-poled LiNbO_3 ," *Electronics Letters* **33**, 1817-1818 (1997).

Abstract *A singly-resonant optical parametric oscillator using PPLN and operating intracavity to a continuous-wave Ti:sapphire laser is described. The oscillator exhibits multi-parameter pump-and grating-tuning of signal and idler wavelengths over the ranges 1.073-1.275 μm and 2.30-3.33 μm and 280mW output power. Observation of thermal lensing in PPLN is also reported.*

The work presented in this chapter has been published as above. The experimental study was jointly undertaken with Graham Turnbull in the School of Physics and Astronomy, University of St Andrews. Due credit and recognition is given to Graham for his contribution to this experimental work and subsequent analysis.

This chapter describes the study of an Ti:Sapphire pumped intracavity SRO based on the Periodically-Poled LiNbO_3 (PPLN). This nonlinear material represents the state of the art for nonlinear materials in the 0.5-5 μm transparency range as far as effective nonlinearity is concerned. With an effective nonlinear coefficient of $d_{\text{eff}} \approx 17 \text{ pm/V}$, PPLN is an attractive choice for many applications in nonlinear

optics. This material has placed SRO thresholds within the practical reach of conventional external CW laser output powers [1]. High efficiencies have been observed in such externally pumped devices [2]. Despite the success of PPLN based external SROs, the intracavity pumping approach is able to reduce the primary pump power requirements even lower, to the sub-Watt level domain [3]. Clearly, the possibility of utilising the high nonlinearity of PPLN to achieve low threshold, high output power intracavity SRO operation made the material a compelling choice for this experimental study.

This chapter describes the study of a Ti:sapphire pumped intracavity SRO based on PPLN. Multi-parameter tuning of the device is achieved and outlined. The expected high output power operation of the device is hindered by poor thermal properties of the material when subjected to the high circulating fields within the Ti:sapphire laser. The implications of using an intracavity oven include increased laser instabilities. A brief study of the thermal effects is presented.

5.2 Experimental design

To avoid the possibility of photorefractive damage, devices based on standard undoped LiNbO_3 must be operated at elevated temperatures. This necessitated the use of a servo-controlled oven around the crystal. The cavity design of the ICSRO outlined in chapter four was modified to accommodate the ~50mm diameter commercial Eskma oven. This modified design is shown in figure 1. The secondary intracavity focus of the Ti:sapphire laser is formed by an 80mm focal length intracavity lens, anti-reflection coated ($R < 0.3\%$) for the pump wavelength bandwidth. This lens forms an intracavity beam waist having a sagittal pump confocal parameter of 19.8mm and a tangential pump confocal parameter of 18.0mm located at the centre of the PPLN crystal. The signal cavity is formed by discriminating the resonant signal field from the pump field using a dichroic beamsplitter placed at 45 degrees to the incident pump field and located 30mm to the right of lens L2. Mirrors M6 and M5 define the resonant signal cavity. With the exception of the intracavity lens, all mirrors and components have identical

specifications and optical coatings to those described previously in chapter 4. The layout is simply a modified version of that used for the KTA experiment.

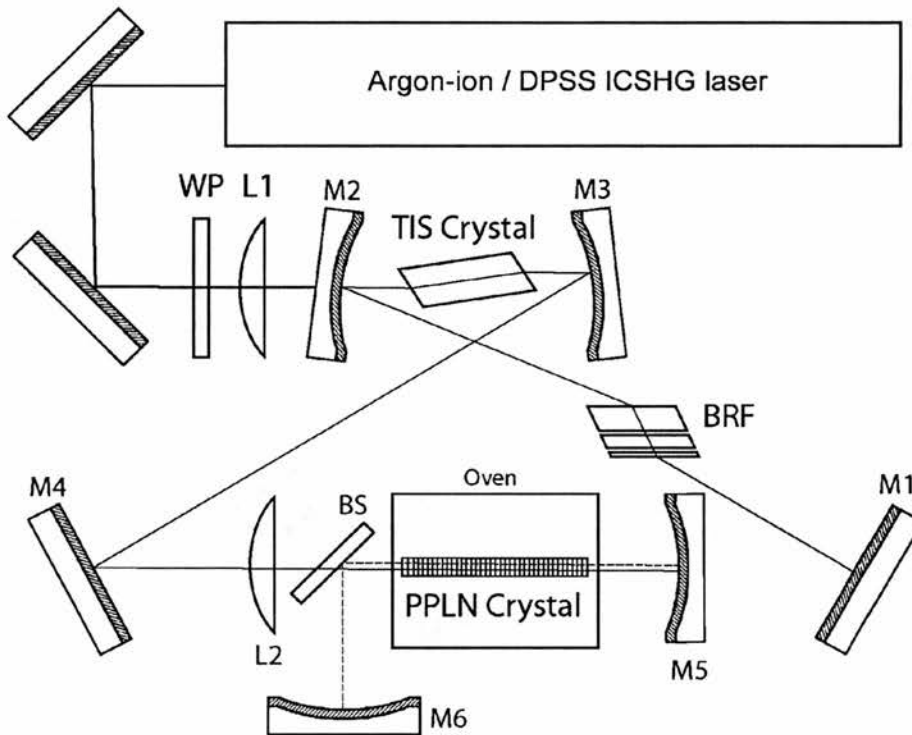


Figure 1. PPLN ICSRO experimental design.

Ti:Sapphire Laser Cavity Parameters

Mirror/Lens	ROC (mm)	Angle (Deg)	Separation	Distance (mm)
M1	∞	N/A	D1	680.0
M2	100	9.8	D2	48.7
			LX1	7.6
M3	100	9.8	D3	48.7
M4	∞	N/A	D4	780.0
L2	f=80	0	M4-L2	700.0
			L2-BS	30.0
M5	200	0	BS-M5	*162.4

Table 1. Ti:Sapphire laser cavity parameters of the layout illustrated in figure 1. Separation notation D1-D4 refers to figure 7(a) of chapter 3.

*includes physical length of PPLN crystal

OPO Cavity Parameters				
Mirror	ROC (mm)	Angle (Deg)	Separation	Distance (mm)
M6	200	0	M6-BS	98.8
M5	100	0	BS-M5	*162.4

Table 1. SRO Cavity parameters of the layout illustrated in figure 1.

*includes physical length of the PPLN crystal.

Optimum component spacing parameters are given in tables 1 and 2 for the laser and SRO cavities respectively. For the separation shown, the SRO cavity forms a beam waist with a confocal parameter of 18.8mm at the centre of the PPLN crystal.

5.2-1 Nonlinear material

The PPLN crystal used in this experiment was obtained commercially [4] and had a total of eight QPM gratings ranging from 21.0 - 22.4 μm in 0.2 μm steps. Overall dimensions were 19 x 11 x 0.5 mm as shown in figure 2.

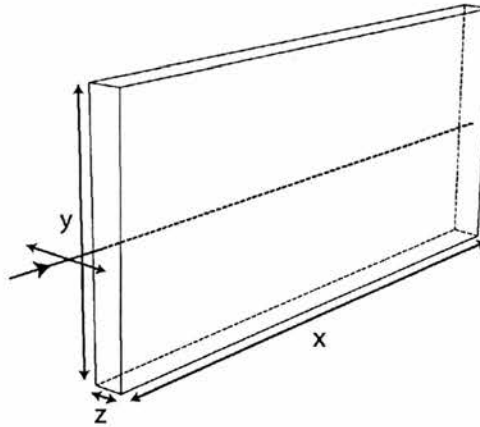


Figure 2. Dimensions and orientation of the PPLN crystal. All the parametrically interacting waves are polarised along the crystallographic z axis as shown. Dimensions are $x \times y \times z = 19 \times 11 \times 0.5\text{mm}$.

The QPM grating periods of the material were designed to phase-match Pump wavelengths from 800 - 840nm over the signal mirror bandwidth of 1.1 - 1.3 μm . The calculated pump tuning characteristics of the device are shown in figure 3.

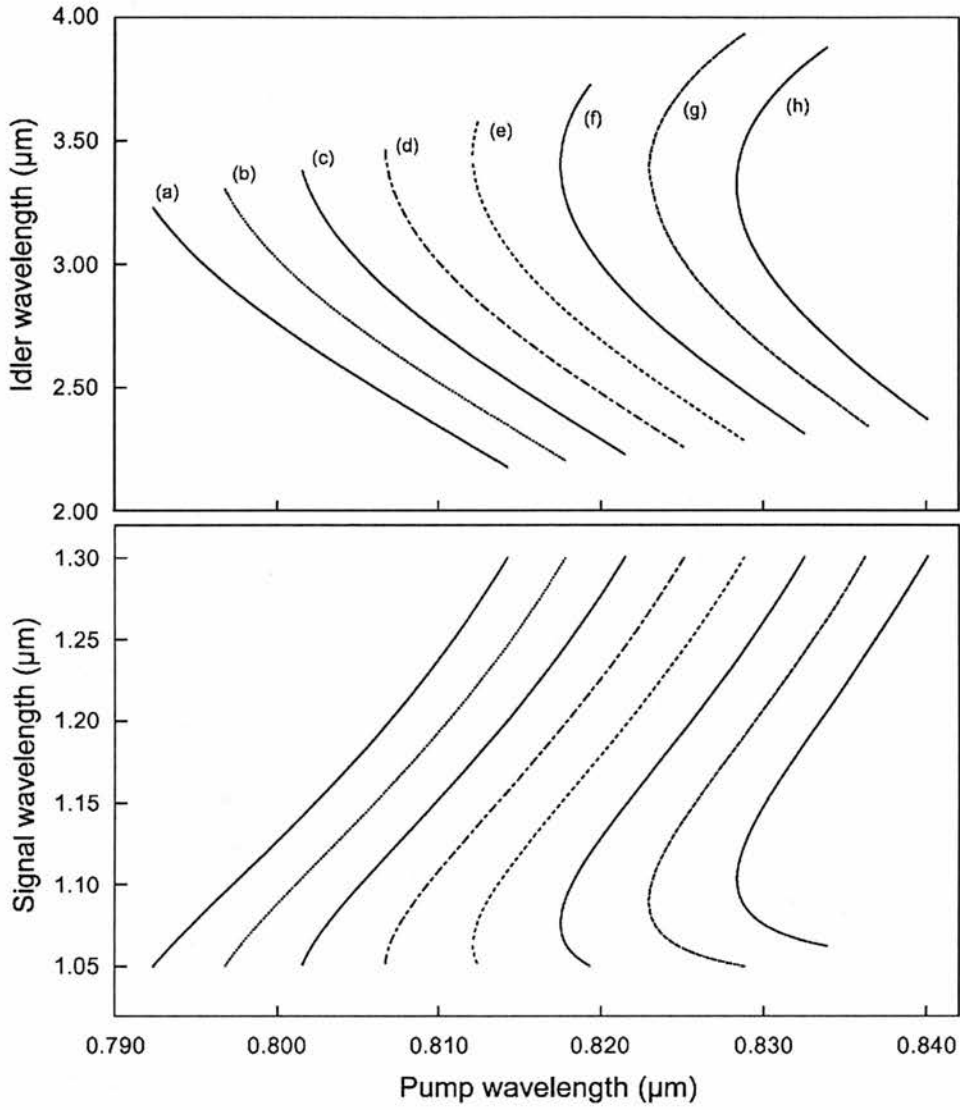


Figure 3. Calculated pump tuning curves for PPLN at 165°C . The eight separate QPM gratings periods are: (a) $21.0\mu\text{m}$, (b) $21.2\mu\text{m}$, (c) $21.4\mu\text{m}$, (d) $21.6\mu\text{m}$, (e) $21.8\mu\text{m}$, (f) $22.0\mu\text{m}$, (g) $22.2\mu\text{m}$, (h) $22.4\mu\text{m}$.

The tuning curve of figure 3 is obtained by numerically solving the following equation

$$\Delta k = \frac{n_z(\lambda_p)}{\lambda_p} - \frac{n_z(\lambda_s)}{\lambda_s} - \frac{n_z \left(\frac{\lambda_p \lambda_s}{\lambda_s - \lambda_p} \right)}{\left(\frac{\lambda_p \lambda_s}{\lambda_s - \lambda_p} \right)} - \frac{1}{\Lambda} = 0 \quad (5.1)$$

where energy conservation considerations have been made and $n_z(\lambda)$ is calculated from published sellmeier data for LiNbO_3 [5] which shows good agreement for data up to the $5.5 \mu\text{m}$ transparency edge of the material. It can be seen from figure 3 that there is a significant amount of overlap in the tuning range of each grating period. For a laser as widely tunable as Ti:sapphire, the grating periods having $0.6\text{-}0.8 \mu\text{m}$ spacing would be more appropriate for the given signal mirror bandwidth. This would enable a far wider idler tuning range to be exploited by accessing a wider pump tuning range. Choice of appropriate signal mirror bandwidths would enable the generation of any idler wavelength from degeneracy to the practical limit of the material transparency at $\sim 4.5 \mu\text{m}$. It should be emphasised that the present coating bandwidths were designed to accommodate the operation of birefringently phase-matched materials. PPLN also shows a significant degree of temperature tunability as shown in figure 4.

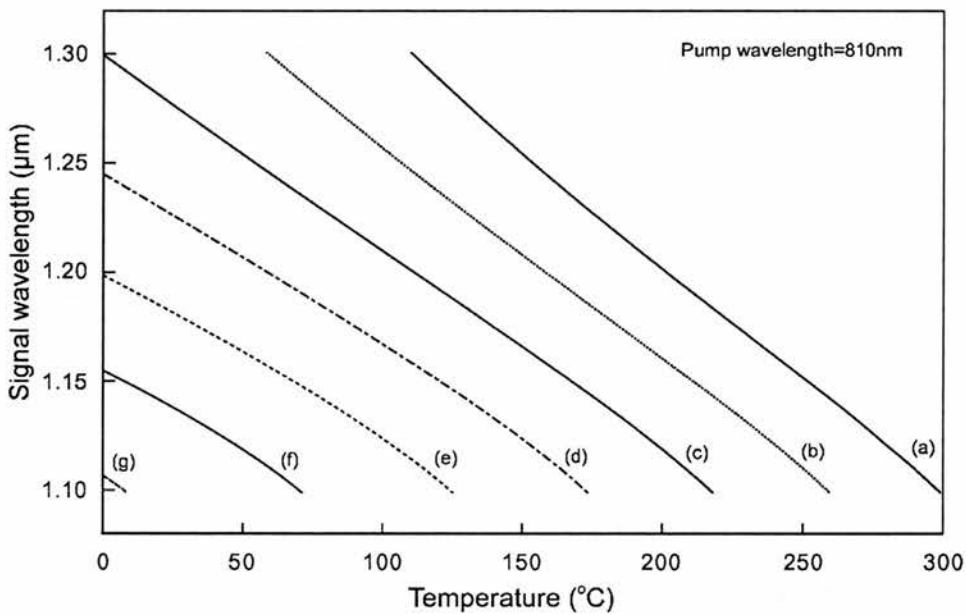


Figure 4. Temperature tuning of the signal field for PPLN at a pump wavelength of 810nm. QPM gratings periods are: (a) $21.0\mu\text{m}$, (b) $21.2\mu\text{m}$, (c) $21.4\mu\text{m}$, (d) $21.6\mu\text{m}$, (e) $21.8\mu\text{m}$, (f) $22.0\mu\text{m}$, (g) $22.2\mu\text{m}$.

The wide temperature tunability of PPLN is an attractive characteristic of the material for applications involving fixed-frequency pump laser sources. The rapid pump tunability of the Ti:sapphire laser removes the necessity of temperature

tuning which is a far slower mechanism. The multi-parameter combination of pump, grating and temperature tuning of the PPLN ICSRO allows a wide range of tuning schemes to be accessed. The implications of this high degree of flexibility include the ability of the PPLN ICSRO to operate at integer ratio output frequencies. This optical frequency division aspect to the tuning of the device is an attractive prospect for reference chain synthesis, discussed later in this chapter.

With a high coercive field of $\sim 21\text{kV/mm}$, PPLN is hard to produce with apertures of greater than 1mm. This presents problems during the optimising of devices with large path lengths. A 19mm long 0.5mm wide aperture inside the laser cavity presents a significant alignment challenge and hinders rapid power optimisation. This factor, coupled with the need to operate the material at elevated temperature, has a notable impact on the development prospects of the intracavity PPLN SRO. Recent progress in the development of wide aperture PPLN samples [6] and MgO-doped PPLN [7] shows promise for the solution of these material problems.

Problems arising from the thermal properties of this nonlinear material are discussed in a separate section.

5.2-2 SRO cavity alignment

The alignment procedure for the SRO cavity implemented in this experiment is slightly different from that outlined in the previous chapter. With the plane-mirror terminated SRO cavity of chapter 4, once lateral alignment of the retro-reflected pump is achieved SRO operation should commence. In the case of the PPLN SRO, lateral and longitudinal alignment must be made as the SRO cavity is terminated by a curved mirror M6.

The key to quick and effective alignment of mirror M6 is good initial alignment. M6 should be placed just behind the calculated optimum position from the beamsplitter. A screen located behind the beamsplitter as shown in figure 4 of chapter 4 must be used to examine the divergent back-reflected spots from the beamsplitter. Rudimentary alignment of M6 should give rise to a ring interference pattern between the back-reflected spot off the beamsplitter and the retro-reflected curved

wavefront from M6. The general idea is to increase the diameter of these rings, when overlapped, by moving M6 towards the beamsplitter. This will ensure that the two curved wavefronts will converge and bring the SRO cavity into stability and alignment. Clearly, if the rings get smaller, pull the mirror outwards. A good deal of patience is required here, ensure that the laser is tuned to the correct wavelength for the grating period being used and try and use a good viewing scope to get better contrast for the ring patterns (which can be very faint). The first indication of SRO operation will be the observation of a small amount of visible orange SHG of the signal wavelength. This is an effect of the high-order QPM processes that give finite conversion for odd-orders of the grating period. Sum frequency generation of the pump and signal is also clearly visible.

5.3 PPLN ICSRO power characteristics

The large effective nonlinearity of PPLN enabled the ICSRO to operate with an intracavity power threshold of 4.4 ± 0.5 W (one-way circulating). This corresponded to an input argon-ion power of 2W. The device, operating with a Ti:sapphire laser threshold of 0.7W, generated a total measured idler output power of 238 mW at a maximum input power of 6W. The total generated idler power (accounting for the 85% coupling efficiency of the SRO cavity) was 280mW at this pump power. With respective signal and idler wavelengths of 1.21 and 2.46 μm , the total downconverted power was inferred to be 0.85W at a pump wavelength of 811nm corresponding to 75% of the optimum Ti:sapphire output power at 6W of argon-ion input.

The lower power threshold of this device made it suitable for pumping with an all-solid-state frequency-doubled Nd:YVO₄ laser [8]. With a maximum green output power at 532nm of 5.3W a total measured idler power of 120mW was generated. This was tunable over the same range as measured for the argon-ion pumped configuration and detailed in the next section. The total downconverted power was inferred from the measured idler power and amounted to 360mW at the maximum input power of 5.3W.

From the outset of operation, the device showed poor amplitude stability with large temporal and spatial fluctuations on ~ 1 - 10 second timescales. These fluctuations increased with input power, and at 6 W of argon-ion input the best power amplitude stability was $\sim \pm 9\%$ as shown in figure 5.

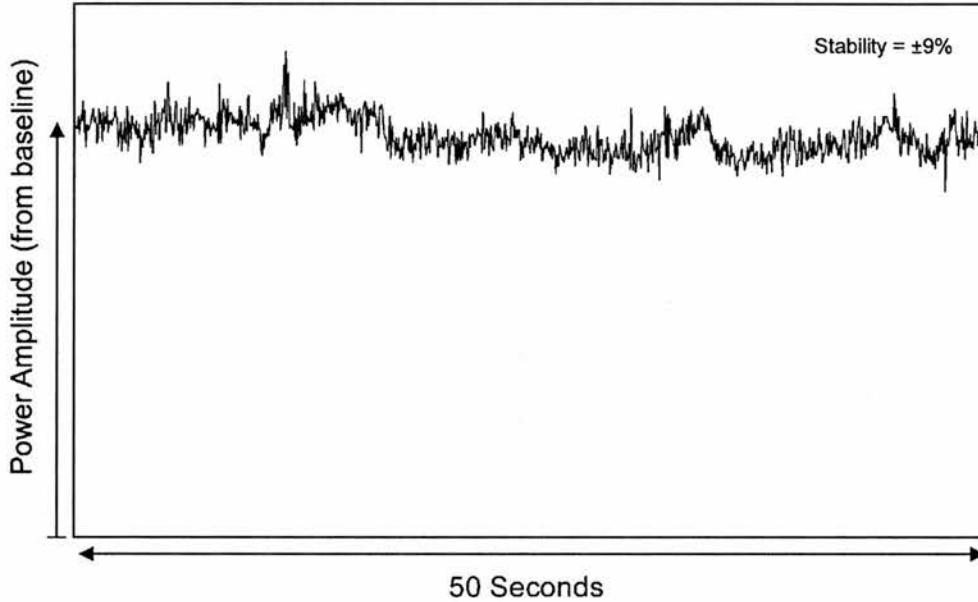


Figure 5. PPLN ICSRO amplitude stability over 50 seconds.

The power amplitude fluctuations were also observed for the Ti:sapphire laser in the absence of SRO operation. This indicated that the PPLN crystal and oven were the primary cause of the instabilities. Despite having a negligible effect on the laser threshold, insertion of the PPLN crystal into the laser cavity reduced the Ti:sapphire output powers by ~ 25 - 50% at argon-ion pump powers of 6 - 8 W. The observed degradation in laser performance at high input powers is attributed to power-induced thermal lensing in the PPLN crystal. A significant number of the short (~ 10 ms) timescale fluctuations appear to be caused by the intracavity oven itself. At an operating temperature of 165°C , the oven introduces air currents and dynamic refractive index effects analogous with mirage effects. An appreciable reduction in the output instabilities was achieved through the use of intracavity beam tubes around the oven input and output facets. These stabilised the gas temperature gradients close to the oven and also reduced convection currents. The larger timescale fluctuations were not affected by this measure.

5.3-1 PPLN thermal lens effects

The amplitude instabilities observed in the PPLN ICSRO diverted experimental attention towards an investigation of the thermal lensing effect of PPLN. Evidence of a large thermal lens induced by the intracavity laser field came from two distinct observations. The first, and perhaps most conclusive observation, was that the residual argon-ion pump light that is found approximately collinear with the intracavity laser field was affected by the presence of the laser field. When the intracavity laser field was blocked and released, the residual argon-ion light showed a series of rapidly expanding ring-fringes implying the dynamic establishment of a refractive index change along the axis of the laser field. This fringe expansion stopped once an equilibrium had been established. The second effect manifested itself in the "thermal latching" of the SRO. It was often observed that despite repeated attempts to align the SRO at input powers of ~6W, oscillation could only be achieved if the argon-ion input power was reduced by ~1W or the PPLN crystal was displaced slightly in the lateral direction. The qualitative inference is that at high intracavity power levels the stability conditions and/or cavity waist size induced by the thermal lens is such that the SRO cannot operate unless the intracavity field is reduced slightly. Once operational, the SRO keeps the intracavity field reduced due to the clamping effect such that the power may then be increased up to the maximum input power of 6W once more. When blocking the signal field and subsequently releasing the aperture, SRO operation often failed to commence despite the alignment of the cavity remaining the same.

To measure the strength of the induced thermal lens in PPLN, a He-Ne probe laser experiment was undertaken as illustrated in figure 6. A He-Ne laser operating a 633nm was coupled into the laser cavity off the SRO beamsplitter which placed it collinear with the intracavity laser field. Upon propagation through the PPLN crystal, the residual He-Ne laser light was monitored using a linear photodiode array (shown PDA in figure 6). The probe laser was focused with a 150mm focal length lens forming a waist at the centre of the PPLN crystal. This waist had a confocal parameter ~35% smaller than that of the laser field at the centre of the PPLN crystal ensuring that the aberrations were minimised. The He-Ne beam profiles in the

presence and absence of the intracavity laser field are shown in figure 7. These profiles were taken at a distance of 340 ± 1 mm from the centre of the PPLN crystal.

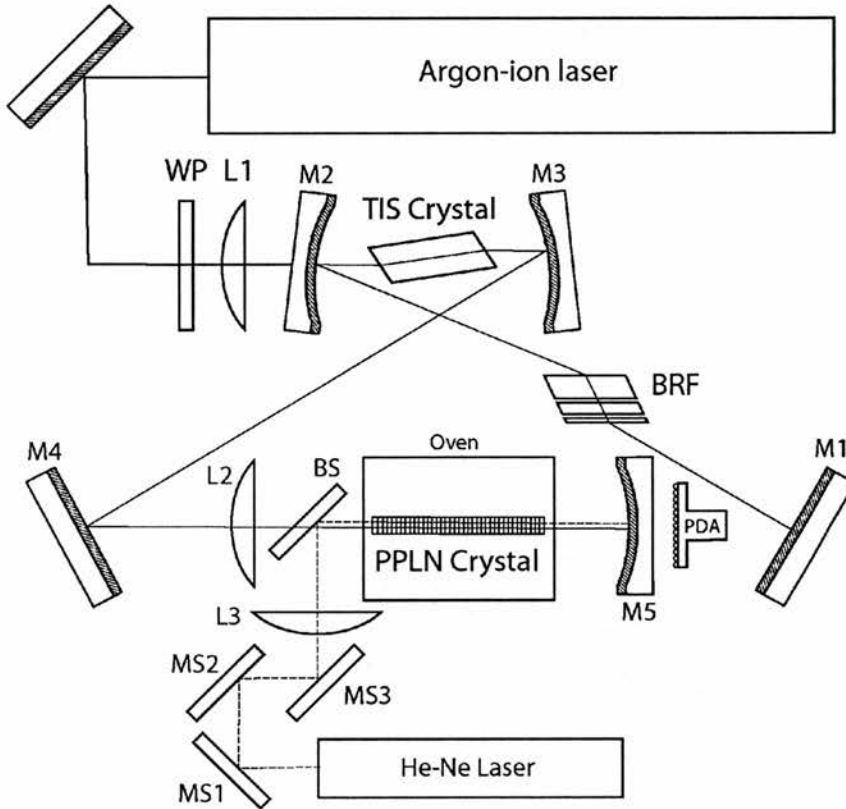


Figure 6. Experimental arrangement of the PPLN thermal lens study showing the He-Ne probe laser and photodiode array (PDA).

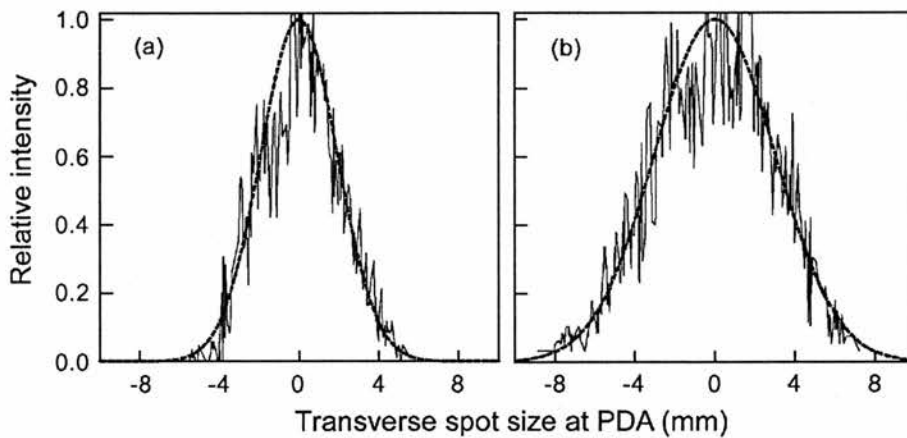


Figure 7. Transverse He-Ne spot size at PDA (a) without and (b) with 25W circulating intracavity field.

In the presence and absence of a circulating intracavity field of 25W, the beam profiles of figure 7 were used to infer the thermally induced focal length in the PPLN crystal. Using an ABCD analysis of the probe laser beam propagation, the PPLN crystal matrix was modelled as a lens duct with a transverse refractive index profile given by

$$n(r) = n - \frac{n_2}{2r^2} \quad (5.2)$$

having an effective focal length f_{eff} , of

$$f_{eff} = \frac{1}{n_2 l} \quad (5.3)$$

Adjusting the parameter n_2 for a crystal length $l = 19mm$ such that the beam divergences observed in figure 7 were obtained, gave an inferred thermal lens focal length of $f_{eff} = 10 \pm 4mm$. The effective focal length of the PPLN thermal lens may be calculated following the procedure of Innocenzi *et al.* [9]. Taking the absorption of $LiNbO_3$, α , at 800nm to be $0.15\%cm^{-1}$ [10] and a thermal conductivity value of $K_c = 5.6Wm^{-1}K^{-1}$ [11], a calculated value of $f_{eff} = 3.4mm$ is obtained. The analytical solution used is approximate and the exact numerical method yields a slightly longer focal length. Both results show that under intracavity operation, with its associated high circulating fields, PPLN suffers from significant thermally induced lensing. This qualitatively explains the poor power stability of the device. The location of this strong lens at the intracavity laser focus is a critical factor in minimising its effects on the cavity. Despite this, as the thermal lens builds with scaled input pump power it will effect the Ti:sapphire crystal beam waist; reducing laser gain and setting the cavity at a sensitive equilibrium where further increases in pump power are offset by the reduction in laser gain. The cavity itself will be close to its stability range. This hypothesis is highly speculative and has not been verified. That the thermal lens in PPLN has a severely detrimental effect on the high power operation of the ICSRO is in much less doubt.

5.4 Spectral properties

The pump wavelength tuning of the PPLN ICSRO is shown in figure 8. The data were obtained with an argon-ion input power of 6W at an oven temperature of 165°C. Idler wavelength values are inferred from measurements of pump and signal wavelengths using an optical spectrum analyser operating with a resolution of 0.1nm. Conservation of energy is assumed.

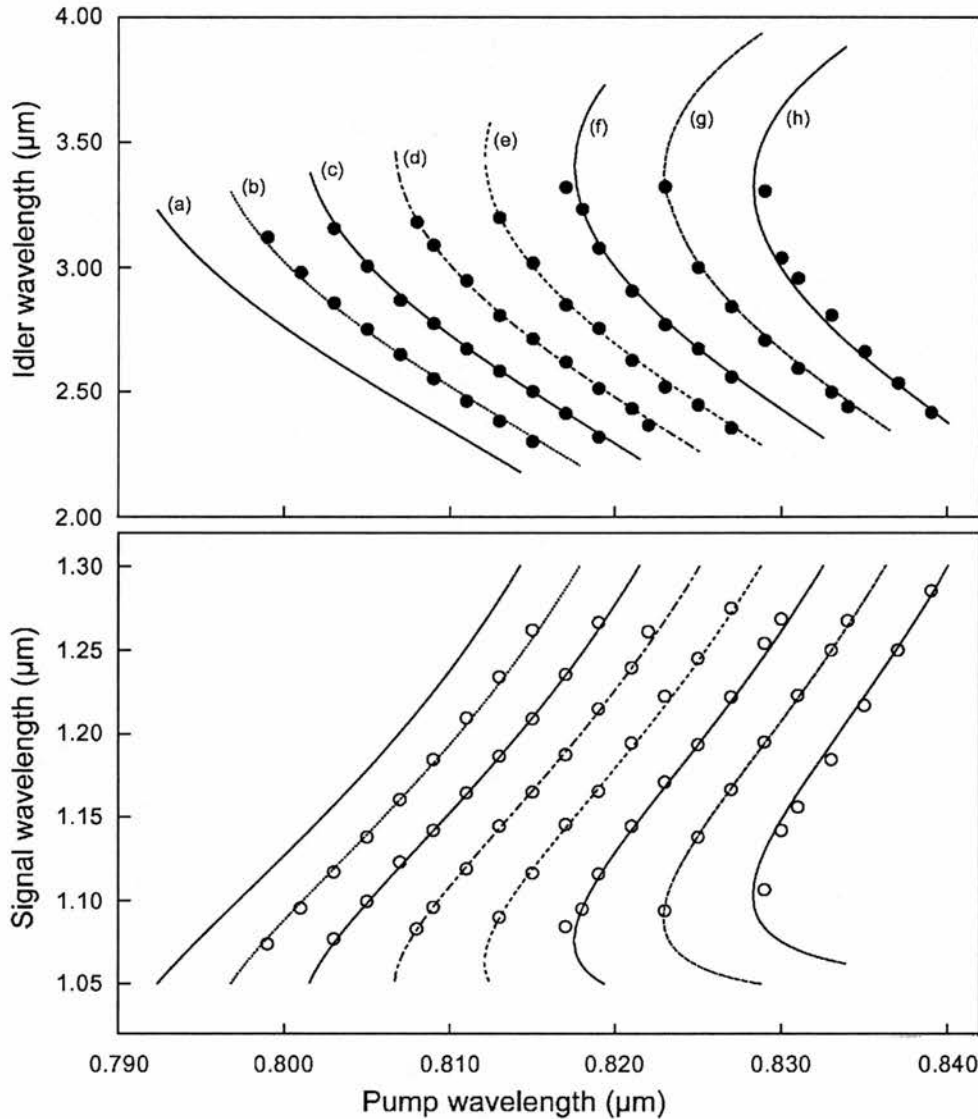


Figure 8. Pump wavelength tuning of PPLN ICSRO. Gratings are designated: (a) 21.0 μm , (b) 21.2 μm , (c) 21.4 μm , (d) 21.6 μm , (e) 21.8 μm , (f) 22.0 μm , (g) 22.2 μm , (h) 22.4 μm

The oven insert used to mount the PPLN crystal made the 21.0 μm grating inaccessible to the intracavity laser field and data for this grating are missing. The experimental data is in excellent agreement with the theoretical curves calculated using equation (5.1). In contrast to its poor power performance, the PPLN ICSRO showed a great deal of tuning flexibility. The signal field operated over the entire mirror bandwidth from 1.073 to 1.257 μm corresponding to an idler tuning range of 2.30 to 3.33 μm . For an individual QPM grating period, the pump tuning range is reduced to $\sim 17\text{nm}$, significantly less than the $\sim 130\text{nm}$ pump tuning range of the KTA ICSRO of chapter 4 for similar signal tuning ranges.

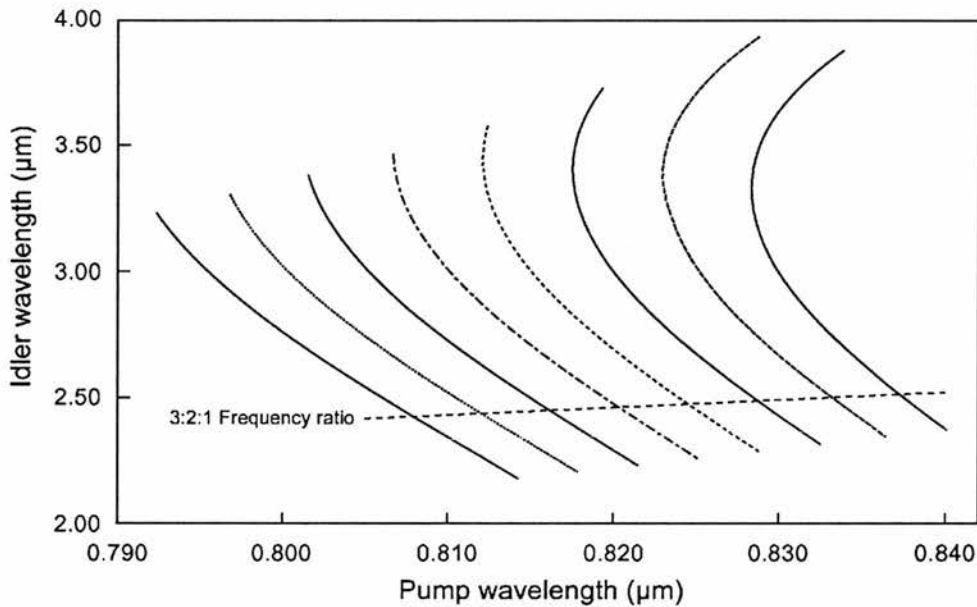


Figure 9. Frequency ratio condition showing 3:2:1 Pump:Signal:Idler.

An important consequence of the multi-parameter tuning behaviour exhibited by the PPLN ICSRO is shown in figure 9. Combinations of pump, grating and temperature tuning allow frequency division synthesis [12] over a wide range of pump wavelengths. Figure 9 shows eight distinct solutions (intersections of the lines shown) for which the pump signal and idler frequencies are in a 3:2:1 ratio. Examination of figures 4 and 9 clearly shows that a $\sim 50^\circ\text{C}$ temperature tuning range would tune each intersection solution to its nearest neighbour, giving a complete coverage of the labelled ratio line shown. This is only possible due to the

combination of the three tuning parameters available to the tunable Ti:sapphire pumped ICSRO. Due to the conservation of energy condition central to the operation of the OPO, one of its outputs, when locked to an external frequency reference, allows the other outputs to be referenced to this same source when they are locked in an integer ratio.

The external reference would commonly be an atomic transition. The internal reference is generated by the parametric process itself. For example, when the pump, signal and idler frequencies are in a 3:2:1 ratio the second harmonic of the signal field coincides in frequency with the sum frequency of the idler and pump fields providing a suitable ratio "lock point". It is worth noting that high order nonlinear process in the QPM structure simultaneously phase-match all the possible parametric process (albeit with very poor efficiencies). By virtue of the fact that the QPM material is immersed in two multi-Watt circulating fields (signal and pump) even the poor efficiencies of these high order process are enough to clearly see the visible SHG and SFM output. It is often possible to scatter this output from a diffraction grating and watch the SHG signal field and the SFM pump and idler scan towards each other as the pump wavelength is tuned. This is a practical demonstration unique to the Ti:sapphire pumped ICSRO. For higher conversion efficiencies, the secondary nonlinear processes can be individually phase-matched to enable a strong beat frequency between the coincident processes [13, 14]. In some circumstances, the secondary nonlinear process itself can self-injection lock the OPO parametric process [15].

A suitable frequency reference scheme for the PPLN ICSRO has been devised by Turnbull [16]. This scheme involves referencing an idler field at $3.39\mu\text{m}$ to the $P(7)$ branch of the ν_3 Methane band. A single frequency pump (such as that obtained in the PPKTP device of chapter 7) at 848nm driving a QPM PPLN ICSRO with a grating period of $23.0\mu\text{m}$ at 175°C would give the desired frequency ratio and idler output. Internal parametric locking would be obtained via a coincidence of the idler SHG and the DFM of the signal and idler. The resultant frequency chain could stretch from $3.39\mu\text{m}$ to the SHG of the pump wavelength at 424nm under suitable phase-matched conditions.

5.5 Chapter 5 summary

An intracavity SRO based on QPM LiNbO₃ (PPLN) has been implemented. The device operates with a low primary pump threshold of 2W placing it well within the pump power domain of efficient all-solid-state diode pumped laser sources. The flexible combination of pump, grating and temperature tuning enables the device to operate over a range of useful frequency division output frequencies. Adjustment of the resonant signal mirror bandwidths and QPM grating period would allow an even greater flexibility of output frequencies with comparable device performance.

The high power stability of the device is poor due to the superposition of two independent factors. The first concerns effects induced through the insertion of a high temperature oven at 165°C into the Ti:sapphire laser cavity. Convection currents and associated dynamic refractive index gradients of the air surrounding the oven cause instabilities of the output power for both the laser and ICSRO. Enclosing the intracavity beam path near the oven facets with tubes results in a marked decrease in the output power instability. Clearly, a desirable improvement would be to operate the oven at a reduced temperature, advances in the MgO-doping of LiNbO₃ [7, 17, 18] may well allow operation at, or close to, room temperature without the effects of photorefractive damage. The use of intracavity ovens requires a far greater degree of cavity engineering than is required for room temperature operation. This is a significant factor in the favour of poled materials such as PPRTA and PPKTP which can be operated at room temperature without the observation of photorefractive damage.

The second factor affecting the power stability of the device is the observation of a large thermally induced lens in the PPLN crystal when immersed in high circulating Ti:sapphire fields. The intracavity pumping geometry utilised here couples the two intracavity beam waists such that a significant change in the focussing conditions at one waist location will adversely effect those at the other waist. In this way a sensitive equilibrium between induced thermal lens in the PPLN crystal and its associated effect on the gain of the laser mode is established. Instabilities in output power are observed on ~1-10 second timescales as well as dynamic changes in

spatial mode quality of the laser and SRO outputs. Solutions to this problem are inherently material based. Of the few cavity improvements that may be made, a cavity design which replaces mirror M5 with a plane mirror (having the same coating specification) placed close to the rear surface of the PPLN crystal is less intolerant to thermal lensing. This is due to the fact that the axial location of the secondary beam waist is now defined at the plane mirror. The disadvantage of this method is that the parametric gain is reduced as the beam waist is located away from the centre of the PPLN crystal. Problems of optical coating damage may also arise by forming the secondary intracavity focus directly onto the plane mirror and close to the end facet of the PPLN crystal. Cavity desensitising of thermal lensing has been successfully employed for a low power Nd:YVO₄ ICSRO based on PPLN [3] where the use of an intracavity focussing element coupled with low circulating fields and long PPLN interaction lengths reduces the effects of thermally induced lensing.

In conclusion it is worthwhile to note the absence of high power continuous wave applications for internally pumped PPLN. The frequency doubled Nd:YVO₄ laser utilised in a section of this experiment is a prime example. This laser successfully operates with an intracavity oven (all beam paths in the laser are enclosed) but uses the nonlinear material LBO to achieve intracavity SHG. This material has an effective nonlinearity ~4 times lower than that of PPLN.

Chapter 5 references

- 1 W. R. Bosenberg, A. Drobshoff, J. I. Alexander, L. E. Myers and R. L. Byer, "Continuous-wave singly resonant optical parametric oscillator based on periodically poled LiNbO₃," *Optics Letters* **21**, 713 (1996).
- 2 W. R. Bosenberg, A. Drobshoff, J. I. Alexander, L. E. Myers and R. L. Byer, "93% pump depletion, 3.5-W continuous-wave, singly resonant optical parametric oscillator," *Optics Letters* **21**, 1336 (1996).
- 3 D. J. M. Stothard, M. Ebrahimzadeh and M. H. Dunn, "Low pump threshold, continuous-wave, singly resonant, optical parametric oscillator," *Optics Letters* **23**, 1895 (1998).
- 4 PPLN Crystal, Crystal Technology, Inc., 1040 East Meadow Circle, Palo Alto, CA 94303-4230.,
- 5 D. H. Jundt, "Temperature-dependent Sellmeier equation for the index of refraction n_e in congruent lithium niobate," *Optics Letters* **22**, 1553 (1997).
- 6 M. Nakamura, T. Tsunekawa, H. Taniguchi and K. Tadamoto, "Optical parametric oscillator on 1-mm-thick periodically poled LiNbO₃ with 29 mm interaction length," *Japanese Journal of Applied Physics Part 2-Letters* **38**, L1175-L1177 (1999).
- 7 M. Nakamura, M. Sugihara, M. Kotoh, H. Taniguchi and K. Tadatomo, "Quasi-phase-matched optical parametric oscillator using periodically poled MgO-doped LiNbO₃ crystal," *Japanese Journal of Applied Physics Part 2-Letters* **38**, L1234-L1236 (1999).
- 8 5W Millennia Laser, Spectra Physics Inc., 1335 Terra Bella Ave., Mountain View, CA 94043,
- 9 M. E. Innocenzi, H. T. Yura, C. L. Fincher and R. A. Fields, "Thermal Modeling of Continuous-Wave End-Pumped Solid-State Lasers," *Applied Physics Letters* **56**, 1831-1833 (1990).
- 10 V. G. Dmitriev, G. G. Gurzadyan and D. N. Nikogosyan, *Handbook of nonlinear optical crystals*. (2nd ed.) (Springer-Verlag, Berlin, Heidelberg, New York, 1997).
- 11 P. F. Bordui and M. M. Fejer, "Inorganic crystals for nonlinear optical frequency conversion," *Annual Review of Material Science* **23**, 321 (1993).
- 12 N. C. Wong, "Optical frequency division using an optical parametric oscillator," *Optics Letters* **15**, 1129 (1990).
- 13 O. Pfister, J. S. Wells, L. Hollberg, L. Zink, D. A. VanBaak, M. D. Levenson and W. R. Bosenberg, "Continuous-wave frequency tripling and

- quadrupling by simultaneous three-wave mixings in periodically poled crystals: application to a two-step 1.19-10.71- μ m frequency bridge," *Optics Letters* **22**, 1211-1213 (1997).
- 14 P. T. Nee and N. C. Wong, "Optical frequency division by 3 of 532nm in periodically poled lithium niobate with a double grating," *Optics Letters* **23**, 46 (1998).
- 15 D. H. Lee, M. E. Klein, J. P. Meyn, P. Gross, R. Wallenstein and K. J. Boller, "Self-injection-locking of a CW-OPO by intracavity frequency-doubling the idler wave," *Optics Express* **5**, 114-119 (1999).
- 16 G. A. Turnbull, *Continuous-wave intracavity optical parametric oscillators*, PhD thesis, St Andrews University (1999).
- 17 A. Harada and Y. Nihei, "Bulk periodically poled MgO-LiNbO₃ by corona discharge method," *Applied Physics Letters* **69**, 2629-2631 (1996).
- 18 A. Harada, Y. Nihei, Y. Okazaki and H. Hyuga, "Intracavity frequency doubling of a diode-pumped 946-nm Nd:YAG laser with bulk periodically poled MgO-LiNbO₃," *Optics Letters* **22**, 805-807 (1997).

6. ICSRO based on QPM- $RbTiOAsO_4$

6.1 Introduction

Paper T. J. Edwards, G. A. Turnbull, M. H. Dunn, M. Ebrahimzadeh, H. Karlsson, G. Arvidsson and F. Laurell, "Continuous-wave singly resonant optical parametric oscillator based on periodically poled $RbTiOAsO_4$," *Optics Letters*, **23**, 837-839 (1998).

Abstract *We report a continuous-wave optical parametric oscillator (OPO) based on periodically poled $RbTiOAsO_4$ (PPRTA). The singly resonant OPO, which is located within a Ti:Sapphire laser, has a high-finesse signal cavity and delivers a maximum output power of 270 mW to the nonresonant idler wave at 2.92 μm , through a 4.5-mm PPRTA crystal. For room-temperature operation and a crystal with a 30- μm grating period, pump tuning over 838-848 nm results in OPO turning over 1.13-1.27 μm (signal) and 2.53-3.26 μm (idler), limited by the bandwidth of optical coatings. PPRTA exhibits thermal properties superior to those of periodically poled $LiNbO_3$.*

This chapter describes the study of a Ti:Sapphire pumped intracavity SRO based on periodically poled $RbTiOAsO_4$ (PPRTA). In the Autumn of 1997 we were fortunate enough to have, on loan, one of two PPRTA crystals acquired for picosecond pulsed Ti:Sapphire pumping in the School of Physics and Astronomy, St Andrews University (this work was subsequently published [1, 2]). The crystal, which was the longer of the two acquired, measured just 4.5mm in length and offered a unique opportunity to attempt the first observation of CW optical parametric oscillation in this newly-poled material. The intracavity pumping

approach was well placed to overcome the high SRO threshold conditions presented by the small interaction length of the crystal. The tight focussing geometry required to minimise threshold placed the cavity geometry under tight stability constraints. Despite this, SRO operation was observed for input pump powers twice above threshold. Characterisation of this device was subject to limited time constraints dictated by the research schedule of the group from which it originated. The crystal used in this experiment was subsequently characterised in picosecond Ti:Sapphire OPO systems [1, 2].

6.2 Experimental design

The cavity arrangement and design of the PPRTA was similar to that of the KTA device discussed in chapter 4. To accommodate the much shorter nonlinear crystal the pump focussing was increased in the SRO branch of the cavity by specifying mirror M5 with a radius of curvature (ROC) of 100mm.

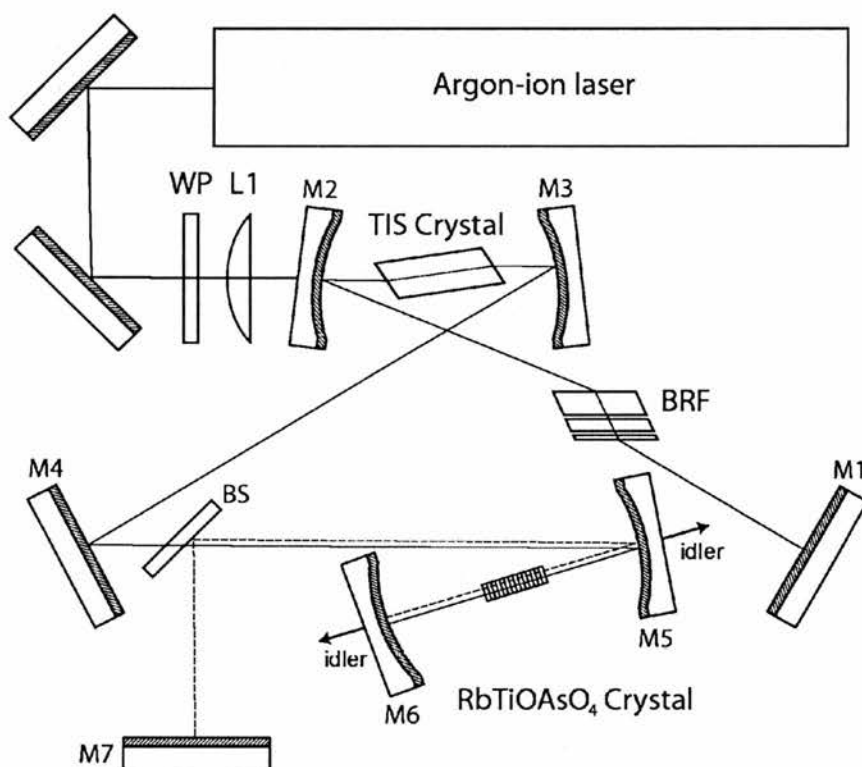


Figure 1. PPRTA experimental cavity layout

Deviations from the cavity design outlined in chapter 4 are the replacement of the Spectra-Physics 171 argon-ion with a more reliable Spectra-Physics 20-30 model, and the reduction in laser waist size in the SRO branch by specifying M5 with a 100mm ROC. To reduce the overall cavity size for convenient positioning of cavity optical mounts, mirror M6 was also specified with a ROC of 100mm. Optical coatings on both these optics were identical to those previously used. Other than these minor changes the cavity is unchanged from that described in chapter 4.

The consequences on the dual stability criterion of both laser and SRO cavities arising from reduced SRO pump and signal mode waists is illustrated in figure 2.

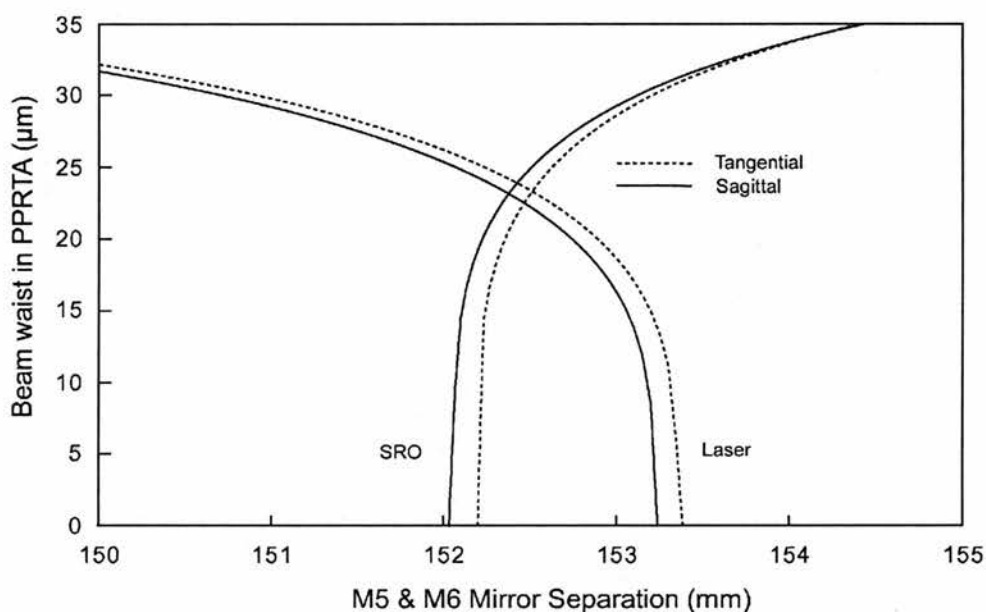


Figure 2. Beam waist in the centre of the PPRTA crystal as a function of mirror separation of M5 & M6. Laser and SRO cavities are stable over a ~ 1 mm range in contrast to the ~ 4 mm common stability range of the KTA configuration of chapter 4.

It can be seen from figure 2 that the laser and SRO cavities satisfy the common stability criterion for ICSRO operation over a separation range of ~ 1 mm. Both cavities are operating close to the edge of stability. The analysis was performed for a pump wavelength of 840nm and a signal wavelength of 1180nm with cavity

spacing measured from the operational ICSRO device. The measured cavity component spacing is given in tables 1 and 2.

Ti:Sapphire Laser Cavity Parameters				
Mirror	ROC (mm)	Angle (Deg)	Separation	Distance (mm)
M1	∞	N/A	D1	645.0
M2	100	9.8	D2	48.7
			LX1	7.6
M3	100	9.8	D3	48.7
M4	∞	N/A	D4	680.0
			D5	680.0
M5	100	3.5	D6	49.8
			LX2	4.5
M6	100	3.5	D7	98.4

Table 1. Ti:Sapphire laser cavity parameters of the layout illustrated in figure 1. Separation notation refers to figure 7(a) of chapter 3.

OPO Cavity Parameters				
Mirror	ROC (mm)	Angle (Deg)	Separation	Distance (mm)
M7	∞	N/A	D1	223.0
			D2	377.0
M5	100	2	D3	49.8
			LX2	4.5
M6	100	2	D4	98.4

Table 1. SRO Cavity parameters of the layout illustrated in figure 1. Separation notation refers to figure 8(a) of chapter 3.

The optimum mirror separation of mirrors M5 and M6 is found to be 152.7 mm for maximum SRO output power. The pump laser mode sizes at this optimum separation are $21 \times 20 \mu\text{m}$ in the Ti:Sapphire crystal and $20 \times 22 \mu\text{m}$ at the centre of the PPRTA crystal for a pump wavelength of 840nm. The respective PPRTA signal field waist size was $27 \times 26 \mu\text{m}$ for a wavelength of 1180nm.

6.2-1 Nonlinear material

The single-grating PPRTA crystal used here was prepared from an 8 mm long \times 1 mm thick sample by patterning a photoresist grating with a period of $30\ \mu\text{m}$ upon the c^+ face [3]. Electrical contact with the crystal was made by a KCl electrolyte, and the sample was poled with 12-ms-long voltage pulses of 2.0 kV. Evaluation of the quality of the quasi-phase-matched (QPM) structure was performed by carrying out sixth-order second-harmonic generation with a CW source with a fundamental wavelength of 914 nm. The width of the obtained phase-matching peak implied an effective interaction length equivalent to $\sim 80\%$ of the total grating length and a nonlinear coefficient of $d_{\text{eff}} \approx 8\ \text{pm/V}$. The sample was then cut to obtain a 4.5 mm long crystal whose end faces were then polished and subsequently coated with an antireflection coating centred for pump and signal wavelengths respectively. The orientation of this crystal with respect to the pump polarisation is shown in figure 3.

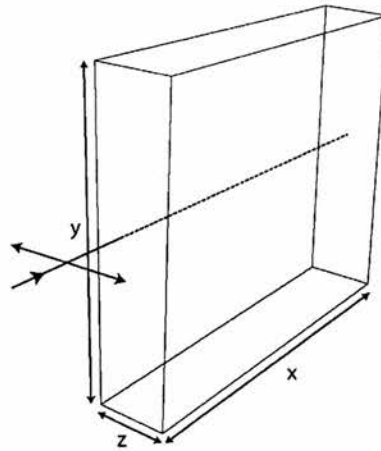


Figure 3. PPRTA showing the pump polarisation orientated along the z axis of the crystal. Dimensions in the $x \times y \times z$ crystallographic directions are $4.5 \times 5 \times 1\ \text{mm}$. The single-grating period is $\Lambda = 30\ \mu\text{m}$.

The wavelength transparency range of RTA extends beyond $5\ \mu\text{m}$ and the QPM phase-matched geometry allows phase-matching over the entire transparency range. The coating bandwidths of the Ti:Sapphire ICSRO optics constrain the resonant signal field to a 200nm bandwidth centred at 1200nm. This limits the

potential accessible tuning ranges that are available through the grating-engineered phase-matching geometry.

The QPM phase-matching regime may be calculated by numerically solving the following equation for λ_s , given a particular pump tuning range

$$\Delta k = \frac{n_z(\lambda_p)}{\lambda_p} - \frac{n_z(\lambda_s)}{\lambda_s} - \frac{n_z\left(\frac{\lambda_p\lambda_s}{\lambda_s - \lambda_p}\right)}{\left(\frac{\lambda_p\lambda_s}{\lambda_s - \lambda_p}\right)} - \frac{1}{\Lambda} = 0 \quad (6.1)$$

Here, $n_z(\lambda)$ is calculated from published sellmeier data [4]. Common with many QPM interactions, all the interacting parametric fields are polarised along the crystal axis that accesses the highest nonlinear d coefficient. In the case of RTA this is along the z axis, which accesses a published coefficient of $d_{33} = 12.1 \text{ pm/V}$ [5]. As outlined in chapter 2, the effective nonlinear coefficient for first order QPM accessing the d_{33} nonlinear coefficient is given by

$$d_{eff} = \frac{2}{\pi} d_{33} \quad (6.2)$$

This gives an effective nonlinear coefficient of $d_{eff} = 7.6 \text{ pm/V}$ for the data of reference [5], in good agreement with the experimental measurement. Equation (6.1) may be solved for phase-matched signal and idler ranges (assuming energy conservation) for a given pump wavelength range and grating period Λ . Alternatively, (6.1) may be used to calculate a range of grating periods suitable for a particular pump wavelength and signal mirror bandwidth. This second method is often the first stage of the QPM design process for a particular application. The resultant curves generated by this approach taking a range of Ti:Sapphire pump wavelengths are shown in figure 4. As the grating period of the material will not be a continuously tunable variable (with the exception of a small change in period with crystal tilt) the correct choice of grating must be made at the outset of the design stage. The choice of grating period will be tied to the accuracy of the sellmeier data

used to model the tuning curves. For materials such a RTA which lack a wide range of published sellmeier data there is scope for error when specifying a particular QPM period. A great advantage of the Ti:Sapphire ICSRO pumping approach is that the wide tunability of the device is able to accommodate most design errors of the QPM period by operating over different pump wavelength ranges. Coupled with its ability to overcome the stringent CW threshold requirements of newly-developed materials (which often have short interaction lengths when first developed), the ICSRO is uniquely placed as a test-bed for new QPM materials. The pump wavelength "agility" mentioned above is illustrated in figures 4 and 5.

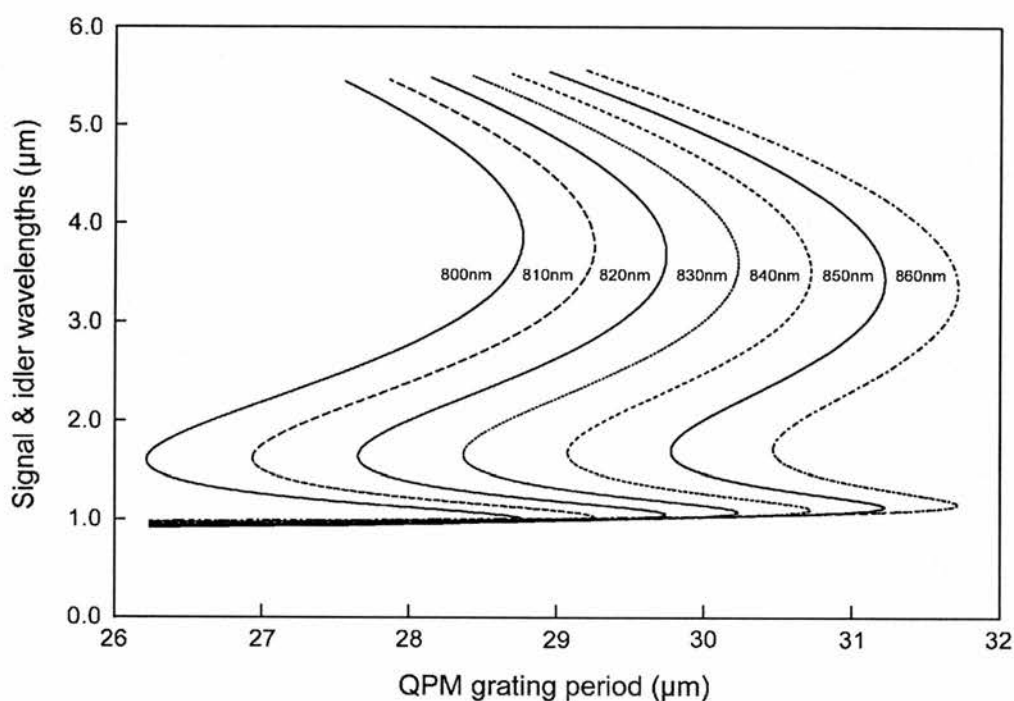


Figure 4. PPRTA calculated signal and idler QPM wavelengths as a function of grating period for a range of Ti:Sapphire pump wavelengths. An expanded view showing the signal mirror bandwidth is given in figure 5.

The resonance constraints of the signal field, dictated by our mirror bandwidths will define the tuning scheme that is accessed for a particular QPM period. There are multiple solutions of signal and idler pairs. Starting at degeneracy on one of the curves shown in figure 4 (at $\sim 1.6\mu\text{m}$) the possible signal field solutions of (6.1) track downwards in wavelength and the idler solutions track upwards in wavelength. The signal and idler solutions remain paired for each QPM period. Where multiple pair

solutions exist for one QPM period, the lowest signal wavelength matches the highest idler wavelength (the n_{th} signal solution below the degenerate point will be paired with the n_{th} idler solution above degeneracy). The coatings specified on the ICSRO optics access signal and idler solutions for which $n = 1$, i.e. the 1st paired solutions beyond the degenerate point. An expanded view of figure 4 over the ICSRO mirror bandwidths is given in figure 5.

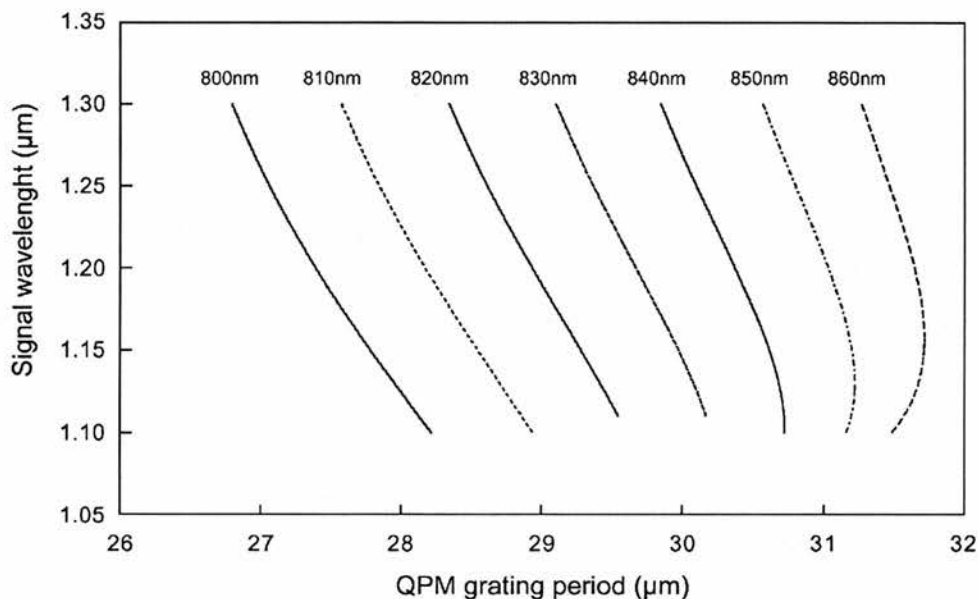


Figure 5. Expanded view of the PPRTA signal QPM wavelengths as a function of grating period.

It can be seen from figures 4 and 5 that the 30 μm grating period specified on the PPRTA crystal is predicted to phase-match the mirror bandwidth range of 1.1-1.3 μm at pump wavelengths around 830-840nm (for the given sellmeier data [4]). This was the desired operating scheme for the intended application. As the ICSRO had previously been extensively characterised for pump wavelengths around 810nm then ideally, a theoretical grating period of $\sim 28.3 \mu\text{m}$ would have allowed ICSRO operation at this wavelength (for which transmissions of the cavity optics were already known). A more useful tuning curve, placing the continuously variable wavelength parameters along the axes and keeping the QPM grating period constant in (6.1), is shown in figure 6 for the 30 μm PPRTA grating specified. This represents the static pump-tuning of the crystal.

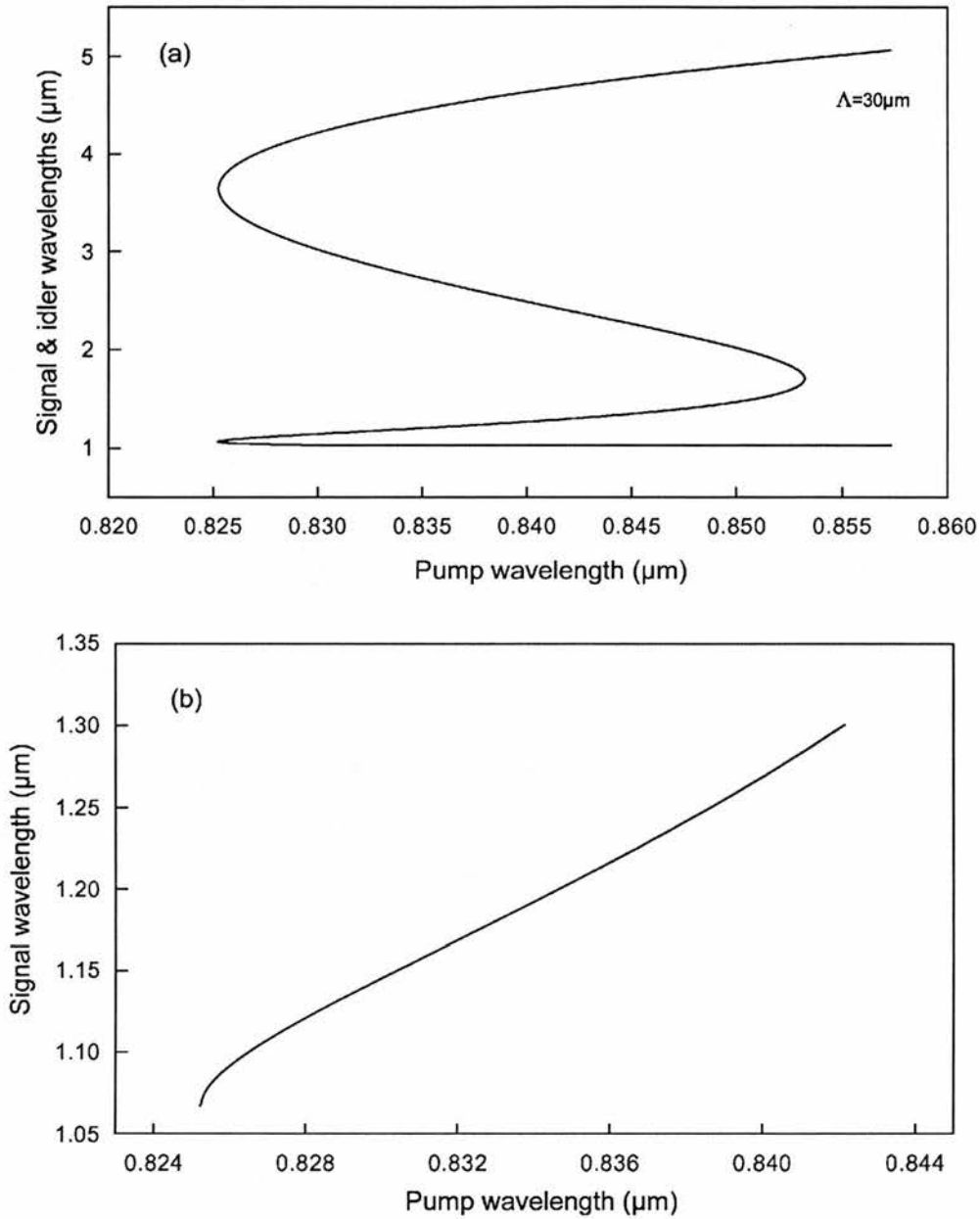


Figure 6. (a) Calculated pump wavelength tuning for 30 μm grating PPRTA sample. (b) Expanded view of resonant signal bandwidth.

The calculated pump tuning range is ~826-842nm corresponding to 16nm. This contrasts greatly with the case of birefringently phase-matched KTA, which had an equivalent 125nm pump tuning range. This reduction in pump bandwidth required to cover the entire signal tuning range and subsequent rapid pump tuning is a common characteristic of QPM schemes.

6.2-2 SRO cavity alignment

Having a common signal cavity geometry to the KTA ICSRO of chapter 4 results in a very similar alignment procedure. The first priority is to correctly align the pump laser cavity and optimise it for power with a suitable output-coupler at M1 and then replace this optic with a pump high-reflector (optimising the pump leakage field). As before, the return residual pump spots from mirror M7 should be overlapped with those reflected from the beamsplitter face opposite the mirror. The slight difference with this procedure is due to the fact that the common cavity stability condition is far more stringent. With only ~1mm of travel over this stability range, care must be taken to obtain the correct separation and also to locate the PPRTA at the centre of the intracavity focus. To obtain parametric oscillation it may be necessary to slowly adjust the separation of mirrors M5 & M6 whilst optimising the pump leakage field. Upon each adjustment the SRO cavity alignment should be attempted.

It is important to highlight the importance of persistence here. The quality of many nonlinear materials is often "dubious" every crystal will have "sweet-spots" and the minor transverse translations of the material through the pump focus can often have significant effects on both pump and SRO performance. Paying close attention to this fact will avoid the observation of a "null-result", or "no-PO" as is has come to be known in the course of this work, for the majority of cases where persistence and numerous cycles of crystal translation and pump optimisation eventually pays dividends.

6.3 PPRTA ICSRO power characteristics

Power characterisation of the PPRTA SRO was limited to 6 W of input argon-ion power. The nature of the tight focus required in the PPRTA and its associated constraints on the stability ranges of both SRO and laser cavities caused a rapid decline in laser and SRO performance at high input powers. This decline is attributed to a small amount of thermal lensing at high input powers and circulating intracavity fields which may alter the relative waist sizes and affect stability. Unfortunately, a combination of time constraints (the crystal being on loan) and the

fact that the optics used were originally obtained with the intent of using much longer nonlinear materials, resulted in little experimental investigation of this effect. The decision was made to characterise the device initially within the linear range of its operation and invest any spare time into the investigation of this effect, especially as it was similar in nature to that observed in KTA at high input powers. To date, this investigation has not been performed.

The power characterisation of the device was undertaken at pump, signal and idler wavelengths of 0.840, 1.18 and 2.92 μm respectively.

6.3-1 Intracavity power

The intracavity power of the Ti:Sapphire laser, with all mirrors specified as highly reflecting, was monitored by calibrated leakage field from mirror M4 at a pump wavelength of 840nm. Calibration of this field was performed by monitoring the leakage for differing levels of output coupling of the Ti:Sapphire laser. The measured intracavity power characteristic is shown in figure 7.

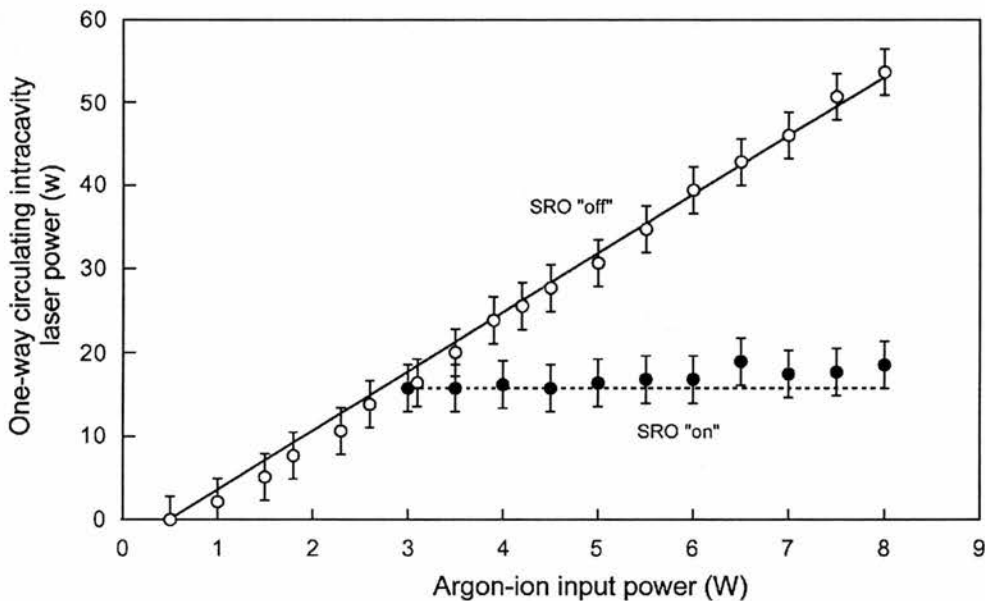


Figure 7. Intracavity power characteristic of the PPRTA ICSRO showing the pump clamping effect above SRO threshold. Open circles show the intracavity field in the absence of SRO operation.

The Ti:Sapphire laser operates with an incident argon-ion threshold of 0.5 W. In the absence of SRO operation, the internal laser field increases linearly with input power to a maximum one-way circulating field of 54 W at 8 W of input power. At an argon-ion input power threshold of 3.0 W the SRO clamps the intracavity laser field at 16 ± 3 W shown in figure 7. The laser field remains clamped for input powers up to 5 W then increases slightly at higher input powers. This is attributed to slight thermal effects in the Ti:Sapphire crystal effecting cavity mode size in the PPRTA crystal.

6.3-2 Output power and efficiency

As with all the standing wave SRO devices studied, the idler field is generated in both directions of interacting fields within the nonlinear crystal. Thus the total measured idler is twice the value of the measured idler through one of the cavity mirrors M5 or M6. The total measured idler (not accounting for the coupling efficiency of the cavity optics) is shown in figure 8.

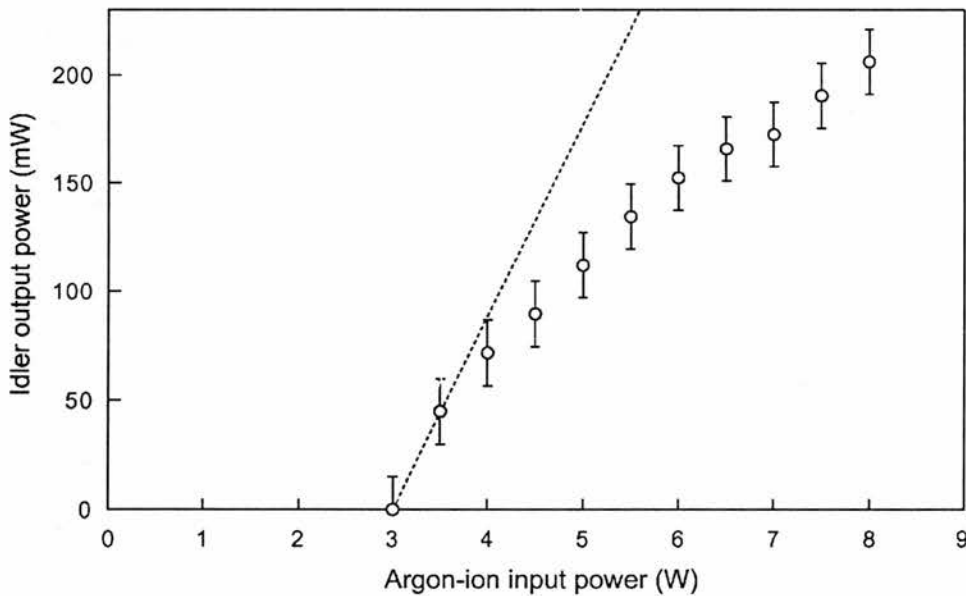


Figure 8. Total measured idler power at $2.92 \mu\text{m}$ as a function of argon-ion input power. The dashed line represents the theoretical prediction of idler output power based on the laser and SRO thresholds and accounting for the idler coupling efficiency η_i from the SRO cavity.

Above SRO threshold, the idler output power increases to a maximum value of 206 mW at 8 W of argon-ion input power. Recalling the expressions for optimum laser output power and downconverted power, namely

$$(P_{out}^L)_{\max} = \gamma_{\max} \left(\sqrt{P_{in}} - \sqrt{P_{th}^L} \right)^2 \quad (6.3)$$

and

$$P_{DC} = \gamma_{\max} (P_{in} - P_{th}^{SRO}) \left(1 - \frac{P_{th}^L}{P_{th}^{SRO}} \right) \quad (6.4)$$

where

$$\gamma_{\max} = \eta_{in} \eta_{abs} \frac{\lambda_{p-in}}{\lambda_p} = 0.49 \quad (6.5)$$

we can deduce the theoretical idler output power. For signal and idler wavelengths λ_s , λ_i of 1.18 μm and 2.92 μm respectively, the total downconverted idler power is given by

$$P_{DC}^i = P_{DC} \left(1 + \frac{\lambda_i}{\lambda_s} \right)^{-1} \quad (6.6)$$

where P_{DC} is calculated from equation (6.4) using measured laser and SRO thresholds of 0.5 and 3.0 W respectively and a maximum input power of 8 W. Note that the value of γ_{\max} here is slightly larger than that measured for the KTA ICSRO which utilised an older Spectra-Physics 171 argon-ion laser. The theoretical idler output power then given by

$$P_{out}^i = P_{DC}^i \eta_i \quad (6.7)$$

where $\eta_i = 0.76$ is the measured idler coupling efficiency from the SRO cavity. Equation (6.7) is shown by the dotted line in figure 8. The maximum theoretical idler output given by (6.7) is 588 mW at 8 W of argon-ion input power (not shown on graph). This is some 380 mW greater than the measured experimental value, a

factor of 2.8 difference. Possibilities for this discrepancy are discussed at the end of this section. The overall downconversion performance is illustrated in figure 9.

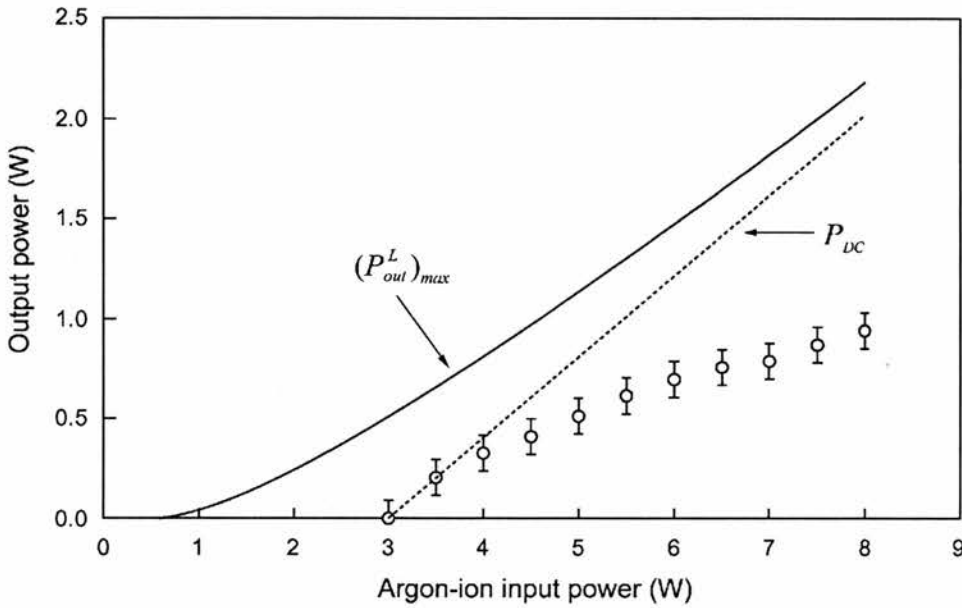


Figure 9. Downconverted power of the PPRTA ICSRO. Theoretical laser and SRO output powers are shown by solid and dashed lines respectively.

It can be seen from figure 9 that the optimum input power required to achieve a maximum 100% downconversion efficiency lies beyond the 8 W input power used for characterisation of the PPRTA ICSRO. Using the power optimising expression

$$P_{in} = \frac{(P_{th}^{SRO})^2}{P_{th}^L} \quad (6.8)$$

the calculated input power for maximum downconversion is 18 W. Whilst an input power of this magnitude was available from the 20-30 argon-ion laser, the device failed to operate above ~12 W of input power, an effect attributed to thermal lensing causing the laser and SRO cavities to become unstable. Within the reduced input power scheme investigated, the Ti:Sapphire laser delivers a maximum theoretical output power of 2.2 W at 8 W of argon-ion input power. Of this power, the SRO can potentially downconvert 2.0 W to the signal and idler fields as shown by the dashed line of figure 9. With the present arrangement, an inferred total downconverted

power of 940 mW was produced leaving a shortfall of 1.08 W from the theoretical prediction. This reduced the downconversion efficiency from a potential 92% at 8 W of argon-ion input power to an measured efficiency of 43% as shown in figure 10.

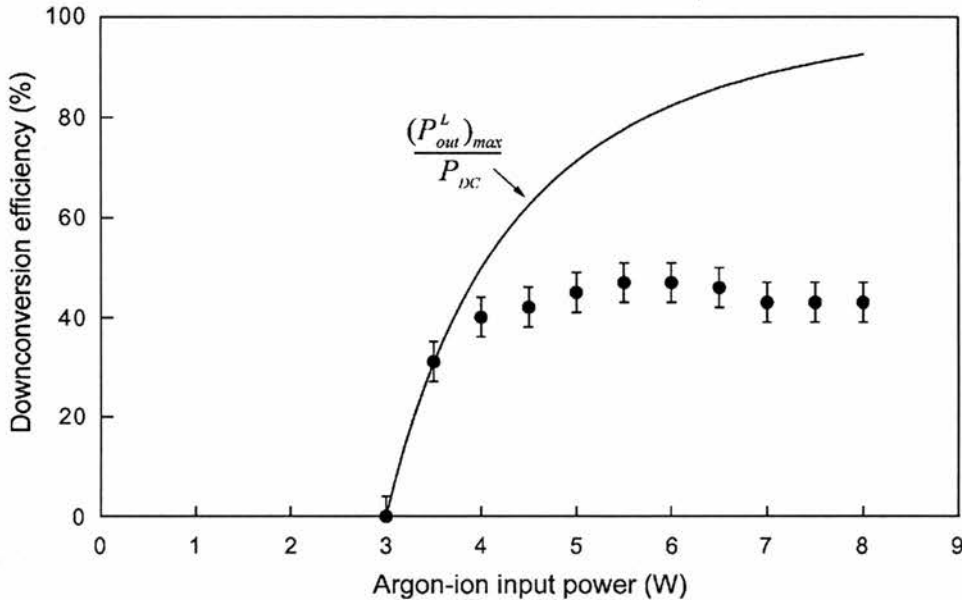


Figure 10. PPRTA ICSRO downconversion efficiency as a function of argon-ion input power. There is a clear drop in efficiency at higher input powers.

Despite the reduction in measured efficiency from that predicted by theory it is still useful to take the wider view that, for a crystal of such a short interaction length, a CW conversion efficiency of 43% is highly respectable. This does not excuse the fact that the deviation from theoretical performance must be accounted for. The fact that the intracavity laser field shown in figure 7 remains roughly clamped over the input power range of the device rules out the possibility that the SRO threshold is simply increasing with input power due to thermal effects. In fact, the intracavity SRO threshold increases to only 18.5 ± 4 W corresponding to an inferred input power threshold of ~ 3.2 W. With this threshold the calculated downconverted power would be reduced from 2.04 W to 1.98 W which does not account for the reduced efficiency observed.

The idler field wavelength was not monitored during power characterisation. The SRO was pumped at a wavelength of 840nm corresponding to the maximum device

output power. At this pump wavelength the signal wavelength was measured to be 1.18 μm corresponding to an idler wavelength of 2.92 μm . Cavity coupling efficiency for the optics was measured with the pump wavelength at 840nm and it was assumed that the idler wavelength was identical to that previously measured. Subsequent tuning analysis of the device, outlined in the next section, showed an erratic tuning behaviour, which casts into doubt the validity of the idler coupling efficiency measurement. Unfortunately time constraints did not allow a complete re-characterisation of the ICSRO power performance. The effects of this erratic tuning on inferred efficiency are outlined in the conclusions of this chapter.

6.4 PPRTA ICSRO spectral properties

As mentioned above the tuning characteristics were erratic and inconsistent. Several attempts were made at obtaining consistent tuning behaviour from the device. The data obtained is displayed graphically in figure 11. Of the datasets that are represented in figure 11, datasets 1 and 5 show simultaneous phase-matching of one or more signal modes. It should be noted that the idler could not be directly measured and the plot of idler wavelength is that inferred from signal and pump wavelength measurements. The wavelengths were measured using a 1m monochromator and a germanium photodiode detector. The monochromator was calibrated using He-Ne lasers operating at 0.633 and 1.152 μm . Each dataset represents a pump tuning range for which the cavity alignment was unchanged. Subsequent re-alignment necessary to operate the ICSRO each time the device was used on separate days, produced a different tuning characteristic. This implies that there was an issue of material quality, possibly an irregular QPM grating geometry coupled with poor crystal homogeneity. Evidence of this is observed in dramatic changes of ICSRO output power with transverse deviation of the nonlinear material through the intracavity pump focus. This erratic tuning may explain a degree of the efficiency shortfall observed in the power characterisation process, as this process assumes a constant cavity coupling parameter for the idler field. The simultaneous phase matching of multiple signal modes for dataset 1 of figure 11 shows a signal wavelength spacing of 17-20nm. This excludes the possibility of the

separate modes being adjacent cavity modes. Another possible explanation is required.

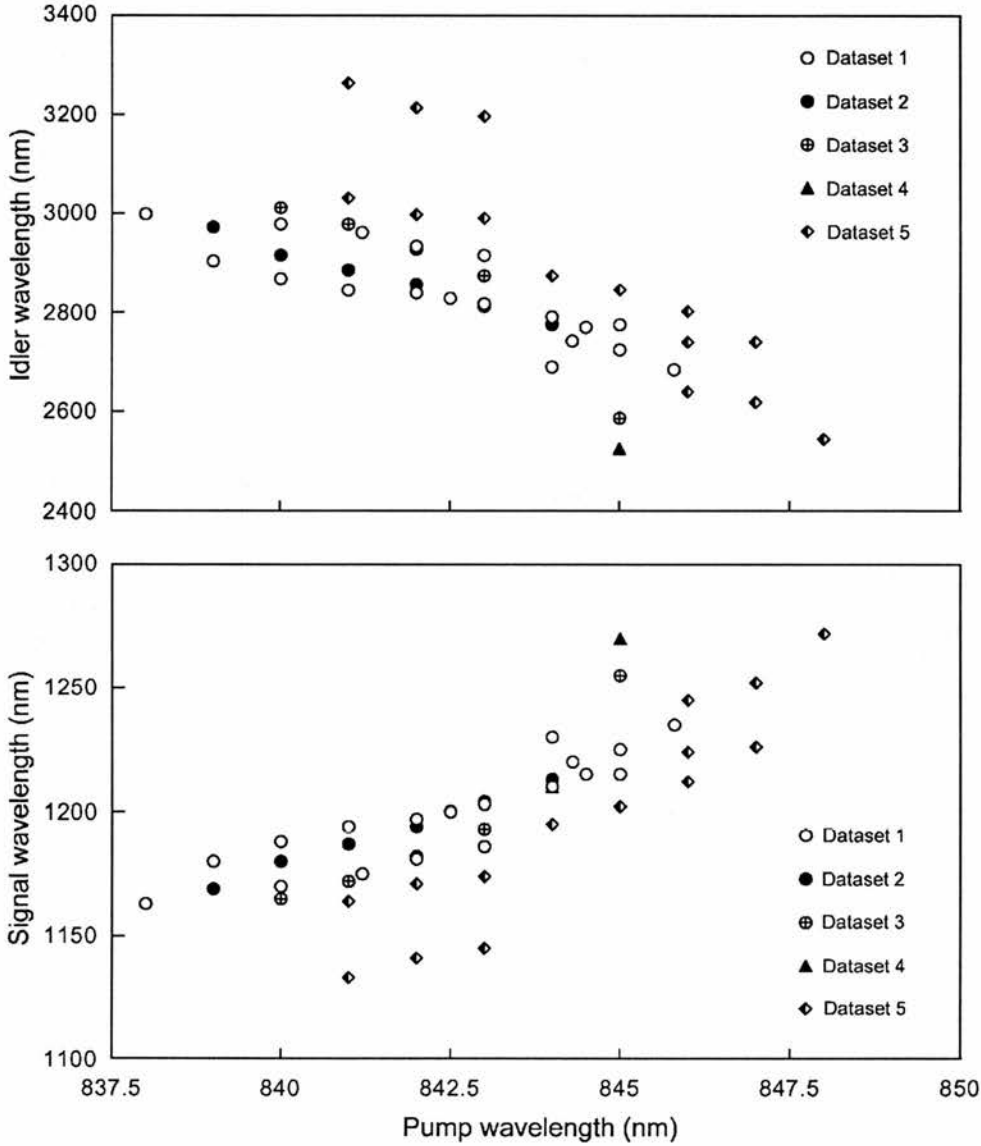


Figure 11. Erratic wavelength characteristics of the PPRTA ICSRO.

A possibility that was investigated was that the pump laser itself may be operating on widely-spaced modes (possibility adjacent peaks of the birefringent tuner). Observation of the pump laser field with an optical spectrum analyser having a resolution of 0.5nm did not show any such modes for the simultaneously phase-matched condition. The adjacent modes of the birefringent tuner are ~10nm apart and thus cover the entire signal pump tuning range of the laser. The possibility of

the signal field accessing the lower branch of the QPM tuning curves (figure 4) is unlikely as this would require a signal mode spacing of far greater than the $\sim 20\text{nm}$ observed. This is best illustrated in figure 12.

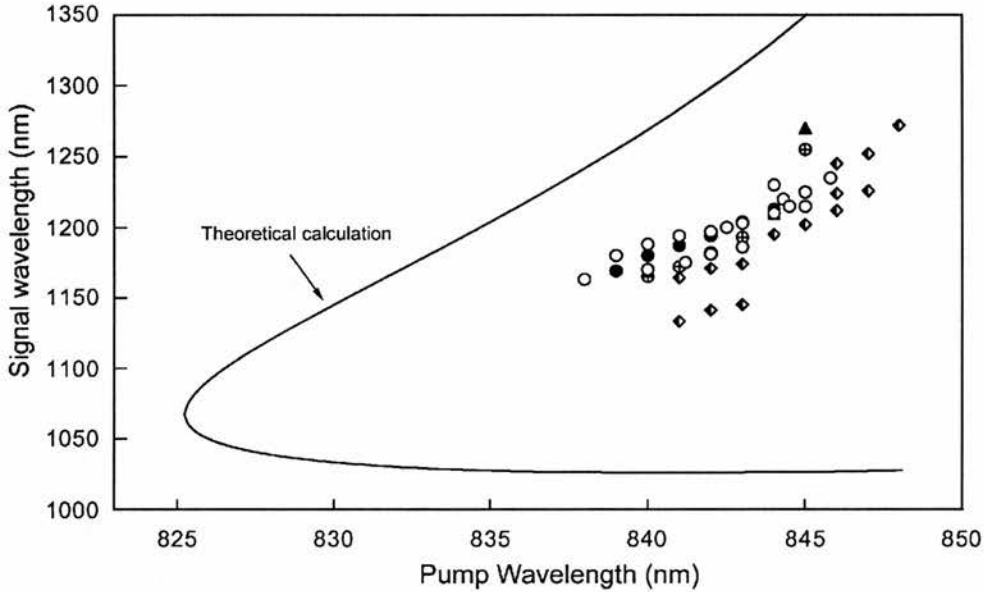


Figure 12. Experimental signal tuning data superimposed onto a plot of the theoretical tuning characteristic as calculated from Sellmeier data.

Although the theoretical curve does not match the tuning curve obtained by experiment, it serves to illustrate the argument discounting the possibility of the signal field simultaneously phase-matching on two solutions of the QPM tuning curve. The form of the theoretical tuning curve would allow a $\sim 20\text{nm}$ spaced signal near the cusp point at 826nm shown in figure 12. Pump tuning away from this point however, would mean that subsequent phase-matched signal pairs would rapidly increase their wavelength separation over a few nanometers of pump tuning. This is not consistent with the observed behaviour of the mode pairs which remain constantly spaced to within $\sim 3\text{nm}$ over a pump tuning range of $\sim 5\text{nm}$. Extending 5nm in pump wavelength from the cusp wavelength of the theoretical curve increases the signal solution spacing by almost 100nm .

Observation of the signal fine frequency spectrum was brief, and showed an unsurprisingly erratic behaviour with multiple mode hops to adjacent cavity modes and operation of the signal wavelength on several simultaneous cavity modes. The

mode spacing of the ~750mm long signal cavity was 200MHz, far smaller than the 4THz spacing observed with the monochromator!

Further characterisation of the PPRTA ICSRO was somewhat hindered by the lapse of the crystal loan period. The crystal was expunged from our system before a full investigation of its frequency properties and also, high input power characteristics could be performed. The concluding remarks of this chapter will leave many important questions unanswered as to the operational characteristics of the PPRTA ICSRO.

6.5 Chapter 6 summary

Continuous-wave parametric oscillation has been observed in the nonlinear material PPRTA. Using a 4.5mm long sample and an intracavity SRO pumping configuration, the device was able to operate ~ 2.5 times above threshold. Measured output power at the idler wavelength exceeded 200 mW for 8 W of input primary pump power. The device operates with a downconversion efficiency of 43% at maximum pump power.

This device was operating at the limits of cavity stability due to the tight intracavity focusing required to achieve threshold conditions. Alternative cavity designs that place both pump and SRO cavities well within their stability ranges would reduce the sensitivity of the ICSRO to thermally induced fluctuations in cavity mode size. For example, specifying mirror M7 with a ~ 3 m radius of curvature and moving it 400mm backwards would double the common stability range and maintain the same signal waist in the PPRTA. Suitable optics to undertake this improvement were not available.

Erratic tuning of the ICSRO signal wavelength casts in doubt the validity of the inferred downconverted power measurement as this is tied to a known cavity coupling efficiency for the idler wave. Experimental tuning would suggest that simply operating the ICSRO at 840nm is no guarantee that the idler wavelength will remain consistently at 2.92 μm . Resolution of this uncertainty would involve re-characterisation of the power performance with intermittent checks on the signal field wavelength to ensure consistency.

The cause of the erratic tuning has yet to be established. The strong dependence on lateral crystal position and output power would suggest the quality of the sample investigated is not optimum. The resultant effects that this may have on the poling process may include a certain degree of non-uniformity of the QPM grating structure within the crystal itself. It would not be surprising for a degree of domain error in the QPM structure to cause unpredictable tuning characteristics. Again, until

this can be investigated it remains pure conjecture and serves only as a guide for future studies of the material itself.

Behind this incomplete picture of the PPRTA ICSRO lies one factor that must not be overlooked. The very fact that CW parametric oscillation could be achieved at all in such a sample is a resounding endorsement of the ICSRO pumping approach. The Ti:Sapphire wavelength tunable pump source has underlined its own versatility in the flexible accommodation of new nonlinear materials. The discrepancy between calculated and experimental tuning ranges may well have been the difference between a working device and a redundant crystal had the Sellmeier equations been utilised to design a grating for a fixed wavelength device.

With an ever-greater emphasis being placed on the development of new nonlinear materials, uncertainty in the design process of the QPM period will inevitably produce errors in the phase-matched schemes derived. The Ti:Sapphire ICSRO by virtue of its frequency agility and ability to surpass multi-Watt level CW thresholds, has an unprecedented capacity to characterise these new materials.

Chapter 6 references

- 1 D. T. Reid, G. T. Kennedy, A. Miller, M. Sibbett and M. Ebrahimzadeh, "Widely tunable, near-to mid-infrared femtosecond and picosecond optical parametric oscillators using periodically poled LiNbO₃ and RbTiOAsO₄," *IEEE Journal of Selected Topics in Quantum Electronics* **4**, 238-248 (1998).
- 2 G. T. Kennedy, D. T. Reid, A. Miller, M. Ebrahimzadeh, H. Karlsson, G. Arvidsson and F. Laurell, "Near- to mid-infrared picosecond optical parametric oscillator based on periodically poled RbTiOAsO₄," *Optics Letters* **23**, 503-505 (1998).
- 3 H. Karlsson, F. Laurell, P. Henriksson and G. Arvidsson, "Frequency-doubling in periodically poled RbTiOAsO₄," *Electronics Letters* **32**, 556 (1996).
- 4 D. L. Fenimore, K. L. Schepler, D. Zelmon, S. Kuck, U. B. Ramabadran, P. Von Richter and D. Small, "Rubidium titanyl arsenate difference-frequency generation and validation of new Sellmeier coefficients," *Journal of the Optical Society of America B-Optical Physics* **13**, 1935 (1996).
- 5 J. R. Han, Y. S. Liu, W. Min and D. Z. Nie, "Flux Growth and Properties of RbTiOAsO₄ (RTA) Crystals," *Journal of Crystal Growth* **128**, 864-866 (1993).

7. ICSRO based on QPM- KTiOPO₄

7.1 Introduction

Paper T.J. Edwards, G.A. Turnbull, M.H. Dunn and M. Ebrahimzadeh, "Continuous-wave, singly-resonant, optical parametric oscillator based on periodically poled KTiOPO₄," *Optics Express*, **6**, 58-63 (2000).

Abstract *A continuous-wave singly-resonant optical parametric oscillator (SRO) has been implemented using a 20 mm long crystal of periodically poled KTiOPO₄ (PPKTP) intracavity-pumped at room temperature within a Ti:Sapphire laser. The device delivers a maximum output power of 455 mW at a non-resonant idler wavelength of 2.47 μm. The 28.5-μm grating PPKTP crystal provides SRO tuning over 1.14-1.27 μm (signal) and 2.23-2.73 μm (idler) limited by optical coating bandwidths and corresponding to a pump tuning range of 805.5-811.2 nm. Temperature tuning of the device generated signal and idler ranges of 1.18-1.26 μm and 2.29-2.57 μm, respectively, corresponding to an average tuning rate of 1.2 nm/degree (signal) and 4.5 nm/degree (idler). Ring-cavity configuration of the device resulted in generation of 115 mW of single-frequency idler output at 2.35 μm.*

This chapter reviews the study of a Ti:Sapphire based ICSRO implemented with a crystal of periodically poled KTiOPO₄ (PPKTP). This work has been published in the above paper. PPKTP offers the significant advantages of QPM grating engineered phase-matching and an enhanced effective nonlinearity due to the ability of the QPM process to access the highest nonlinear d coefficient of the material. The material properties of KTP are well known through its widespread use

as an established birefringently phase-matched nonlinear material [1]. The implementation of the QPM regime for this material offers a further continuous tuning parameter beyond those of the birefringently phase matched case. As all the interacting fields of the QPM parametric process are polarised along a common crystal direction, the absolute change in refractive index with temperature will give rise to a significant amount of temperature tuning. In contrast, the birefringence of the material shows little temperature tuning as all three principal refractive indices show the same relative change in absolute refractive index and thus maintain the index difference that gives rise to birefringence. This opens up an important degree of freedom for the tuning of an ICSRO device that is based on a fixed frequency laser source for which there is often little scope for tuning in other manners due to potential misalignment of the laser itself. The investigation of this material and its associated tuning properties under ICSRO operation forms the greater part of the work outlined in this chapter. In total, three different cavity geometries are employed at different stages of the investigation. The third geometry studies the possibility of implementing the ICSRO device in a ring-ring geometry, that is, a ring cavity SRO operating within a ring cavity Ti:Sapphire laser. The advantages of this configuration are that all the parametrically interacting fields may be made to resonate with single longitudinal modes. Further to this advantage, the uni-directional nature of the fields will give rise to idler output in one direction only, avoiding the problem of bi-directional idler output that characterises the standing-wave ICSRO configuration.

7.2 Experimental design

We shall cover the study of the ring-configured PPKTP ICSRO in the latter part of this chapter as its implementation is significantly different from the standing wave devices encountered previously. The two cavity configurations used to characterise the standing wave device are outlined below.

7.2-1 Power and pump tuning analysis - cavity design

The main body of power and spectral characterisation was undertaken in the familiar standing wave geometry of the modified commercial Schwartz *Titan* laser

[2] as illustrated in figure 1. Cavity optics and their arrangement have been described in chapter 4. The exceptions in the case of the PPKTP ICSRO are, obviously, the location of a 20 mm long PPKTP at the secondary intracavity focus of the Ti:Sapphire laser and the utilisation of a more reliable Spectra-Physics 20-30 argon-ion primary pump laser capable of delivering ~18 W of multi-line green output power.

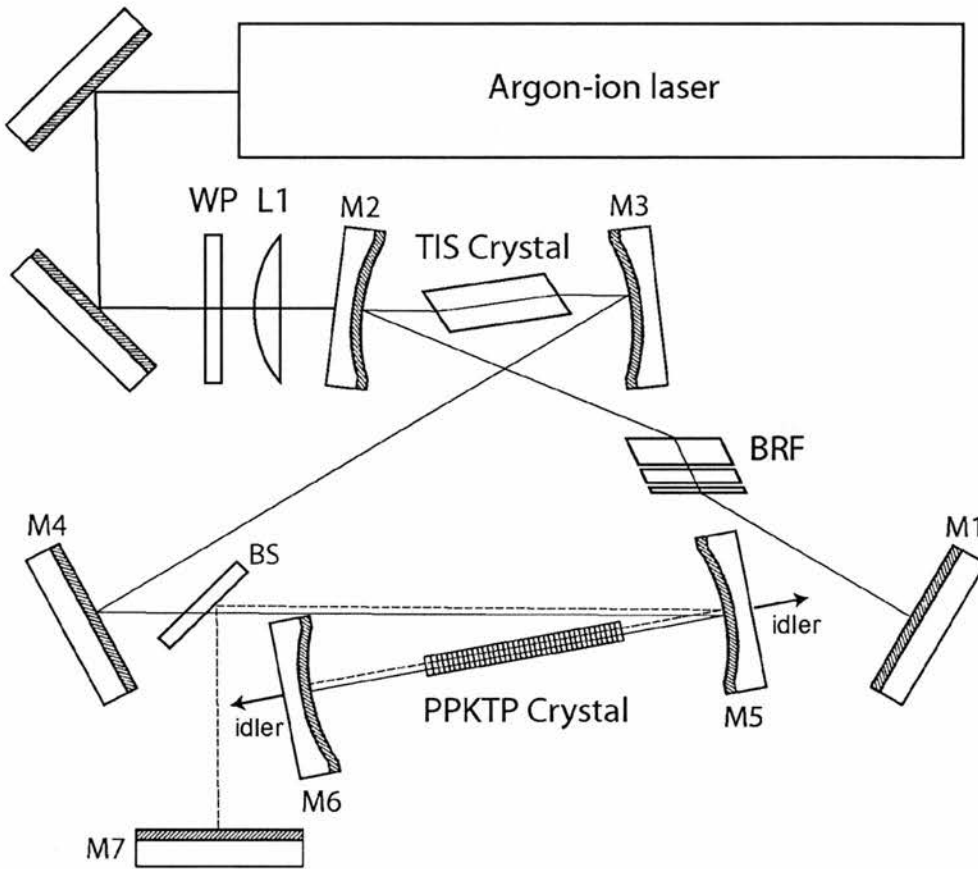


Figure 1. Cavity arrangement of the PPKTP ICSRO for power and pump tuning studies.

The cavity configuration above utilised a 200mm ROC mirror at M5 and M6 which resulted in the common laser and SRO stability condition being satisfied over a mirror separation of ~309-313.5 mm as shown in figure 2. The optimum mirror separation was found to be 312.7 mm which corresponded to a laser mode waist of $35 \times 34 \mu\text{m}$ ($\lambda_p = 808\text{nm}$) and a signal mode waist of $51 \times 52 \mu\text{m}$ ($\lambda_s = 1200\text{nm}$) at

the centre of the PPKTP crystal. The mode waist at the centre of the Ti:Sapphire crystal measured $19 \times 20 \mu\text{m}$. Cavity spacing parameters for the laser and SRO cavities are given in tables 1 and 2 with spacing notation being taken from figures 7(a) and 8(a) of chapter 3.

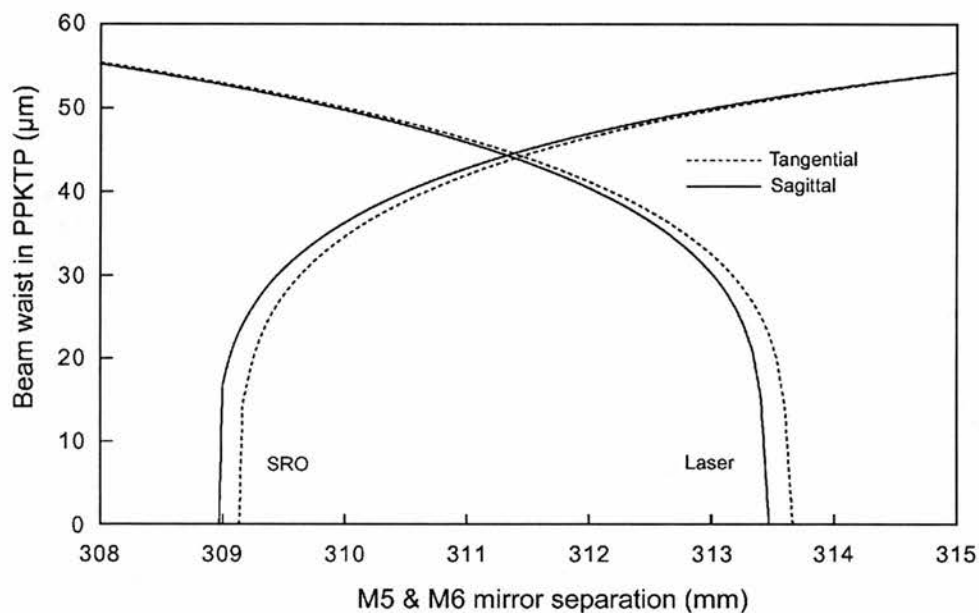


Figure 2. Laser and SRO waist sizes in PPKTP crystal as a function of mirror separation.

Ti:Sapphire Laser Cavity Parameters I

<i>Mirror</i>	<i>ROC (mm)</i>	<i>Angle (Deg)</i>	<i>Separation</i>	<i>Distance (mm)</i>
M1	∞	N/A	D1	645.0
M2	100	9.8	D2	48.7
			LX1	7.6
M3	100	9.8	D3	48.7
M4	∞	N/A	D4	700.0
			D5	786.0
M5	200	2	D6	98.3
			LX2	20
M6	200	0	D7	194.4

Table 1. Ti:Sapphire laser cavity parameters of the layout illustrated in figure 1. Separation notation refers to figure 7(a) of chapter 3.

SRO Cavity Parameters I				
Mirror	ROC (mm)	Angle (Deg)	Separation	Distance (mm)
M7	∞	N/A	D1	420.0
M5	200	2	D2	370.0
			D3	98.3
M6	200	0	LX2	20
			D4	194.4

Table 2. SRO Cavity parameters of the layout illustrated in figure 1. Separation notation refers to figure 8(a) of chapter 3.

7.2-2 Temperature tuning analysis - cavity design

The cavity layout used to study the temperature tuning characteristics of the PPKTP ICSRO had to accommodate a temperature-controlled oven situated around the nonlinear material. This rendered the cavity layout described in figure 1 inoperable. The commercial Eskma oven had a diameter of some 50mm, increasing the fold angle of the SRO branch of the laser cavity such that the collimated arm of the cavity passes the main bulk of the oven would introduce a prohibitive amount of astigmatism to the cavity mode. For this reason, the experimental temperature tuning of the ICSRO was undertaken with a modified laser and SRO cavity design as shown in figure 3.

In this design, a second intracavity laser focus is introduced through the use of an intracavity lens L2 with a focal length of 100 mm. The lens was broad-band anti-reflection coated for the resonant pump field only and placed external to the resonant SRO cavity. This enabled the resonant laser mode to pass through the centre of the oven containing the PPKTP crystal with the signal field being discriminated from that of the pump with the use of a 45° beamsplitter (identical to the optic used in the cavity design of figure 1). This design liberates the SRO cavity from utilising the common focusing mirror M5 in figure 1, allowing greater flexibility over the stability range. Thus, the common cavity stability criterion may be satisfied for the SRO cavity over any stability variation of the laser. Clearly, the essential issue that must be satisfied, beyond that of cavity stability, is that appropriate signal and laser mode sizes must be maintained at the centre of the nonlinear material.

For the purpose of this experiment, the intracavity lens was chosen to produce an identical laser waist to that formed by mirror M5 in figure 1. In practice this mode will be slightly less astigmatic as, correctly aligned, lens L2 should not introduce astigmatism to the resonant laser mode.

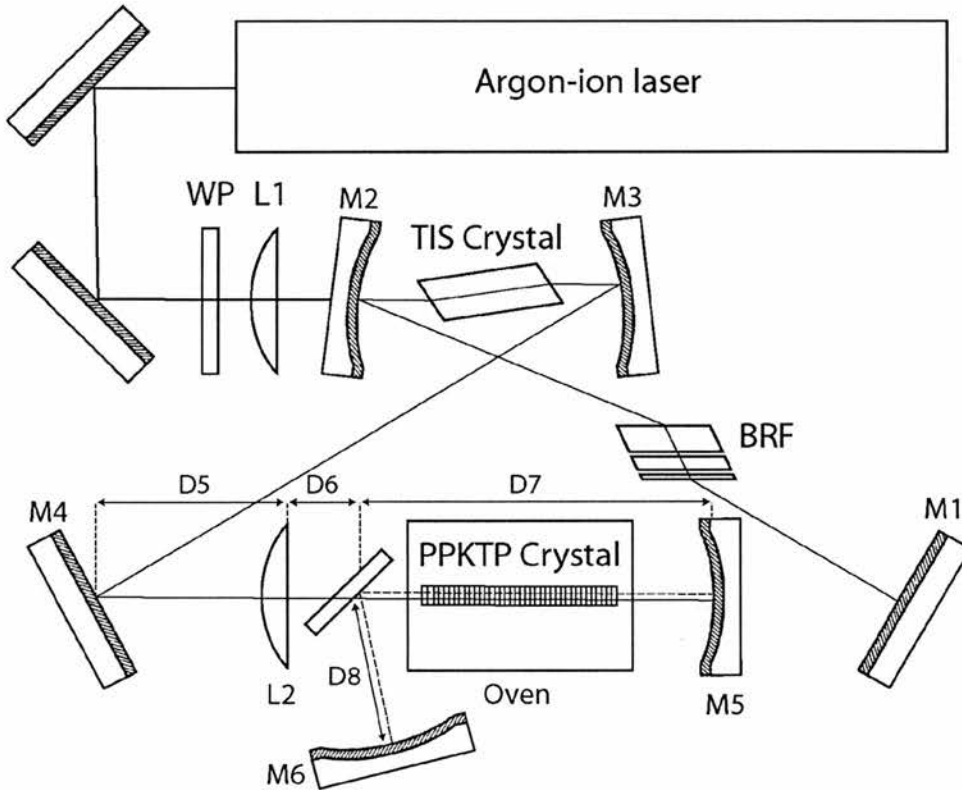


Figure 3. Modified ICSRO cavity design for the study of PPKTP temperature tunability.

A comparison of figures 1 and 3 shows that, from mirrors M1 to M4, the laser cavity arrangement is identical. The only cavity modifications occur in the cavity branch from M4 to M5&6. Cavity spacing parameters are given in tables 2 and 3. At these optimum separations astigmatism is negligible and the respective pump and signal waist sizes are $35\ \mu\text{m}$ and $57\ \mu\text{m}$ at the centre of the PPKTP crystal. Despite the greater flexibility of the SRO cavity design shown in figure 3, it should be noted that the cavity spacing parameters of table 4 place the SRO cavity close to the edge of stability in order to minimise the signal waist within the PPKTP crystal. When operating well within the stability range of the SRO cavity the signal waist increases

to approximately twice its value for optimum mirror separation. With the exception of the intracavity lens L2, all optical components are identical to those used in previous experiments.

Ti:Sapphire Laser Cavity Parameters II				
<i>Mirror</i>	<i>ROC (mm)</i>	<i>Angle (Deg)</i>	<i>Separation</i>	<i>Distance (mm)</i>
M1	∞	N/A	D1	645.0
M2	100	9.8	D2	48.7
			LX1	7.6
M3	100	9.8	D3	48.7
M4	∞	N/A	D4	700.0
L2	f=100		D5	586.0
			D6	50.0
M5	200	0	D7	262.7

Table 3. Ti:Sapphire laser cavity parameters of the layout illustrated in figure 3. Separation notation to mirror M4 refers to figure 7(a) of chapter 3. All other separations refer to figure 3.

OPO Cavity Parameters II				
<i>Mirror</i>	<i>ROC (mm)</i>	<i>Angle (Deg)</i>	<i>Separation</i>	<i>Distance (mm)</i>
M6	100	0	D8	45.2
M5	200	0	D7	262.7

Table 4. SRO Cavity parameters of the layout illustrated in figure 3.

7.2-3 Nonlinear material

Potassium titanyl phosphate (KTP) is well established as a birefringent nonlinear material [1]. With good thermal properties, high damage threshold and excellent optical homogeneity KTP is an admirable candidate for promotion to the QPM operating regime. A significant advantage of this material over QPM LiNbO₃ (PPLN) is its resistance to photorefractive damage at room temperature and low coercive field. These factors, coupled with a simple lattice structure make the domain inversion and subsequent use of this material a good deal less complicated. Minor

drawbacks of the material itself include a relatively high ionic conductivity, which hinders domain resolution and promotes high electrical currents during the poling process. This can be resolved through the use of Rb^+ ionic doping to reduce the number of mobile K^+ ions in the crystal lattice [3]. Perhaps more serious, for tunable mid-infrared applications, are the two absorption features of the material. A narrow OH^- absorption at $2.8 \mu\text{m}$ and a more pronounced lattice absorption from 3.8 to $4.5 \mu\text{m}$ must be excluded from operational signal and idler tuning bandwidths if maximum efficiency is to be maintained. Of course, the very nature of the QPM process itself allows the phase-matched process to be engineered away from these material absorption bands.

The PPKTP crystal used in the experiments outlined in this chapter was obtained from the Department of Physics, Royal Institute of Optical Technology, Sweden, and prepared according to reference [3]. Dimensions and crystal orientation relative to the incident pump laser polarisation are shown in figure 4.

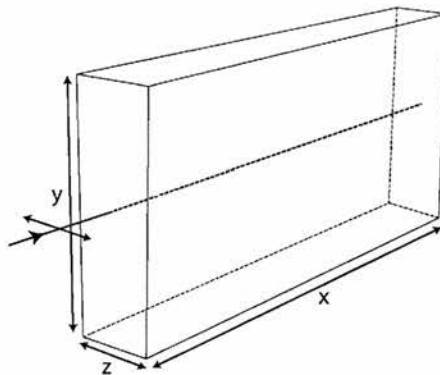


Figure 4. PPKTP showing orientation of the pump polarisation along the z axis of the crystal. Dimensions in the $x \times y \times z$ crystallographic directions are $20 \times 3 \times 1 \text{ mm}$. The single-grating period is $\Lambda = 28.5 \mu\text{m}$.

The grating period of the PPKTP was chosen to phase-match a pump wavelength of 810nm to a resonant signal wavelength of $1.2 \mu\text{m}$. This placed the phase-matched condition at the centre of the signal mirror bandwidth. Using the sellmeier data of Dyakov *et al* [4] a grating period of $28.5 \mu\text{m}$ was calculated from the following first-order QPM phase-matching equation

$$\Delta k = \frac{n_z(\lambda_p)}{\lambda_p} - \frac{n_z(\lambda_s)}{\lambda_s} - \frac{n_z\left(\frac{\lambda_p\lambda_s}{\lambda_s - \lambda_p}\right)}{\left(\frac{\lambda_p\lambda_s}{\lambda_s - \lambda_p}\right)} - \frac{1}{\Lambda} = 0 \quad (7.1)$$

As with its close crystal family member PPRTA, PPKTP is poled to access the highest d_{33} nonlinear coefficient along the crystallographic z axis. Thus only sellmeier data for $n_z(\lambda)$ is required. A plot of signal and idler wavelengths as a function of grating period for a range of pump wavelengths is shown in figure 5.

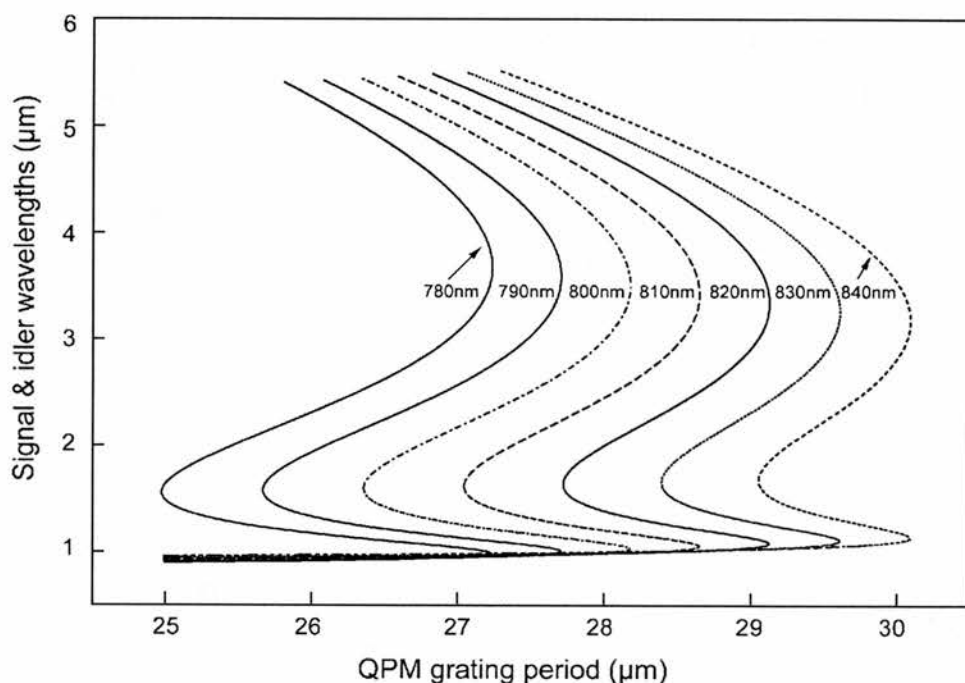


Figure 5. Calculated signal and idler wavelengths as a function of QPM grating period for PPKTP using sellmeier data of reference [4].

It can be seen from figure 5 that a small variation in grating period can have a dramatic effect on the phase-matched condition. Specifying a particular idler grating period for a fixed frequency source requires sub-micron accuracy for the poling mask. Fortunately PPKTP has a respectable amount of temperature tunability as will be seen later in this chapter. This allows for errors in the grating period design to be tuned onto phase-matching. Avoiding the necessity to temperature tune the

nonlinear material, the Ti:Sapphire ICSRO can quickly accommodate such errors via the tunability of the pump laser. To illustrate one of the major problems faced when designing a particular QPM grating scheme for PPKTP, a plot of the pump tuning characteristic of PPKTP having a grating of $28.5 \mu\text{m}$ is shown in figure 6 for several published sources of sellmeier data.

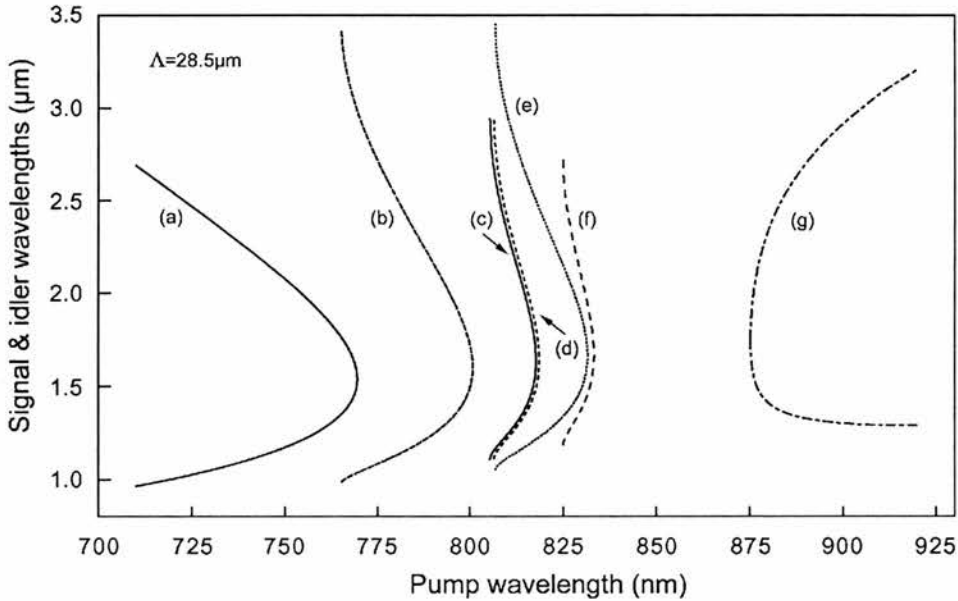


Figure 6. Pump tuning characteristic of a $28.5 \mu\text{m}$ grating PPKTP crystal calculated from the following sellmeier data: (a) Liao et al [5], (b) Anthon et al. [6], (c) Vanherzeele et al. [7], (d) Kato [8], (e) Dyakov et al. [4], (f) Fradkin et al. [9] and Fan et al. [10].

Clearly, care must be taken to select the correct sellmeier source if mistakes are to be avoided. Examination of the experimental data range over which the sellmeier equations have been fitted is essential. In this way, only those equations fitted to experimental data within the desired phase matching regime should be considered. Following this general rule does not provide a conclusive candidate from among the published data. For the phase-matched pump and signal ranges of this experiment, the four centrally placed curves in figure 6 are potential tuning curves. An expanded view of these calculated curves is shown in figure 7. Of the four calculated sellmeier tuning curves shown in figure 7, the curve derived from the data of Vanherzeele et al. [7] is found to most closely match the experimental data of the ICSRO experiments outlined in this chapter. It should be noted that this is not the actual

sellmeier reference from which the design of the 28.5 μm QPM grating was derived. In the context of fixed frequency pump sources, this inherent uncertainty in the design process of the QPM period may well give rise to wide deviations from the desired phase-matching regime.

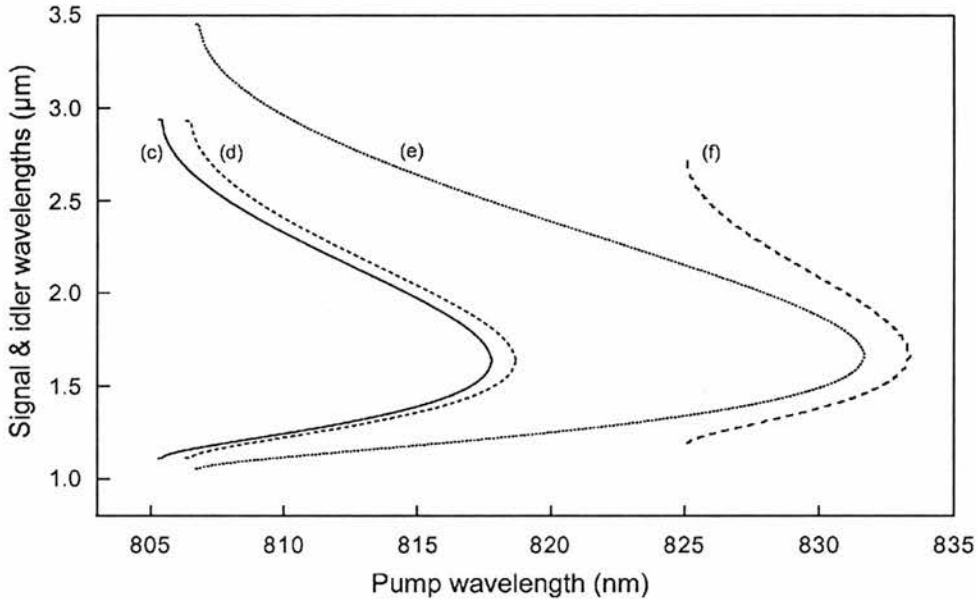


Figure 7. Expanded view of figure 6 showing the four best sellmeier candidates for phase-matching calculations of the 28.5 μm PPKTP sample. (c) Vanherzeele *et al.* [7], (d) Kato [8], (e) Dyakov *et al.* [4], (f) Fradkin *et al.* [9]

The first order QPM interaction of the PPKTP sample is designed to access the highest d coefficient of the material. In the case of PPKTP this is the d_{33} coefficient with a common value of $d_{33} \approx 16 \text{ pm/V}$ [11, 12]. This gives an effective first order QPM nonlinear coefficient of $d_{\text{eff}} \approx 2/\pi \times 16 \text{ pm/V} \approx 10 \text{ pm/V}$, which represents the highest expected value of d_{eff} . In practice, the experimentally observed d_{eff} may be as low as $d_{\text{eff}} \approx 5 \text{ pm/V}$ [13]. The temperature dependence of the indices of refraction for KTP are taken from published literature [14, 15] and may be used to model the temperature tuning characteristics of PPKTP given that all the parametrically interacting waves are polarised along the z-axis. Where appropriate, the theoretical calculations of temperature tuning will be presented in the relevant section of this chapter.

7.2-3 SRO cavity alignment

The cavity geometry of figure 1 follows an alignment procedure identical to that of the KTA ICSRO of chapter 4. Here alignment is further aided by the QPM high-order phase-matching process giving rise to a small amount of visible output that is collinear with the incident pump field within the nonlinear crystal. Rough alignment can be made by retro-reflecting the doubled Ti:Sapphire field (@~400nm) from M7 (figure 1) back towards the beamsplitter. In a few cases this procedure alone is enough to bring the SRO into alignment. Confirmation of SRO action is similarly straightforward as a small amount of SHG at the signal wavelength will produce orange light that is easily visible to the naked eye. Sum-frequency generation of the pump and signal wavelengths will produce a small amount of blue-green output which, by accident, coincides with wavelength output of the argon-ion laser. This makes it hard to differentiate from the residual argon-ion light inside the laser cavity. It is worth noting that, for a photon arising from transitions inside the argon laser, it has been quite a journey through the physical processes of the experimental system as a whole to end up being converted back to a green photon once more. This process has a wall-plug efficiency of $\sim 10^{-8}$!

The narrow pump-tuning range of the PPKTP crystal (~10nm) requires the pump laser to be tuned to the centre of this range before alignment is attempted. Clearly, once the pump tuning range has been established this does not present a great problem. Initially, the only guideline as to where the SRO will operate over the pump tuning range is that provided from sellmeier data. Errors in the predictions of the sellmeier data can give rise to many fruitless hours attempting to align the SRO at a pump wavelength for which it has no intention of working. If the device fails to work where predicted, the best course of action is systematic incremental tuning of the pump together with systematic alignment. This can take a long time.

Alignment of the cavity of figure 2 follows the procedure used for the PPLN ICSRO in chapter 5. This cavity should be aligned once the operating wavelength has been established with the more simply aligned cavity of figure 1. This is a prime reason to perform this temperature tuning experiment after the power and pump tuning characterisation of the ICSRO.

7.3 PPKTP ICSRO power characteristics

Power measurements for the PPKTP ICSRO were performed at a pump wavelength of 808nm which corresponded to the maximum idler output at 2.47 μm . The corresponding signal wavelength was measured as 1.2 μm . Argon-ion input power was limited to 10 W as the ICSRO operated above maximum efficiency for this input power. The power characterisation was limited to the cavity layout shown in figure 1. No power characterisation was performed for the cavity layout shown in figure 2, which was implemented to accommodate the temperature controlled oven for temperature tuning experiments. Thus, all power measurements were undertaken at room temperature.

7.3-1 Intracavity power

The intracavity power performance of the PPKTP ICSRO, with all SRO and laser mirrors specified as highly reflecting, is shown in figure 8.

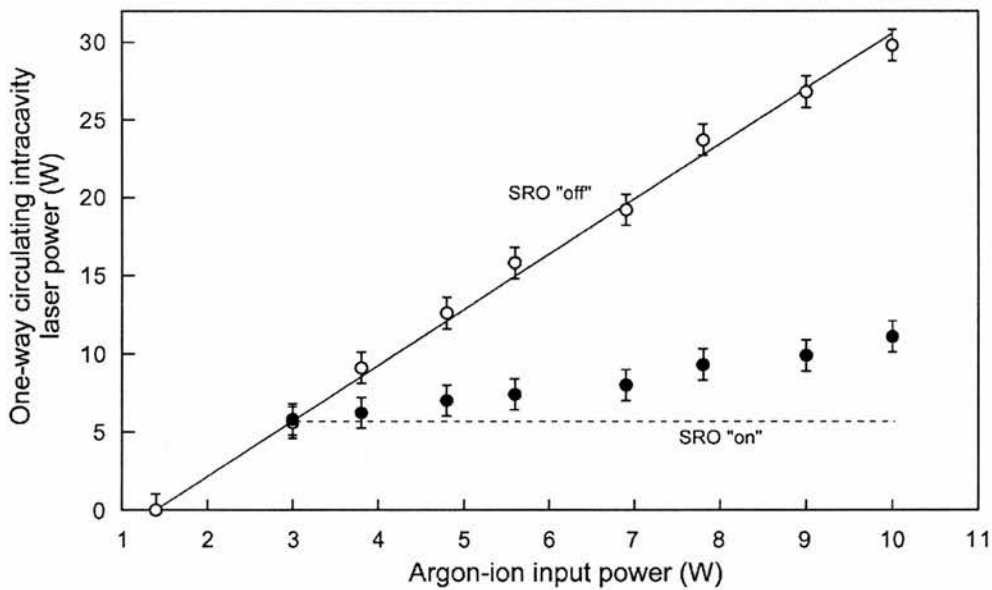


Figure 8. Intracavity power characteristic of the PPKTP ICSRO showing a slight increase in pump clamping above SRO threshold with increased input power. Open circles show the intracavity laser power in the absence of SRO operation.

SRO operation commences at 6 ± 1 W of circulating intracavity laser power. This corresponds to an incident argon-ion input power of 3 W. Above SRO threshold, the clamped field slowly increases to a maximum of 11 ± 1 W. This is not consistent with the SRO theoretical analysis of chapter 3 (shown by the dotted line in figure 8). The increased clamping field indicates that the SRO threshold is increasing with incident argon-ion input power. A possible explanation for this increase is a slight increase in the pump waist size in the PPKTP due to a small amount of thermal lensing in the Ti:Sapphire crystal. Again, the true nature of this effect remains the subject of debate and is, at the time of writing, a matter of conjecture. The 20-30 argon-ion laser was operating well below its maximum output and showed no signs of beam-degradation at 10 W. The laser threshold was found to be 1.4 W of argon-ion input power. This indicates a high insertion loss of the PPTKP crystal at the pump wavelength when compared to other nonlinear materials investigated in this thesis.

7.3-2 Output power and efficiency

The total measured idler field - accounting for the two-way output of the standing-wave configuration - is shown for various argon-ion input powers in figure 9.

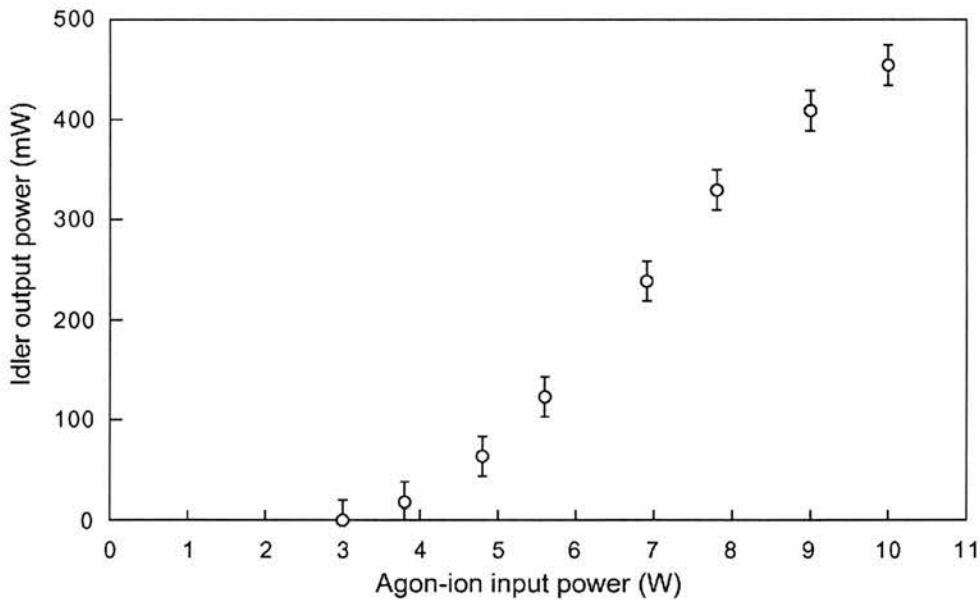


Figure 9. Total measured idler power as a function of argon-ion input power.

The maximum idler output power at $2.47 \mu\text{m}$ is 455 mW for 10 W of argon-ion pump power. With a cavity coupling efficiency of $\eta_i = 0.91$, this corresponds to a total generated idler power P_{DC}^i , of 500 mW . Thus, the total downconverted power may be found using the equation

$$P_{DC} = P_{DC}^i \left(1 + \frac{\lambda_i}{\lambda_s} \right) \quad (7.2)$$

where $\lambda_s = 1.2 \mu\text{m}$ and $\lambda_i = 2.47 \mu\text{m}$. The maximum total downconverted power at 10 W of incident pump power is 1.53 W . The downconversion performance of the PPKTP SRO is shown in figure 10.

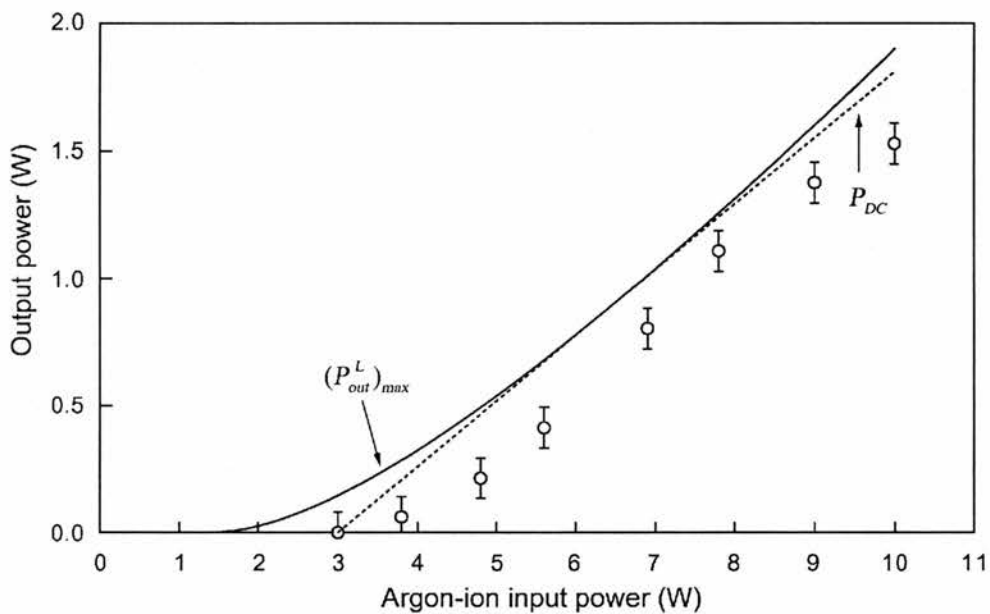


Figure 10. Downconverted power of the PPKTP ICSRO. Theoretical laser and SRO output powers are shown by solid and dotted lines respectively.

Examination of figure 10 shows that, for the first time in the experimental work presented in this thesis, the input power condition for 100% downconversion of the optimum laser output power falls within the pump power range. The familiar equation describing the optimum pumping input power P_{in} for a given pump and SRO input power threshold is

$$P_{in} = \frac{(P_{th}^{SRO})^2}{P_{th}^L} \quad (7.3)$$

For laser and SRO thresholds of 1.4 W and 3 W respectively, the optimum input power given by (7.3) is 6.4 W. This means that the SRO is operating above the optimum level for an input power of 10 W suggesting that the SRO threshold should be increased by utilising a suitable output-coupler. For a measured signal cavity round trip loss of $2.8 \pm 0.6\%$ the appropriate choice of output coupler to satisfy (7.3) for 10 W of input power is a 99.4% reflective mirror. This would raise the SRO threshold to 3.7 W and also provide useful output at the signal wavelength. At the time the study was undertaken a suitable output coupler was not available. The optic previously used in the KTA ICSRO of chapter 4 had become integrated into a pulsed laser system at the valid discretion of the optic's owner. The realisation of this useful output-coupling potential has led to the possibility of implementing an intracavity SHG scheme for the signal field. A suitable QPM engineered crystal has been designed and purchased for this purpose. Intracavity SHG and SFM process for the PPKTP ICSRO will be discussed in the concluding chapter.

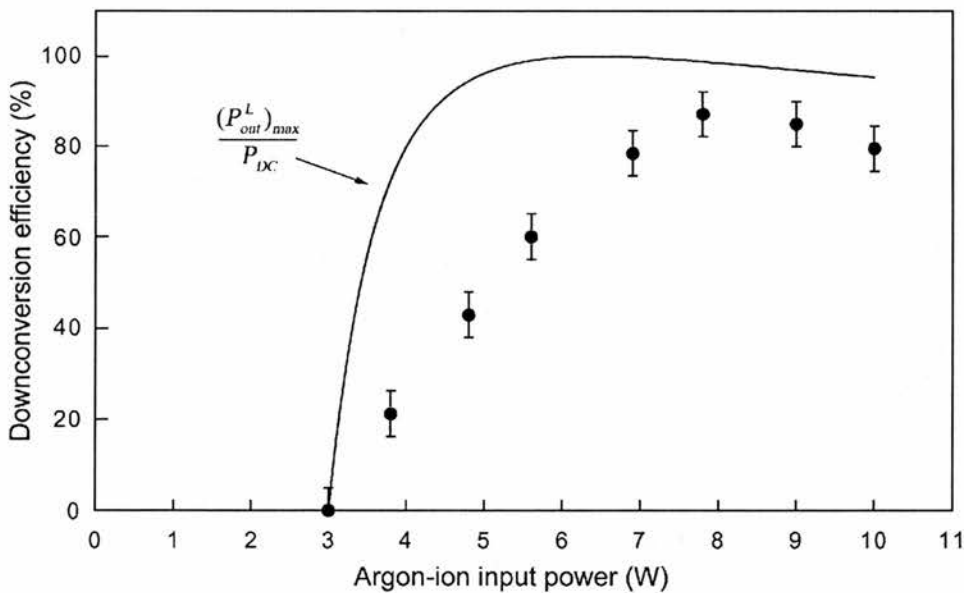


Figure 11. PPKTP ICSRO downconversion efficiency.

The efficiency of the PPKTP ICSRO under the present operating configuration is shown in figure 11. The efficiency reaches a maximum of 87% at 7.8 W of input power. At higher input powers the efficiency decreases as the SRO is operating above the optimum pumping condition. Discrepancies between the observed and predicted efficiencies are attributed to the steady increase in SRO threshold indicated by figure 8.

The present discussion of the ICSRO power output concludes with the simple observation that the PPKTP ICSRO shows ample potential for the output-coupling of the signal field by some means. This could be via a conventional output coupler or, more interestingly, via an internal SHG process within the SRO cavity itself. The output of such a SHG process would reflect the tunability of the signal field, given a degree of tunability of the SHG phase-matching. As we shall see in the next section, a PPKTP SHG scheme will show a useful degree of temperature tunability due to the common polarisation of all the interacting fields of the parametric process..

7.4 PPKTP ICSRO spectral characteristics

The pump tuning data detailed in this section was measured with the ICSRO configured as shown in figure 1. Measurements were made for the pump and signal wavelengths with the idler wavelength being inferred from these measurements. Direct measurement of the idler wavelength was not made due to the lack of a suitable detector at $>2 \mu\text{m}$. Conservation of energy considerations makes the deduction of the idler wavelength from signal and pump measurement a valid method.

7.4-1 Pump tuning

The pump tuning curves for room temperature operation are shown in figure 12. Pump tuning is relatively rapid when compared to the birefringently phase-matched ICSRO of chapter 4. For a pump tuning range of 805.5 to 811.2nm the signal wavelength covers almost the entire SRO mirror bandwidth from 1.14 - 1.26 μm

corresponding to an idler tuning range of 2.23 - 2.73 μm . The closest match to the published sellmeier data was found to be that of reference [7], a calculated tuning plot derived from this source is shown alongside the experimental data in figure 12. To place the excellent agreement that the experimental data shows to the sellmeier data of reference [7] in its wider context, figure 13 shows the previous sellmeier plots of figure 7 together with the experimental data of figure 12.

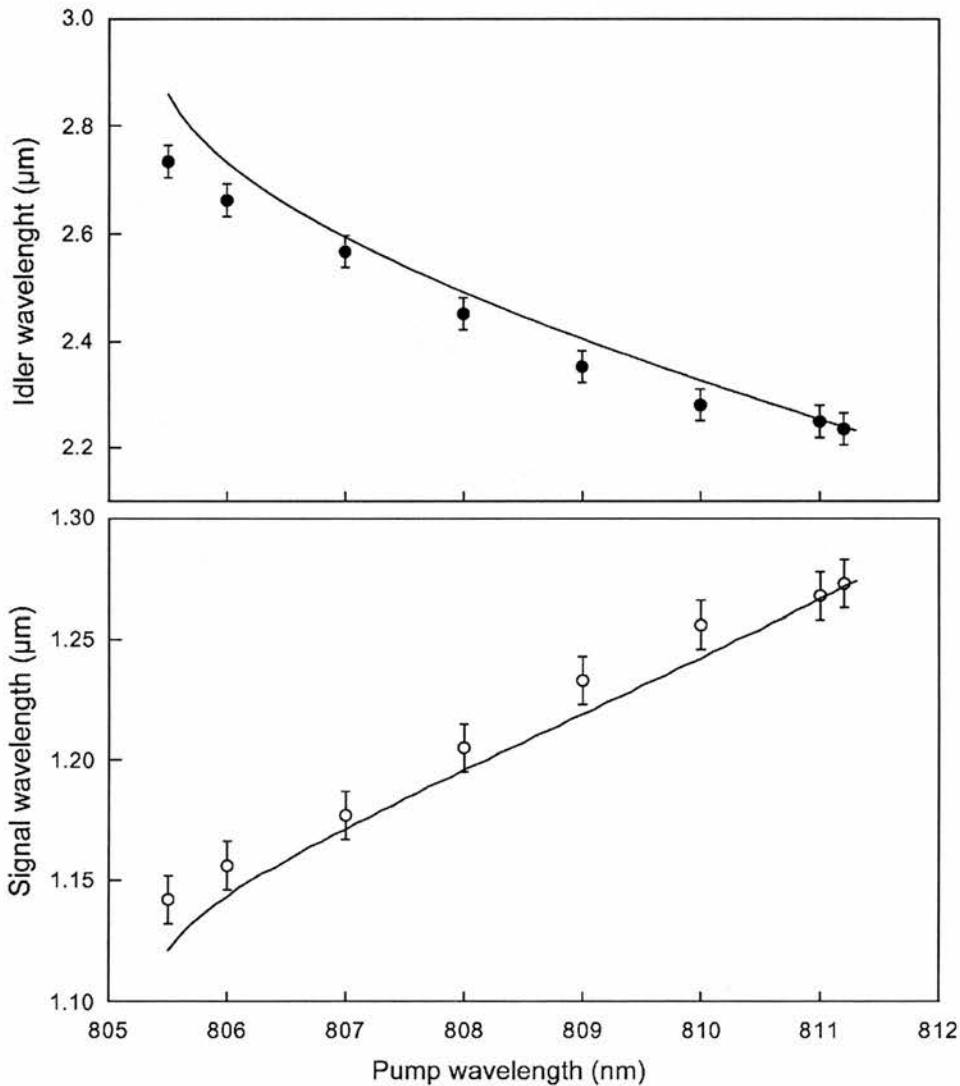


Figure 12. Pump tuning data at room temperature for the PPKTP ICSRO. The solid line represents theoretical tuning calculated from the sellmeier data of Vanherzeele *et al.* [7].

The pump tuning data presented in figures 12 and 13 have a wider significance than the simple observation of yet more pump tuning of an Ti:Sapphire ICSRO. That such a device is widely tunable is indeed a notable characteristic, amply demonstrated in the experimental work of the previous chapters. More importantly, here, useful tuning data is presented that covers a wavelength range for which there is a wide variation in the predicted tuning performance of PPKTP as figure 13 illustrates. With increasing interest being shown in the relatively new QPM phosphates and arsenates, tuning data is a vital commodity for the design process of the QPM grating period. For QPM gratings designed for near to mid-infrared applications in PPKTP the data presented here is a timely contribution to the QPM design process. As previously stressed, this becomes far more important where the pump source shows little or no tunability and cannot accommodate errors to the same degree as the Ti:Sapphire laser.

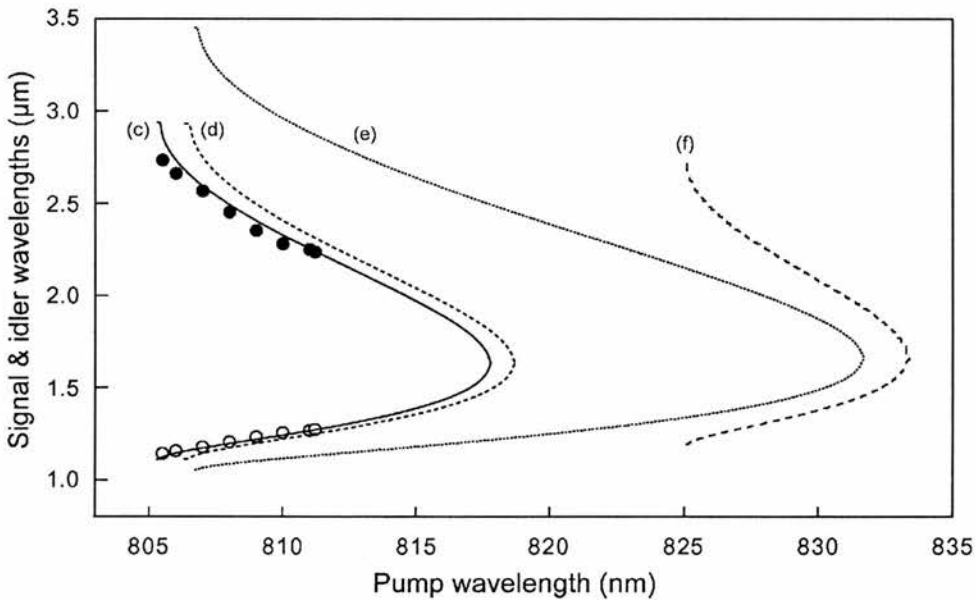


Figure 13. Pump tuning data superimposed upon the plot of figure 7. The labelled plots correspond to the following sellmeier data: (c) Vanherzeele *et al.* [7], (d) Kato [8], (e) Dyakov *et al.* [4], (f) Fradkin *et al.* [9].

Another point worthy of note regards the rapid pump tuning of the device. For one nanometer of pump tuning range, the idler field varies over almost 100nm. This presents attractive possibilities for utilising PPKTP in a high-power 810nm-diode pumped DRO or pump enhanced SRO. With the diode configured in an external-

feedback cavity design, a single-frequency idler source with wide pump tunability could be realised. Of course, another alternative would be an ICSRO configured in a ring-ring geometry as discussed later in this chapter.

7.4-2 Temperature tuning

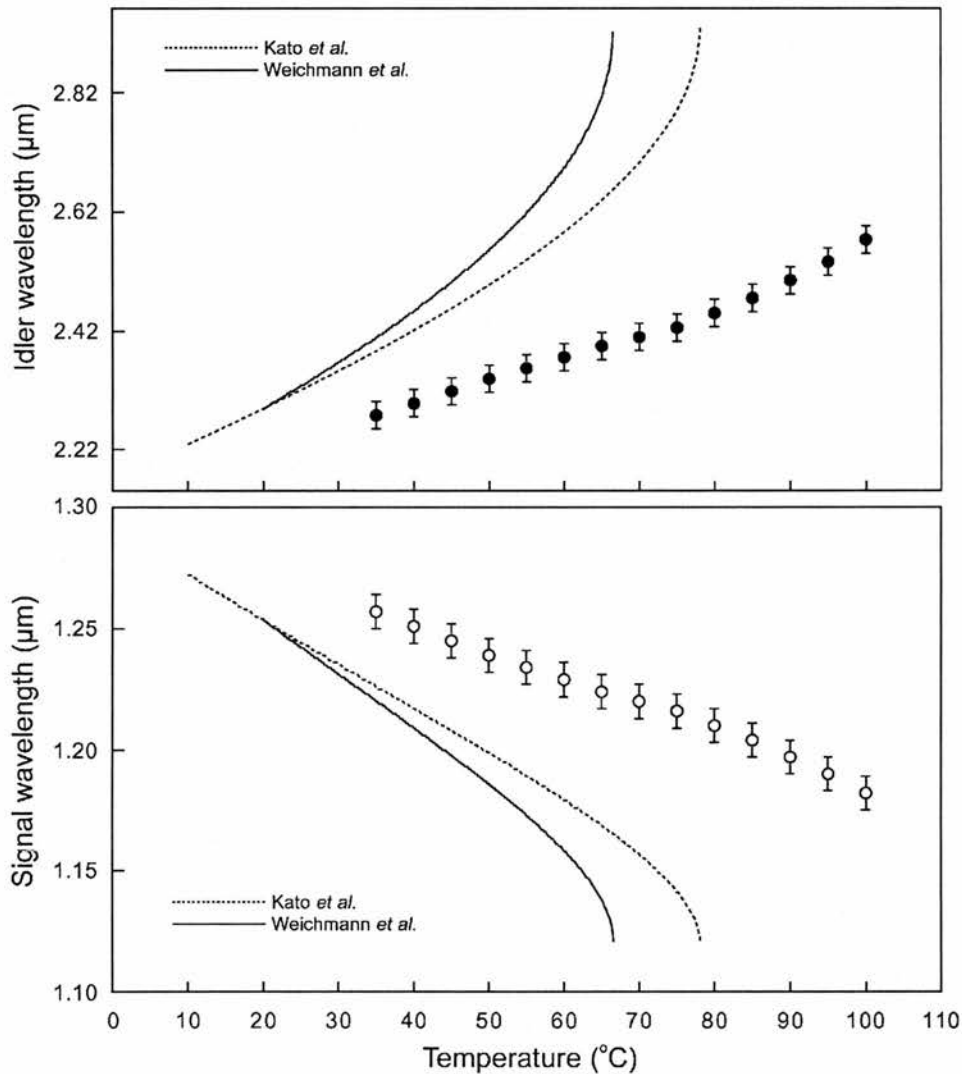


Figure 14. Temperature tuning of PPKTP ICSRO at a pump wavelength of 810nm. Solid and dashed lines refer to the temperature derivatives of Weichmann *et al.* [14] and Kato *et al.* [15]. Sellmier data is from Vanherzeele *et al.* [7].

As previously discussed, birefringent KTP shows little temperature tunability of phase-matched parametric interactions. The reason for this is that whilst the absolute values of the refractive indices vary with temperature their difference remains essentially unchanged. Thus, the birefringence utilised for a particular phase-matching scheme will show little temperature tunability. The advent of QPM interactions in poled KTP has not only opened up the possibilities of grating engineered phase-matching, it has also liberated the temperature insensitivity of the material. All the parametrically interacting fields access the highest nonlinearity of the crystal along the z-direction and hence their phase-matching is governed by the absolute refractive index along z.

The greater degree of temperature tunability shown by PPKTP over the birefringent material was shown early on in its development [13]. There is some degree of discrepancy between the published temperature derivatives of the material [14, 15] and the observed tunability of the material shown in figure 14. The data that is shown in this figure was measured using the modified SRO cavity shown in figure 2 to accommodate the ~50mm diameter oven around the PPKTP crystal. The pump wavelength was fixed at 810nm which allowed the ICSRO to tune towards shorter signal wavelengths with increasing temperature. Overall, an average temperature tuning rate of 1.2nm/degree for the signal field and 4.5nm/degree for the idler field was observed. This corresponded to a signal and idler tuning ranges of 1.18 - 1.27 μm and 2.29 - 2.57 μm respectively.

The theoretical temperature tuning was calculated from the z-axis temperature derivatives of references [14] and [15] together with the sellmeier data of Vanherzeele *et al.* [7]. Deviations between the measured data and the theoretical curves are attributed to the bias of the published temperature derivatives towards the visible region of the spectrum. It appears that PPKTP has a near to mid-infrared temperature derivative with a magnitude of about half that in the visible region.

7.4-3 Fine frequency studies

The fine frequency characteristics of the signal field were examined using a 2GHz scanning confocal interferometer. The signal field commonly oscillated on one

longitudinal mode of the signal cavity with frequent mode hops to adjacent cavity modes on millisecond timescales. Insertion of a 1mm thick uncoated etalon into the signal cavity suppressed the frequency of the mode hops but did not induce the same stable single longitudinal mode operation observed in the birefringently phase-matched KTA ICSRO. Active frequency stabilisation of the PPKTP SRO was not attempted in any way and efforts towards the generation of single frequency output at the signal *and* idler wavelengths was subsequently directed towards the implementation of a ring cavity ICSRO. A suitable interferometer for the idler wavelength was not obtainable during this experiment and it is assumed that the idler field was generated with the same ~20GHz measured bandwidth of the standing-wave pump laser.

7.5 Ring cavity PPKTP ICSRO

The high effective nonlinearity of the PPKTP crystal coupled with its long interaction length make it a suitable candidate for the implementation of a ring cavity SRO. In the course of the ICSRO research outlined in this thesis, one successful attempt was made to construct a Ti:Sapphire ring-cavity based ICSRO with the KTA nonlinear crystal. This device operated just above threshold and it became clear that to achieve a substantial improvement in the design, a nonlinear material with a higher parametric gain was required. Alongside the motivation towards a ring based device, suitable optics and materials were acquired for the construction of a more compact design of the Ti:Sapphire laser (a glance at the component spacing given in any of the experimental chapters will show that the overall cavity length of the modified Schwartz laser was almost 2.5m). The intended all solid-state green pump source for this compact laser failed to make the commonly neglected transition from "planned" to "actual" that befalls such expensive pieces of laboratory equipment. In this way, the opportunity to try and implement a ring cavity PPKTP ICSRO arose. The spirit of this investigation was to try and identify the particular design needs of the project and attempt to obtain all single frequency operation. It was clear at an early stage that a full characterisation of the device would be almost a PhD thesis in its own right. Thus it is here that the clear division between the limited results that are presented in this section and

those expected of a full and scientifically rigorous investigation should be made. With this in mind we shall continue with an explanation of the cavity design process, device layout and initial ICSRO performance.

7.5-1 Cavity layout and design

Figure 15 shows the layout of the ring-ring PPKTP ICSRO design. The signal field is shown by a dotted line and the laser field by a solid line. Small arrows superimposed on these lines indicate the travelling direction of the two fields.

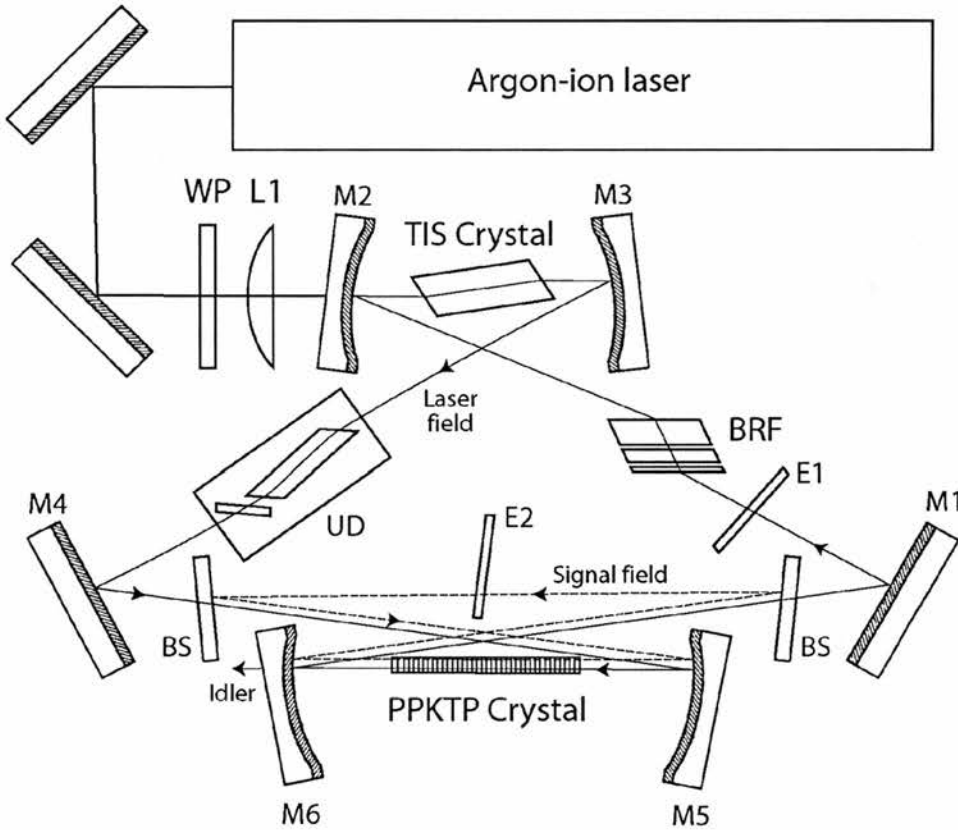


Figure 15. Ring cavity PPKTP ICSRO cavity layout. UD is a uni-directional Faraday rotator, E1 and E2 are uncoated etalons and BS indicates a 5-degree beamsplitter (x2).

The ring cavity ICSRO (RICSRO) shares many common components with the standing-wave ICSROs outlined in this, and previous, chapters. All the cavity mirrors (M1-M6) are either identical to those previously used (M5 & M6) or share

exactly the same specifications. The birefringent tuner (BRF) is that previously used in the standing wave experiments. The 20-30 argon-ion laser and all relevant beam coupling optics (L1, WP) are unchanged. Components that have been specially acquired are: a new Ti:Sapphire Brewster crystal [16], small-angle beamsplitters (BS) and a unidirectional device.

The new 10mm long Ti:Sapphire crystal has a figure of merit (FOM) (ratio of absorbed green light to absorbed pump light) of ~ 250 . This is a substantial improvement on the much older Schwartz crystal (FOM ~ 150) and gives an increased overall argon-ion absorption for the new sample of $\sim 90\%$. The crystal is cooled with tap water at $\sim 15\text{-}20^\circ\text{C}$ via a copper block upon which it is very firmly adhered using silver-loaded epoxy. The Brewster faces of the crystal are easily accessible for cleaning purposes. The design of the SRO cavity required the purchase of a new set of beamsplitters having identical specifications to those previously used with the exception that they have an operational angle of 5 degrees (the previous ones having a 45-degree specification). Using these optics, a separate SRO cavity may be constructed as shown in figure 15. The 5-degree beamsplitters were purchased after attempts to implement the same cavity design with the 45-degree beamsplitters placed SRO operation at the edge of the *mirror* bandwidths. This is due to the shift in the beamsplitter signal coating bandwidth with incidence angle. Common with all Ti:Sapphire ring resonators, a method of maintaining unidirectional operation must be used to avoid competition between travelling waves in opposing directions. The most widely used method involves the use of an intracavity Faraday rotator shown as UD in figure 15. The basic mode of operation takes advantage of the fact that a material with a finite Verdet constant, when immersed in a DC magnetic field, will rotate the plane of polarisation of an incident field. The important factor here is that the direction of this finite rotation depends on the orientation of the magnetic field and not on the direction of the incident field.

The unidirectional device comprises a Brewster-cut Faraday crystal placed in the field of a permanent magnet and a waveplate polished to a thickness that will compensate for the polarisation rotation induced in the Faraday crystal. This compensation will occur for one direction only. Unlike the Faraday crystal, the

waveplate will rotate the plane of polarisation in opposite directions for opposing field directions. In this way, one field direction will have its plane of polarisation rotated and then compensated whereas the opposite field direction will have its plane of polarisation rotated twice in the same direction. The field travelling in this direction will suffer consecutive losses at each Brewster surface of the laser cavity. Thus, the field that experiences no net rotation will dominate and saturate the laser gain at the expense of the opposing field.

A major advantage of this "home-built" laser system is that unlike the Schwartz laser, there is a good deal more flexibility in the choice of the mirror separation of M2 and M3. This opens up another degree of freedom in the design of the resonant cavity mode characteristic. It also transforms the simple ABCD analysis utilised in the standing wave cavity design into a far more involved process. We shall now examine the stability the laser and SRO cavity designs shown in figure 15.

7.5-2 Cavity stability and mode waist analysis

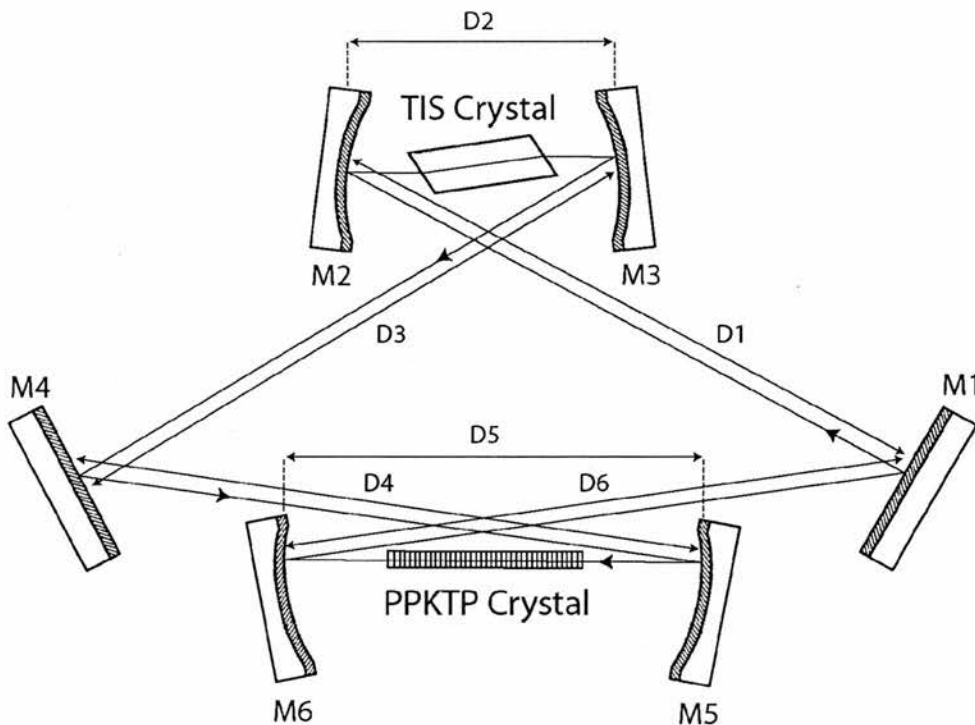


Figure 16. Laser cavity component spacing for ABCD analysis of stability and waist sizes.

For the analysis of the laser cavity stability and waist sizes the SRO and laser cavities were modelled according the ABCD matrix method outlined in chapter 3. A diagram illustrating the laser cavity spacing parameters used in this modelling is shown in figure 16. We have neglected to include intracavity components other than the laser and nonlinear crystals in order to simplify the analysis. The cavi spacing of the SRO cavity is shown in figure 17. The physical lengths of the crystals have been included in the relevant spacing of the cavity mirrors. The Brwester crystal fold angle compensation given in chapter 3 and reference [17] must be increased to 11.2 degrees to take account of the increased Ti:Sapphire crystal length of 10 mm. The Overall resonant cavity mode is slightly astigmatic due to the ~3 degree fold angle of mirrors M5 and M6. This is accounted for in the following analysis. The appropriate cavity spacing parameters are given in tables 5 and 6.

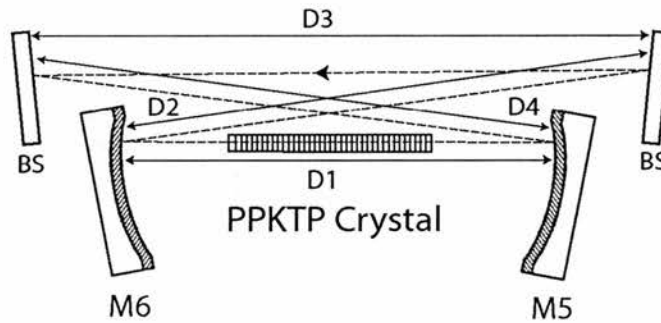


Figure 17. SRO cavity component spacing

Considering the laser cavity in the first instance, the stability was analysed for various values of mirror separation $D2$ and $D5$ shown in figure 16. The behaviour of the laser cavity stability for which the round trip ABCD matrix satisfies

$$\frac{|A + D|}{2} \leq 1 \quad (7.4)$$

is shown in figure 18. The shaded contours indicate the magnitude of $A + D$ where darker areas indicate minimum values of $|A + D|$. The boundary solid line to the stability zones indicates that beyond this point *either* the sagittal or tangential or both round trip ABCD matrices do not satisfy (7.4).

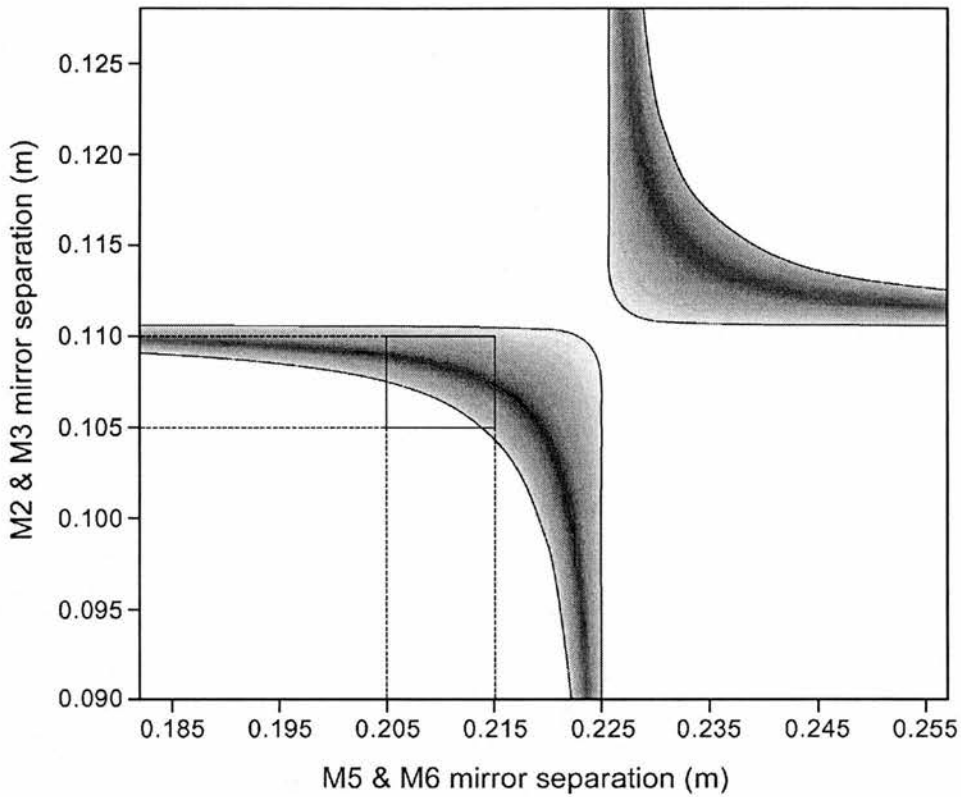


Figure 18. Stability plot of the laser cavity shown in figure 16. Darker regions represent minimum values of $|A+D|$. Stability regions are bounded by solid lines beyond which one or both of the principle planes are unstable. The region indicated contains the optimum separation of both mirror pairs.

Ti:Sapphire Ring Laser Cavity Parameters

<i>Mirror</i>	<i>ROC (mm)</i>	<i>Angle (Deg)</i>	<i>Separation</i>	<i>Distance (mm)</i>
M1	∞	N/A	D1	700.0
M2	100	11.2	D2	*108.0
M3	100	11.2	D3	700.0
M4	∞	N/A	D4	685.0
M5	200	3	D5	*214.0
M6	200	3	D6	685.0

Table 5. Ti:Sapphire ring laser cavity parameters of the layout illustrated in figure 16. *variable parameter.

As well as satisfying the stability criterion (7.4) the resonant laser cavity mode must locate suitable waist sizes at the centres of the Ti:Sapphire and PPKTP crystals. This requires a $\sim 17\text{-}20\ \mu\text{m}$ Ti:Sapphire crystal waist and a $\sim 35\text{-}45\ \mu\text{m}$ PPKTP crystal waist (due to the dimensions of the two crystals used and the tight focussing of the argon-ion laser into the Ti:Sapphire crystal). The most suitable region of figure 18 that is able to accommodate waist sizes of this magnitude is highlighted by a square. Plots of the Ti:Sapphire and PPKTP crystal waist sizes over this region are shown in figures 19 and 20 for the sagittal plane only.

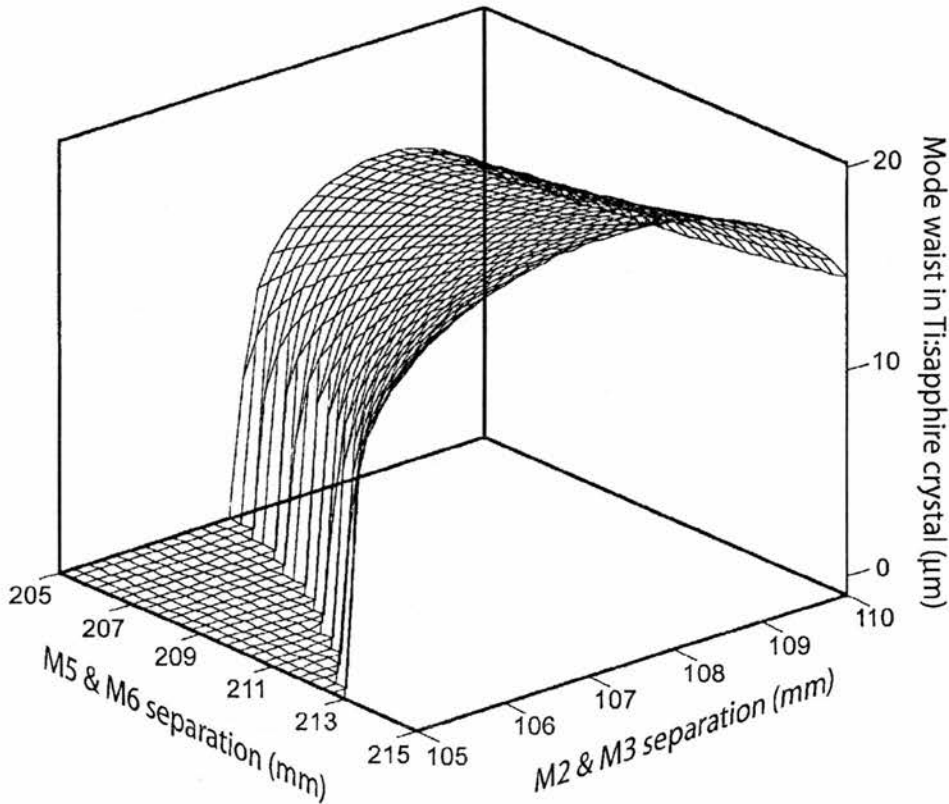


Figure 19. Sagittal waist size at the centre of the TiSapphire crystal for the region highlighted in figure 18.

There is little difference in waist size or stability range for the sagittal and tangential planes. To avoid clutter, plots of the sagittal waist are shown. The nature of the curves is essentially the same and a "feel" of the relationship between mirror separation and waist size may be gained from plots of either plane. It can be seen that, unsurprisingly, the waist size in the Ti:Sapphire crystal is very sensitive to the

mirror separation of M2 and M3. In contrast the separation of mirrors M5 and M6 do not alter the Ti:Sapphire waist size appreciably. The waist size inside the PPKTP crystal, also for the sagittal plane, is shown in figure 20.

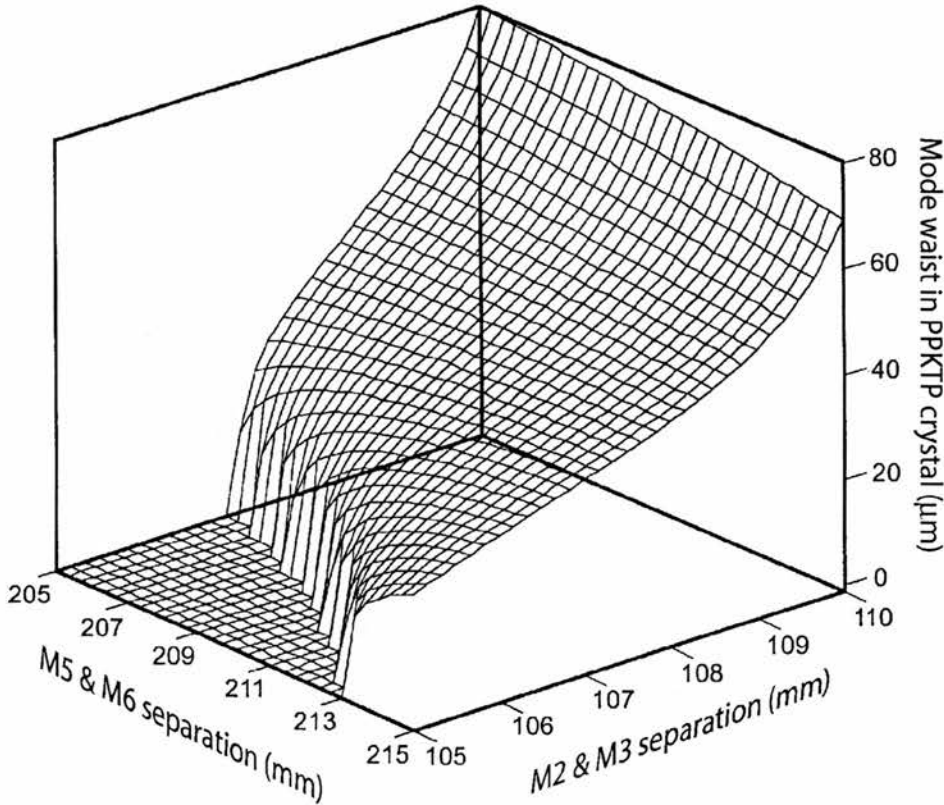


Figure 20. Sagittal waist size at the centre of the PPKTP crystal for the region highlighted in figure 18.

The final stage in the stability analysis is to examine the signal cavity stability. The analysis of the SRO cavity shown in figure 17 is somewhat simpler than that for the ring laser as it contains only one tight beam waist. A plot of the signal waist size inside the PPKTP crystal over an identical separation range of M5 and M6 as shown in figures 19 and 20, is given in figure 21. It can be seen that for the smaller separation range of M5 and M6 the signal cavity is unstable. Beyond ~ 209.2 mm the signal waist sizes rapidly increases with mirror separation to achieve a spot size of $56 \times 55 \mu\text{m}$ at an optimum separation of ~ 214 mm. The pump laser waists at this optimum separation are $19 \mu\text{m}$ in the Ti:Sapphire crystal and $43 \times 44 \mu\text{m}$ in the PPKTP crystal. Pump and signal wavelengths were set at 800 nm and 1200 nm

respectively. It should be noted that increasing the overall length of the signal cavity will reduce the signal waist inside the PPKTP crystal. This is a very weak effect and requires cavity length changes of the order of 0.5m to see an appreciable change in spot size. Limited cavity space makes this an impractical adjustment to utilise.

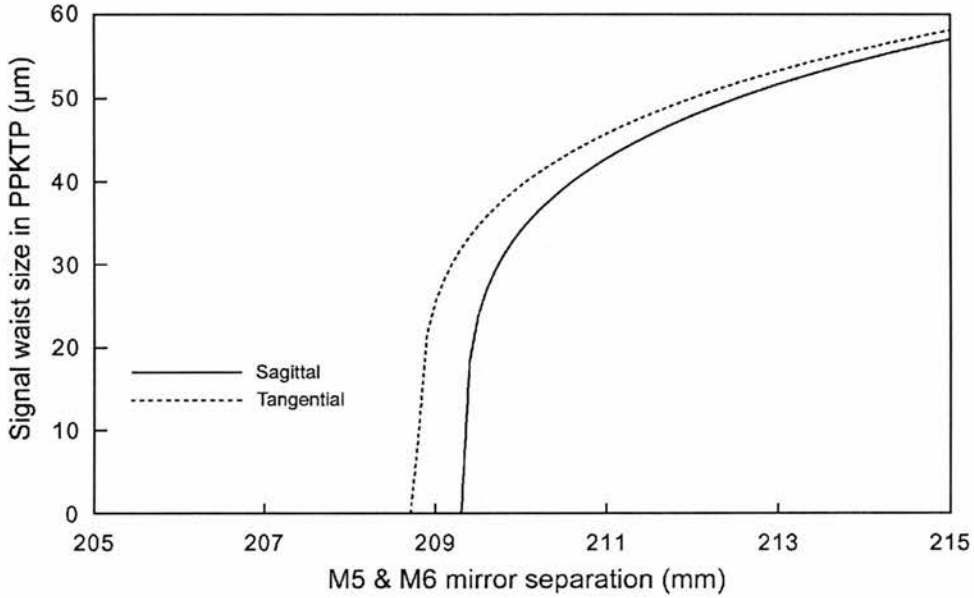


Figure 21. Signal mode waist size in the PPKTP crystal for the cavity of figure 17.

SRO Ring cavity Parameters

<i>Mirror</i>	<i>ROC (mm)</i>	<i>Angle (Deg)</i>	<i>Separation</i>	<i>Distance (mm)</i>
M5	200	3	D1	*214.0
M6	200	3	D2	280.0
BS	∞	3	D3	343.0
BS	∞	3	D4	280.0

Table 6. SRO ring cavity parameters for the layout illustrated in figure 17.

*adjustable parameter.

In the laboratory, figures 19, 20 and 21 serve as useful guides to the implications of a particular mirror adjustment. We shall now look at how to tackle the problem of cavity alignment for both ring cavities.

7.5-3 Cavity alignment

Alignment of ring cavities presents a greater number of difficulties than for the standing wave geometry. This arises from the fact that, rather than a simple retroreflection back along a common path, the ring laser mode must be made to return to exactly the same point via a separate path. The primary aids to alignment are a pair of pinholes, a good viewing scope with high response at $\sim 800\text{nm}$ and patience. The starting point for laser alignment is to place all the cavity components in roughly their correct positions and to configure the laser as a standing wave bow-tie cavity. All this optimisation will be performed with M1 replaced with a laser output coupler. This initial configuration is shown in figure 22.

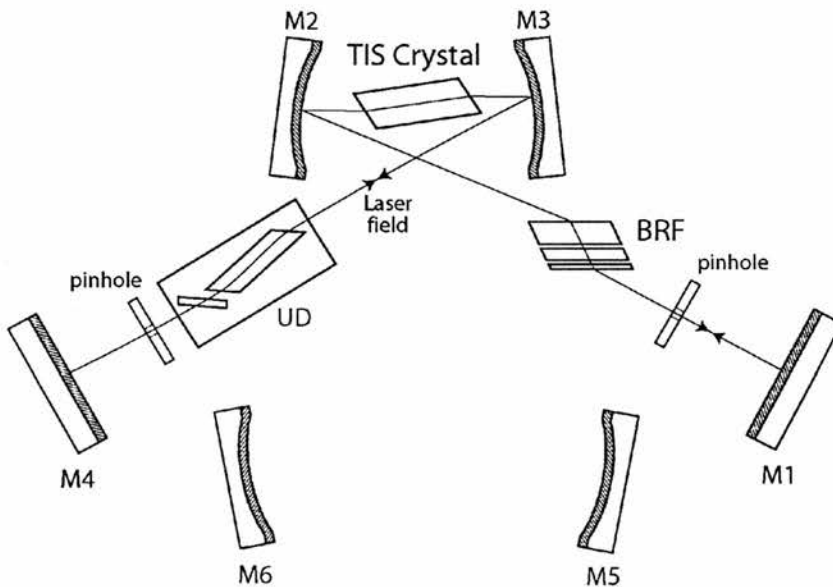


Figure 22. Standing wave configuration for initial ring alignment.

The best course of action is to align the standing wave cavity without the unidirectional device (UD) or pinholes. Once working and optimised for power, insert the UD and re-optimize. The laser has more than sufficient gain to tolerate the loss presented by the UD in this configuration. Here, small angular "tweaks" on the position of the UD often bring the power output up a little. Once satisfied that the cavity is power optimised, the pinholes should be put in place and *firmly* clamped in place (a nudge of these at a later stage could undo a morning's work). The next task is to slowly rotate mirrors M4 and M1 towards each other using the viewing

scope to monitor the fluorescence from the laser crystal. A rough guide to the alignment of these mirrors is to look for the residual argon-ion light which is roughly collinear with the laser mode. Rotate mirror M4 and guide the argon light onto the centre of mirror M1. Then rotate M1 and guide the argon light (or fluorescence if it is easier to see) onto the centre of M4. Viewing the face of the pinholes closest to each of these mirrors should show a spot of fluorescence reflected from the mirror. The task is now to guide this spot through the pinhole **using the furthest mirror**. Mirror M1 guides the spot through the pinhole near M4 and *vice-versa*. This is important, as each subsequent movement of the mirrors will slightly misalign the previous adjustment. The method involves repeating this procedure until the laser starts to operate. The resultant cavity is shown in figure 23.

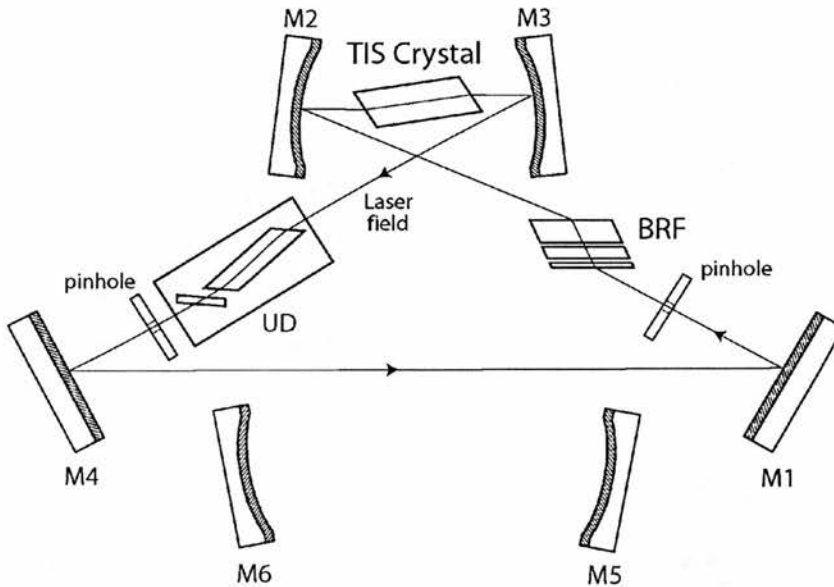


Figure 23. Second stage of the laser alignment procedure.

Once the laser operates in the configuration shown in figure 23 the pinholes should be removed. This allows the resonant cavity mode more room to move during optimisation. The power optimisation should involve more minor "tweaks" of the UD as this often yields a noticeable amount of power gain. Once optimisation of the power is complete the pinholes should be replaced and firmly clamped in position once more.

The next stage of the process is to introduce the secondary intracavity focus to the ring laser cavity. Initial positioning of mirrors M5 and M6 is important and they should be placed as close to the optimum separation (~206-207mm without the PPKTP) as possible before commencing alignment. Checking that the pinholes are in place, rotate mirror M1 to guide the intracavity fluorescence onto the edge of mirror M6. Make sure that the spot is at least 2mm from the edge to avoid the "thinning" of the coating near the mirror edges. Next, rotate mirror M4 to guide the fluorescence onto mirror M5 in the same manner. Now rotate M6 such that the fluorescence guided from M1 overlaps the spot on M5 that is guided from M4. Repeat this procedure for M5, overlapping the fluorescence guided from M4 onto the spot on M6. If all is well, viewing the faces of the pinholes should show the two fluorescence spots.

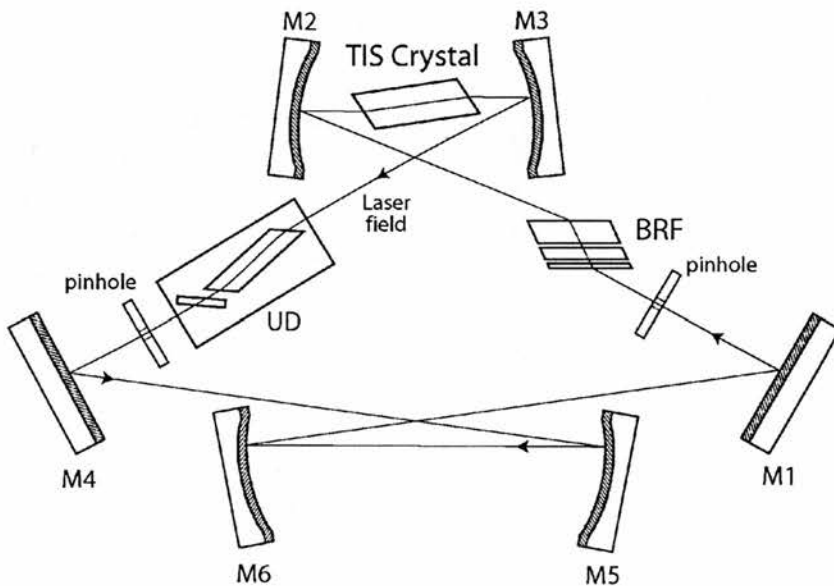


Figure 24. Inclusion of the secondary intracavity focus.

Lasing should be achieved by steering the spot through the pinhole nearest M1 using M6 and repeating for M5 and the pinhole nearest M4. Again, once laser operation is achieved, the pinholes should be removed during power optimising. The pinholes should be replaced once more upon completion of power optimisation. The last stage in the process is to include the PPKTP crystal and beamsplitters.

Inserting the PPKTP crystal is a matter of increasing the separation of M5 and M6 to accommodate the increased optical path length and then placing the crystal at the centre of the focus, observing the focused fluorescence on each face of the crystal. Using M5 and M6 to return the fluorescence back through the pinholes should be enough to achieve lasing. Once more, remove the pinholes and power-optimize the cavity. Insertion of the beamsplitters is straightforward as the cavity can tolerate a little misalignment, inserting them on-axis and slowly tilting them to the correct angle whilst optimizing the power is the standard procedure. The final laser cavity is shown in figure 25.

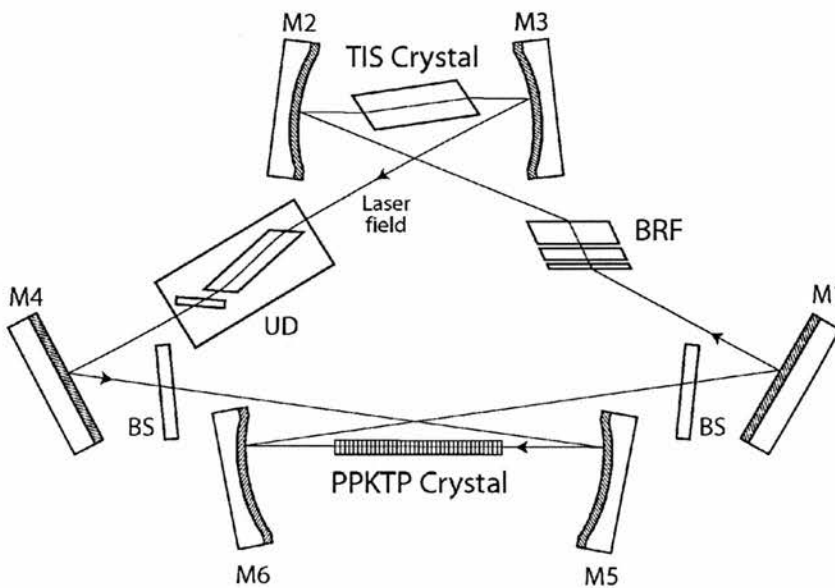


Figure 25. Final laser cavity configuration.

We now consider the alignment of the SRO cavity itself. This should only be attempted once the laser itself has been optimized for power output and mirror M1 replaced with a high reflector at the pump wavelength. To monitor the intracavity field of the laser a photodiode (PD) is used to measure the leakage field from mirror M5 as shown in figure 26. A very useful aid to the alignment of the signal cavity is the fact the PPKTP will cause a small amount of SHG of the pump field due to high-order QPM effects. This visible blue light will be collinear with the pump and a significant amount is reflected off the beamsplitters (BS). The most productive

alignment technique involves the use of an optical chopper placed in the beam path of the signal cavity as shown in figure 26.

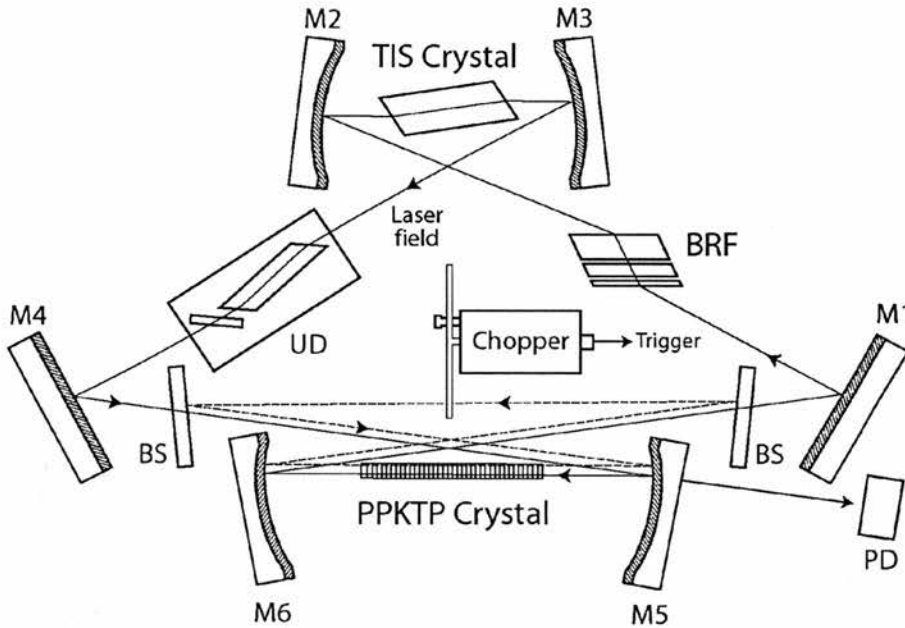


Figure 26. Method of aligning the SRO cavity with an optical chopper.

The key to the SRO cavity alignment method is the provision of a visual key to the degree of enhancement inside the laser cavity. This enhancement is a direct result of the residual pump field reflecting off the beamsplitters (BS) and being returned to the laser cavity. The enhancement effect is much weaker than that seen for the standing wave SRO cavities in previous chapters, as the residual pump light must now be reflected twice off a 99.7% transmitting optic. Nonetheless, a small amount of residual pump light will be returned to the laser cavity via a round-trip of the correctly aligned SRO cavity.

The SRO alignment method requires the use of an optical chopper (shown in figure 26) which is used to trigger an oscilloscope trace driven by the signal from a monitor photodiode (PD in figure 26). As the SRO cavity comes into alignment, a small step function is visible superimposed on the monitor PD signal. This step function is the periodic chopping of the enhancement. Alignment involves maximising the modulation depth of this step function thereby maximising the

feedback enhancement of the SRO cavity. SRO operation is confirmed by the sudden drop of the "troughs" of the step modulation corresponding to a clamped laser field. A visual aid to SRO operation is, of course, the observation of a small amount of orange light corresponding to SHG of the signal field at high orders of the QPM period. This concludes the rather lengthy discussion on the alignment of the laser and SRO cavities.

7.5-4 PPKTP RICSRO operation

A rigorous characterisation of the RICSRO is not presented. This is due partly to time constraints and mostly to the unresolved issue of bi-directional lasing caused by the nonlinear loss of the SRO. It was found that under SRO operation the pump laser would lase in both directions. This was attributed to the fact that the intracavity loss presented to the laser field by the parametric process exceeded the differential loss presented by the unidirectional device. Measurements of the polarisation plane rotation of the unidirectional device showed a ~ 3 degree rotation of the suppressed-direction polarisation plane. This amounts to a total differential loss of only $\sim 0.3\%$ for the twelve Brewster surfaces of the laser cavity. Despite the problem of bi-directional operation, a rudimentary attempt at achieving single longitudinal mode (SLM) operation was made. Using two uncoated glass etalons of 1mm thickness shown as E1 and E2 in figure 15, simultaneous pump and signal SLM operation was observed. This was achieved by adjusting the angles of E1 and E2 slightly. The pump and signal fields were observed on two separate 2GHz scanning confocal interferometers driven by the same high-voltage ramp generator. This ensured that the traces showed a simultaneous pump and signal field scan.

The output frequency spectrum of the pump and signal fields is shown in figure 27. These traces correspond to pump signal and idler wavelengths of 0.809, 1.23 and 2.35 μm respectively. The idler field could not be directly measured as a suitable interferometer was not available at the time. The SLM operation of the idler field may be inferred from the SLM nature of the pump and signal fields. SLM mode hop free operation of the passive RICSRO was maintained under free-running conditions for periods of up to ~ 10 seconds. Both laser and SRO outputs suffered from mode hops to adjacent longitudinal modes of their respective cavities over

longer timescales. The argon-ion input pump power at the time of measurement was 10 W. This corresponded to a maximum measured idler output of 115 mW. The device was operating 3 times above its 2.5 W input power threshold, with a measured laser threshold of 1.4 W.

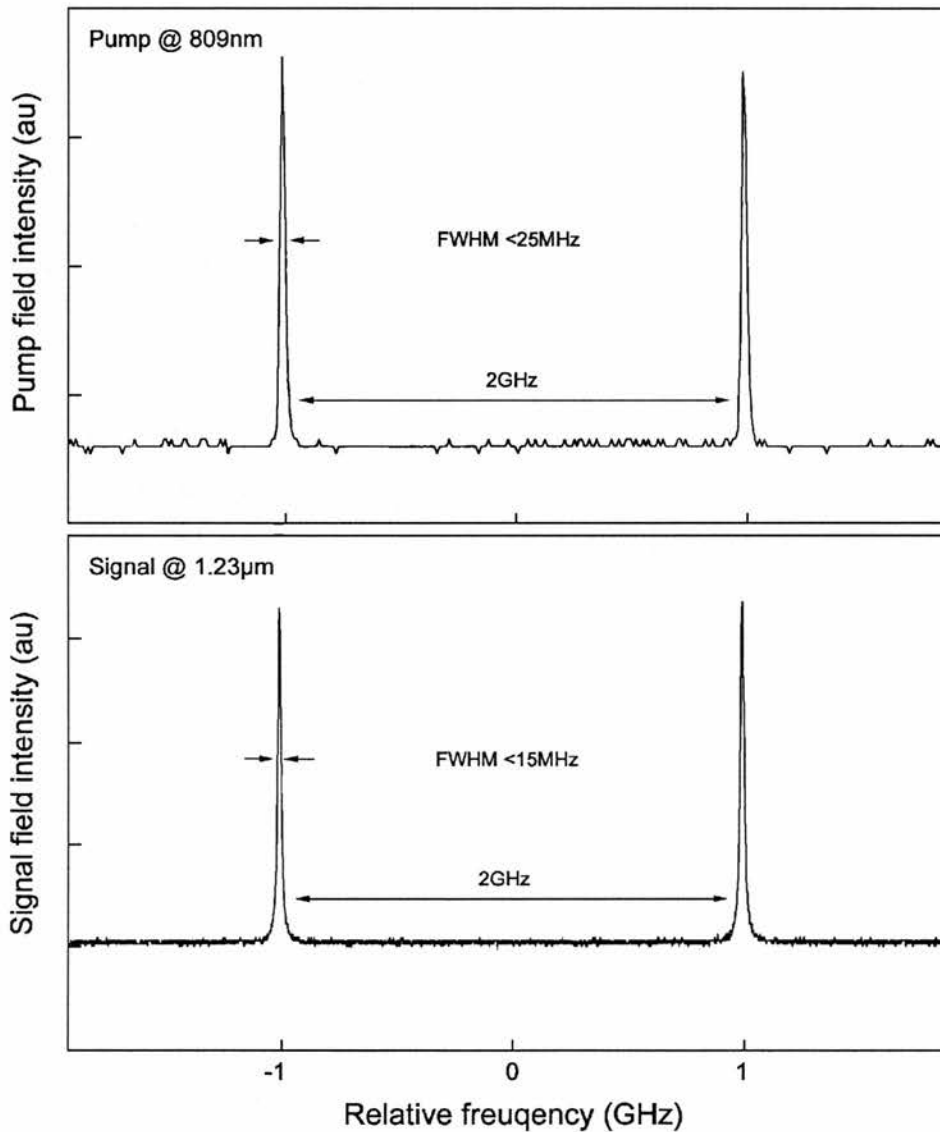


Figure 27. Pump and signal simultaneous output spectrums confirming SLM operation of the 115 mW idler field.

The output spectrums show that ring cavity geometry of the RICSRO has achieved SLM pump operation at a linewidth (FWHM) of $<20\text{MHz}$. Together with the

measured simultaneous SLM operation of the signal field (FWHM <15MHz), it may be deduced that, unlike the standing wave geometry of previous chapters, single frequency idler has been generated. The observation of SLM idler operation with good passive stability concludes the viability study of the RICSRO. Further characterisation of this device awaits the resolution of the bi-directional operation issue presented by the parametric loss of the SRO above threshold.

The potential of the RICSRO geometry has been examined and shows promise as an all-single-frequency source. The excessive amount of further analysis and design that this device requires, as previously mentioned, is an experimental thesis in its own right. Some manner of active frequency control must be devised to provide continuous, mode hop free tuning. This will require servo scanned etalons and cavities and sophisticated control electronics. Some method of increasing the differential loss of the unidirectional device must be found. There is a trade off here between increasing total insertion loss and differential loss. Materials with high Verdet constants providing greater net rotation become increasingly lossy. There are many design issues to consider, their resolution is not the subject of this section. This section serves to record the *progress* towards the development of the Ti:Sapphire RICSRO. This progress, albeit brief, provokes useful discussion and serves to provide a basis for the concentrated development of this device.

7.6 Chapter 7 summary

A PPKTP ICSRO has been implemented in both standing wave and ring cavity geometries. In the standing wave geometry, the power performance and tuning characteristic of the device have been studied. The study shows that the utilisation of PPKTP as a nonlinear material in the SRO configuration offers significantly lower thresholds than for birefringently phase-matched materials. There is further potential to increase the output power of this device through the use of a signal output coupler, raising the SRO threshold to 3.7 W of input pump power.

Rapid pump tuning of the material is demonstrated giving nearly 100nm of idler tuning for every 1nm of pump tuning. Temperature tuning of the material has been investigated and significant tuning has been achieved through this method. This characteristic is unique to the QPM regime and is not observed in the birefringently phase-matched material. The tuning data presented is a valuable contribution to the published tuning data of KTP and PPKTP in the near to mid-infrared. It has been shown that there is a good deal of uncertainty in the Sellmeier data of KTP in this spectral region. The design stage of the QPM manufacturing process relies heavily upon the accuracy of the Sellmeier data and the possibility of mistakes occurring through the wrong choice of such data is apparent. It is unclear as to how much of the wide range of conflicting predictions may be attributed to the spectral bias of the fitted data or the general material inconsistency of KTP. Caution is therefore advisable when choosing a QPM period for a fixed frequency source. The flexibility of the pump tuned ICSRO approach is underlined in the context of this discussion.

The high parametric gain offered by the PPKTP would allow the signal cavity to tolerate the inclusion of an intracavity SHG crystal for the signal field, opening up the possibility of the generation of tunable output at around 600nm. This will be discussed in the concluding chapter.

Finally, progress has been made towards the implementation of a ring cavity geometry for the ICSRO. Initial cavity stability studies are presented together with a discussion of some of the design issues arising from the subsequent operation of

the ring ICSRO (RICSRO). On a more practical level, detailed instructions as to the alignment procedure for both the laser and SRO ring cavities are presented. The design issues covered in the RICSRO section of this chapter provide a basis for the greater body of work that is yet to be done with this device.

Observation of simultaneous single longitudinal mode (SLM) operation for the pump and signal fields has allowed the inference of SLM operation of the idler field at $2.35\ \mu\text{m}$ at powers exceeding 100 mW. It is envisaged that the excessive amount of optimisation yet to be performed should see a significant increase in this output power. The passive stability of the device is promising in the context of active frequency control of the resonant fields.

Chapter 7 references

- 1 M. N. Satyanarayan, A. Deepthy and H. L. Bhat, "Potassium titanyl phosphate and its isomorphs: Growth, properties, and applications," *Critical Reviews in Solid State and Materials Sciences* **24**, 103-191 (1999).
- 2 Titan Ti:Sapphire Laser, Schwartz Electro Optics Inc. 3404, N. Orange Blossom Trail, Orlando, FL 32804 USA,
- 3 H. Karlsson and F. Laurell, "Electric field poling of flux grown KTiOPO₄," *Applied Physics Letters* **71**, 3474 (1997).
- 4 V. A. Dyakov, V. V. Krasnikov, V. I. Pryalkin, M. S. Pshenichnikov, T. B. Razumikhina, V. S. Solomatin and A. I. Kholodnykh, "The Sellmeier Equation and Tuning Characteristics of KTP- Crystal Frequency-Converters in the Range from 0.4 to 4.0-Mu-M," *Kvantovaya Elektronika* **15**, 1703-1704 (1988).
- 5 H. Liao, H. Y. Shen, Z. D. Zheng, T. Q. Lian, Y. P. Zhou, C. H. Huang, R. R. Zeng and G. F. Yu, "Accurate Values for the Index of Refraction and the Optimum Phase Match Parameters in a Flux Grown Ktiopo₄ Crystal," *Optics and Laser Technology* **20**, 103-104 (1988).
- 6 D. W. Anthon and C. D. Crowder, "Wavelength Dependent Phase Matching in KTP," *Applied Optics* **27**, 2650-2652 (1988).
- 7 H. Vanherzeele, J. D. Bierein and F. C. Zumsteg, "Index of refraction measurements and parametric generation in hydrothermally grown KTiOPO₄," *Applied Optics* **27**, 3314 (1988).
- 8 K. Kato, "2nd-Harmonic and Sum-Frequency Generation to 4950-a and 4589-a in KTP," *IEEE Journal of Quantum Electronics* **24**, 3-4 (1988).
- 9 K. Fradkin, A. Arie, A. Skliar and G. Rosenman, "Tunable mid-infrared source by difference frequency generation in bulk periodically poled KTiOPO₄," *Applied Physics Letters* **74**, 914-916 (1999).
- 10 T. Y. Fan, C. E. Huang, B. Q. Hu, R. C. Eckardt, Y. X. Fan, R. L. Byer and R. S. Feigelson, "Second harmonic generation and accurate index of refraction measurements in flux-grown KTiOPO₄," *Applied Optics* **26**, 2390 (1987).
- 11 A. Arie, G. Rosenman, V. Mahal, A. Skliar, M. Oron, M. Katz and D. Eger, "Green and ultraviolet quasi-phase-matched second harmonic generation in bulk periodically-poled KTiOPO₄," *Optics Communications* **142**, 265-268 (1997).

- 12 V. Pasiskevicius, S. H. Wang, J. A. Tellefsen, F. Laurell and H. Karlsson, "Efficient Nd : YAG laser frequency doubling with periodically poled KTP," *Applied Optics* **37**, 7116-7119 (1998).
- 13 G. M. Gibson, G. A. Turnbull, M. Ebrahimzadeh, M. H. Dunn, H. Karlsson, G. Arvidsson and F. Laurell, "Temperature-tuned difference-frequency mixing in periodically poled KTiOPO₄," *Applied Physics B-Lasers and Optics* **67**, 675-677 (1998).
- 14 W. Wiechmann, S. Kubota, T. Fukui and H. Masuda, "Refractive-Index Temperature Derivatives of Potassium Titanyl Phosphate," *Optics Letters* **18**, 1208-1210 (1993).
- 15 K. Kato, "Temperature Insensitive SHG at 0.5321 μm in KTP," *IEEE Journal of Quantum Electronics* **28**, 1974-1976 (1992).
- 16 Ti:Sapphire crystal, AtraMet Inc, 222 Sherwood Avenue, Farmingdale, NY 11735-1718,
- 17 D. M. Kane, "Astigmatism compensation in off-axis laser resonators with two or more coupled foci," *Optics Communications* **25**, 379 (1989).

8. Conclusion

8.1 Concluding summary of results

The experimental research presented in this thesis has brought to light the operational versatility and broad potential of an emergent singly-resonant OPO configuration. Centred upon the characterisation of four separate SRO devices, the thesis delivers a scientific contribution that is essentially "proof of principle" in nature. As such, this initial work may be viewed as a step towards the final embodiment of a practical coherent light source for the near to mid-infrared. How many further steps are required, and the research investment that is necessary to complete them should be considered. Recapitulating the preceding chapters is a reasonable place to start.

Importantly, chapter 4 demonstrates practical, amplitude-stable and Watt-level tunable SRO operation using a conventional birefringently phase-matched nonlinear material. The intracavity pumping approach is able to address the multi-Watt SRO threshold and drive the interaction over three times above threshold. Coupled with the ~90% downconversion efficiency of this device and its wide tunability this work delivers a firm endorsement of the ICSRO's potential. The intrinsic tunability of the Ti:sapphire laser may be harnessed to deliver wide tunability of the ICSRO.

Chapter 5 sought to investigate the further power enhancement of this device through the use of PPLN. Although the enhanced effective nonlinearity of this material brought a marked decrease in device threshold, thermal lensing effects in the nonlinear crystal become a limiting factor to stable, high power operation. Engineering considerations arising from the use of an intracavity oven first became

apparent in this device configuration. The perturbations caused by convection currents around the intracavity oven contribute to the overall power instability of the PPLN ICSRO. The combination of pump, grating and temperature tuning assessable through this device configuration lead to attractive possibilities for the generation of integer ratio frequency outputs. The device offers an unparalleled degree of tuning flexibility.

Chapter 6 illustrates a unique advantage of the ICSRO configuration: its ability to accommodate new nonlinear materials at the very earliest stage of their development. SRO operation was observed for the first time in a cw device using the nonlinear material PPRTA. Despite possessing an interaction length of only 4.5mm the PPRTA crystal was configured as an SRO operating at pump powers well over twice the device threshold. Erratic tuning behaviour was observed, possibly arising from irregularities in the PPRTA sample although this remains to be confirmed experimentally. Importantly, discrepancies in the theoretical tuning behaviour and the observed tuning range may be compensated by tuning the Ti:sapphire laser to the correct pump wavelength. This is possible through temperature tuning only in a fixed-frequency laser configuration.

Chapter 7 describes the characterisation of an ICSRO based on the nonlinear material PPKTP. Again, the ICSRO configuration is able to comfortably exceed the device threshold. The device was observed to operate beyond the condition for maximum downconversion efficiency described in chapter 3. This presents the possibility of extracting further power from the SRO via signal output-coupling (successfully achieved for the KTA SRO of chapter 4). Initial design work towards, and experimental configuration of a ring-based PPKTP ICSRO was presented. Utilising the ring configuration resulted in generation of single frequency idler output and the potential for further device optimisation was discussed.

The tuning ranges and output powers of the ICSRO devices presented in this thesis are summarised in table 1. It should be noted that a common set of laser and SRO optics were used for all these experiments and that the tuning ranges of these devices reflect this. It can be seen that the resonant signal field is always centred upon $\sim 1.2\mu\text{m}$ corresponding to the centre of the signal mirror bandwidth on the

optics. A choice of suitable mirror bandwidths for the signal would allow the phase-matching of any of the ranges shown within the transparency range of the nonlinear materials used.

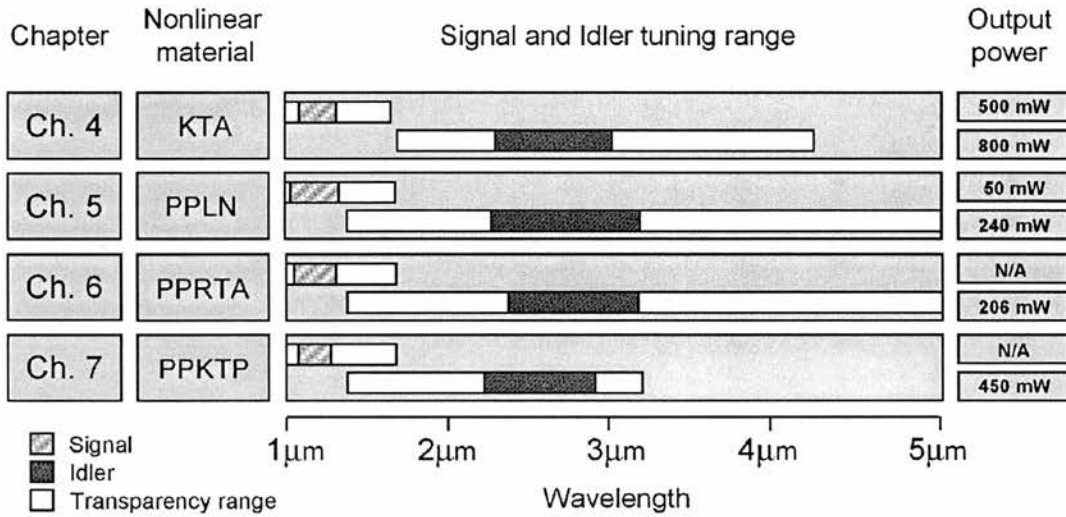


Table 1. Summary of the devices implemented in the experimental studies of this thesis.

The potential of the Ti:sapphire-pumped ICSRO has been highlighted by the work presented here. It's ability to accommodate the high thresholds and grating-design errors of emergent poled nonlinear materials is perhaps its strongest asset as a research tool. Manoeuvring the device towards more commercial applications is somewhat hindered by the unwieldy Argon-ion primary pump laser source. In the course of this work, efficient cw frequency-doubled green pump lasers with output powers of up to 10W have become commercially available and may help to drive device development towards the commercial sector. The success and prevalence of the Ti:sapphire laser itself is a good yardstick as to the potential spectrum of applications to which the Ti:sapphire-pumped ICSRO may begin to contribute. To realise the full potential of this SRO pumping approach, there are still a number of research and developmental stages to address. A brief summary of these follows.

8.2 Further research and development.

A subject that arises in the characterisation of all the devices presented here is that of maintaining simultaneous cavity stability for both the laser and SRO cavities. The optics used all have typical "off-the-shelf" radii of curvature and thus limit the range of cavity configurations that are available. An area that requires more design input is that of resonant cavity configuration. Future devices should try to avoid the situation where, though both laser and SRO cavities are stable under initial conditions, a small amount of thermal lensing within the nonlinear or laser crystal pushes one of the resonant cavities towards the limit of stability. At the limit of stability, spot sizes at both intracavity foci rapidly change and this in turn begins to limit the power-scaling of the ICSRO. A knowledge of the thermal lensing properties of the nonlinear material will play a significant part in the design optimisation of ICSRO cavity design. The starting point for this design process must be a consideration of alternative cavity designs that de-sensitise the two intracavity foci from any lensing that may scale with input power. This has been successfully achieved through the use of an intracavity lens in a Nd-based laser ICSRO [1]. This is a non-trivial engineering problem for ICSRO designs based on laser materials which possess strong thermal lensing properties. For these ICSRO devices the thermal lens itself may well be incorporated into an optimised design that remains stable only for the maximum input primary pump power. A suggestion of this effect is given by the observation of the "thermal latching" experienced with the PPLN ICSRO of chapter 5. Addressing this problem for the case of PPLN may allow for the extraction of higher output powers, although the current lack of high-power commercial PPLN devices points to (among other factors) the thermal-lensing limitations presented by this otherwise excellent nonlinear material.

For poled nonlinear materials, the observation of parasitic nonlinear processes involving the phase-matched parametric fields of the OPO process provides a visual suggestion for a further area of research. By phase-matching one or more of these mixing processes (SHG or SFM), tunable visible output may be achieved. With this in mind, two separate PPKTP crystals have been designed and acquired. The first

is used to phase-match the SHG process for the signal field in an intracavity design shown in figures 1 and 2.

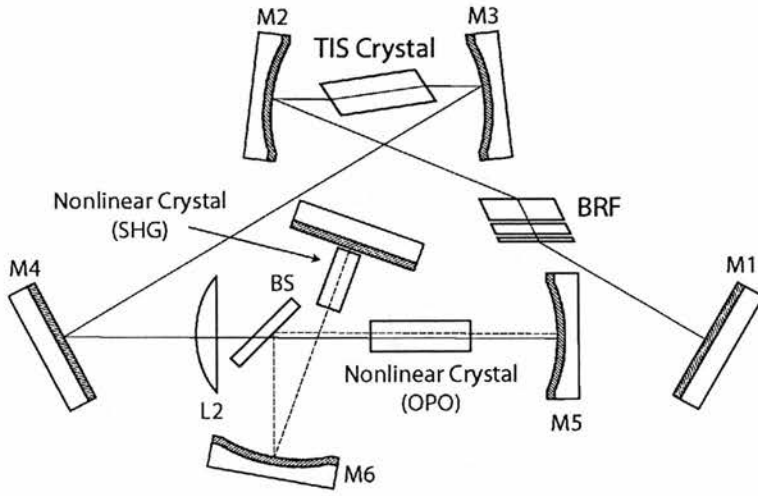


Figure 1. Cavity design for the phase-matched SHG of the signal field.

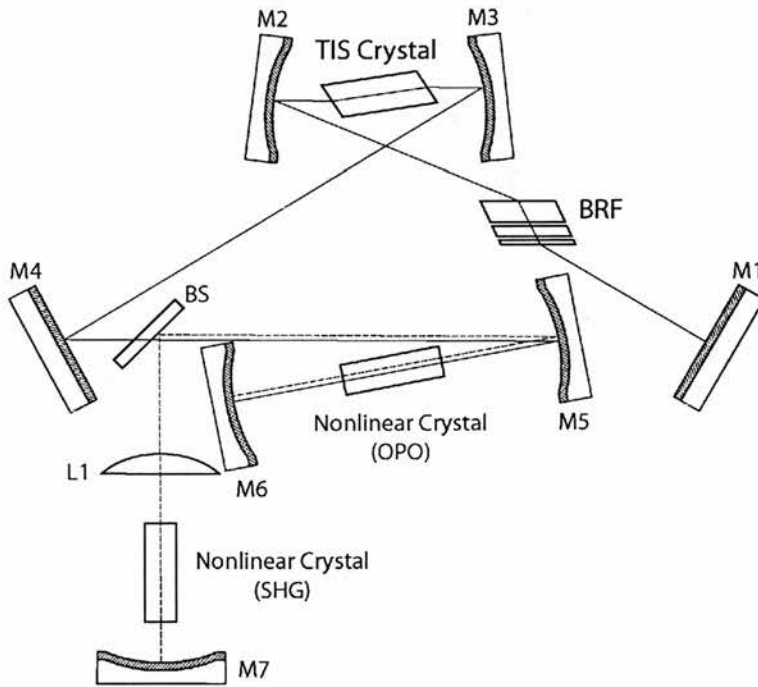


Figure 2. Alternative cavity design for SHG of the signal field.

Figures 1 and 2 show two possible designs for the implementation of the SHG experiment. A second intracavity focus must be introduced in the resonant signal cavity. A PPKTP crystal with a $12.77\mu\text{m}$ grating period located within a servo controlled oven located at this focus is calculated to phase match the signal SHG process as shown in figure 3.

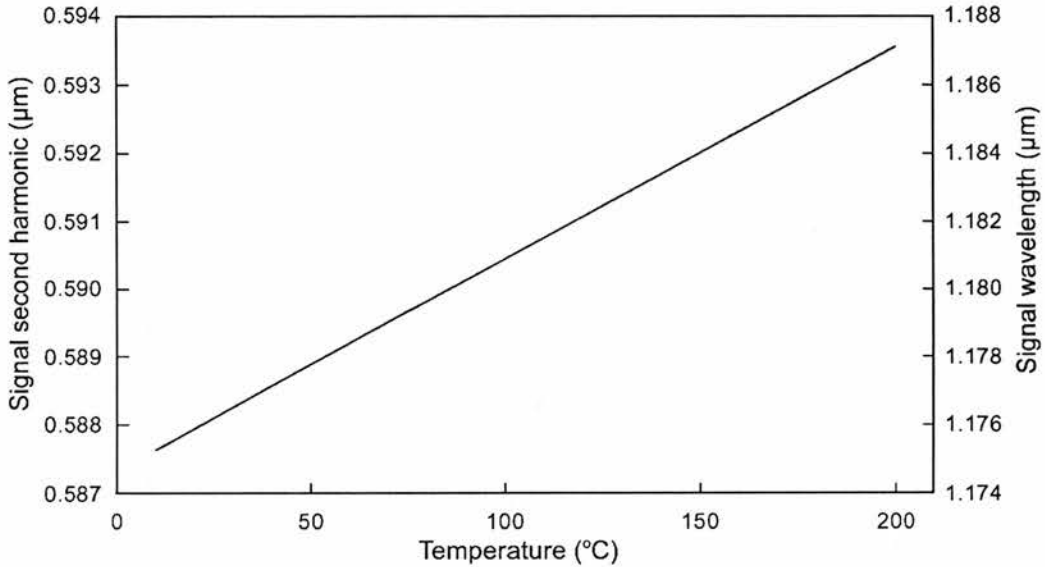


Figure 3. Calculated tuning of the signal SHG process for a PPKTP crystal with a $12.77\mu\text{m}$ grating period.

The temperature tunability of PPKTP allows for a small degree of tunability of the SHG process. Increased tuning ranges could be achieved by utilising a multi-grating crystal. It should be emphasised that the introduction of a secondary nonlinear process together with the increased round-trip losses associated with the extra signal cavity optics will increase the ICSRO threshold. Fortunately, the ICSRO pumping approach is uniquely placed to address the high threshold conditions incurred by this cavity design. An alternative approach to the design of this experiment would be to include the SHG and OPO grating on one crystal, a method successfully employed for the SFM process in an external cavity SRO [2]. With this method however, it is not possible to independently temperature-tune the second nonlinear mixing process and the OPO process. With this in mind, alternative implementations of the SFM process of pump and signal mixing is illustrated in figures 4 and 5.

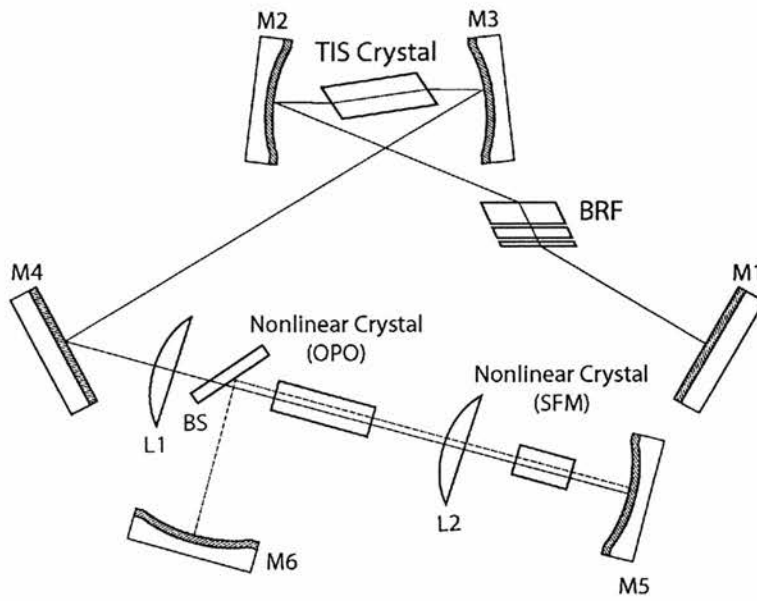


Figure 4. Possible cavity configuration of SFM pump and signal process

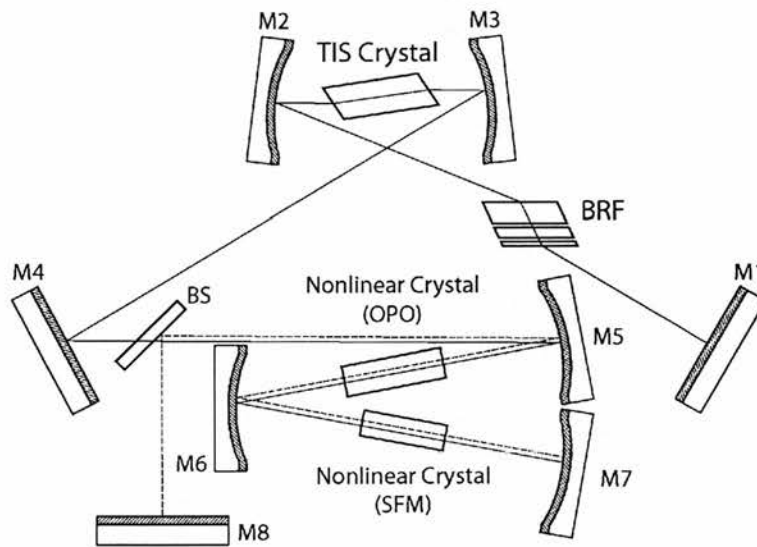


Figure 5. Alternative SFM cavity configuration

The consequence of such an experimental configuration for the Ti:sapphire laser is the generation of tunable blue-green output at about 480nm. The PPKTP crystal required to phase-match this interaction has a grating period of $6.86\mu\text{m}$ and is calculated to generate tunable blue output as shown in figure 6.

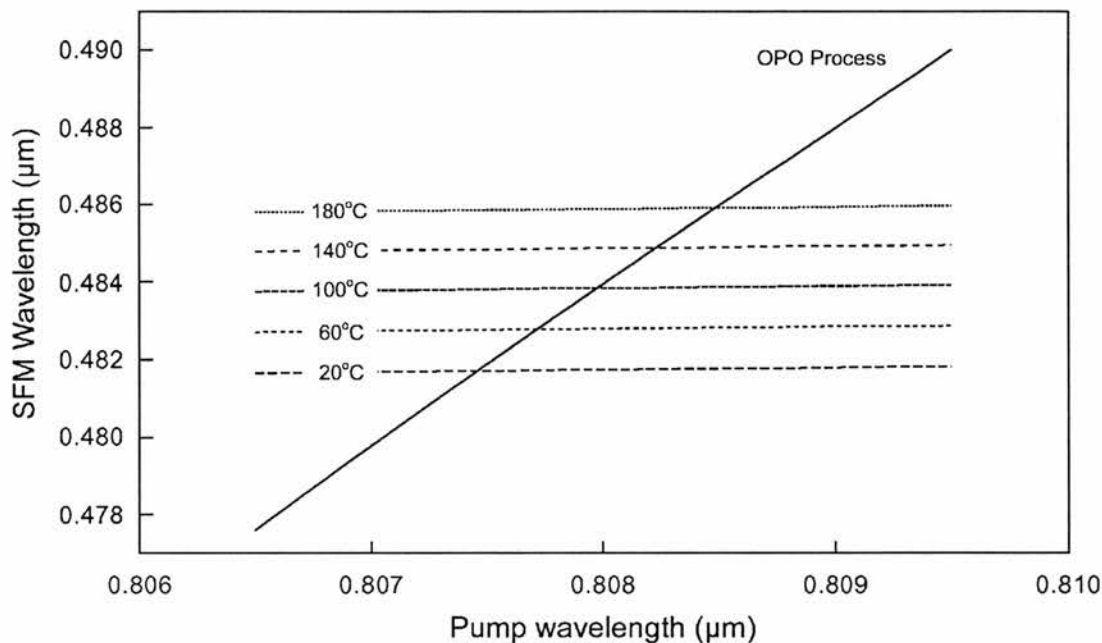


Figure 6. Calculated phase-matched output of the pump and signal SHG processes. The solid line shows the theoretical tuning as calculated from the OPO process. The dashed lines show the calculated phase-matching curves of the SHG crystal at different temperatures.

This brief overview is intended to illustrate the possible manifestation of a second nonlinear process within the SRO cavity. Further investigations will have to address the optimum strengths of the respective parametric processes. This is especially important in the case of pump and signal SFM where pump photons are required to drive both processes and thus an optimum balance must be obtained between the OPO and SFM processes in order to maintain both.

Regarding overall improvements to design, another engineering factor is that the use of intracavity ovens must be revised and appropriate engineering steps made to limit the effect of convection currents within the beam path. For a laser cavity with an overall length approaching 2m, effects of dynamic refractive index changes in the air around an oven are patently obvious in the output instability of both the laser and SRO output power. Common with many laboratory based devices, the ICSROs described in this thesis were by no means optimised as far as mechanical design is concerned. To reduce overall output instabilities, care must be taken to improve the mounting of optical components of the laser and SRO cavities.

In order to generate tunable single-frequency idler output the ICSRO must be configured with a laser ring cavity. Work towards this aim is outlined in chapter 7. One factor that emerges from initial investigations of this configuration is that the nonlinear process itself generates a unidirectional loss that drives the Ti:sapphire laser into bi-directional laser action. The simple unidirectional devices found in many ring Ti:sapphire lasers do not provide enough differential loss to compete with the parametric loss of the OPO process. Until this problem is addressed, possibly with a hybrid between an optical isolator and a unidirectional device, the further characterisation of this promising device is left in stasis.

To conclude the discussion on future research directions it is helpful to shift the perspective a little with regard to the Ti:sapphire ICSRO device as a whole. The natural commercial development process of this device seems to lie with Nd-laser based configurations. This is entirely appropriate it introduces the many advantages of diode-pumped solid state laser technology. The major drawback of this is the loss of pump tunability and subsequent reliance on the nonlinear material for device tunability. Coupled with the added complexity of the thermal characteristics for many Nd-laser host materials and this places a distinct advantage in trying to circumvent the perceived (and real) cost of Ti:sapphire based technology for which the primary pump source alone is considered a considerable investment. Rather than considering the Ti:sapphire ICSRO as a unit device, it could be considered as a simple "add-on" to an existing Ti:sapphire laser. Consider figure 7.

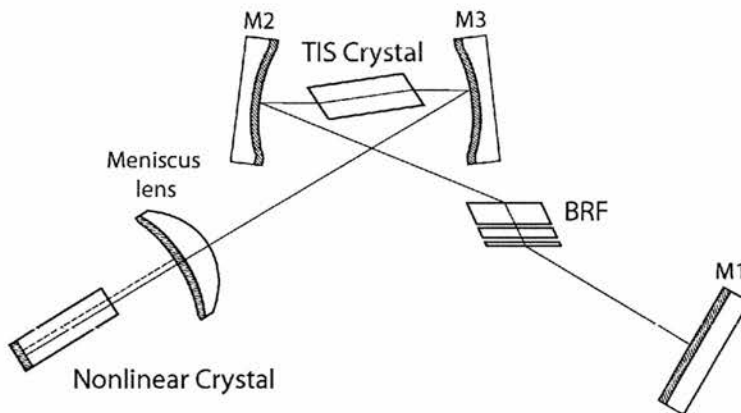


Figure 7. Simplified ICSRO design.

The layout in figure 7 shows a greatly simplified ICSRO design in which the SRO cavity is defined by the rear surface of a meniscus lens and one plane side of the nonlinear material itself. The focussing of the pump field is performed by the meniscus lens and as far as the Ti:sapphire laser is concerned the whole optical section is equivalent to a plane laser output coupler. Indeed, the Ti:sapphire ICSRO could be engineered and supplied as a simple module which replaces the output coupler already present in the laser, the laser device engineering needing no further modification. In this way, the ICSRO could reach a great number of existing Ti:sapphire laser users.

The research outlined in this thesis commenced with the aims and good intentions of realising a practical and efficient method of generating widely tunable near to mid-infrared cw coherent light. In this respect it mirrors the aims and aspirations of all scientific research in this area. It seems quite acceptable to ask what windows of opportunity have arisen and what contributions have been made by all this infrared generation and all these diagrams? This is a research field in which the arrival of a new nonlinear material can have a huge impact. That cw SROs have such large oscillation thresholds will always come down to the effective nonlinearity of the chosen material and this in turn will depend on the available interaction lengths. Beyond this, transparency range and ease of poling are other significant factors. The cw SRO above all OPO devices, relies upon accessing as high an effective nonlinearity as possible and this drastically reduces the choice of nonlinear material. In many ways, the ICSRO has proven itself unique in that it is greatly liberated from the constraints of high SRO oscillation threshold. This allows the device to accommodate an unparalleled variety of nonlinear materials whilst operating at high efficiency. This attractive characteristic is complemented by a wide variety of attractive features such as broad tunability, high efficiency and high output powers.

The research work presented highlights the ICSRO as a practical candidate for future development into a flexible spectroscopic source. The opportunities for this development span frequency spectrums from the visible to the mid-infrared and once explored, should cast new light on the pragmatic application of ICSRO technology.

Chapter 8 references

- 1 D. J. M. Stothard, M. Ebrahimzadeh and M. H. Dunn, "Low pump threshold, continuous-wave, singly resonant, optical parametric oscillator," *Optics Letters* **23**, 1895 (1998).
- 2 W. R. Bosenberg, J. I. Alexander, L. E. Myers and R. W. Wallace, "2.5W, continuous-wave, 629nm solid-state laser source," *Optics Letters* **23**, 207 (1998).

Appendix A

A 1.0 *KTP sellmeier equations along n_z*

Reference H. Liao, H. Y. Shen, Z. D. Zheng, T. Q. Lian, Y. P. Zhou, C. H. Huang, R. R. Zeng and G. F. Yu, "Accurate Values for the Index of Refraction and the Optimum Phase Match Parameters in a Flux Grown Ktiopo4 Crystal," *Optics and Laser Technology* **20**, 103-104 (1988).

Sellmeier
$$n_z(\lambda) = \sqrt{0.1494 + \frac{3.1315\lambda^2}{\lambda^2 - 0.0237}}$$

Reference D. W. Anthon and C. D. Crowder, "Wavelength Dependent Phase Matching in Ktp," *Applied Optics* **27**, 2650-2652 (1988).

Sellmeier
$$n_z(\lambda) = \sqrt{2.006239 + \frac{1.2965213\lambda^2}{\lambda^2 - 0.04807691} + \frac{1.1329801\lambda^2}{\lambda^2 - 100}}$$

Reference H. Vanherzeele, J. D. Bierein and F. C. Zumsteg, "Index of refraction measurements and parametric generation in hydrothermally grown KTiOPO₄," *Applied Optics* **27**, 3314 (1988).

Sellmeier
$$n_z(\lambda) = \sqrt{2.3136 + \frac{1.00012}{1 - \left(\frac{0.23831}{\lambda}\right)^2} - 0.01679\lambda^2}$$

Reference K. Kato, "2nd-Harmonic and Sum-Frequency Generation to 4950- μ m and 4589- μ m in Ktp," *IEEE Journal of Quantum Electronics* **24**, 3-4 (1988).

Sellmeier
$$n_z(\lambda) = \sqrt{3.3134 + \frac{0.05694}{\lambda^2 - 0.05658} - 0.01682\lambda^2}$$

Reference V. A. Dyakov, V. V. Krasnikov, V. I. Pryalkin, M. S. Pshenichnikov, T. B. Razumikhina, V. S. Solomatin and A. I. Kholodnykh, "The Sellmeier Equation and Tuning Characteristics of Ktp- Crystal Frequency-Converters in the Range from 0.4 to 4.0- μ m," *Kvantovaya Elektronika* **15**, 1703-1704 (1988).

Sellmeier
$$n_z(\lambda) = \sqrt{1.9446 + \frac{1.36170}{1 - \frac{0.047}{\lambda^2}} - 0.01491\lambda^2}$$

Reference K. Fradkin, A. Arie, A. Skliar and G. Rosenman, "Tunable mid-infrared source by difference frequency generation in bulk periodically poled KTiOPO₄," *Applied Physics Letters* **74**, 914-916 (1999).

Sellmeier
$$n_z(\lambda) = \sqrt{2.12725 + \frac{1.18431}{1 - \frac{5.148252 \cdot 10^{-2}}{\lambda^2}} + \frac{0.6603}{1 - \frac{100.00507}{\lambda^2}} - 9.68956 \cdot 10^{-3} \lambda^2}$$

Reference T. Y. Fan, C. E. Huang, B. Q. Hu, R. C. Eckardt, Y. X. Fan, R. L. Byer and R. S. Feigelson, "Second harmonic generation and accurate index of refraction measurements in flux-grown KTiOPO₄," *Applied Optics* **26**, 2390 (1987).

Sellmeier
$$n_z(\lambda) = \sqrt{2.25411 + \frac{1.06543}{1 - \frac{0.05486}{\lambda^2}} - 0.02140\lambda^2}$$

Appendix B

B 1.0 Journal Publications

- 1 G. A. Turnbull, T. J. Edwards, M. H. Dunn and M. Ebrahimzadeh, "Continuous-wave singly-resonant intracavity optical parametric oscillator based on periodically-poled LiNbO₃," *Electronics Letters* **33**, 1817-1818 (1997).
- 2 T. J. Edwards, G. A. Turnbull, M. H. Dunn, M. Ebrahimzadeh and F. G. Colville, "High-power, continuous-wave, singly resonant, intracavity optical parametric oscillator," *Applied Physics Letters* **72**, 1527-1529 (1998).
- 3 T. J. Edwards, G. A. Turnbull, M. H. Dunn, M. Ebrahimzadeh, H. Karlsson, G. Arvidsson and F. Laurell, "Continuous-wave singly resonant optical parametric oscillator based on periodically poled RbTiOAsO₄," *Optics Letters* **23**, 837-839 (1998).
- 4 M. Ebrahimzadeh, G. A. Turnbull, T. J. Edwards, D. J. M. Stothard, I. D. Lindsay and M. H. Dunn, "Intracavity continuous-wave singly resonant optical parametric oscillators," *Journal of the Optical Society of America B-Optical Physics* **16**, 1499-1511 (1999).
- 5 T. J. Edwards, G. A. Turnbull, M. H. Dunn and M. Ebrahimzadeh, "Continuous-wave, singly-resonant, optical parametric oscillator based on periodically poled KTiOPO₄," *Optics Express* **6**, 58-63 (2000).

B 1.1 Conference Publications

CLEO 1997, Baltimore, USA (May 1997)

- 1 F.G. Colville, T.J. Edwards, G.A. Turnbull, M.H. Dunn and M. Ebrahimzadeh, "Continuous-wave intracavity optical parametric oscillators".

Quantum Electronics 13, Cardiff, UK (September 1997)

- 2 T.J. Edwards, G.A. Turnbull, M.H. Dunn and M. Ebrahimzadeh, "High power, continuous-wave singly-resonant intracavity optical parametric oscillator".
- 3 G.A. Turnbull, T.J. Edwards, M.H. Dunn and M. Ebrahimzadeh, "A continuous-wave singly-resonant intracavity optical parametric oscillator based on PPLN".

CLEO 1998, San Francisco, USA (May 1998)

- 4 T.J. Edwards, G.A. Turnbull, M.H. Dunn and M. Ebrahimzadeh, "Continuous-wave singly-resonant optical parametric oscillator based on periodically-poled RbTiOAsO₄". (*Invited talk*)

CLEO/Europe 1998, Glasgow, UK (September 1998)

- 5 T.J. Edwards, G.A. Turnbull, M.H. Dunn and M. Ebrahimzadeh, "Continuous-wave singly-resonant optical parametric oscillator based on periodically-poled RbTiOAsO₄".

Physics Research for Britain, Oxford, UK (November 1998)

- 6 T.J. Edwards, G.A. Turnbull, D.J.M. Stothard M.H. Dunn and M. Ebrahimzadeh, "Laser Sources for the Near-to-Mid Infrared".

CLEO 1999, Baltimore, USA (May 1999)

- 7 T.J. Edwards, G.A. Turnbull, M.H. Dunn, M. Ebrahimzadeh, H. Karlsson and F. Laurell "Continuous-wave singly-resonant optical parametric oscillator based on periodically-poled KTiOPO₄".